UNIVERSITY OF
CAMBRIDGE

Weighing the Universe with Weak Gravitational Lensing

Richard James Massey

Clare College
Institute of Astronomy

This dissertation is submitted for the degree of Doctor of Philosophy

Contents

Declaration

I hereby declare that my dissertation entitled *Weighing the Universe with Weak Gravitational Lensing* is not substantially the same as any that I have submitted for a degree or diploma or other qualification at any other University. I further state that no part of my dissertation has already been or is being concurrently submitted for any such degree, diploma or other qualification.

This dissertation is the result of my own work and includes nothing which is the outcome of work done in collaboration, unless stated explicitly. Those parts of this dissertation which have been published, or are in press, are listed below:

- Chapter 3 draws upon work published in "*Cosmic Shear with Keck: Systematic Effects*", Massey, Bacon, Refregier & Ellis 2001, in A New Era in Cosmology, eds. T. Shanks and N. Metcalfe; and "*Joint Cosmic Shear Measurements with the Keck and William Herschel Telescopes*", Bacon, Massey, Ellis & Refregier 2003, MNRAS 344, 673; and submitted for publication in MNRAS as "*Cosmic Shear results from the William Herschel Telescope*", Massey, Refregier, Bacon & Ellis 2004.
- Chapter 4 draws upon work in "*Polar shapelets*", Massey & Refregier 2004, in preparation, to be submitted to MNRAS.
- Chapter 5 draws upon work published in "*Image Simulation with Shapelets*", Massey, Refregier, Conselice & Bacon 2004, MNRAS in press.
- Chapter 6 draws upon work published in "*Weak Lensing from Space I: Prospects for the SuperNova/Acceleration Probe*", Rhodes, Refregier, Massey *et al.* 2004, Astroparticle Physics 20,377; "*Weak Lensing from Space II: Dark Matter Mapping*", Massey, Refregier, Rhodes *et al.* 2004, AJ in press; "*Weak Lensing from Space III: Cosmological Parameter Estimation*", Refregier, Massey, Rhodes *et al.* 2004, AJ in press; and "*Probing Dark Matter and Dark Energy with Space-Based Weak Lensing*", Massey, Refregier & Rhodes 2003, in Gravitational Lensing: a Unique Tool for Cosmology, eds. J.-P. Kneib, D. Valls-Gabaud & G. Soucail.

This dissertation contains fewer than 60,000 words.

Richard Massey
Cambridge
January 2004.

Abstract

Weak gravitational lensing by large-scale structure provides a unique probe of density fluctuations in the universe. Gravitational lensing is directly sensitive to mass (rather than light), and is therefore closely tied to modern cosmological theories, whose predictions are dominated by the distribution of an otherwise invisible component of dark matter. The "cosmic shear" effect induces coherent distortions in the shapes of distant galaxies, caused by gravitational light deflection from foreground matter along their line-of-sight. The analysis of cosmic shear data therefore relies upon the geometry of the foreground matter distribution, and the accurate measurement of galaxy shapes. This technique is equally sensitive to all mass, regardless of its nature or state. In particular, its systematic biases are not limited by unknown physics such as biasing or the mass-temperature relation for x-ray selected galaxy clusters.

In this thesis, we perform a cosmic shear survey using the 4.2m William Herschel Telescope on La Palma and the 10m Keck telescope on Hawaii, to a depth of $R = 26$ ($z \approx 1$). The shear power spectrum is measured on scales from $1'$ to $16'$, and, by fitting theoretical models, we obtain constraints on cosmological parameters with a precision approaching that possible with other methods. We find that the normalisation of the matter power spectrum on 8 Mpc scales, $\sigma_8 = 1.09 \pm 0.12 \times (\Omega_m/0.3)^{-0.51}$, with the the current density of mass in the universe Ω_m between 0.25 and 0.8.

To calibrate new shape measurement algorithms, and to investigate the possible precision of future surveys, we have developed a method to accurately simulate deep astronomical images. These include realistic galaxy morphologies and telescope characteristics drawn from engineering models. The galaxies are based upon Hubble Deep Field objects, and parameterized according to the "shapelets" formalism, which has been further developed for our purposes. The complete shapelet basis set enables the modelling of spiral arms, bars, discs, arbitrary radial profiles and even dust lanes or knots: an important advance for high-precision shape measurement. We demonstrate that the images are realistic by showing that simulated and real data have consistent distributions of morphology diagnostics including galaxy size, ellipticity, concentration and asymmetry statistics.

The unique nature of its systematic errors, coupled with high resolution and stable imaging from space, makes the outlook for cosmic shear highly promising. A proposed

300 square degree survey to $R \simeq 28$ should determine Ω_m to within 1.5%. It will also create projected mass maps with a resolution of 1 arcmin^2, and mass-selected cluster catalogues with a 1σ sensitivity of approximately $10^{13} M_\odot$ at $z = 0.25$. These will trace the evolution of structure over time, testing the gravitational instability paradigm, and providing the ideal laboratories to investigate those complex astrophysical processes which are the limiting systematics in other cosmological tests.

Acknowledgements

I've always quite a hopeless idealist about such things as science, and I have to confess that my ambition has been to place just one more brick in the wall of human knowledge. All in all, this thesis is that brick (even if it may get more frequently used as a door-stop or a bookend). I can not claim to have always held a burning desire for my particular brick to be in the field of astronomy. Nor can I claim, like some, that I grew up looking through telescopes in the back garden (quite the contrary as poor old Anthony would testify). So I should first ascribe the inspiration to look upwards on my way home from the pub to Roger Davies. While I was an undergraduate at Durham, I was persuaded to spend a summer holiday at the Anglo-Australian Telescope: with Quentin Parker, Malcolm Hartley, Céline Péroux and the friendly folk of Coonabarabran. There are few diversions in Coona, so I spent a long time between observations chasing kangaroos across the outback, sitting in the Jolly Cauli coffee shop, and listening to their one Bryan Adams CD on repeat. There really are *no* music shops in Coona! Nevertheless, this astronomy malarkey was certainly more appealing than the national minimum wage in the double-glazing factory back home.

Spending a second university summer holiday at the Joint Astronomy Centre in Hawaii confirmed my growing enthusiasm to study faraway and exotic physical environments. I am very grateful to Andy Adamson and Tim Hawarden for teaching me everything about telescopes that I should have picked up from nights in the back garden with Anthony. Thanks also to Douglas Pierce-Price, Deepak, Brad, Chad and Kristen for keeping me entertained during the long, hard days at the beach! While we are on the subject of Hawaii, I should also thank Alice Shapley for pointing out the best Mai-Tai beach bar on the island. If I ever piece together the fuzzy memories and recall exactly where it is, I'll be lounging back on their hammocks in a flash.

I am very grateful for Shaun Cole's dedicated help supervising my master's thesis back at Durham. I don't know what I started doing wrong when I then moved to Cambridge, for I scared off so many PhD supervisors in the course of only three years. However, I really don't mind: thank you all for the opportunity for expense-account jollies to your new universities! Of course, I am most endebted to Alexandre Refregier, who has always made himself available at the other end of a phone. You have reassured me that it *is* possible to sneak a bit of "proper" maths into astronomy, but thank you also

for the incidental instruction in politics, modern art and strong black coffee: the *entente cordiale* is alive and well. Richard Ellis's transatlantic aid packages have also been indispensable, and I am very grateful for his stalwart support throughout: be it in dollars, telescope time, or the friendly reassurance and football commentary only possible from a fellow Brit over in the colonies. Ofer Lahav very kindly stepped into the breach and was thanked at the time with a barrage of red tape. Also David Bacon, who took me under his wing and guided me through such day-to-day conundrums as why there *really* need to be quite so many commas in IDL.

Collaborators and other astronomers I've enjoyed meeting include Justin Albert, Gary Bernstein, Richard Bower, Sarah Bridle, Tarun Deep-Saini, Phil Marshall and Lindsay King. I've particularly enjoyed getting to know the political views of Jason Rhodes and Chris Conselice — at least Chris has the excuse that he comes from Florida! I'm also very grateful to Andy Bunker, Simon Hodgkin, Ian Parry, Jochen Weller and Dr. Lisa Wright for periodically supplementing my student grant at the poker table.

My years at the IoA would have been far less fun and certainly contained fewer tea breaks without my contemporaries here: including Adam Amara, Richard Alexander, Carine Babusiaux, Clemens Bayer, Fraser Clarke, Jim Dale, Eduardo Delgado-Donate, Richard Edgar, Pirin Erdogdu, Colin Frayn, Poshak Gandhi, Maggie Hendry, Anthony Horton, Rob Izzard, Peter Johansson, Chris Jordinson, Phil Kendall, Dougal Mackey, Steve Moody, Enrico Ramirez-Ruiz, Justin Read, Sam Rix, Jeremy Sanders, Rob Sharp, Mark Sullivan, Will Thorne and Viv Wild. I have particularly fond memories of the camaraderie developed during the giant snowball battle of 2003, when our forces rallied against an invading horde from the Cavendish. Our crack suicide squads, and a concentrated bombardment from our rooftop snipers, sent the horde fleeing straight into "flanking manoeuvres" by our concealed artillery. Or perhaps they were just trying to stay concealed?

Thank you throughout to all of my other, non-astronomy friends for being variously more dippy, dodgy, cool, clever, Yorkshire or U than me; thus giving my every mood swing somewhere to feel at home. You know who you are (and you can pick your own adjective). But the very biggest thanks, of course, go to my nearest and dearest, friends and family. Lisa, who has kept me laughing at everything and singing in the shower (it's only the water that makes it sound out of tune, honest). Mum and Dad, for not *really* minding that their son is still at university at the age of 26. And Granny, hey look! Cosmology: I finally got an "ology"!

Thank you all,
Richard

Just remember that you're standing on a planet that's evolving,
And revolving at 900 miles an hour,
That's orbiting at 19 miles a second, so it's reckoned,
A sun that is the source of all our power.
The sun and you and me and all the stars that we can see,
Are moving at a million miles a day,
In an outer spiral arm at 40,000 miles an hour,
Of the Galaxy we call the Milky Way.

Our Galaxy itself contains 100 billion stars
It's 100,000 light years side to side.
It bulges in the middle, 16,000 light years thick,
But out by us it's just 3,000 light years wide.
We're 30,000 light years from galactic central point,
We go round every 200 million years
And our galaxy is only one of millions of billions
In this amazing and expanding Universe.

The Universe itself keeps on expanding and expanding,
In all of the directions it can whizz.
As fast as it can go, at the speed of light you know,
12 million miles a minute and that's the fastest speed there is.
So remember when you're feeling very small and insecure
How amazingly unlikely is your birth,
And pray that there's intelligent life somewhere up in space,
Because there's bugger all down here on Earth.
— Monty Python.

Included for my own reference as much as anything else.

1 Introduction for non-astronomers

1.1 Our expanding universe

The universe began about 13 thousand million years ago, in a hot Big Bang. During a brief period known as "inflation", which lasted only for a tiny fraction of a second, the universe expanded rapidly. Immediately after inflation, the rate of expansion dropped dramatically; but the universe continued to expand slowly. The universe then coasted for the next 9 thousand million years. During all that time however, this expansion was being gradually slowed by the gravitational attraction of the universe's own contents, which was trying to pull it back together. The gravity of normal "baryonic" matter (which includes stars, dust, and everything else that we can see around us) was being helped in this task by an additional component of invisible "dark matter". Although dark matter seems to have the same gravitational attraction as baryonic matter, it does not emit light, at any wavelength. This makes it very difficult to detect directly, and it is only by the indirect gravitational influence of dark matter that we know it is there at all.

During this slow overall expansion, small, isolated pockets of mass began to collapse. The first stars and galaxies were formed from clouds of hydrogen in the early universe. Figure 1.1 shows galaxies after about 6 thousand million years of evolution, some already with spiral arms that resemble those in the modern Milky Way. As more galaxies were created, their random motions within the universe brought them into collisions with their neighbours. Galaxies merged, a process that further changed their shapes; and galaxies joined together into gravitationally-bound groups or clusters. This hierarchical growth has continued until today, creating a complex filamentary network of

large-scale structure, from the bottom up. The most massive objects in the universe are now giant super-clusters of galaxies, each having captured several thousand individual galaxies and weighing some 100-1000 billion times the mass of the sun.

Around 4 thousand million years ago, the universe appears to have entered a new and unexpected stage of evolution. By that time, the universe's expansion had diluted both its baryonic and its dark matter content. As the influence of their gravity weakened, a previously unnoticed form of mass-energy began to emerge into dominance from underneath it. Frustratingly, this substance is again not directly visible, and it has been given the equally unilluminating name "dark energy". The properties of dark energy are less-understood and even more peculiar than those of dark matter. For instance, it has a strange negative pressure. This acts like a source of anti-gravity, and is beginning to re-accelerate the expansion of the universe, long after the big bang. Science fact can indeed turn out stranger than science fiction!

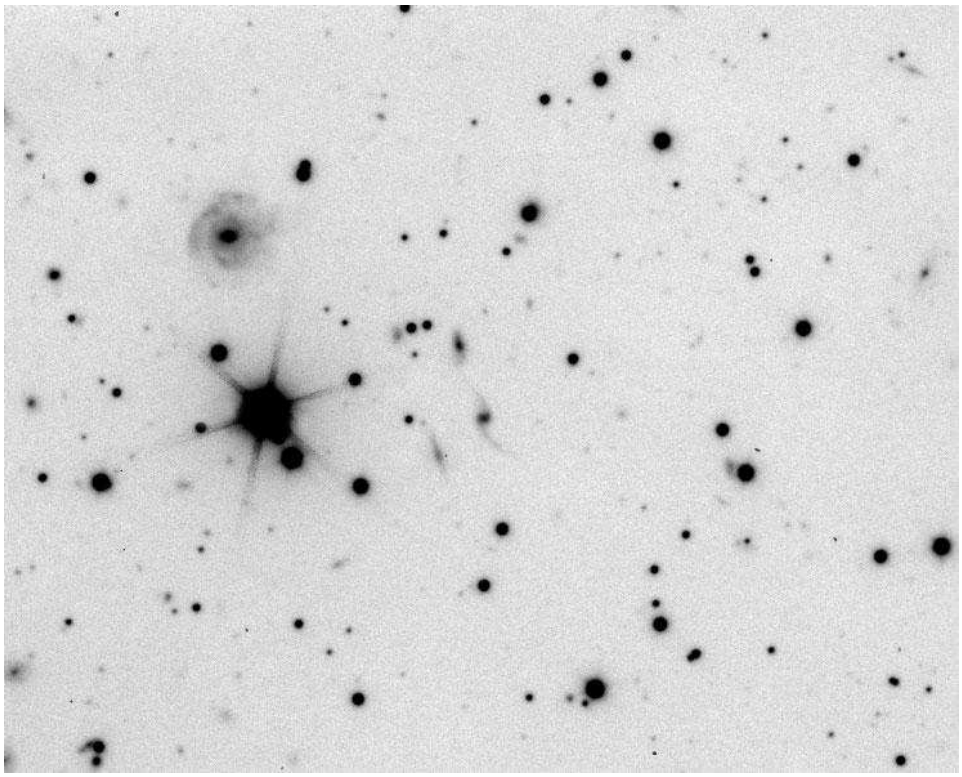

Figure 1.1: A deep image of the night sky taken with the 10m Keck telescope on Mauna Kea, Hawaii. The large, hexagonal object is a bright foreground star; everything else is a distant galaxy. Because of the finite speed of light, we see these galaxies as they would have looked a long time ago. The faintest objects are from the early universe and are the progenitors of galaxies like the Milky Way. The size of this whole image is just 2×1.5 minutes of arc: It would take almost 300 of these patches to cover the full moon.

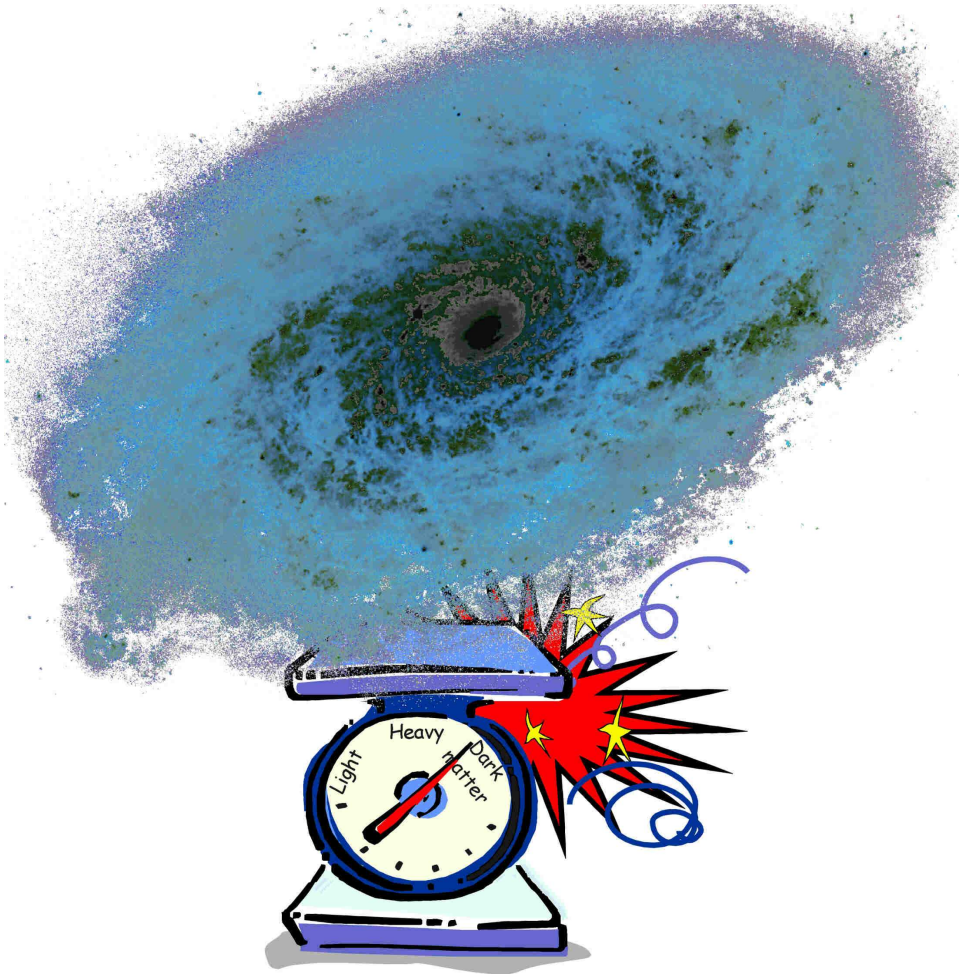

Figure 1.2: An increasing number of astrophysical phenomena cannot be accounted for if the mass in the universe were limited to the normal "baryonic" matter that forms stars and shines in the night sky. Spiral galaxies like NGC 4414 (Hubble Space Telescope image courtesy of NASA)spin around too fast at their edges. Whole galaxies stay gravitationally bound within clusters, despite reaching speed that ought to fling them out. All of these objects, and the universe itself, must contain an extra and mysterious component of invisible "dark matter". There is about five times as much dark matter in the universe as there is baryonic matter: enough to also affect the overall evolution of the universe.

1.2 The dark side of the universe

Normal baryonic matter makes up only about a sixth of the mass in the universe today, distributed amongst dust clouds, stars and galaxies. This amount is insufficient to account for an increasing array of astrophysical phenomena without an additional component of dark matter. For example, spiral galaxies like the Milky Way or galaxy NGC 4414 (shown in figure 1.2) spin around faster at their edges than would be possible if they only contained the mass within their visible stars. Clusters of galaxies must also be far more massive than they seem from counting just their visible light, because the galaxies in them sustain velocities that would otherwise fling them out of the cluster.

And if the entire mass of the universe were limited to only the visible galaxies and clusters of galaxies, the rapid expansion started by the Big Bang could not yet have been sufficiently slowed for the world around us to be assembled. Indeed, if there turns out to be a lot of dark matter, the expansion of the universe will eventually stop, and it will collapse back in on itself for a "Big Crunch" in another few tens of thousand million years. On the other hand, the new dark energy component may instead re-accelerate the expansion of the universe, and eventually tear it apart in a "Big Rip"!

We are left with the unsettling prospect that our fate, along with some 83% of the mass in the universe, is of completely unknown form. Theories in cosmology and astrophysics are chiefly able to deal with just mass and gravity; they cannot therefore distinguish between baryonic and dark matter. Dark energy is even further beyond everyday experience, and it is a bewildering coincidence that mankind has evolved at precisely the same moment that dark energy becomes important. Standard physics does not yet have a satisfactory explanation for either of these substances. Indeed, we know neither *what* they are, nor even exactly *where* they are!

I shall not be able to directly investigate the nature of dark matter or dark energy in this thesis, but I will examine how much dark matter there is, and begin to find out how it is distributed. Is it spread thinly but everywhere, in a uniform soup? Or is it clumpy, with substructure like clusters, walls and voids? The first port of call in any exploration has always been to draw a map of the unexplored territory, and to figure out the size of whatever it is that we're up against. In the search for dark matter, the map will certainly be large, and the "You Are Here" sign is going to be right at the centre. We shall embark on this exploration using a technique rooted in Einstein's theory of General Relativity, but which has only been of practical use within the last ten years. Recent advances in telescope technology and the improved precision of optical instruments have made this measurement possible.

1.3 Using gravity to look around corners

Of all the theories drummed home by earnest physics teachers, the first one to forget is that light always travels in straight lines! Although this is certainly true most of the time, it is not always necessary. And the reason for this comes down to the way that gravity works. Gravity goes one better than dropping apples onto unsuspecting scientists' heads. According to general relativity, gravity in fact bends the entire fabric of the universe!

A common way to demonstrate this bending needs a big sheet of rubber (see figure 1.3). The rubber sheet represents a two-dimensional slice through space. When the mass of a planet or a star is placed in the centre of the sheet, the rubber sheet stretches, and the grid drawn upon it is warped. In figure 1.3, the central mass has sunk out of view. A second massive body is illustrated by the yellow sphere. This experiences the

Figure 1.3: Rubber sheet analogy to describe the distortions wrought into the fabric of space and time by the action of gravity. A mass in the centre of the grid, which has sunk out of view off the bottom of the image, has stretched space around it like a sheet of rubber. A second mass, shown as a yellow sphere, will either fall into or orbit around the first mass, depending upon its initial velocity along the sheet. But because the very universe has been distorted, so is everything within it: not just falling apples and orbiting planets, but even the previously straight paths of light rays.

curved space around the first object as gravitational pull towards the centre. An apple would fall towards the centre of the Earth. A planet would either fall into the sun or orbit safely around it, depending upon its initial velocity along the sheet.

But gravity is more subtle than that. Since the entire fabric of the universe has been stretched, *every* part of the tapestry woven into it becomes distorted. This even includes rays of light. The light paths that were once straight lines now also curve towards the central mass. For example, a black hole is just an object so extremely dense that nearby light paths are curved right in on themselves, so the light can never escape. Near a massive object, it is therefore possible to see around corners. The first experimental confirmation of this theory came during a solar eclipse in 1919. It is obviously impossible to see stars next to the sun most of the time. But when the moon passed in front of the sun, and the sky went dark, their positions could be measured. Stars near the sun had moved slightly from their normal positions, because the sun's gravity was deflecting their light. In fact, light rays which graze the surface of the sun are bent by $1.75''$, or 0.0005°. Modern techniques using radio telescopes to accurately determine the positions

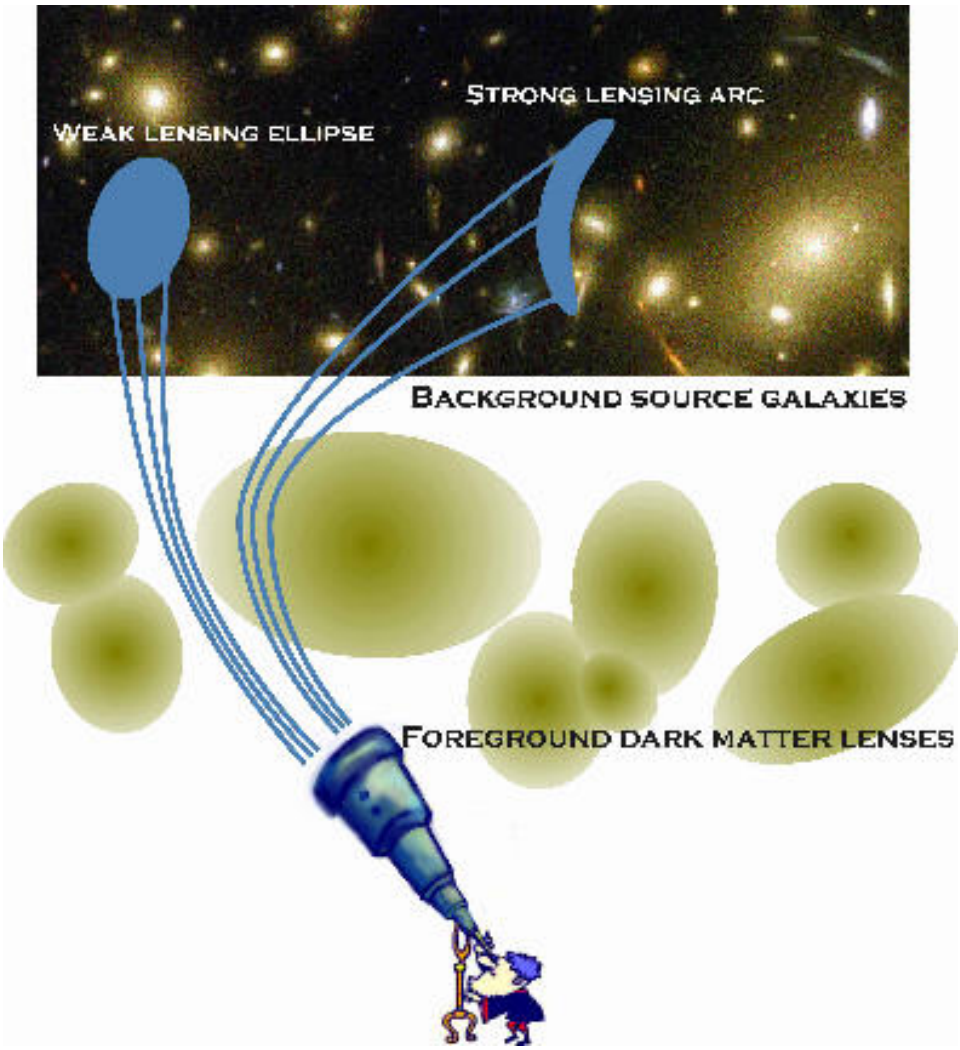

Figure 1.4: Exaggerated cartoon illustrating the effect of gravitational lensing. Foreground dark matter haloes around galaxy clusters deflect the light paths from background galaxies and distort their shapes. A circular source in the "weak lensing" regime around the outskirts of a cluster is stretched into an ellipse observed from Earth. If the light passes through the "strong lensing" regime near the centre of a cluster, the source can be highly distorted into giant arcs and multiple images. In the background is a Hubble Space Telscope image of cluster Abell 2218 (source: NASA).

of stars have confirmed the theory with astonishing precision.

Crucially, this light deflection is due only to the gravitational pull of the central object. As that mass increases, light is deflected through larger and larger angles. And because gravity does not distinguish between baryonic matter and dark matter, a measurement of this effect will be sensitive to the *total* mass of an object, irrespective of its nature and composition. Now that our telescopes are capable of measuring the small angles involved, we can explore the universe in ways that were previously unavailable to astronomy. Using just basic geometry to work out some deflection angles, we can map out the otherwise invisible distribution of dark matter.

1.3.1 Strong gravitational lensing

The distortion of light rays is greatest near massive clusters of galaxies like Abell 2218, which is shown in the background of figure 1.4. This cluster is so massive that the light from galaxies behind it has been deflected through angles large enough to stretch their images into arcs. In fact, each background galaxy may be visible as several distinct arcs, like the "multiply-imaged" pair of light blue objects in the top right-hand corner. In this case, there were at least two different routes that the light could take around the cluster and still get deflected towards the Earth. If a background galaxy is lined up exactly with the foreground cluster, light from it can take any route around the intervening mass, so the arcs stretch into a full circle known as an *Einstein ring*.

Gravitational light deflection is known as "lensing" because a similar bending and focussing of light also happens in the lens from a pair of spectacles or a magnifying glass. The arcs in figure 1.4 have also been highly magnified by the gravitational lensing of cluster Abell 2218. A massive cluster acts like a giant natural telescope, enabling us to see fainter or more distant objects than is otherwise possible. The arcs are indeed much farther away than similarly bright objects elsewhere in the figure. That extra distance makes this picture fascinating, because the finite speed of light means that its light has taken a long time to reach us. In fact, light from the faintest arcs around Abell 2218 left a galaxy up to 12 thousand million years ago, letting us directly observe conditions in the very early universe.

1.3.2 Weak gravitational lensing

Clusters of galaxies are relatively rare objects. To measure the *average* density of the universe today, we need to look away from clusters and find a more representative sample. The large-scale distribution of galaxies has already been investigated using surveys like the Anglo-Australian Telscope's "2dF" survey, named after the instrument's 2 square degree field of view. Results from 2dF, reproduced in figure 1.5, show that galaxies are distributed in a cellular network, with small concentrations making up filaments and walls around huge empty voids.

The network of 2dF galaxies roughly trace the foreground mass distribution, which gravitationally lenses background objectss — although in less spectacular style than around massive clusters. Light gets only slightly deflected when it passes through the large-scale structure or the outskirts of a cluster. In the same way that text appears distorted when it is viewed through the edge of a cheap magnifying glass, the images of distant galaxies appear slightly stretched in one direction. All distant galaxies are viewed through this ubiquitous network, and weak lensing makes any deep observation seem like a view through a distorted window pane, or one of those terrible glass bricks used in 1970's bathrooms.

The small distortions created by weak gravitational lensing are not visible to the

naked eye, and are not detectable in the image of any individual galaxy. The distortion has to be measured statistically, by averaging the shapes of many distant galaxies in a patch of sky. The galaxies' own spiral or elliptical shapes cancel out when they are averaged, and produce a circle. However, if the shapes of adjacent galaxies have all been elongated a little *in the same direction*, the residual after averaging will instead be an ellipse like that shown in figure 1.4. From the orientation and axis ratio of such ellipses, it is possible to infer the intervening mass along a lone of sight. The mass can then be mapped out to determine the location of dark matter clumps, and analysed statistically to measure the total weight of the universe.

At the risk of spoiling the ending, but to save your searching through the rest of this thesis, I shall give away the answer. The average density of the universe is approximately 10^{-23} grams (about one hydrogen atom plus five equivalent units of dark matter) per cubic metre. That might not seem much, but then the universe is *very* big!

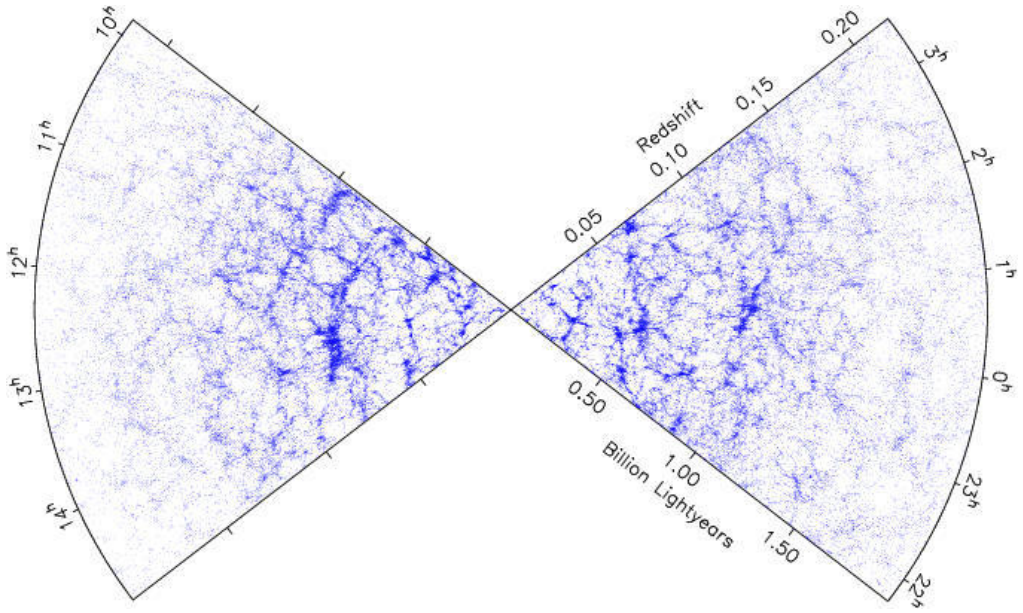

Figure 1.5: The large-scale structure of the universe seen by the Anglo-Australian Telescope 2dF Galaxy Redshift Survey (Colless *et al.* 2001). The Earth is at the centre, and every blue dot represents the location of a galaxy in two thin slices extending out into the universe. The observed density of galaxies decreases far away from the Earth because they appear fainter and are more difficult to detect. Notice the cellular and filamentary patterns in the distribution of large-scale structure. These all act as small gravitational lenses, distorting light rays from background galaxies as they navigate through this network to produce the cosmic shear effect.

2 Background theory

2.1 Cosmology

2.1.1 The Big Bang and expansion of the universe

The key discoveries in the development of modern cosmological models began with Hubble's 1929 observation that galaxies in all directions are moving away from the Milky Way, caught up in the overall expansion of the universe. As Layzer (1957) and Shane *et al.* (1959) looked on larger and larger scales, a surprising homogeneity became apparent in the distribution of galaxies: even regions of the universe too far apart to be causally connected today were sufficiently close to have interacted in the past. Penzias & Wilson (1965) then discovered the ubiquitous Cosmic Microwave Background (CMB) radiation, a remnant of the hot early universe that had been cooled by the subsequent expansion of the universe to its current temperature of 2.7K. The standard picture of the universe that we have today is based around the "Big Bang inflationary model", pioneered by Guth (1981).

The cornerstone for all of this is *Hubble's law*

$$\vec{v} = H\vec{r}\,, \tag{2.1}$$

which relates an object's recession velocity $\vec{v}$ away from us to its overall distance $\vec{r}$. The constant of proportionality is known as *Hubble's constant*. We can parameterize the size of the universe by a *scale factor* $a(t)$, which is normalised so that its size today is unity. (The present value of other time-varying quantities will be denoted by a subscript 0.)

Noting that the proper (real space) separation $\vec{r}$ between two galaxies is proportional to $a(t)$, we recover Hubble's law if

$$H = \frac{\dot{a}(t)}{a(t)} , \tag{2.2}$$

where the dot denotes differentiation with respect to time, and the comoving size is related to the *cosmological redshift* z by

$$a(t) = \frac{1}{1+z} . \tag{2.3}$$

Notice that Hubble's "constant" can in general vary as a function of time. For later convenience, we define a dimensionless parameter h based upon its value today

$$H_0 \equiv 100h \,\mathrm{km\,s^{-1}\ Mpc^{-1}} . \tag{2.4}$$

The best measurements of this parameter are from the HST key project: $h = 0.72 \pm 0.02$ (Freedman *et al.* 2001) and WMAP+SDSS: $h = 0.70^{+0.04}_{-0.03}$ (Tegmark *et al.* 2003). This positive value means that the universe is currently expanding.

The distance between two points is not uniquely defined in a universe that is expanding, and which may not be Euclidean. The most useful quantity for gravitational lensing will be the *angular diameter distance*,

$$D(z) \equiv \frac{\lambda_{\mathrm{phys}}(z)}{\theta_{\mathrm{apparent}}(z)} , \tag{2.5}$$

defined in analogy to the flat space relation between the physical size of an object λ_{phys} and its apparent size $\theta_{\mathrm{apparent}}$ for a distant observer. In currently-favoured models, the apparent angular size of an object does decrease with distance, until $z \sim 1$. Beyond that, however, it starts to increase again, in a counterintuitive fashion: with more distant objects appearing larger (but fainter).

The set of points that are sufficiently close to have exchanged a photon since the Big Bang (and have therefore been causally connected) define the distance to a *particle horizon*

$$R_H(t) = a(t) \int_0^t \frac{c\mathrm{d}t'}{a(t')} . \tag{2.6}$$

For more details of these and other distance measures, see Hogg (2000).

2.1.2 Geometry of the universe

Robertson (1935) and Walker (1936) found the most general space-time metric that can describe an expanding universe filled with isotropic and homogeneous matter. The *Robertson-Walker metric* is

$$\mathrm{d}s^2 = -\mathrm{d}t^2 + a^2(t)\left[\frac{\mathrm{d}r^2}{(1-Kr^2)} + r^2(\mathrm{d}\theta^2 + \sin^2\theta\mathrm{d}\phi^2)\right] , \tag{2.7}$$

differing from the flat Minkowski metric of special relativity in the addition of $a(t)$ plus one further free parameter K, which describes the overall curvature of the universe and is very close to zero today. Inflation flattened the universe by rapidly pushing the scales of curvature beyond the observable horizon.

In General Relativity, the curvature of the universe is related to its total stress-energy tensor $T_{\mu\nu}$ by *Einstein's equation*

$$R_{\mu\nu} - \frac{1}{2}g_{\mu\nu}R = 8\pi G T_{\mu\nu} + \Lambda g_{\mu\nu} , \tag{2.8}$$

where the Ricci tensor $R_{\mu\nu}$ and Ricci scalar R are functions of the metric tensor $g_{\mu\nu}$, and where Λ is a constant of integration. We assume that matter in the universe is indeed a perfect fluid (homogeneous, isotropic and with no shear stress). The stress-energy tensor of the universe $T_{\mu\nu}$ is then guaranteed to be diagonal, and may be constructed from the components of density ρ and pressure p, with $T_{00} = -\rho c^2$ and $T_{ij} = pg_{ig}$ (using the fact that the pressure is just the flux density of x-momentum in the x direction).

Evaluating the temporal and spatial components of Einstein's equation results in the two *Friedmann equations*

$$\dot{a}^2 = \frac{8\pi G}{3}\rho a^2 - K \tag{2.9}$$

$$\ddot{a} = -\frac{4\pi G}{3}a(\rho + 3p) . \tag{2.10}$$

Note that the first of these can also be derived from Newtonian theory, up to a constant of integration, by considering the conservation of energy for an expanding shell of the universe. The second is then the time-derivative of the first, coupled with the assumption about mass conservation in equation (2.15). The Friedmann equations form the basis of modern cosmological models, and a full derivation can be found in *e.g.* Peebles (1993) or Peacock (1999).

Solving these differential equations provides a clearer illustration of the effect of the curvature of the universe upon its growth. During the first, "radiation dominated" stage in the evolution of the universe, its pressure and density are related by $p = \rho/3$. This leaves three possibilities for the evolution of its scale factor

$$a(t) \propto \begin{cases} \sqrt{\frac{8\pi G\rho_r K}{3}}\left[1-\left(1-t\sqrt{\frac{3}{8\pi G\rho_{r0}}}\right)^2\right]^{\frac{1}{2}} & \text{for } K>1 \\ 2\left(\frac{2\pi G\rho_r}{3}\right)^{1/4}\ t^{1/2} & \text{for } K=0 \\ \sqrt{\frac{8\pi G\rho_r K}{3}}\left[\left(1+t\sqrt{\frac{3}{8\pi G\rho_r}}\right)^2-1\right]^{\frac{1}{2}} & \text{for } K<1 \end{cases} \tag{2.11}$$

This reveals the direct connection between the density of the universe ρ and its global curvature K. A convenient analogy can be drawn to the escape velocity of a rocket from the Earth. The rocket's eventual trajectory is determined by its initial velocity and the mass of the Earth. In cosmology, the initial velocity of expansion is determined after inflation; it is the mass of the universe that will determine its eventual trajectory and fate. We can define a *density parameter*

$$\Omega \equiv \frac{\rho}{\rho_c} = \frac{8\pi G}{3H^2}\rho\ , \tag{2.12}$$

relative to the *critical density* of the universe ρ_c.

If $\Omega < 1$, the universe has negative global curvature (or an open space-time) and, no matter what the ratio between different types of matter, it will continue to expand for ever. If $\rho = \rho_c$, and $\Omega = 1$, the universe has no curvature (or a flat space-time). It has escape velocity and although it will always slow down, (if $\Lambda = 0$) it will just continue to expand for ever. If $\Omega > 1$, the universe has positive global curvature (or a closed space-time). In the absence of Λ, it will eventually collapse back onto itself in a "Big Crunch". However, as we shall see in the next section, the addition of non-zero Λ can alter this behaviour by accelerating the expansion at very late times.

2.1.3 Contents of the universe

The density ρ and pressure p, of the universe are in general related by an *equation of state*

$$p = w\rho\ , \tag{2.13}$$

with a parameter w that we shall discuss in a moment, and where we now choose units such that the speed of light is unity.

The net mass-energy in a volume element V of the universe is $U = \rho V$, plus a negligible term containing its gravitational potential energy. As the universe expands, this volume element does work on the external pressure, but conservation of energy demands that

$$\begin{aligned} \mathrm{d}U &= -p\mathrm{d}V \\ \rho\mathrm{d}V + V\mathrm{d}\rho &= -p\mathrm{d}V\ , \end{aligned} \tag{2.14}$$

where we have expanded the product $\mathrm{d}(\rho V)$. Thus the energy density scales as

$$\begin{aligned} \dot{\rho} &= -(p+\rho)\frac{\dot{V}}{V} = -3(p+\rho)\frac{\dot{a}}{a} \\ \frac{\dot{\rho}}{\rho} &= -3(1+w)\frac{\dot{a}}{a}\,. \end{aligned} \tag{2.15}$$

The universe may in fact consist of several separate components of mass and energy. The standard "ΛCDM" cosmological model that will be assumed in this thesis contains normal baryonic matter, non-interacting Cold Dark Matter, radiation, and a cosmological constant Λ. These are differentiated by their independent equation of state parameters w_i and the total energy density is $\rho = \rho_m + \rho_r + \rho_\Lambda$.

- **Baryonic matter**

  Baryonic matter is the stuff from which stars, planets and astronomers are made; It includes everything that shines. We denote the mean density of baryons in the universe by ρ_b. Since they are strongly clustered and separated by voids, it is a reasonable approximation to assume that they exert no pressure on large scales. Hence we adopt the usual equation of state for dust, with $w_b = 0$.

  Substituting this relation into equation (2.15) shows that the density of baryons scales, as expected from conservation of mass, like the inverse volume of the expanding universe $\rho_b \propto a^{-3}$.

- **Dark Matter**

  Dark matter does not interact with photons or other matter by the electromagnetic force. It is therefore difficult to detect directly, because it does not shine. However, dark matter is indistinguishable from baryons in respects of its gravity. It has exactly the same attraction, and produces exactly the same gravitational lensing effects. Since we can therefore detect them equally, and since the values of the concordance cosmology show that there is vastly more dark matter than baryons, we choose to subsume both types into one measurable density, ρ_m. Neither baryons nor dark matter have any pressure, so ρ_m evolves $\propto a^{-3}$.

  The temperature of the dark matter reflects its average kinetic energy and affects its virial radius under gravitational infall. Since it does not shine, it can not cool by photon emission. Its energy is gradually lost into the expansion of the universe, but this is a much slower process. In current cosmological models, dark matter decoupled from the radiation very early in the evolution of the universe, and it has indeed had a long time to become cold dark matter (CDM).

- **Neutrinos**

  Neutrinos are present throughout the universe, and interact weakly with baryonic matter. For many years, they were a potential candidate for the unknown constituents of dark matter. By contrast with standard CDM, neutrinos have a lot of kinetic energy, and they would make *hot* dark matter. The *free streaming* of neutrinos into voids would produce a larger coherence length for large-scale structure (White, Frenk & Davis 1983) and cluster sizes (White, Davis & Frenk 1984) larger than those observed. Alternatively, galaxies would have needed to have formed uncomfortably recently, at $z < 2$ (Frenk, White & Davis 1983).

  Although neutrinos apparently do not have enough mass to contribute to the evolution of the universe, recent measurements suggest that it is indeed non-zero. Their total mass could be around the level of the baryonic contribution (Abazajian & Dodelson 2003) but, for simplicity, we assume $\rho_\nu \equiv 0$ in this thesis.

- **Radiation**

  The sea of photons throughout the universe can be regarded as a perfect fluid, with a traceless stress tensor, mean density ρ_r, and equation of state parameter $w_r = 1/3$.

  Substituting this into equation (2.15) shows that the radiation density scales as $\rho_r \propto a^{-4}$. This is easily explained in terms of an a^{-3} volume dilution plus a further a^{-1} due to the cosmological redshift raising the wavelength of light and lowering its energy. As witnessed by the very cold temperature of the CMB today, radiation currently provides a negligible contribution to the total mass density of the universe today. However, it was dominant in the early universe, immediately after inflation.

- **Cosmological constant/dark energy**

  Einstein (1917) first hypothesized the existence of a cosmological constant Λ as the constant of integration for energy conservation in Einstein's equation (2.8). This allowed the possibility of a static universe, which was a more appealing prospect prior to the acceptance of Hubble's results. However, there is no *a priori* reason why Λ need be zero just because modern models allow an expanding universe, and it emerges as the energy density of the vacuum $\rho_\Lambda = \Lambda/(8\pi G)$.

  An equation of state parameter $w_\Lambda \equiv -1$ ensures that $\rho_\Lambda \propto a^0$ is indeed at constant density throughout the evolution of the universe. It will therefore become the dominant energy contribution at very late times, once the other components have been rarified. The negative pressure of a cosmological constant then re-accelerates the expansion of the universe.

Recent models replace the relatively simple cosmological constant with *quintessence* or *dark energy*, whose equation of state parameter w_Q is not only $\neq -1$ but which may also vary as a function of time. Current observations of supernova prefer models where w_Q is close to -1 today (*e.g.* Knop 2003), but its evolution remains completely unconstrained. Some basic models of dark energy will be considered in chapter 6, but in general we shall assume that $w_\Lambda \equiv -1$.

Combining all of these components, we find that, for a ΛCDM model, the total density and pressure of the universe scale as

$$\rho(t) = \frac{\rho_m}{a^3(t)} + \frac{\rho_r}{a^4(t)} + \rho_\Lambda \tag{2.16}$$

$$p(t) = \frac{\rho_r}{3a^4(t)} - \rho_\Lambda \tag{2.17}$$

The universe has undergone several distinct periods of evolution, each dominated by one of these different forms of energy density. The early universe (at small a) was dominated by radiation. As the universe expanded and the energy density of radiation decreased, there came a time when $\rho_r = \rho_m$ known as *matter-radiation equality* a_{eq}. This was followed by a period of matter dominance, during which the temperature fell sufficiently for matter and radiation to decouple and the universe to become translucent. As both matter and radiation become more and more diluted in very late times, the contribution from a cosmological constant or dark energy is now becoming significant. The universe is currently entering what may be the final stage in its evolution, with the energy density dominated by a cosmological constant, and its expansion accelerating once again.

2.1.4 Mass inhomogeneity in the early universe

The distribution of mass fluctuations immediately after inflation sets the inital conditions that will determine its subsequent evolution. As we have seen, the vacuum energy density of the universe is non-zero: the universe is full of a small-scale quantum froth with mass-energy continually appearing and disappearing. At the moment of inflation, this inhomogeneous distribution was suddenly enlarged to spatial scales beyond the influence of quantum mechanics. Although the amplitudes of these density fluctuations relative to the mean density $\langle\rho\rangle$,

$$\delta(\vec{x},t) = \frac{\rho(\vec{x},t) - \langle\rho((\vec{x},t)\rangle}{\langle\rho((\vec{x},t)\rangle}\,, \tag{2.18}$$

were very small, the quantum fluctuations were thus enlarged to macroscopic scales and captured. They provided the seeds for later structure formation via gravitational instability.

Since the initial fluctuations were produced by a large number of random quantum events, the central limit theorem ensures that their distribution was a Gaussian random field. The phases of such a perturbed density field are random, and all of its statistical properties of the distribution are furthermore described by its initial *Power Spectrum*

$$P_i(\vec{k}) \equiv \frac{\left\langle \widetilde{\delta}\left(\vec{k}\right) \widetilde{\delta}\left(\vec{k}'\right) \right\rangle}{(2\pi)^3 \, \delta^3\left(\vec{k} - \vec{k}'\right)} \tag{2.19}$$

where tildes denote a Fourier transform and δ^3 is a three-dimensional delta function.

The homogeneity of the universe ensured that the power spectrum is isotropic, so $P_i(\vec{k}) = P_i(k)$, where a real space distance $\lambda \propto 1/k$. Although the shape of the power spectrum is not precisely predicted by inflationary theory, there is no reason to favour any one scale over all others, so $P(k)$ must be a power law, parameterized only by its amplitude on one scale and an index n

$$P_i(k) \propto k^n \, , \tag{2.20}$$

which expresses the balance between small-scale and large-scale structure.

2.1.5 Linear growth of structures

In the radiation dominated era immediately after inflation, the universe was approximately flat and expanding (as shown by the solution of the Friedmann equations 2.11) at a rate $a \propto t^{1/2}$. The physical scale of density fluctuations $\lambda_{\rm phys}$ grew with this inflation

$$\lambda_{\rm phys} \propto a \propto t^{1/2} \, . \tag{2.21}$$

The amplitude of the density fluctuations simultaneously began to grow, as surrounding matter began to flow towards the primordial seeds under gravitational instability. Relativistic perturbation theory is required to include an analysis of fluctuation modes on super-horizon scales (*e.g.* Padmanabhan 1993), but it shows that the growth of the amplitude of small fluctuations ($\delta \ll 1$) in an approximately Einstein-de Sitter universe is linear in time

$$\delta(\vec{x}, t) \propto t \, . \tag{2.22}$$

Thus the initial power spectrum (2.20) began to rise on all scales. During the radiation dominated era however, the smallest and most dense perturbations became internally supported by radiation pressure, and could not condense further than the particle horizon (strictly the Jeans length λ_J, in analogy with the collapse of stars, but this scale is proportional to the particle horizon). Evaluating equation (2.6) during this epoch, shows that the particle horizon was growing as

$$R_H \propto t \,, \tag{2.23}$$

which is faster than the growth of the physical scale of the fluctuations.

When a fluctuation then inevitably "entered the horizon", *i.e.* $R_H \geqslant \lambda_{\text{phys}}$, its growth was halted. Let us denote this time $t_J(\lambda)$. The amplitude of the fluctuation continued to oscillate under the opposing influences of its gravity collapse and internal pressure, but remained constant when averaged over time. Combining equations (2.21) and (2.23), it is clear that

$$t_J(\lambda) \propto \lambda^2 \,, \tag{2.24}$$

which left the amplitude of large-scale fluctuations at the end of the radiation-dominated era

$$\begin{aligned} \delta\left(\vec{x},t\right) &\propto \lambda^2 \delta\left(\vec{x},t\right) \\ &\propto \frac{\delta\left(\vec{x},t\right)}{k^2} \,. \end{aligned} \tag{2.25}$$

In terms of power spectra, this emerges as an effective suppression of power on small scales known as the *Mészáros effect*

$$P_\delta(k) \propto \frac{P_i(k)}{k^4} = k^{n-4} \,. \tag{2.26}$$

Measurements of the CMB at large scales from WMAP give $n \simeq 1$. Therefore

$$P_\delta(k) \propto \begin{cases} k & \text{for } k \ll k_0 \\ k^{-3} & \text{for } k \gg k_0 \end{cases} \tag{2.27}$$

where k_0 defines the turnover point in the power spectrum, determined by the horizon size at the end of the radiation-dominated era (the time of which is influenced by Ω_m). Inserting the measured values from the concordance cosmology model and performing the calculation numerically,

$$k_0 \approx 0.083(\Omega_0 h^2)\,\text{Mpc}^{-1} \,. \tag{2.28}$$

After matter-radiation equality, the radiation pressure support was removed from density fluctuations. There was nothing to prevent the further growth of structures during the matter-dominated era, until they became much more dense at very late times, which we shall deal with in the next section. The expansion of the universe caused the physical scale of fluctuations to grow as $a \propto t^{2/3}$, but fluctuations collapsed equally on all scales and the amplitude of the power spectrum was raised without changing its shape.

The final prediction for the matter power spectrum by linear evolution is plotted in

figure (2.1). The change in shape induced by the Mészáros effect from the initial power spectrum is often referred to as the *transfer function* $T(k)$. The amplitude is conventionally parameterized by the rms σ_8 of fluctuations that would be found inside independent $8h^{-1}$ Mpc spheres scattered throughout the universe. This particular scale is chosen so that the parameter is roughly unity. It can be calculated from the power spectrum via

$$\sigma_8^2 \equiv \int P(k)W(k,R_f)\mathrm{d}k \tag{2.29}$$

where the Fourier transform of a spherical top hat window function with $R_f = 8h^{-1}$ Mpc

$$W(k,R_f) = \frac{3k^2}{2\pi^2(kR_f)^3}\left(\sin(kR_f) - kR_f\cos(kR_f)\right) \ , \tag{2.30}$$

peaks around $k = 1/(8h^{-1}\,\mathrm{Mpc})$ but also covers a range of scales.

The amplitude and shape of the linear matter power spectrum are primarily determined by two parameters, Ω_m and σ_8. It is these that define both the density and the first-order distribution of matter in the universe, and therefore towards measurements of these parameters that we shall direct our efforts in this thesis.

2.1.6 Non-linear growth of structures

Like all astronomical techniques, weak lensing requires its own calibration, has observational limitations and hindrances, and is subject to possible systematics that must be controlled. One of the most significant problems is that current cosmic shear surveys are sensitive to spatial scales where mass overdensities have already grown in amplitude beyond the point where linear perturbation theory is valid. As the perturbations grew, the rate of gravitational infall accelerated around them, and power was shifted from large scales onto small scales. Unfortunately, practical calculation of the many and complicated higher-order terms involved in this gravitational collapse requires large n-body simulations.

Peacock & Dodds (1994, 1996) ran numerical simulations of large-scale structure in several standard cosmological models, and derived fitting functions for the resulting power spectra. These fitting functions were based upon an assumption of *stable clustering* on small scales, where the resolution of their simulations was limited. This purports that collapsing objects will eventually support themselves on small scales and stop collapsing. Since they will continue to move farther apart in the Hubble flow, $P(k) \to k^{-3}$ on small scales. Ma (1998) expanded the numerical simulations to incorporate cosmological models containing dark energy. These will be used to predict the sensitivity of future cosmic shear surveys in chapter 6.

The results in chapter 3 of this thesis use the recently updated numerical simulations of a ΛCDM cosmology by Smith *et al.* (2003). Their higher resolution VIRGO n-body simulations provided more accurate fitting functions for the mass power spectrum, and

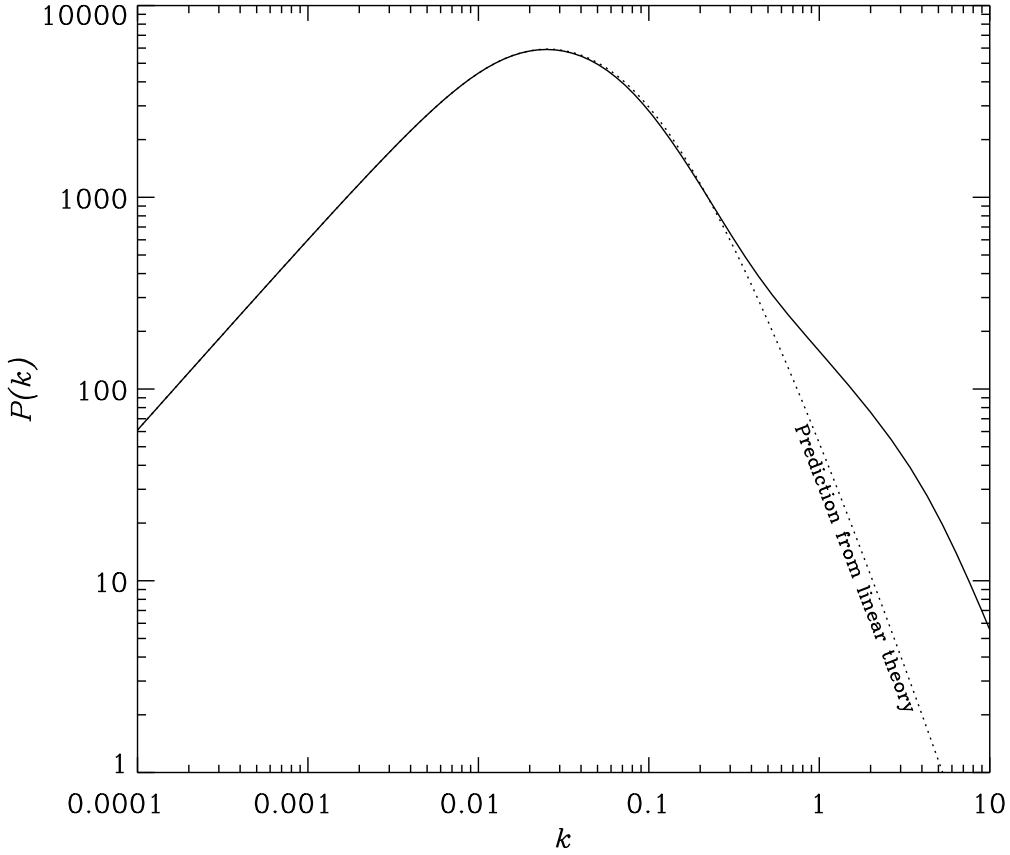

Figure 2.1: Three-dimensional mass power spectrum $P(k)$. The dotted line shows the prediction from linear theory. The solid line includes the full non-linear correction, using the fitting functions from Peacock & Dodds (1996) and the values for cosmological parameters given in equations (2.31) to (2.34).

these are shown in figure 2.1. These simulations were able to probe sufficiently small scales that the profile of individual clusters becomes dominant. The observed "NFW" profile (Navarro, Frenk & White, 1995) truncates the power spectrum at high k. However, this is of limited consequence for weak gravitational lensing measurements, which do not probe such small scales. The major impact for our work is in the interpolation between this regime and large scales, in which current surveys are most sensitive. The more accurate simulations from Smith *et al.* (2003) have lowered weak lensing estimates of σ_8 by between 5% and 10% compared to those by Peacock & Dodds (1996). It will be a clause throughout this thesis that the interpretation of our cosmic shear results relies upon the accuracy of fitting functions derived from numerical simulations to correct for the non-linear evolution of the power spectrum.

2.1.7 Concordance cosmology?

Independent cosmological tests and observational techniques are largely beginning to agree upon the values of most of the universe's fundamental parameters. This con-

vergence has prompted the currently-favoured ΛCDM model to become known as the *concordance cosmological* model. Measurements of temperature fluctuations in the CMB are highly sensitive to the global curvature of the universe, and to the matter density at the time of last-scattering. The latest results from the Wilkinson Microwave Anisotropy Probe (Spergel *et al.* 2003; hereafter WMAP) have successfully confirmed that the universe is indeed flat (or very nearly), and has a relatively small matter component that implies the existence of a significant cosmological constant.

However, the CMB probes only very early times in the evolution of the universe, which were far removed from our present situation. The cosmological constant was insignificant during this epoch, so predictions from just CMB data are highly model-dependent, and parameter constraints have many degeneracies. Tighter constraints can be drawn upon Λ by combining CMB data with information about current large-scale structure. Knowledge of the power spectrum $P(k, z)$ during these two widely-separated redshifts traces the growth of structure, and measures the competing influences of Ω_m and Ω_Λ, over time. Local data is typically obtained from galaxy redshift surveys like the Anglo-Australian Telescope two degree field survey (Colless 1999; hereafter 2dF) or the Sloan Digital Sky Survey (York *et al.* 2000; hereafter SDSS). The best measurements of current cosmological parameters, as fractions of the critical density, are

$$\Omega = 1.06 \pm 0.05 \tag{2.31}$$
$$\Omega_b = 0.048 \pm 0.005 \tag{2.32}$$
$$\Omega_m = 0.30 \pm 0.04 \tag{2.33}$$
$$\Omega_\Lambda = 0.70 \pm 0.04\ , \tag{2.34}$$

using SDSS plus WMAP data (Tegmark *et al.* 2003).

A direct measurement of the expansion of the universe, and on a finer resolution of time-steps, can be obtained from the distances to type Ia supernovæ at various redshifts (Perlmutter *et al.* 1998; Riess *et al.* 1999; Knop *et al.* 2003). Supernovæ are bright enough to be seen from great distances; yet after various calibration factors (to account for variable source metallicity and dust obscuration along the line of sight, which can be determined from their spectra), all type Ia supernovæ have the same brightness. They therefore act as standard candles, and can be used to detect deviations from Hubble's law (2.1).

$$\Omega_m = 0.28 \pm 0.10 \tag{2.35}$$
$$\Omega_\Lambda = 0.72 \pm 0.10\ . \tag{2.36}$$

(Knop *et al.* 2003). Supernova observations also provide the main evidence for the acceleration of the universe caused by dark energy.

The baryon density, and the time available for nucleosynthesis immediately after the Big Bang predict the abundances of light elements in the early universe (Burles, Nollett & Turner 1999). Comparing these predictions to the observed abundances in local, metal-poor regions, like isolated HI clouds (Copi, Schramm & Turner 1995; Kirkman *et al.* 2003) or quasar absorption systems (Tytler *et al.* 2000) that have experienced little subsequent star formation, gives

$$\Omega_b \;=\; 0.044 \pm 0.015 \; . \tag{2.37}$$

As we can see, the agreement between these results is impressive. However, the interpretation of these numbers is still model-dependent. To find out what they really mean, and to witness the process of structure formation in action, requires a more direct detection and mapping of the mass distribution. However, all classical cosmological tests are hindered by the overwhelming prevalence of dark matter compared to light emitting material. Galaxy redshift surveys detect only the biased light distribution (*e.g.* Weinberg *et al.*2003). Detecting the majority of mass in the universe is only possible via indirect techniques, which require subsequent physical interpretation.

Crucially, different measurement methods currently disagree about the amplitude of the mass power spectrum, at approximately the 1σ level. The combination of SDSS plus WMAP data by Tegmark *et al.* (2003) gives

$$\sigma_8 \;=\; 0.91^{+0.11}_{-0.10} \; . \tag{2.38}$$

However, Lahav *et al.* (2002) use 2dF and (pre-WMAP) CMB data instead, finding

$$\sigma_8 \;=\; 0.73 \pm 0.05 \; . \tag{2.39}$$

Until recently, peak statistics of the mass distribution obtained from x-ray selected cluster counts, had given

$$\sigma_8 \left(\frac{\Omega_m}{0.3} \right)^{0.65} \;=\; 1.0 \pm 0.07 \; , \tag{2.40}$$

(Pierpaoli, Scott & White 2001; see also consistent estimates by Viana, Nicholl & Liddle 2002 and Eke *et al.* 1998). However, the mass of these clusters requires calibration via the mass-temperature relation (*e.g.* Huterer & White 2003). The cluster normlisation has recently been revised to a lower value, mainly due to improved observations of the mass-temperature relation replacing simulated ones. Using these observations, Seljak (2001) finds

$$\sigma_8 \left(\frac{\Omega_m}{0.3} \right)^{0.44} \;=\; 0.75 \pm 0.06 \; . \tag{2.41}$$

Different results again are given by surveys of weak gravitational lensing. Refregier

(2003) compiled an average of several recent survey results, which gives

$$\sigma_8 \;=\; 0.83 \pm 0.04 \;. \tag{2.42}$$

Some or all of these methods must clearly be contaminated by unknown systematic effects. Yet weak gravitational lensing possesses the unique benefit that its calibration factors do not rely upon complicated or poorly-understood physics. As we shall see in the next section, the analysis of weak gravitational lensing data is a purely geometric task, and the main difficulties in its measurement concern careful image analysis and the parameterization of galaxy shapes. These difficulties can be overcome with new algorithms that are being developed to perform more accurate data reduction. Existing weak lensing surveys already constrain cosmological parameters at a level similar to those from other techniques. In the near future, weak lensing promises to be the most trusted probe of the dark matter distribution, and to provide a direct test of the gravitational paradigm for structure formation.

2.2 Gravitational lensing

2.2.1 The lens equation

The most general isotropic space-time metric to describe a section of the universe containing a central mass concentration M, but otherwise empty, is the *Schwarzchild metric*

$$\mathrm{d}s^2 = -\left(1 - \frac{2GM}{r}\right)\mathrm{d}t^2 + \frac{\mathrm{d}r^2}{\left(1 - \frac{2GM}{r}\right)} + r^2\left(\mathrm{d}\theta^2 + \sin^2\mathrm{d}\phi^2\right) \;. \tag{2.43}$$

Its null geodesics are circular at the *Schwarzchild radius* $r_S = 2GM$, and are still curved farther out. This results in the deflection of light rays when they pass near a massive body, as illustrated in figure 2.2. Following the full analysis of the null geodesics in the vacuum (*e.g.* Schutz 1985), it can be shown that, for an *impact parameter* $\vec{\xi}$, the *deflection angle*

$$\hat{\vec{\alpha}} = -4GM\frac{\vec{\xi}}{|\vec{\xi}|^2} \;. \tag{2.44}$$

in the *weak field limit* where $3GM/\vec{\xi} \ll 1$. This will certainly be acceptable for cosmic shear studies which are concerned with the vast majority of the universe away from the central cores of clusters.

Note that the deflection is exactly twice that predicted in Newtonian theory, due to the warping of both space and time in general relativity. Contact can be recovered with classical quantities via the relation

$$\hat{\vec{\alpha}} = \frac{-2}{c^2} \int \vec{\nabla}_\perp \Phi \mathrm{d}\ell \,, \tag{2.45}$$

where we have reinserted the speed of light; the integral is along the geodesic; and $\vec{\nabla}_\perp \Phi$ is the gradient of the Newtonian gravitational potential taken in the plane perpendicular to this path. In the weak field limit, the small angles involved ensure that is is acceptable to integrate along the unperturbed path of the light ray.

Note that the equation (2.45) is exactly equivalent to that describing the deflection of light by an optical lens with refractive index $n = 1 - 2\Phi/c^2$. Hence it really is appropriate to use the word *lensing*, even though the light is not focussed to a point by a gravitational lens. Furthermore, this refractive index and the deflection angle are independent of the nature of the intervening mass and of the wavelength of the light. Measurements of gravitational lensing will therefore be equally sensitive to baryonic or dark matter lenses; and a survey may be performed in any colour. Optical bands are normally the most convenient because of the comparatively advanced detector technology and high number density of background sources, but gravitational lensing has also been detected in the near infra-red (Gray *et al.* 2001; King *et al.* 2002) and with high spatial resolution in radio observations (Chang & Refregier 2003).

Measurements are similarly unaffected by astrophysical contaminants like the reddening or absorption of light by intervening dust (which can be an inconvenience, given that natural targets are often located behind a massive cluster), the physical nature of the lens, or the evolution of the source galaxies. Gravitational lensing is instead a purely geometric effect. Of course, calculation of the geometry does require knowledge of the distance to the source D_S and to the intervening lens D_L. Recalling the definition of the angular diameter distance (equation 2.5), we define the *reduced deflection angle*

$$\hat{\vec{\alpha}} \equiv \frac{D_{\mathrm{LS}}}{D_{\mathrm{S}}} \vec{\alpha} \,, \tag{2.46}$$

where D_{LS} is the angular diameter distance between the lens and the source ($D_{LS} \neq D_S - D_L$). Bearing in mind the sign of $\vec{\alpha}$, we can then simply read off the *lens equation*

$$\vec{\beta} = \vec{\theta} + \vec{\alpha}(\vec{\theta}) \,. \tag{2.47}$$

directly from figure 2.2. This defines a mapping from the source plane ($\vec{\theta}$) to the lens plane ($\vec{\beta}$).

Although the real universe does not consist of one completely isolated point mass, a galaxy is made of many individual stars and a cluster of many individual galaxies. The linear equations (2.45) and (2.47) are therefore also valid for any system built up from a superposition of lenses, as long as the mass distribution ρ_m is geometrically thin ($\ll D_L$, D_S). If we project such a mass distribution onto the lens plane, it can be described by the dimensionless *surface mass density*

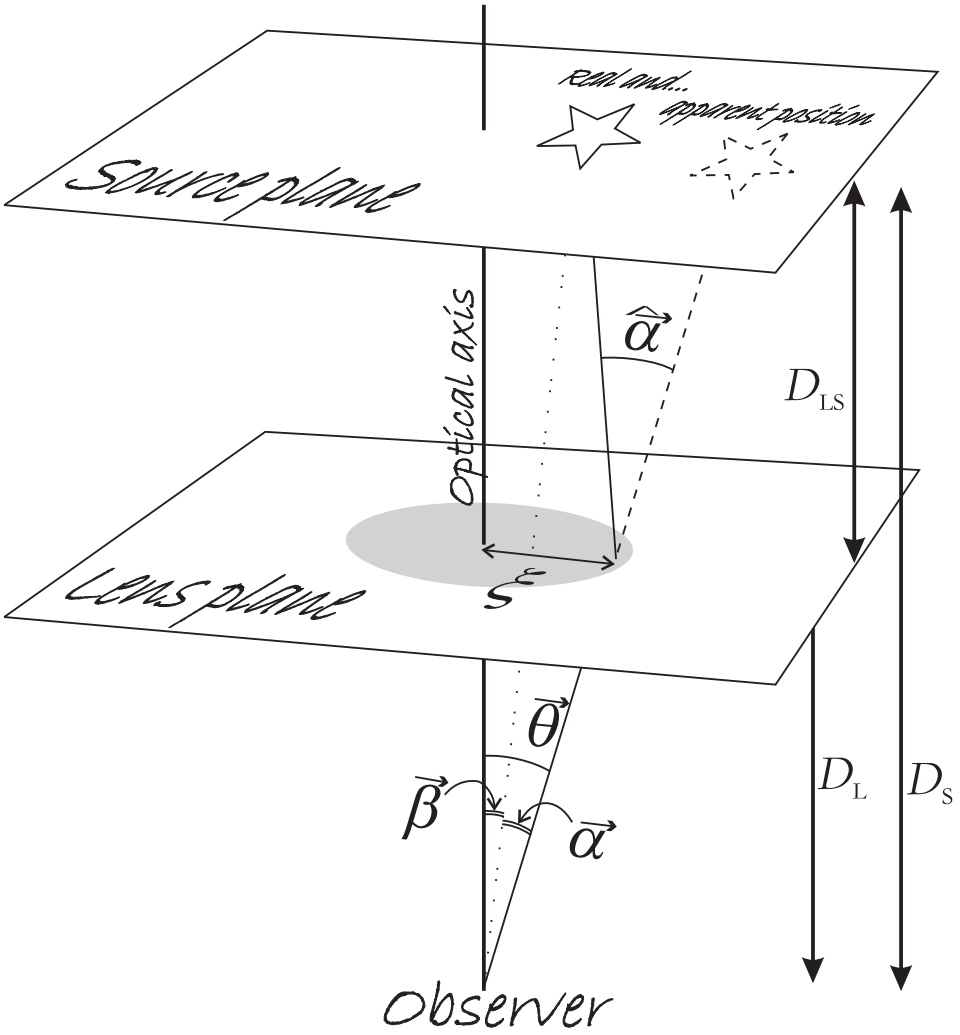

Figure 2.2: Sketch of a typical gravitational lens system.

$$\kappa(\vec{\theta}) = \frac{4\pi G}{c^2}\int \frac{D_{\rm L} D_{\rm LS}}{D_{\rm S}}\rho_m(\theta,\ell)d\ell \tag{2.48}$$

$$\equiv \frac{\Sigma(\vec{\theta})}{\Sigma_{\rm C}}\,, \tag{2.49}$$

where the *critical surface mass density*

$$\Sigma_{\rm C} = \frac{c^2}{4\pi G}\frac{D_{\rm S}}{D_{\rm L} D_{\rm LS}} \tag{2.50}$$

conveniently contains the relevant distances in the lensing geometry. Continuing this two-dimensional analogy, we can also define a projection of the Newtonian potential Φ as the *lensing* or *deflection potential*

$$\Psi(\vec{\theta}) = \frac{D_{\rm LS}}{D_{\rm L} D_{\rm S}} \frac{2}{c^2} \int \Phi(D_{\rm L}\vec{\theta}, z) {\rm d}z \quad (2.51)$$

$$= \frac{1}{\pi} \int \kappa(\vec{\theta'}) \, \ln|\vec{\theta} - \vec{\theta'}| \, {\rm d}^2\vec{\theta'} \, . \quad (2.52)$$

In this case, the potential $\Psi(\vec{\theta})$ satisfies the Poisson equation

$$\nabla^2 \Psi(\vec{\theta}) \, = \, 2\kappa(\vec{\theta}) \, , \quad (2.53)$$

and the deflection angle is simply

$$\vec{\alpha}(\vec{\theta'}) = -\nabla\Psi \quad (2.54)$$

$$= \frac{-1}{\pi} \int \kappa(\vec{\theta'}) \, \frac{\vec{\theta} - \vec{\theta}}{|\vec{\theta} - \vec{\theta}|^2} \, {\rm d}^2\vec{\theta'} \, . \quad (2.55)$$

2.2.2 The differential deflection of adjacent light rays

Without knowing where an image would appear in the absence of lensing, measuring the observed position of a point source does not tell us anything about a gravitational lens. Fortunately, spatially extended and resolved background sources are more useful. Since two adjacent light rays from the source pass through an intervening lens at slightly different distances $\vec{\xi} = D_L\vec{\theta}$ from the optical axis (see figure 2.2), they are deflected through slightly different angles $\vec{\alpha}$. This differential deflection distorts the image seen by the observer.

The deflection of light rays and the mapping from source plane to image plane is completely described by the lens equation (2.47). Around a strong lens, this can be a complicated expression, producing the multiple images and large arcs seen frequently around massive clusters. In this thesis, we shall instead consider the *weak lensing regime*, defined by $\kappa \ll 1$, where we shall find that the mapping is one-to-one and invertible.

We shall require source galaxies to be resolved, but smaller than the scale on which variations occur in the slope of the lens's gravitational potential $\Phi(\vec{\theta})$. Substructure does exist within lenses, and the local fluctuations created in a gravitational potential have been found to alter the magnification ratios between multiple images in strong lens systems. However, we shall be able to gather a very large population of sources and average over all such local deviations.

In this case, the lensing equation (2.47) has a (first-order) Jacobian

$$\mathcal{A}_{ij}(\vec{\theta}) = \frac{\partial\beta_i}{\partial\theta_j} \, = \, \delta_{ij} - \frac{\partial^2\Psi(\vec{\theta})}{\partial\theta_i\partial\theta_j} \quad (2.56)$$

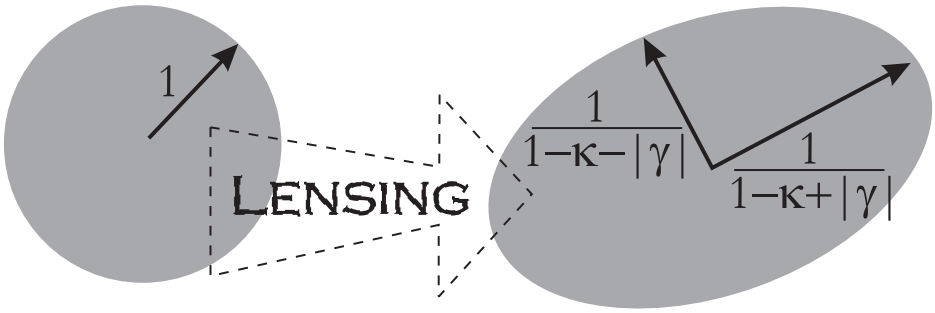

Figure 2.3: Cartoon showing the distortion of a resolved unit circle source by the differential deflection of light rays with slightly different paths.

$$\mathcal{A}(\vec{\theta}) \;=\; \begin{pmatrix} 1-\kappa(\vec{\theta})-\gamma_1(\vec{\theta}) & -\gamma_2(\vec{\theta}) \\ -\gamma_2(\vec{\theta}) & 1-\kappa(\vec{\theta})+\gamma_1(\vec{\theta}) \end{pmatrix}, \tag{2.57}$$

where, dropping the explicit dependence upon position for brevity, we have introduced the *convergence*

$$\kappa \;\equiv\; \frac{1}{2}\left(\frac{\partial^2\Psi}{\partial x^2}+\frac{\partial^2\Psi}{\partial y^2}\right), \tag{2.58}$$

and the two components of *shear*

$$\gamma_1 \;\equiv\; \frac{1}{2}\left(\frac{\partial^2\Psi}{\partial x^2}-\frac{\partial^2\Psi}{\partial y^2}\right) \tag{2.59}$$

$$\gamma_2 \;\equiv\; \frac{\partial^2\Psi}{\partial x\partial y}, \tag{2.60}$$

which in practice are all of the same order of magnitude. Comparing equations (2.53) and (2.58), we see that the value of the convergence is no less than the ratio κ of the surface mass density to the critical density, justifying our use of the same Greek letter. Our definition of the weak lensing regime, $\kappa \ll 1$, is therefore equivalent to a requirement that the lens equation indeed be a linear mapping, with negligible second-order terms (of order κ^2, γ_i^2) in its Jacobian.

A cartoon showing the effect of gravitational lensing on a circular object is displayed in figure 2.3. To see the effect on a more realistic galaxy image, see figure 4.43. However, the two operations are easily interpreted by rewriting equation (2.57) as

$$\mathcal{A} = \mathcal{I} - \kappa\begin{pmatrix} 1 & 0 \\ 0 & 1 \end{pmatrix} - \sqrt{\gamma_1^2+\gamma_2^2}\begin{pmatrix} \cos(2\phi) & \sin(2\phi) \\ \sin(2\phi) & -\cos(2\phi) \end{pmatrix}. \tag{2.61}$$

We see that the convergence produces an isotropic enlargement of the image. Since gravitational lensing conserves surface brightness, this enlargement also increases the

total observed flux from an object by a *magnification factor*

$$\mu = \frac{1}{\det \mathcal{A}} = \frac{1}{(1-\kappa)^2 - \gamma_1^2 - \gamma_2^2} \, . \tag{2.62}$$

By Taylor expansion in the weak lensing limit, this becomes

$$\mu \approx 1 + 2\kappa \, . \tag{2.63}$$

Although the convergence and magnification effects are very closely linked to the mass distribution of the lens, they are difficult to measure in practice. The usual method (*e.g.* Schneider *et al.* 2000) attempts to find spatial variations in the observed number density of a magnitude-limited sample of galaxies. However, even in ideal observing conditions, gravitational lensing changes the observed galaxy density in a complicated way that depends upon the slope of the number counts (*e.g.* Schneider 2002). *Magnification bias* pushes faint galaxies into the catalogue, but competes with the stretching of solid angles that dilutes the observed density of galaxies in a fixed region. Gray *et al.* (2002) observed in the near-IR where the slope is steeper, but there the total number density is lower, and they found no overall benefit.

The two components of shear are easier to observe. Made from the trace-free part of the Jacobian matrix, they stretch the image in two different directions: γ_1 along the x-axis and γ_2 at 45° from it. They can be combined to form a convenient complex quantity (Blandford *et al.* 1991)

$$\gamma \equiv \gamma_1 + i\gamma_2 = |\gamma| e^{2i\phi} \, , \tag{2.64}$$

where the modulus represents the amount of shear and the phase represents its direction. Differentiating equation (2.44), it can be seen that the shear induced around a point mass lens is everywhere tangential and falls off in magnitude as $\gamma \propto 1/r^2$. A circular source is thus mapped into an elliptical image, where $\phi \in [0, \pi)$ is the angle from the x-axis to the major axis of the ellipse. Defining the new *major* and *minor axes*

$$a = \frac{1}{1 - \kappa - |\gamma|} \tag{2.65}$$

$$b = \frac{1}{1 - \kappa + |\gamma|} \, , \tag{2.66}$$

we can measure its *ellipticity*

$$\varepsilon \equiv \frac{a^2 - b^2}{a^2 + b^2} \, . \tag{2.67}$$

To measure shear in practice, we do not even need to assume that galaxies are intrinsically circular; just that their intrinsic orientations are random. In this case, stack-

ing many galaxy images in the absence of lensing will produce a combined object that does have concentric, circular isophotes. Galaxies' own intrinsic orientations cancel, and $\langle\varepsilon\rangle = 0$ (but see the discussion concerning possible intrinsic alignments of neighbouring objects in §3.3.6). If the galaxies had instead been distorted by a (smooth) shear field, nearby objects become coherently elongated in the same direction. The result of stacking *these* images is an elliptical profile that depends only upon the local shear field, the average radial profile of the galaxies and their ellipticity distribution. This information is contained within the *shear susceptibility*

$$P^{\gamma} \equiv \frac{\langle\varepsilon\rangle}{\gamma} \,, \tag{2.68}$$

which we shall return to discuss in more detail in section §3.2.3. For now, we simply state that it is a constant scalar that can be measured. Note also that because of the symmetry of an ellipse, both ε and γ rotate like 2-spinors rather than vectors.

2.2.3 Dark matter mapping

From an observed shear field, or pattern on the sky, it is possible to recover the convergence field: which is a projected mass map of both baryonic and dark matter. This can therefore bridge the gap between observation, which can otherwise detect only luminous objects, and theory, which typically deals only with mass. Many known foreground clusters have been mapped with lensing, to determine their overall mass and structure (*e.g.* Joffre *et al.* 2000; Dahle *et al.* 2002). Kaiser & Squires (1993) developed the first shear-inversion technique for creating two-dimensional mass maps. Since both shear and convergence are second derivatives of the lensing potential $\Psi(\vec{\theta})$, they are related simply in Fourier space. One merely needs to represent the two differentiations in Fourier space by multiplication then division by different factors of θ, then transform back to real space. The end result (Bartelmann & Schneider 2001) is

$$\kappa\left(\vec{\theta}\right) = \int_{\mathbb{R}^2} \Re\left[\mathcal{D}\left(\vec{\theta}-\vec{\vartheta}\right)\gamma\left(\vec{\vartheta}\right)\right] \mathrm{d}\vartheta^2 + \kappa_0 \,, \tag{2.69}$$

where

$$\mathcal{D}\left(\vec{\vartheta}\right) \equiv \frac{\vartheta_2^2 - \vartheta_1^2 + 2i\vartheta_1\vartheta_2}{|\vec{\vartheta}|^4} = \frac{-1}{(\vartheta_1 - i\vartheta_2)^2} \tag{2.70}$$

and κ_0 is an unknown constant of integration, known as the mass sheet degeneracy: a shear field is unchanged by a constant mass. This is a concern only for observations with a small field of view, where the data can only be integrated over a small region of $\mathbb{R}^2$. In this case, use of magnification data can break the degeneracy. In fact, Schneider *et al.* (2000) showed that magnification data can provide more accurate measurements of the radial profiles of clusters than shear information, but both are required to determine the

total mass. Large modern cameras overcome the problem using only the observed shear field, by extending data to regions so far from the cluster that there is no foreground mass. The outer regions of such a mass map can thus be used to constrain the zeropoint κ_0.

It is never desirable to have to take Fourier transforms of observational data. The edges of the CCD, and missing data behind saturated stars, typically create a complicated window function. Several other techniques have been developed to avoid Fourier transform, and the most widespread technique involves the *aperture mass*

$$M_{\rm ap}(\theta) \equiv \int {\rm d}^2\vec{\vartheta}\, Q\left(|\vec{\vartheta}|;\theta\right)\ \gamma_t\left(\vec{\vartheta}\right)\ , \tag{2.71}$$

where γ_t is the component of shear tangential to the direction $\vec{\theta}$ from the cluster centre (Schneider & Bartelmann 1997). This calculates the projected mass density κ within circular window functions $Q(\vartheta)$ on the sky that are narrow in Fourier space. As we shall see in section §2.2.7, replacing the tangential components of shear with those at 45° from the line to the centre of the cluster, will provide an estimate of noise

$$M_\perp(\theta) \equiv \int {\rm d}^2\vec{\vartheta}\, Q\left(|\vec{\vartheta}|;\theta\right)\ \gamma_r\left(\vec{\vartheta}\right)\ . \tag{2.72}$$

The window function $Q(|\vec{\vartheta}|;\theta)$ can be matched to optimise detection or parametrization of particular cluster profiles. However, almost equally good results are obtained (Bartelmann, King & Schneider 2001) using a simple Mexican hat filter

$$Q(\vartheta;\theta) = \frac{6}{\pi\theta^2}\frac{\vartheta^2}{\theta^2}\left(1-\frac{\vartheta^2}{\theta^2}\right){\rm H}(\theta-\vartheta)\ , \tag{2.73}$$

where θ defines an angular scale of the aperture and the Heaviside step function H truncates the weight function at high scales.

Weak lensing measurements of cluster masses have even been used to calibrate other techniques, including the x-ray mass-temperature relation and cluster mass/light ratio biasing (Huterer & White 2003; Gray *et al.* 2002; Hoekstra *et al.* 2002b; Smith *et al.* 2003). Maps of untargetted regions of the sky, or wider surveys, can be used to search for previously unknown clusters and to compile mass-selected catalogues. Miyazaki *et al.* (2002) used the Kaiser & Squires (1993) inversion method to identify mass peaks, and Marshall, Hobson, Gull, & Bridle (2002) demonstrate the effectiveness of maximum entropy techniques to identify structures in such maps, using criteria set by Bayesian evidence. The M_{ap} statistic (Schneider 1996, 2002) has been applied successfully to find the locations and masses of clusters in several surveys (*e.g.* Hoekstra *et al.* 2002a; Erben *et al.* 2000). Two clusters have also been found purely by weak lensing mass maps, and spectroscopically confirmed by Wittman *et al.* (2001, 2003).

White *et al.* 2002 argue that using any detection method, a complete mass-selected

cluster catalogue from 2D lensing data would require a high rate of false-positive detections, since the prior probability is for them to be *anywhere* throughout a given survey. This has been avoided in practice by secondary cross-checks of the lensing data with spectroscopy, deep x-ray temperature or SZ observations. However, this does make it harder to resolve the debate on the possible existence of baryon-poor "dark clusters" (*e.g.* Dahle *et al.* 2003). These are a speculative population of clusters which would be physically different to and absent from the catalogues of optically or x-ray selected clusters. Remaining dark-lens candidates (Erben *et al.* 2000; Umetsu & Futamase 2000; Miralles *et al.* 2002) have currently been eliminated as chance alignments of background galaxies (or possibly associations with nearby ordinary clusters Gray *et al.* 2001; Erben *et al.* 2003). If many other candidates could be found in high S/N weak lensing maps, they would present a challenge to current models of structure formation, and need to be accounted for in estimates of $\Omega_{\rm m}$; but they would be unique laboratories to decipher the nature of dark matter.

Cluster counts, and the quantitative study of peak statistics are one of the most promising routes to breaking degeneracies in the estimation of cosmological parameters (Bernardeau, van Waerbeke & Mellier 1997; Cooray, Hu & Miralda-Escudé 2000; Munshi & Jain 2001; Schneider & Lombardi 2003). Furthermore, studying well-resolved groups and clusters individually, rather than statistically, will lead to a better understanding of astrophysical phenomena, the nature of dark matter and the growth of structure under the gravitational instability paradigm (*e.g.* Dahle *et al.* 2003).

2.2.4 Cosmic shear statistics

The shear field in wide, untargetted observations can also be examined statistically. As a light ray threads its way through the large scale structure of the universe, it will be deflected by a succession of many small mass concentrations. As long as each lens is geometrically thin, well-separated from its neighbours, and creating only small deflection angles, the net shear may be calculated as the linear superposition of many deflections. These all deflect the light rays by an amount which depends how close they are to being half-way between the source and the observer. This efficiency of lenses is described by the *lensing weight function*

$$g(\chi) = 2 \int_{\chi}^{\chi_h} \eta(\chi') \, \frac{D(\chi) D(\chi' - \chi)}{D(\chi')} \, a^{-1}(\chi) \, \mathrm{d}\chi' \,, \tag{2.74}$$

where χ is a distance in comoving coordinates (in which the power spectrum is measured), Ds are angular diameter distances, (with the extra factor of a^{-1} converting these into comoving coordinates), and $\eta(\chi)$ is the distribution function of source galaxies in redshift space, normalised so that

$$\int_0^{\chi_h} \eta(\chi)\, \mathrm{d}\chi = 1\,. \tag{2.75}$$

The limits on these integrals extend all the way to the comoving horizon χ_h, at $z = \infty$. Because the angular diameter distance evolves slowly with redshift beyond $z \simeq 1$, it turns out that the results depend only weakly upon the shape of the function $\eta(\chi)$. Since we also want to use sources that are as far away and as faint as possible (because the lensing signal adds cumulatively along a light path), this function is not well known (particularly after the typical exclusion of galaxies based upon their size and ellipticity as well as their magnitude). It is therefore usual to approximate $\eta(\chi)$ with the assumption that all the sources lie in a single sheet at comoving radius χ_s that corresponds to the median redshift z_s of the true distribution, so that $\eta(\chi) \equiv \delta(\chi - \chi_s)$. In this case, the lensing weight function is bell-shaped

$$g(\chi) = 2\frac{r(\chi)r(\chi_s - \chi)}{r(\chi_s)} \tag{2.76}$$

and has its maximum at $z \approx z_s/2$. Ongoing deep redshift surveys will help to constrain it better, but for this analysis we shall need to propagate errors on the median redshift of the sources through the analysis.

We will therefore use the projected and weighted *effective mass distribution*

$$\kappa_{\mathrm{eff}} = \int_0^{\chi_s} W(\chi')\delta(\chi')\mathrm{d}\chi'\,, \tag{2.77}$$

with

$$W(\chi) = \frac{3\Omega_{\mathrm{m0}}H_0^2}{2}\frac{D^A(\chi)}{a(\chi)}\int_\chi^\infty f_s(\chi_s)\frac{D^A(\chi_s - \chi)}{D^A(\chi_s)}\,\mathrm{d}\chi_s\,. \tag{2.78}$$

Using Limber's equation in Fourier space (Kaiser 1998) to relate the three dimensional density field to its projection onto the sky, we can obtain the *convergence power spectrum*

$$C_\ell^\kappa(\ell) = \frac{9}{16}\left(\frac{H_0}{c}\right)^4 \Omega_m^2 \int_0^{\chi_h}\left[\frac{g(\chi)}{D(\chi)}\right]^2 P\left(\frac{\ell}{r}, \chi\right)\,\mathrm{d}\chi\,. \tag{2.79}$$

Here a is the expansion parameter, and H_0 and Ω_m are the present values of the Hubble constant and matter density parameter, respectively.

Conveniently, the two-point statistics of the convergence and shear fields are idential in the weak lensing limit (Bartelman & Schneider 2000). We can therefore directly relate the dark matter distribution to the previously-derived convergence power spectrum (equation 2.79) to the observable *shear power spectrum*,

$$C_\ell^{|\gamma|}(\ell) = C_\ell^\kappa(\ell)\,. \tag{2.80}$$

In fact, it will be easier in practice to measure the real-space correlation functions of shear

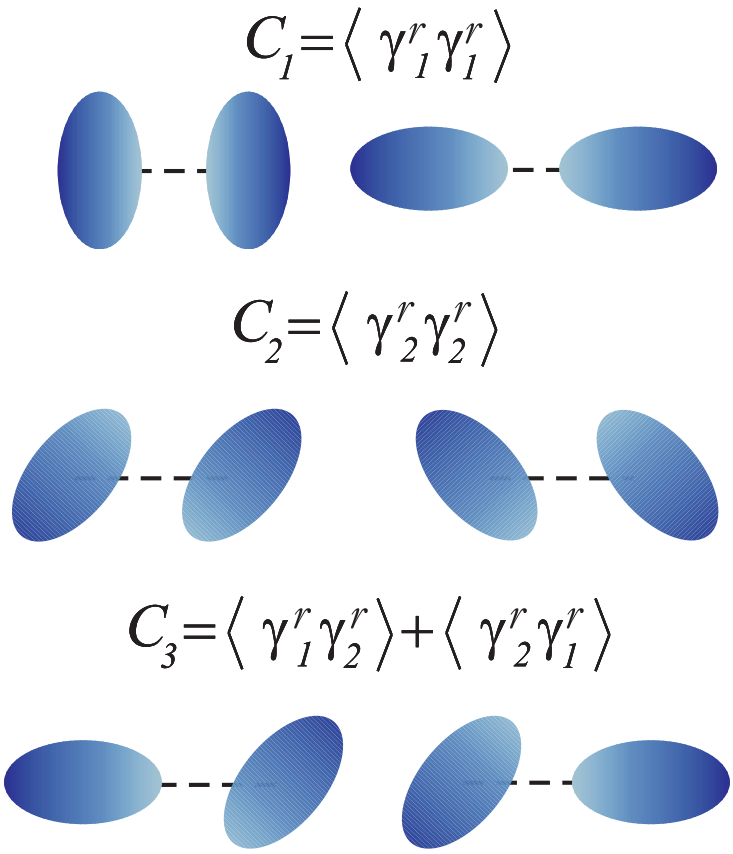

Figure 2.4: Positive contributions to the three shear-shear correlation functions from the relative orientation of galaxy pairs. Negative contributions arise when one of the pair is rotated through 90°.

between galaxy pairs, rather than the Fourier space power spectrum. A typical survey image will contain bright foreground stars or ghost images, cosmic rays and gaps or other effects near the edges of a CCD. Galaxies in these regions need to be excluded from an analysis, and the observed shear field will contain many holes: a horrible window function in Fourier space. Since shear is complex, there are two observable real quantities, and we shall use the *shear-shear correlation functions*

$$C_1(\theta) \equiv \left\langle \hat{\gamma}_1^r(\vec{r})\, \hat{\gamma}_1^r\left(\vec{r}+\vec{\theta}\right)\right\rangle \tag{2.81}$$

$$C_2(\theta) \equiv \left\langle \hat{\gamma}_2^r(\vec{r})\, \hat{\gamma}_2^r\left(\vec{r}+\vec{\theta}\right)\right\rangle , \tag{2.82}$$

from which can be formed

$$\xi_+(\theta) \equiv C_1(\theta) + C_2(\theta) = \frac{1}{2\pi}\int_0^\infty C_\ell^\gamma(\ell)\, \mathrm{J}_0(\ell\theta)\, \ell \mathrm{d}\ell \tag{2.83}$$

$$\xi_-(\theta) \equiv C_1(\theta) - C_2(\theta) = \frac{1}{2\pi}\int_0^\infty C_\ell^{|\gamma|}(\ell)\, \mathrm{J}_4(\ell\theta)\, \ell \mathrm{d}\ell \tag{2.84}$$

plus an additional cross-correlation term between galaxy pairs, $\langle\gamma_1\gamma_2\rangle + \langle\gamma_2\gamma_1\rangle$, which is trivially zero if the universe has no handedness. We have introduced rotated shear estimators $\hat{\gamma}_1^r$ and $\hat{\gamma}_2^r$, which are the projection of the shear γ onto the line between a pair and at $45°$ from it. These are demonstrated in figure 2.4. We can form a shear estimator to directly sample to local mass distribution from the observed shape of every background galaxy in an image (see section §3.2.3). We shall then bin the shear signal on different angular scales in order to reduce observational noise.

Making use of the orthogonality of Bessel functions

$$\int_0^\infty \mathrm{J_n}(\mathrm{s}\theta)\, \mathrm{J_n}(\mathrm{t}\theta)\, \theta \mathrm{d}\theta = \frac{\delta(\mathrm{s}-\mathrm{t})}{\mathrm{t}}\,, \tag{2.85}$$

we can invert relations (2.83) and (2.84) (Schneider *et al.* 2002) to express the power spectrum directly in terms of the measurable correlation functions

$$C_\ell^{|\gamma|}(\ell) = \int_0^\infty [\xi_+(\theta)\, \mathrm{J}_0(\ell\theta) + \xi_-(\theta)\, \mathrm{J}_4(\ell\theta)]\, \theta \mathrm{d}\theta\,. \tag{2.86}$$

2.2.5 Expected signal

Figure 2.5, reproduced from Jain, Seljak & White (2000) shows an example shear field that we could expect to observe. It was calculated by ray-tracing through an n-body simulation of large-scale structure, recording the deflections and magnifications due to structures along each line of sight (the displayed plot is actually calculated in a simulated SCDM rather than ΛCDM universe). Clusters and groups of galaxies can be identified as the coherent tangential structures, where the shear increases towards to centre of the mass overdensity, as described by the derivative of equation (2.44). A greyscale map of the projected mass density in the top-right corner of this particular map can be seen in figure 6.14.

Many examples of galaxy pairs aligned in the specific configurations of shear-shear correlation functions can be picked out by eye on various scales in the shear map of figure 2.5. For instance, pairs of galaxies closer together than the typical scale of clustering tend to be oriented in the positive form of both $C_1(\theta)$ and $C_2(\theta)$. However, galaxies separated by larger distances tend to lie around the outskirts of clusters, and the negative form of C_2 becomes dominant. This is reflected in the predicted forms of shear-shear correlation functions calculated from the non-linear mass power spectrum according to equation (2.79) and shown in figure 2.6: C_2 does indeed become negative at large separations (the absolute value is plotted).

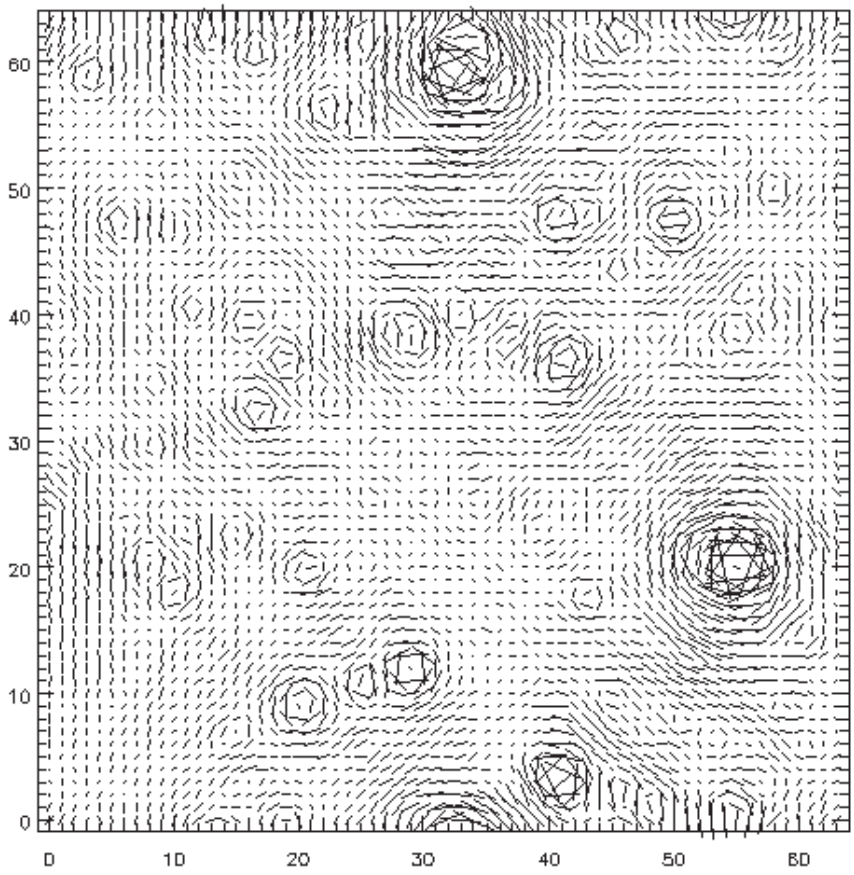

Figure 2.5: A simulated shear field, $60' \times 20'$, reproduced from Jain, Seljak & White (2000). Each vector shows the amplitude and direction of shear, calculated by raytracing through an n-body simulation of large-scale structure and summing the gravitational light deflection from mass overdensities along each line of sight. Clusters and groups can be identified as those locations around which the shear field is tangential and increasing. Mass underdensities and voids are surrounded by radial shear fields.

2.2.6 Shear variance in cells

By analogy with the definition of σ_8, cosmic shear results are frequently expressed as the variance of the shear field $\sigma_\gamma^2 \equiv \langle\, |\overline{\gamma}|^2 \,\rangle$ inside circular cells on the sky. For a top-hat cell of radius θ, this is related to the shear correlation functions by

$$\langle\, |\overline{\gamma}|^2 \,\rangle = \frac{2}{\pi} \int_0^\infty C_\ell^{|\gamma|}(\ell)\, [\mathrm{J}_1(\ell\theta)]^2\, \ell \mathrm{d}\ell \tag{2.87}$$

$$\simeq \frac{2}{\theta^2} \int_0^\theta \xi_+(\vartheta)\, \mathrm{d}\vartheta\,, \tag{2.88}$$

where we have used a small angle approximation. This alternative measurement is now

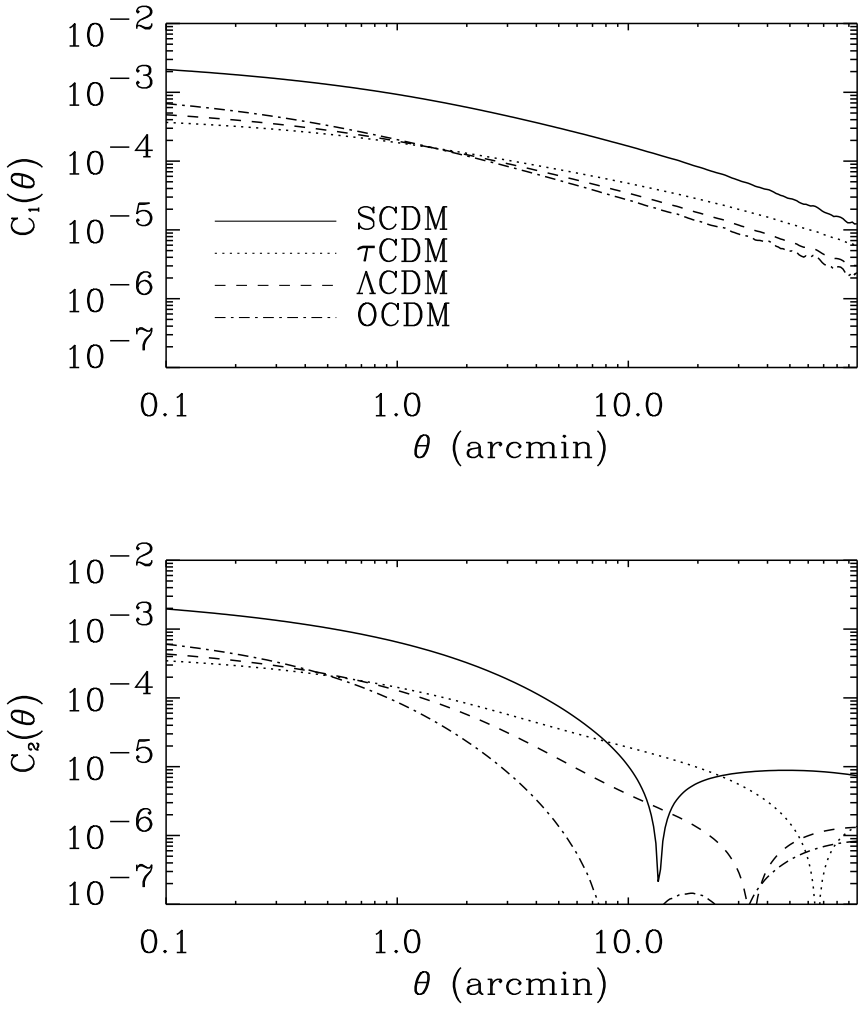

Figure 2.6: Predicted form of the two two-point shear-shear correlation functions as a function of separation between galaxy pairs, reproduced from Bacon *et al.* (2002). $C_2(\theta)$ becomes negative at large separations, so the absolute value has been plotted for the sake of clarity. The four lines in each case apply to different cosmological models discussed by Peacock & Dodds (1994). The curve for "standard" SCDM is higher because it is normalised to COBE data, while the rest are normalised to x-ray selected cluster counts.

used only for historical reasons, because it offers no new information or perspective, and the integration merely acts to strongly correlate measurements on different angular scales.

In real observations, data is typically not available on all scales, particularly at very small θ. If this is omitted from the intergral (2.88), the strong covariance pulls down the calculated values of σ_γ^2 on all scales. This calculation will therefore be delayed until cosmological parameters can be fitted from the shear correlation function data. The best-fit cosmological model will then be susbstituted on the small scales where real data is not available.

2.2.7 E-B decomposition

A vector field can be split into two components called, by analogy with electromagnetism, E- and B-modes. These correspond to the vector gradient and curl of a scalar field and are illustrated in figure 2.7. As seen graphically in figure 2.5, and as is apparent from equation (2.44), gravitational lensing produces only E-modes. The presence of any B-modes in observational data is therefore a useful diagnostic of noise or systematic errors in the data reduction and analysis process. Ideally, a survey's B-mode signal should be zero. But if it is not, it can be added in quadrature to the error bars on the E-mode signal (van Waerbeke *et al.* 2001). If, as commonly assumed, systematics effects would affect E- and B-modes equally, a non-zero B-mode signal should also be subtracted from the E-mode signal itself. Schneider, van Waerbeke & Mellier (2002) found that a very small B-mode contribution can induced by second order effects due to multiple light deflections by several lenses clustered along a line of sight, but this occurs at a level well below current sensitivities.

E- and B-modes correspond to patterns within an extended region on the sky, and cannot be separated locally; this unfortunately requires the integration of the shear correlation functions over a range of angular scales. As was the case for shear variance, this data is typically not available on all necessary scales, so the calculation can be performed only up to an unknown constant of integration. This constant mirrors the mass-sheet degeneracy. In this case, a constant shear within a finite field (*i.e.* a constant mass gradient) can not be uniquely split into E- and B-mode components.

The variance of the aperture mass provides a convenient way to separate the two components, as a function of the scale size of the weight function. Crittenden *et al.* (2001) showed that $M_{\rm ap}$ (equation (2.71)) contains only contributions from the E-mode signal and that $M_\perp$ (equation (2.72)) contains only the B-mode signal. Although the ensemble average of $M_{\rm ap}$ vanishes, $\langle M_{\rm ap}\rangle = 0$, Schneider *et al.* (2002) derived expressions for the variance of these statistics. Using the Mexican hat weight function from equation (2.73),

$$\left\langle M_{\rm ap}^2 \right\rangle(\theta) = \frac{1}{2}\int_0^{2\theta} \frac{{\rm d}\vartheta\vartheta}{\theta^2}\left[\xi_+(\vartheta)T_+\left(\frac{\vartheta}{\theta}\right) + \xi_-(\vartheta)T_-\left(\frac{\vartheta}{\theta}\right)\right] \tag{2.89}$$

$$\left\langle M_\perp^2 \right\rangle(\theta) = \frac{1}{2}\int_0^{2\theta} \frac{{\rm d}\vartheta\vartheta}{\theta^2}\left[\xi_+(\vartheta)T_+\left(\frac{\vartheta}{\theta}\right) - \xi_-(\vartheta)T_-\left(\frac{\vartheta}{\theta}\right)\right], \tag{2.90}$$

where

$$\begin{aligned} T_+(x) = {} & \frac{6(2-15x^2)}{5}\left[1 - \frac{2}{\pi}\arcsin\left(\frac{x}{2}\right)\right] \\ & + \frac{x\sqrt{4-x^2}}{100\pi}(120 + 2320x^2 - 754x^4 + 132x^6 - 9x^8) \end{aligned} \tag{2.91}$$

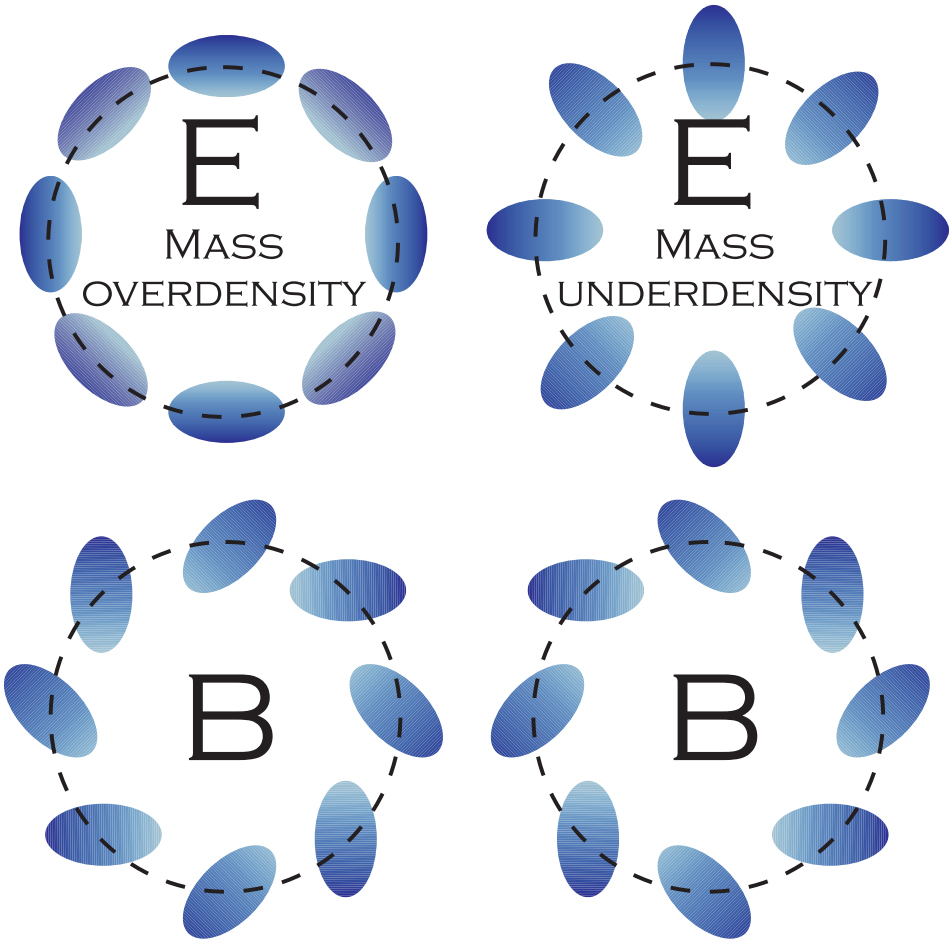

Figure 2.7: Gravitational lensing produces only E modes, with a positive signal around mass overdensities, and a negative signal around mass underdensities. The clustering of mass in the universe determines on which scales their combination is positive and on which scales it is negative. Gravitational lensing does not generally create B modes in the shear field, and their presence can therefore be used as a diagnostic of systematic errors in observational data.

$$T_-(x) \;=\; \frac{192}{35\pi}x^3\left(1-\frac{x^2}{4}\right)^{7/2} \tag{2.92}$$

for $x < 2$ and $T_+(x) = T_-(x) = 0$ for $x \geq 2$.

The variance of $M_{\rm ap}$ is related to the shear power spectrum by

$$\left\langle M_{\rm ap}^2\right\rangle(\theta) \;=\; \frac{288}{\pi}\int_0^\infty C_\ell^\gamma(\ell)\,\frac{[\mathrm{J}_4(\ell\theta)]^2}{\ell^4\theta^4}\,\ell\mathrm{d}\ell\,. \tag{2.93}$$

Unfortunately, the integrals in equations (2.89) and (2.90) are numerically unstable when performed on binned data like that in chapter 3. The function $T_+(x)$ places a lot of weight upon the value of the correlation functions at small angular scales. Since this is changing rapidly, the end result os highly sensitive to the spacing of the bins; and because of small-scale effects like overlapping galaxy isophotes, the values at very small ϑ

are frequently unreliable in real data. Performing the integrals without this data is usually assumed to be equivalent to adding an unknown constant of normalisation to both $\langle M_{\rm ap}^2 \rangle$ and $\langle M_\perp^2 \rangle$ (van Waerbeke *et al.* 2003; Hoekstra *et al.* 2002). However, this is not the case: since the weight functions $T_\pm(x)$ are so complicated, the unknown normalisation will actually vary as a function of θ.

We shall therefore prefer to use an alternatively weighted pair of correlation functions

$$C_E(\theta) \equiv C_1(\theta) + 2\int_\theta^\infty \left(1 - \frac{3\theta^2}{\vartheta^2}\right) \frac{\xi_-(\vartheta)}{\vartheta}\, {\rm d}\vartheta \tag{2.94}$$

$$C_B(\theta) \equiv C_2(\theta) - 2\int_\theta^\infty \left(1 - \frac{3\theta^2}{\vartheta^2}\right) \frac{\xi_-(\vartheta)}{\vartheta}\, {\rm d}\vartheta\,. \tag{2.95}$$

which also separate the shear field into E- and B-modes (Crittenden *et al.* 2001; Pen, van Waerbeke & Mellier 2002). The weighting function in equations (2.94) and (2.95) is wider in θ than it is in equations (2.89) and (2.90), and again extends to scales on which data will not be available from a real survey. This time, however, the missing data is on very large scales (*i.e.* larger than the width of the field of view), and in this regime, the signal is both of low amplitude and clean from most systematics. The truncation of the integrals will once again introduce an unknown function that can be added to $C_E(\theta)$ and subtracted from $C_B(\theta)$. Assuming a ΛCDM universe, and for truncation at $16'$, as will be the case with our major survey, this function is roughly constant at $\sim 2 \times 10^{-05}$. However, since the amplitude normalisation of all these statistics is basically ill-constrained from the data, cosmological parameter fitting will be performed directly upon $C_1(\theta)$ and $C_2(\theta)$ correlation function. In a similar manner to the calculation of shear variance in cells, the E- and B-mode decomposition methods will only be used after the fact, as a consistency check for contamination by observational systematics.

2.3 Scientific aims of this thesis

- Outline the controlled observational techniques and careful data reduction methods necessary for weak lensing measurement.
- Acquire data from two independent but state-of-the-art telescopes and measure cosmological parameters $\Omega_{\rm m}$, the current density of mass in the universe, and σ_8, the normalization of the amplitude of the matter power spectrum on 8 Mpc scales. The independent instrumental systematics from the two data sets will provide further information on the level of instrumental systematics.
- Manufacture detailed and morphologically accurate simulations of astronomical images, with which to test and calibrate galaxy shape measurement techniques, and to assess the impact of observational systematics.
- Investigate the limitations of current techniques. Quantify the prospects for future shear measurement methods and the next generation of surveys using custom-built telescopes.

2.4 Outline of this thesis

This thesis is organised in the following way:

Chapter 3 presents the results from cosmic shear surveys with both the Keck and William Herschel Telescopes. The survey strategies, instruments and observing conditions are described in section §3.1; section §3.2 describes the shear measurement method. The careful steps taken to control systematic errors are outlined in section §3.3. Measurements of the shear-shear correlation function (2.81) on various scales are presented in section §3.4 and, by fitting theoretical models, constraints are obtained upon cosmological parameters σ_8 and Ω_m.

Chapter 4 introduces the "shapelets" formalism for advanced image analysis and the parametrization of arbitrary galaxy morphologies. Section §4.1 discusses why this is important. The functional form of the shapelet basis functions is derived in §4.2. Section §4.3 expresses the manipulation of images as co-ordinate transforms in polar shapelet space, and a series of estimators linearly dependent upon or invariant under these transforms are constructed. These include galaxy flux, centroid, size and higher-order morphology indices. Section §4.4 describes an improved implementation of the shapelet decomposition, taking into account the practical problems of dealing with noise, pixellisation and seeing in real data. Section §4.5 discusses ways to optimise the decomposition for maximum signal recovery and data compression.

Chapter 5 applies shapelet methods to manufacture simulated astronomical survey images. Section §5.1 discusses the reasons for doing this with shapelets, and §5.2 describes the method. Statistical tests in §5.3 demonstrate that the simulations have similar properties to the HDFs, and that the galaxies they contain have realistic morphologies. We find good agreement between simulations and the real HDF galaxies for measures such as the size-magnitude distribution, ellipticity, concentration, asymmetry and clumpiness indices.

Chapter 6 describes the prospects for future cosmic shear surveys. Short-term and long-term goals are suggested in §6.1. Specific attention is paid in §6.2 to the development of the planned Supernova/Acceleration Probe (SNAP), a space-based imager for which detailed engineering specifications are already available. The shapelet-based image simulations are used once again in §6.3, to make quantitative predictions for the precision of shear recovery under various observing conditions, instrument configurations and survey strategies of the SNAP satellite. An outlook for future cosmic shear surveys is presented in section §6.4.

Chapter 7 draws conclusions and contains a summary of the thesis.

3

Current cosmic shear results

3.1 Data acquisition

3.1.1 Survey strategy

The validity of any cosmic shear result depends sensitively upon the treatment of systematic errors and the control of observational biases. Almost all systematic effects act to increase the observed correlations between galaxy shapes, and thus mimic cosmic shear. To help ascertain the level of our systematics, we shall compare cosmic shear observations taken with independent instruments. We shall present data from the Echelle Spectrograph and Imager (ESI) on the 10m Keck II telescope in Hawaii. This is an off-axis imager at Cassegrain focus, with a distortion corrector. We shall present data from the Wide Field Camera (WFC) mounted at prime focus on the 4.2m William Herschel Telescope (WHT) on La Palma. This has a wide field of view but also has relatively large optical distortions. We also attempted to acquire data from the Deep Imaging Multi-Object Spectrograph (DEIMOS) at Nasmyth focus on Keck, but were defeated by poor observing conditions.

We have adopted a "pencil-beam" survey strategy for both the Keck and WHT observations, acquiring narrow but deep ($z \simeq 1$) images on the many lines of sight shown in figure 3.1. Field locations are all separated by more than 2°, to sample independent structures, and thus minimise uncertainties from "cosmic" (sample) variance. They were also chosen in a quasi-random fashion, without regard to the presence or absence of mass concentrations, in order to obtain a representative sample of density fluctuations

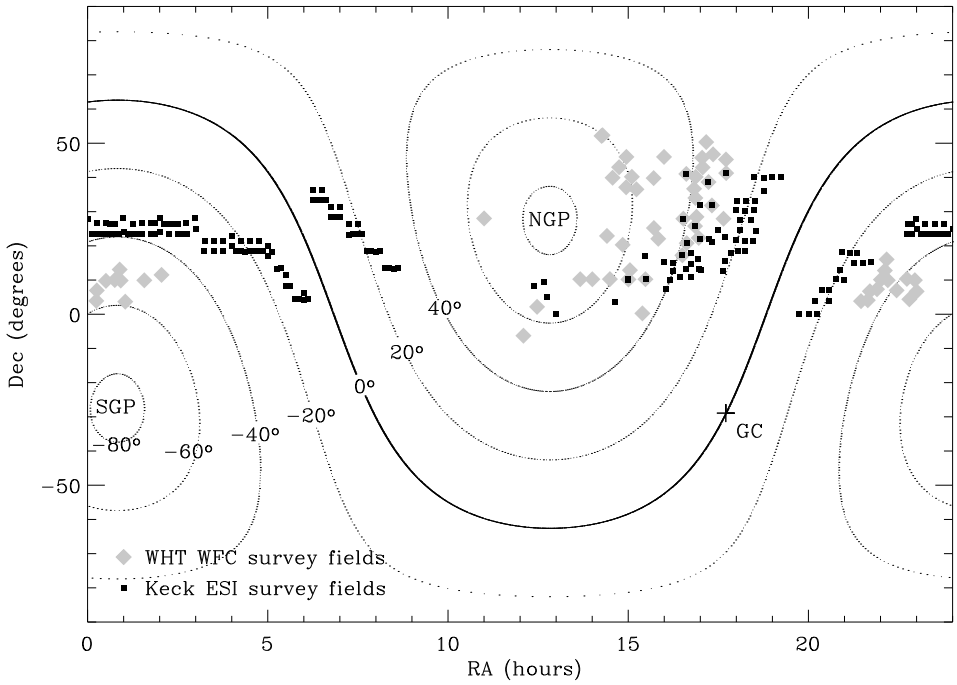

Figure 3.1: The sky location of the cosmic shear fields in the William Herschel Telescope and Keck surveys. Galactic latitudes of 0°, ±20°, ±40°, ±60° and ±80° are shown as contours. The Galactic poles are marked, and the Galactic centre shown as a cross.

in the universe. Field locations were initially placed in a grid of coordinates spanning the accesible RA range, and at Galactic latitudes tuned to ensure ∼50 unsaturated foreground stars in each Keck field, or ∼200 in each WHT field. These stars will be used to measure the Point-Spread Function (PSF) or "seeing" across each image. The STScI Digitised Sky Survey was finally used to find an appropriate field near each set of coordinates, avoiding stars brighter than $R < 11$ in the APM (Automatic Plate Measuring machine) and GSC (Guide Star) catalogues, to prevent large areas of saturation or ghost images.

As a final constraint, every field was observed within 20° of zenith. This minimises image smearing due to atmospheric refraction: particularly above Keck, which does not have an Atmospheric Dispersion Corrector (the excellent image quality described in section §3.1.3 confirms that this is not a serious limitation at low airmass). For both telescopes, the constraint also minimises any image distortion associated with telescope or instrument flexure (§3.3.4).

Since gravitational lensing is achromatic, our observations could be made in any photometric band. R and I bands afford the most efficient deep imaging in a given exposure time, but fringing in the I band with the WFC CCDs (Carter & Bridges 1995) made it most convenient to consistently image in R with both telescopes. The WHT R-band is a standard Harris R filter; the Keck R-band is a specially constructed filter with similar throughput and spectral range ($\bar{\lambda} = 6657$Å, effective FWHM$= 1200$Å). The

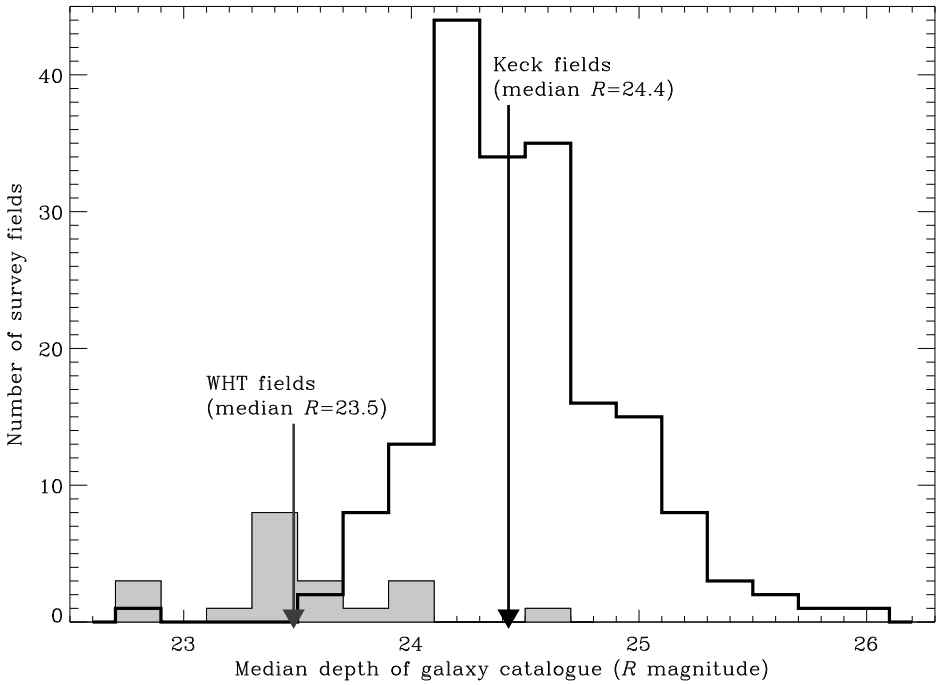

Figure 3.2: Median reddening-corrected R-band magnitude of the galaxies in the final shear catalogue for each Keck field, and a random subset of the WHT fields (analysis by David Bacon). The median magnitude of galaxies in the combined survey is R=23.6.

slightly different galaxy redshift distribution probed by this filter will be taken into account in our estimates of the source redshift uncertainty.

3.1.2 Survey depth

Bacon, Refregier & Ellis (2000) demonstrated that the expected level of cosmic shear signal (see §2.2.5) could be most efficiently measured on the WHT using 1 hour exposures. Such images reach a limiting magnitude of $R = 25.8$ for a point source detected at 5σ. After various selection criteria (see §3.2.2), we keep ~ 16.5 resolved galaxies per square arcminute in the final WHT galaxy catalogues. Precise photometric calibration using standard stars, and including a correction for reddening by galactic dust performed by David Bacon, shows that these have a median magnitude of $R = 23.5 \pm 0.2$ (see figure 3.2). According to *e.g.* Cohen *et al.* (2000), this corresponds to a median source redshift of $z_s = 0.8 \pm 0.08$.

Any shallower a survey would face the danger of contamination by galaxies' intrinsic alignments (see discussion in §3.3.6). Longer exposure times would offer diminishing returns, because the shapes of fainter and therefore smaller galaxies are seriously degraded by a ground-based PSF. Even with a deeper survey, such galaxies would provide noisy and unreliable shear estimators. We therefore aimed to match this depth with our Keck survey, and to probe the same redshift range. An exposure time of 10 minutes

successfully reaches the same S/N of 5 for the detections of point sources at $R = 25.8$. However, the better seeing during our Keck observations (see figure 3.3) results in a slightly fainter magnitude limit for the selected objects than those from the WHT survey. This is entirely acceptable, as we can compare results by scaling the predictions according to the equation $\sigma_\gamma \propto z_s^{0.8}$ (*e.g.* Bacon, Refregier & Ellis 2000).

The final object catalogue from Keck data contains ~ 27.5 resolved galaxies per square arcminute, with a median magnitude of $R \simeq 24.4 \pm 0.2$. The distribution of magnitudes in the catalogue extends substantially fainter than this median, with the galaxy count as a function of magnitude dropping to 50% of maximum at $R = 25.2$. According to Cohen *et al.* (2000), our median magnitude of $R = 24.4$ corresponds to a median source redshift of $z_s \simeq 1.0 \pm 0.1$. This error may be subject to additional sample variance, because the number of measured redshifts in Cohen *et al.* (2000) is relatively small. We shall therefore quote our redshift error separately to other statistical errors, for comparison with future redshift surveys.

3.1.3 Keck telescope data

We have acquired 0.6 square degrees of imaging on the Keck telescope. This was so limited by the size of our R-band filter, which restricts the field of view for each field to $8' \times 2'$. However, the great advantage which Keck presents for measuring cosmic shear is its speed in achieving the necessary depth. The fast data acquisition rate allowed us to obtain 173 independent fields, thus minimising the contribution to noise by cosmic variance. The observations were performed during 6 nights during November 2000 and May 2001, as a good seeing override on an independent spectroscopic programme.

Three 200s exposures were taken for each survey field, each offset by $5''$. This enabled a continual monitoring of astrometric distortions within the telescope/camera, cosmic ray removal, and lower overheads in the event of inclement weather. On-the-fly updates of PSF size and stellar ellipticity, using our SExtractor-based (Bertin & Arnouts 1996) software at the telescope, allowed the occasional exposures with poor seeing or telescope tracking to be retaken when conditions improved. The multiple mirror segments of the telescope were refocused, and observations of standard stars were taken, several times per night. All the fields were observed as they passed near the meridian, in order to minimise image distortion from the atmosphere and from telescope or instrument flexure. But they were taken no closer than 5° to zenith. This reduced the rate of sky rotation, and minimised potential tracking errors on this alt-az telescope.

The median seeing for the observations was $0.58''$, with 75% in seeing better than $0.7''$. Figure 3.3 records the seeing values for all fields. Furthermore, the rms stellar ellipticity for the images was only $\sigma_{e*} = 0.035$. This excellent data quality will assist PSF correction (§3.3.3), and yield a low level of noise on shear measurement. ESI's pixel size of $0.153''$ is also considerably finer than that for WHT, allowing a better sampling of the

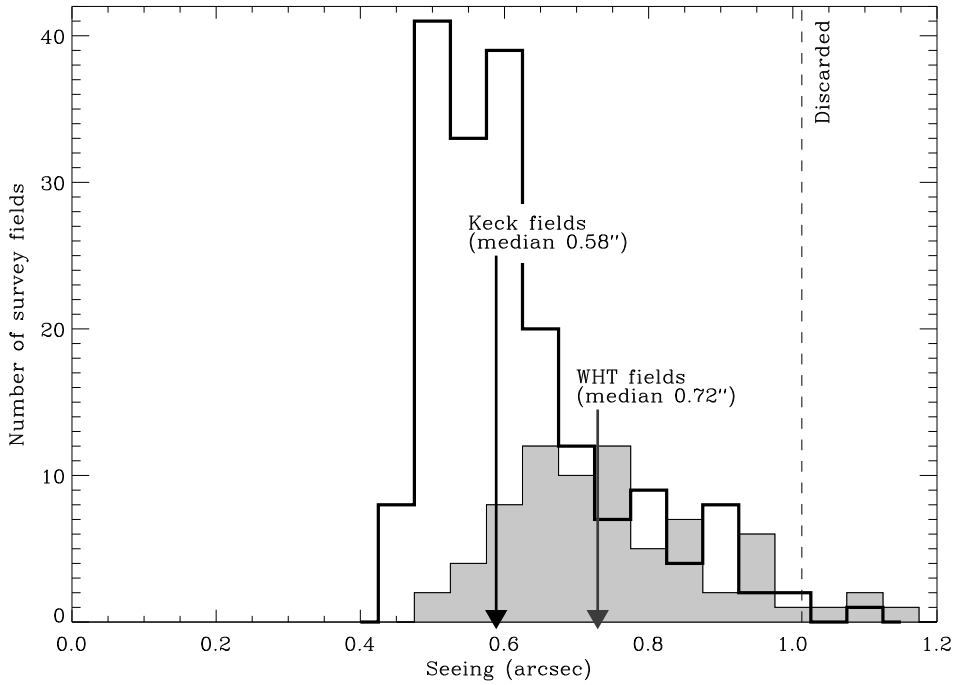

Figure 3.3: Seeing FWHM in all survey fields. Keck data are shown in white; WHT data are shown as shaded. No data with seeing worse than 1″ is used. A combined survey from both telescopes has a median seeing of 0.70″.

galaxy images. The combination of these properties will enable the measurement of the shapes of a higher number density of galaxies and of closer pairs of galaxies. Aside from its relatively small field of view, Keck is therefore an ideal telescope for weak lensing measurements.

The data were then reduced, with care taken to remove background gradients, fringing, and other effects that could affect the measurement of objects' shapes. The overscan region of the ESI CCD proved the most accurate source for bias subtraction. Flat fielding was performed separately for each night's data, using an image created by stacking all of the data from that night, with sigma-clipping to remove objects. Sky- or dome-flats were found to be insufficiently accurate for this purpose, due to the slight differences in colour response across the CCD during twilight observations. Fringing was already below the level of background noise on Keck images and did not need to be removed.

The three dithered exposures for each field were then divided by their median values, to normalise their background levels. They were re-aligned, using bright stars in the image as reference points; no rotation of the field was found to be necessary, and linear interpolation between adjacent pixels was used to implement sub-pixel shifts. The exposures were then stacked, using 3σ-clipping to remove cosmic rays and cosmetic defects. Their combined photometric zeropoints were then calibrated using observations of standard stars, and corrected for galactic dust aborption by David Bacon. A section from one reduced Keck image is shown in figure 1.1.

3.1.4 William Herschel Telescope data

We have acquired 4 square degrees of imaging with the William Herschel Telescope. To the eight $8' \times 16'$ WHT images with which a cosmic shear signal was first detected by Bacon, Refregier & Ellis (2000), we have added 52 new $16' \times 16'$ images. These were obtained over 16 nights during June 2000, June 2002 and August 2002, and take advantage of a second CCD that had been added the Wide Field Camera (WFC) by that time. The pixel size of both CCDs is $0.24''$.

For each survey field we took four 900s exposures, each dithered by a few arcseconds from the last. Once again, this tactic enabled the continual re-calibration of optical distortions in the telescope and camera, the removal of cosmetic defects, and the constant moitoring of observing conditions. Observations of standard stars were taken regularly throughout each night. The median seeing from all observations was $0.72''$, and no data is used with seeing worse than $1''$. The rms stellar ellipticity, averaged across survey fields, was $\sigma_{e*} = 0.05$.

During data reduction, variously stacked combinations of the data from each night were used for both bias subtraction and flat fielding. A fringe frame was also compiled from all of the exposures in each night, and the multiple of that frame which minimised fringing was subtracted from each image. This technique reduced fringing to a negligible level $< 0.1\%$ of the rms background noise. The exposures were then realigned and stacked using the same algorithm as described for the Keck data.

It is not precisely clear how signals from the early, half-sized WHT fields ought to be weighted with respect to those from the later and larger WHT fields, because the ratio of galaxy pairs from each data set varies as a function of the pair separation. However, the low number of smaller fields means that they have little impact upon the final result, so, for simplicity, we weight their contributions 1:2 on all scales.

3.2 Shear measurement

3.2.1 Shear estimators from galaxy shapes

To measure the theoretical framework of correlation functions and cosmological parameters described in chapter 2, we shall need to measure the observed shear field at many points throughout our survey. As we shall find below, it is possible to calculate a shear estimator $\hat{\gamma}$ from the shape of every resolved galaxy. These estimators will all be very noisy, both because of observational noise, and the intrinsically elongated morphologies of real galaxies. Indeed, it will turn out that the latter effect is the most important: even in perfect observing conditions, the typical elongations induced by weak gravitational lensing are an order of magnitude smaller than the scatter of ellipticities already present! However, if the intrinsic orientations of galaxies are assumed to be random (see the discussion in section §3.3.6), by averaging over the shapes of many galaxies, we can

therefore ensure that their intrinsic ellipticities cancel out. Only the coherent distortions created by gravitational shear then remain. We shall therefore require an unbiased shear estimator $\hat{\gamma}$ that can be calculated from galaxy shapes. The average shear estimator for a sample of galaxies $\langle\hat{\gamma}\rangle$ must be proportional to the true local shear γ, and, if the galaxies are unlensed, the average shear estimator must be zero $\langle\hat{\gamma}\rangle = 0$.

The standard shear measurement method for the past decade has been the publicly available IMCAT code introduced by Kaiser, Squires & Broadhurst (1995; hereafter KSB), plus a variety of later additions and refinements (*e.g.* Luppino & Kaiser 1997; Hoekstra *et al.* 1998). It has been tested upon simulated ground-based data by Bacon *et al.* (2001) and Erben *et al.* (2001), and recovers input shear with an accuracy of approximately 10%. This is quite sufficient for the current generation of surveys, and we shall use this method to analyse our own data in section §3, including an *ad hoc* shear calibration factor of $(0.85 \pm 0.04)^{-1}$ that was found to be necessary in the implementation of Bacon *et al.* (2001). Other sources of error, including "cosmic" (sample) variance and statistical errors due to the finite number density of resolved background galaxies still dominate current results. However, the underlying mathematics of KSB is fundamentally ill-defined and is unstable for faint and small galaxies (*e.g.* Kuijken 1999; Bernstein & Jarvis 2002; van Waerbeke *et al.* 2002). New measurement methods will soon be required in order to tighten the constraints upon cosmological parameter from the next generation of large, ground-based surveys dedicated to weak lensing, or high-resolution imaging from space. One adapted version of KSB, which takes advantage of the improved observing conditions in space and thus stabilizes shear estimation, was developed by Rhodes, Refregier & Groth (1998). This will be used with simulated space-based data in chapter 6. Inevitably, though, an entirely new approach will be required. Suggested successors of KSB include shapelets-based techniques (Bacon & Refregier 2003; Massey, Refregier & Bacon in prep.) as well as others (Kaiser 2000; Kuijken 1999; Bernstein & Jarvis 2002; Bridle *et al.* in prep.).

In this analysis we shall use the version of the KSB technique and IMCAT code from Bacon *et al.* (2001), but continue to bear in mind its possible instabilities and include the necessary calibration factors. The KSB method has been widely used and documented, so the following discussion is intended only as a brief review, to outline the salient points and to determine the relevant implications for our data reduction and analysis. For a more complete description of these various issues, see *e.g.* Mellier (1999), Bacon *et al.* (2001), Erben *et al.* (2001), van Waerbeke *et al.* 2002, Bernstein & Jarvis (2003) and Refregier (2003).

3.2.2 Source detection

Individual objects within an image are first isolated using a matched-filter routine known as HFINDPEAKS. This steps across a 2D image, convolving it each time with a compen-

sated "Mexican hat" filter of varying sizes. Each convolution returns a detection significance ν, and objects above a certain threshold are recorded. Their centres and sizes r_g are determined by the placement and width of the filter which gives the maximum significance. The local sky background is then determined using the GETSKY routine, so aperture photometry and shape measurement can be performed on the corrected image by APPHOT and GETSHAPES.

We immediately remove noisy objects from the catalogue by applying cuts in size, signal-to-noise and ellipticity of

$$r_g \geqslant 1 \text{ pixel} , \tag{3.1}$$

$$\nu \geqslant 15 , \tag{3.2}$$

$$\varepsilon \leqslant 0.5 . \tag{3.3}$$

We shall also remove unresolved galaxies ($r_g < r_g^*$) once we have determined the size r_g^* of the PSF locally. Note that after these cuts, all of the galaxies in our survey will carry equal weight. This is not the case in other implementations (Hoekstra *et al.* 2002; van Waerbeke *et al.* 2002), but note that our version of the method has been calibrated (Bacon *et al.* 2001), using the same detection algorithm and catalogue cuts on simulated WHT images with a known input shear.

3.2.3 Shears

A monochromatic image is a real, two-dimensional function $f(\vec{x})$, where f is the surface brightness of an object, or perhaps the total flux within a pixel. In the absence of gravitational lensing, the image of an "average galaxy", *i.e.* the stacked images of many randomly-oriented galaxies, has circular isophotes. It is therefore even more simply parameterized by its one-dimensional radial profile $f(|\vec{x} - \vec{x^c}|)$, where $\vec{x^c}$ is the centre of the object defined by its *dipole moment*

$$\vec{x^c} \equiv \int_{\mathbb{R}^2} \vec{x}\, f(\vec{x})\, W(|\vec{x}|)\, \mathrm{d}^2\vec{x} \tag{3.4}$$

and $W(|\vec{x}|)$ is a radial weight function chosen to isolate the object and ensure that the integral converges. In the KSB method, the same Mexican-hat weight function that was used to detect objects is also used to measure their shapes.

Applying a pure shear to this object will not affect its (azimuthally-averaged) radial profile, but it will introduce a non-zero *quadrupole moment*,

$$Q_{ij} \equiv \int_{\mathbb{R}^2} (x_i - x_i^c)(x_j - x_j^c)\, f(\vec{x})\, W(|\vec{x}|)\, \mathrm{d}^2\vec{x} , \tag{3.5}$$

where $i, j = \{1, 2\}$. Indeed, it is only the quadrupole moment of this object that will be

affected by a shear, because (by definition) only this quantity has the desired angular dependence. It is therefore natural to base a local shear estimator for each galaxy in a survey around some measure of its quadrupole moment. The complication will be to ensure that the estimator is unbiased when averaged over a population ensemble, where each galaxy does not itself have concentric circular isophotes, and where the galaxies span a wide range of sizes and magnitudes.

So that the large or bright galaxies do not dominate an average (they are also likely to be the closest objects with a systematically lower shear than the rest), and so that a change in brightness due to lensing magnification does not affect the results, we form a complex *ellipticity*, or normalized *polarizability parameter*

$$\varepsilon \equiv \left\{ \frac{Q_{11} - Q_{22}}{Q_{11} + Q_{22}}, \frac{2Q_{12}}{Q_{11} + Q_{22}} \right\} , \tag{3.6}$$

in a analogous way to equation (2.67). Kaiser, Squires & Broadhurst (1995) show that this parameter is changed under the application of a small shear by factor that depends upon the object's radial profile and its intrinsic ellipticity $\varepsilon^{\rm intrinsic}$ (an object initially elongated in the direction of a shear is not distorted as much as a previously circular one)

$$\varepsilon_i \rightarrow \varepsilon_i' = \varepsilon_i^{\rm intrinsic} + P_{ij}^{\gamma} \gamma_j + \mathcal{O}(\gamma^2) , \tag{3.7}$$

where a galaxy's shape information is encoded in the its *shear susceptibility tensor*

$$P_{ij}^{\gamma} = 2(\delta_{ij} - \varepsilon_i \varepsilon_j) , \tag{3.8}$$

for the simple case of unweighted ellipticities (*i.e.* $W = 1$, $W' = W'' = 0$). For a general weight function W, the shear susceptibility is a more complicated expression (Kaiser, Squires & Broadhurst 1995). The Kronecker delta symbol above is then replaced by

$$\frac{1}{Q_{11} + Q_{22}} \int_{\mathbb{R}^2} f(\vec{x}) \begin{bmatrix} W(x_1^2 + x_2^2) + W'(x_1^2 - x_2^2)^2 & 2W'(x_1^2 - x_2^2) x_1 x_2 \\ 2W'(x_1^2 - x_2^2) x_1 x_2 & W(x_1^2 + x_2^2) + 4W' x_1^2 x_2^2 \end{bmatrix} \mathrm{d}^2 \vec{x} \tag{3.9}$$

which, for the Mexican hat weight function, is a combination of the object's zeroth-order and octopole moments Q_{ijkl}. These are both defined similarly to equation (3.5), and are calculated from an image by the IMCAT routine GETSHAPES.

For each source galaxy, we are then able to form a *shear estimator*

$$\hat{\gamma}_j \equiv \frac{\varepsilon_i'}{P_{ij}^{\gamma}} . \tag{3.10}$$

However, the interpretation of this tensor division is a matter of debate (van Waerbeke *et al.* 2000; Bacon *et al.* 2001, Hoekstra *et al.* 2002). If the centroid has been well-chosen, the off-diagonal components of equation (3.9) are relatively small: certainly smaller than

the noise in any one object. It will not bias the estimator (on average) if we should choose to discard these components. We can then combine the two remaining diagonal components into a complex scalar version of P^γ. This allows us to relate a complex ellipticity $\varepsilon = \varepsilon_1 + i\varepsilon_2$ to a complex shear γ as before. Equation (3.10) becomes a well-defined, practically calculable and unbiased local shear estimator. Substituting it into equation (3.7), we indeed find

$$\langle\hat{\gamma}\rangle = \left\langle \frac{\varepsilon'}{P^\gamma} \right\rangle = \langle\gamma\rangle + \left\langle \varepsilon^{\text{initial}} \right\rangle = \langle\gamma\rangle \ , \tag{3.11}$$

where the last equality only holds if the intrinsic ellipticities of nearby galaxies are uncorrelated (see discussion in section §3.3.6).

3.2.4 Smears

Sheared light rays and coherently distorted images travel to us in pristine condition from half way across the observable universe. Unfortunately, they are then promptly destroyed during their last few tens of miles, by turbulence in the Earth's atmosphere and imperfect optics in our telescopes. The combined point spread function can be measured from non-saturated stars within an image, and can be split into two components. The isotropic part of the PSF circularizes an image, enlarging shapes and reducing their ellipticity. The anisotropic component elongates all objects within the image, increasing their ellipticity, but all in the same direction. Both therefore affect the measured shear and need to be corrected.

The KSB method adopts a similarly linear approach to PSF correction as it does for shear measurement. The ellipticity ε of a background galaxy changes under PSF convolution by

$$\varepsilon_i \to \varepsilon_i' = \varepsilon_i^{\text{intrinsic}} + P_{ij}^{\text{sm}} \varepsilon_j^* \ , \tag{3.12}$$

where ε^* is the stellar ellipticity and the tensor for a general weight function is given by the somewhat complicated expression

$$P_{ij}^{\text{sm}} = \int_{\mathbb{R}^2} f(\vec{x}) \begin{bmatrix} 2W + 4W'|\vec{x}|^2 + 2W''(x_1^2 - x_2^2)^2 & 4W''(x_1^2 - x_2^2)x_1x_2 \\ 4W''(x_1^2 - x_2^2)x_1x_2 & 2W + 4W'|\vec{x}|^2 + 8W''x_1^2x_2^2 \end{bmatrix} \mathrm{d}^2\vec{x} - \varepsilon_i^*\varepsilon_j^* \ . \tag{3.13}$$

Whilst the effect of shear on an object depends upon its initial shape, the effect of a smear therefore depends only upon its size. For example, a very large galaxy is left virtually untouched by convolution with a PSF; but at the other extreme, a point source attains exactly the shape and size of the same PSF. Furthermore, empirical data shows that $P_{11}^{\text{sm}} = P_{22}^{\text{sm}}$ within the noise, and that the off-diagonal components of P^{sm} are compatible with zero. We should especially like to reduce the noise in this quantity, because it will

appear on the denominator. We shall therefore approximate the isotropic component of $P^{\rm sm}$ with a real scalar, simultaneously using all of the stars within an image to fit $\mathrm{Tr}(P^{\rm sm})/2$ as a function of size r_g^* only.

In ground-based observations, the PSF varies both as a function of position and, rapidly, as a function of time. It is therefore essential to measure the (anisotropic component of the) PSF from stars within individual survey images, as it is likely to have changed by the next exposure. Unfortunately, this means that the moments of the PSF are only known at the positions of the stars and not at the positions of the galaxies. To determine the shape corrections for each galaxy, we interpolate by fitting polynomial functions to each component of the PSF's quadrupole moment.

Combining the isotropic fit and the interpolated quadrupole moments, we can then calculate an *effective shear susceptibility*

$$P^\gamma = P^\gamma_{\rm galaxy} - \frac{P^\gamma_*}{P^{\rm sm}_*} P^{\rm sm}_{\rm galaxy} \,, \tag{3.14}$$

to replace the value used in equation 3.10. Note that we can generally select stars much brighter than the distant galaxies, so their shape measurement is therefore not as affected by background noise. The off-diagonal terms are therefore small, and can once again be neglected to effect the division by $P^{\rm sm}_*$.

3.3 Control of systematic biases

3.3.1 Shear calibration

The most important effort to control systematic biases in our survey was the manufacture of simulated images by Bacon *et al.* (2001), using the ARTDATA package in IRAF (Tody 1993). The simulations have observing conditions and a galaxy sample similar to those in the real data, but with a known input shear. In principle, even a very primitive measurement method could be used to measure cosmic shear if it were first calibrated upon sufficiently realistic simulated images. (An advanced image simulation method will be presented in chapter 5, specialised towards the mimicry of high-resolution space-based cosmic shear surveys. See section §5.1 for a further discussion about the need for image simulations).

Shear estimators from the KSB method were corrected by a calibration factor of $(0.85 \pm 0.04)^{-1}$ derived by Bacon *et al.* (2001). This factor is due to various effects, including object selection biases, shape measurement in noisy images, measurement of P^γ from an already sheared image, and numerical instabilities in PSF correction. It even varies as a function of S/N and must therefore be calibrated on a population with a known size-magnitude distribution (Erben *et al.* 2001). The error upon our calibration factor therefore includes contributions from all of these sources. It will be propagated

through to our final constraints upon cosmological parameters. It does indeed produce a major contribution to the overall error budget (see §3.4).

3.3.2 Preferential detection of certain objects

There are several problems inherent to matched-filter detection methods like HFINDPEAKS. The most significant is the preferential detection of objects with shapes similar its (circular) Mexican hat filter. This effect will exclude faint, highly elliptical objects from our catalogues, reducing the mean ellipticity of source galaxies, and preferentially selecting faint objects aligned 90° away from the direction of the PSF anisotropy. However, a much greater impact is produced by the cut in ellipticity that is necessary to remove cosmetic defects and highly elongated objects that would provide noisy shear estimators.

The impact of this bias depends upon the slope of the ellipticity distribution. Compensating for it highlights the absolute necessity for realistic image simulations. Note that the introduction of a weighting scheme for source galaxies as a function of their size, magnitude or ellipticity (*c.f.* Hoekstra *et al.* 2002; van Waerbeke *et al.* 2002) merely adjusts the regime in which these biases operate, rather than removing them completely.

A very useful diagnostic for this bias, as well as many others that link measured shears to the stellar ellipticity, is provided by the *star-galaxy correlation functions*

$$C_i^{\rm SG} \equiv \frac{\langle\, \gamma_i\, e_i^*\, \rangle^2}{\langle\, e_i^*\, e_i^*\, \rangle}, \tag{3.15}$$

where $i = \{1, 2\}$ are components of galaxies' shear γ or the stellar ellipticity e_i^* before correction.

A significant (anti-)correlation signal was indeed seen for faint galaxies in Bacon, Refregier & Ellis (2000). Whether this be due to selection biases, or the over-correction of the PSF anisotropy upon the shapes of faint galaxies, this is the reason for our relatively conservative S/N cut $\nu \geqslant 15$. A sufficiently high cut was specifically chosen to remove the effect from that dataset. The star-galaxy correlation functions from our updated observations are shown as dashed lines in the top two panels of figures **??** and **??**. They are barely above the x-axis and confirm that the effect is still negligible on all scales. Note that it would also have appeared as a B-mode signal in figure 3.11, which is in fact consistent with zero on all scales.

Other potential problems associated with object detection include the *selection bias* (Kaiser 2000; Bernstein & Jarvis 2002), which increases the detection significance of objects aligned with the local PSF, and the *centroid bias*, which overestimates an object's ellipticity in the direction of the PSF anisotropy. These biases both act proportionally to ν^{-2}, and have negligible < 0.002 impact upon shear estimators from objects passing our relatively conservative S/N cut $\nu \geqslant 15$. See, for example, figures 7 and 8 in Bernstein &

Jarvis (2002).

3.3.3 Correction for the point-spread function

Over- or under-correction for changes in shape due to PSF convolution would also be apparent in the star-galaxy correlation functions (3.15) and E-B decomposition (2.94–2.95). However, the subject warrants further discussion because it is such an important part of the shear measurement method and, although the PSF forms distinctive patterns in observations on all telescopes, their causes are rather poorly understood.

Fortunately, the excellent optical performance of Keck described in section §3.1.3 greatly helps PSF correction, and it does permit some investigation. Some examples of the patterns made by the PSF anisotropy in Keck images are shown in figure 3.4. These are extreme cases, but were all taken on the same night, and the patterns can indeed vary a great deal from even one exposure to the next. The main cause is often found to be imperfect telescope guiding, which typically acts on a delayed feedback circuit, or "wind shake", which creates oscillations in the telescope. These emerge on an alt-az telescope as a uniform PSF anisotropy across the field of view, or as a swirl pattern around the optical axis (within single exposures). Seen in Keck exposures with good tracking, the next dominant effect appears to be astigmatism due to the fact that the CCD is slightly skewed with respect to the focal plane, thus probing optical conditions slightly above and below the focus. Other significant effects are probably created by transient atmospheric conditions, but these are more difficult to disentangle from the ever-changing PSF patterns.

Note that smears could also be introduced by the co-addition of imperfectly-aligned multiple exposures. We have obviously tried to re-align dithered exposures as well as possible. However, our algorithm notably lacks correction for any rotation of the field between exposures. Any such misalignment would reveal itself in stacked exposures with patterns similar to those caused by tracking errors. This component of the PSF can be treated in the same way as the others, and is corrected for along with them by KSB.

The long-thin ($8' \times 2'$) geometry of the ESI field also enhanced some previously unforeseen biases due to edge effects (which also necessitated careful masking of the field: see §3.3.5). The PSF interpolation in the short x direction was often overfit by KSB's simple polynomial fitting. The divergent PSF model overcompensated for the true smearing and spuriously elongated galaxies near to the edges in the y direction. This effect revealed itself as a non-zero $\sim 2\%$ mean shear within each field (perhaps the offset in CFHT data from van Waerbeke *et al.* (2001) has a similar origin). The divergent PSF model also caused a $\sim 1.1\%$ excess in the final shear correlation functions at pair separations around $2'$, the width of the CCD. A more adaptative algorithm was written, which found the smallest degree polynomial possible for a significant fit. Typically, a quadratic or cubic was required in the long y direction; the much narrower x direction generally

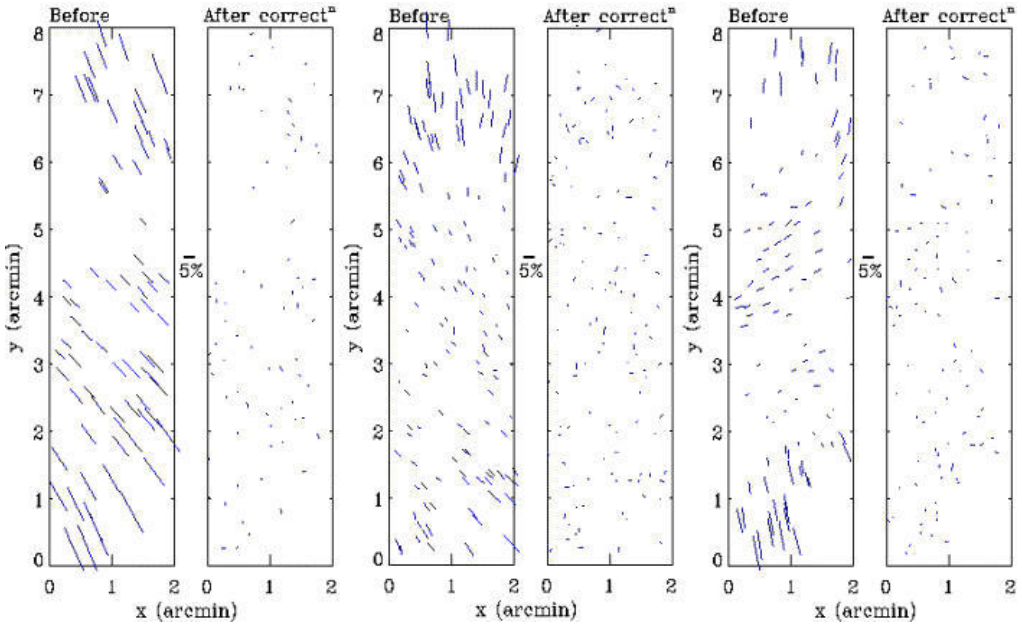

Figure 3.4: Example stellar ellipticity patterns on the Echelle Spectrograph and Imager on the Keck telescope. The patterns vary dramatically between fields: these three are extreme examples, but were still all taken on the same night. The mean PSF ellipticity across the survey is 0.035. The first panel shows a field in which telscope tracking was not perfect. The third panel shows suspected astigmatism. The pattern in the fifth panel is unexplained. Intervening panels show the stellar PSF after correction by the KSB method. This performs well in all cases, and the mean stellar ellipticity is reduced to < 0.001 across the survey, with residual orientations being essentially random. The correction of similar PSF patterns in a WHT image is demonstrated in figure 5 of Bacon, Refregier & Ellis (2000).

suited only a constant or linear function. This algorithm could also be closely monitored, to remove any anomalous stars by hand. In this way, the rms stellar ellipticity was reduced to a negligible level < 0.001.

The WHT PSF can become quite anisotropic over long exposures, with a mean stellar ellipticity of 0.051 ± 0.28. The PSF anisotropy patterns are less clear, but tracking and astigmatism certainly have major roles. The patterns are generally well-fit by quadratic or cubic polynomials in the $8'$ x direction, and by cubic or quartic polynomials in the $16'$ y direction. Application of the same PSF fitting and correction algorithm as for the Keck data, reduced the WHT rms stellar ellipticity to 0.0056 ± 0.0012.

3.3.4 Instrumental distortion

Telescope flexure, or distortions within the camera, can shear an image in a way that precisely that mimics gravitational lensing. This instrumental shear pattern changes as a telescope moves around the sky, or as the camera changes temperature. Fortunately, we can use the accompanying changes in objects' positions on dithered exposures to monitor these "astrometric" distortions in every survey field.

The observed positions of objects are, in general, offset by more than just the point-

ing change between dithers. We first determine SExtractor (Bertin & Arnouts 1996) positions for each galaxy and star found on at least three dithers for a given field. The distortions are then parameterized by

$$\vec{x}_{f'} - \vec{x}_f \simeq \Psi\Big(\langle\vec{x}_f\rangle - \langle\vec{x}_{f'}\rangle\Big)\,, \tag{3.16}$$

where $\vec{x}_f$ and $\vec{x}_{f'}$ are the positions of one galaxy observed on two different dithers; and where $\langle\vec{x}_f\rangle$ and $\langle\vec{x}_{f'}\rangle$ are the positions of the centres of the frames. Using a linear approximation for the *camera's distortion matrix*

$$\Psi \equiv \begin{pmatrix} \kappa+\gamma_1 & \gamma_2+\rho \\ \gamma_2-\rho & \kappa-\gamma_1 \end{pmatrix}\,, \tag{3.17}$$

we can then solve equation (3.16) for the camera shear γ. An extra pair of dithers can be used to find the magnification κ and rotation ρ. This process can be performed for each object in an image, giving the distortion matrix across the whole field; in practice, we create bins within which to measure Ψ, and thus reduce the noise.

Figure 3.5 shows the observed instrumental shear patterns on our two survey instruments. The ESI shear pattern was averaged over 20 fields in order to overcome noise, because the error on the mean shear in a $1'$ square bin is 9% for any one given field. After this averaging, we find that the shear has a mean of 0.2% and is $< 0.3\%$ everywhere; the mean shear fluctuates by $< 0.1\%$ when using different sets of 20 fields. This is a negligible level of contamination to add (in quadrature) to results that will deal with shears of $\sim 1\%$. We can therefore ignore this effect in our analysis of Keck data. The magnification and rotation components are also $< 0.3\%$, and are consequently both negligible with such a small field of view.

Instrumental distortions on the WHT closely follow the engineering predictions in the Prime Focus Imaging Port manual (Carter & Bridges 1995) of $\gamma_{\rm tangential} = 0$, $\gamma_{\rm radial} = -8.2 \times 10^{-5} r^2$, with r measured in arcminutes from the field centre. Fluctuations in the observed value between fields is $< 0.1\%$. The mean shear is also only 0.1%, but the large field of view means that the distortion toward the edges of the field could be detectable in such a large survey. KSB does not supply a prescription to deal with the correction of post-smear shear, so we implement this by simply subtracting the distortion predicted by the engineering model from our final shear catalogues. We perform this subtraction using the shear addition and subtraction operators in Bernstein & Jarvis (2002). Magnification and rotation components on WFC images are both $< 0.4\%$ and therefore again negligible.

3.3.5 Masking of the field

The shear averaged over many survey fields should be consistent with zero everywhere. However, the presence of many other systematics, including problems with flat fielding,

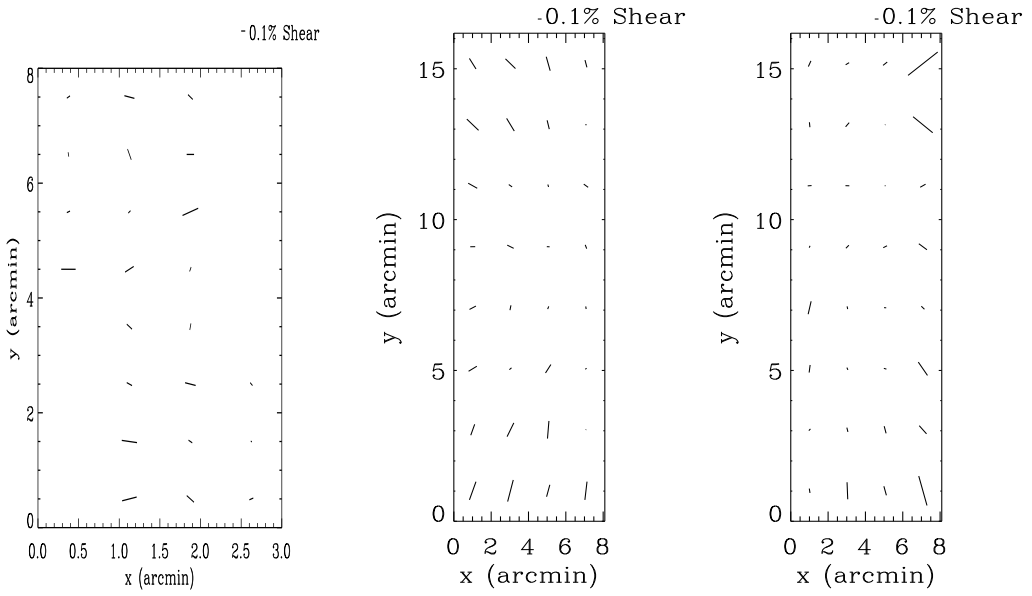

Figure 3.5: Instrumental distortions, reproduced from Bacon *et al.* (2003). Each bar in the left-hand panel represents the magnitude and orientation of distortions in the Echelle Spectrograph and Imager on Keck, averaged over 20 sets of three dithered exposures to reduce noise. Note that the ESI field has an illuminated area that is rotated from the x and y axes by 7°, accounting for the slightly slanted geometry on this figure. The middle and right-hand panels show the distortions in one typical image from the Wide Field Camera on the William Herschel Telescope.

charge transfer effeciency, inhomogeneous read noise, and telescope flexure or vibration, could cause the shear to vary as a function of position on the CCD. Figures 3.6 and 3.7 proved very helpful to diagnose all such problems, and show the observed shear in all of the Keck fields and all of the WHT fields.

Edge effects (including not only the boundaries of the CCD but also chip defects and saturated stars) exaggerated by the long-thin Keck field of view quickly showed the necessity for stringent masking of the chip. Galaxies near an edge *on any one of the dithered exposures* are cut in half, and appear aligned to that boundary. Even if not exactly on the boundary, the flat fielding was poorer near edges ($\sim 10^{-4}$ gradient) and image co-addition failed because of differing background levels in the dithers. If strips of galaxies near the edges of the CCD are not excluded from the final catalogue, the overall mean shear increases by $\sim$2%. We therefore remove all glaxies within $25''$ of any edge.

Saturated stars created a similar problem of background gradients and poor flat fielding. Although their saturation trails and diffraction spikes are already excluded from the object catalogue by the ellipticity cut, we also remove any object within $10''$ of any saturated pixel. The mean shear in the Keck fields then becomes $\langle\gamma_1\rangle = (-0.2 \pm 1.6) \times 10^{-3}$ and $\langle\gamma_2\rangle = (-2.9 \pm 1.6) \times 10^{-3}$. The γ_1 component is consistent with zero offset in the whole ensemble, as we would expect, while the γ_2 component is consistent with zero at

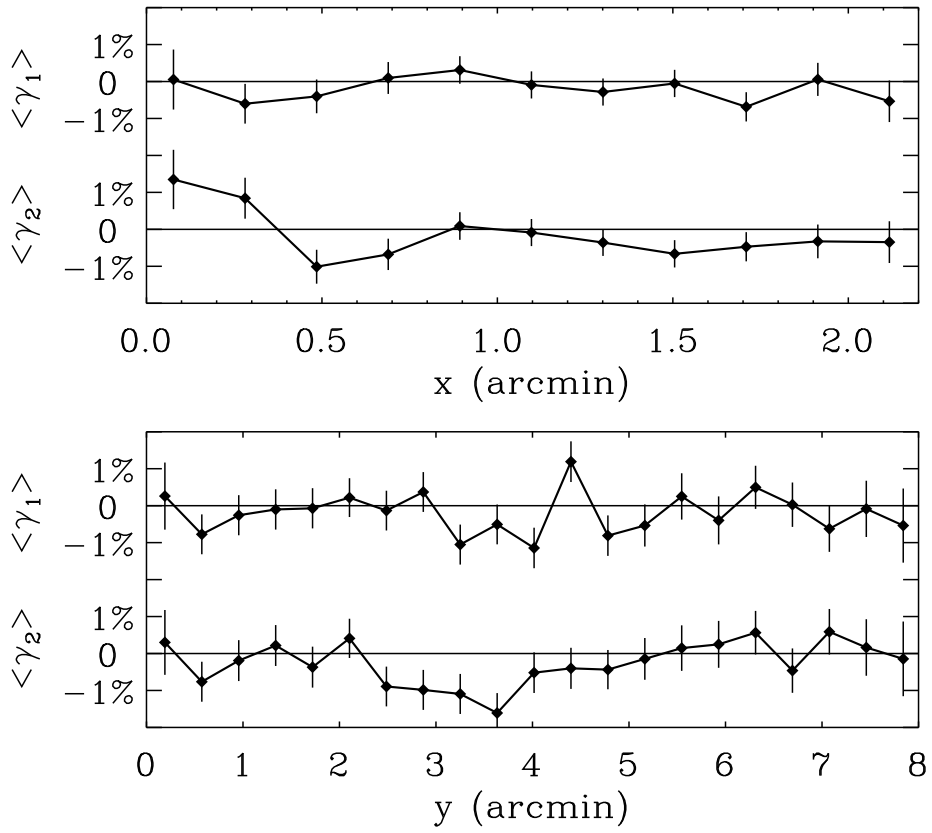

Figure 3.6: Average shear in all Keck survey fields, as a function of CCD position. Overall, $\langle\gamma_1\rangle = (-0.2 \pm 1.6) \times 10^{-3}$ and $\langle\gamma_2\rangle = (-2.9 \pm 1.6) \times 10^{-3}$

the 2σ level. This may represent a small uncorrected distortion; however, given that this adds in quadrature to a shear signal typically at the 2% level, we are free to neglect this small systematic error.

In most observations, the distribution of stellar ellipticities over the field is found to be smooth and slowly varying (see figure 3.4). Some Keck exposures taken during July 2000 were found to have an unexplained, sharp discontinuity in this pattern two thirds of the way up the field. For these fields, only objects on one side of the PSF discontinuity were used. Figure 3.6 further demonstrates that there is no significant structure in the remaining shear values as a function of position on the chip.

The mean components of shear in the entire WHT survey are $\langle\gamma_1\rangle = (1.1 \pm 7.1) \times 10^{-4}$ and $\langle\gamma_2\rangle = (15.6 \pm 7.0) \times 10^{-4}$. Thuis we find similarly negligible systematics as a function of position on the WHT CCD. Other interesting statistics, which will be cited as the typical precision for ground-based shear measurements, include $\langle|\gamma|\rangle = 0.348$, $\langle|\gamma|^2\rangle^{1/2} = 0.413$, $\sigma_{\gamma_1} = \sigma_{\gamma_2} = 0.293$ and $\sigma_{|\gamma|} = 0.223$.

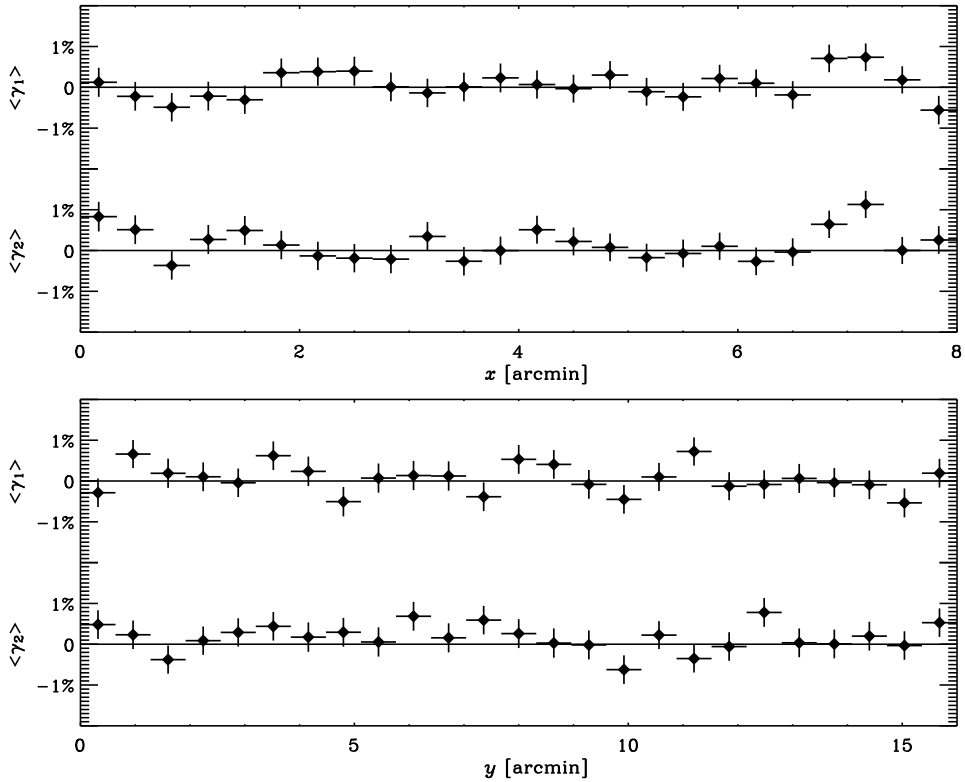

Figure 3.7: Average shear in all WHT survey fields, as a function of CCD position. Overall, $\langle\gamma_1\rangle = (1.1 \pm 7.1) \times 10^{-4}$ and $\langle\gamma_2\rangle = (15.6 \pm 7.0) \times 10^{-4}$.

3.3.6 Intrinsic alignments of neighbouring galaxies

We have needed to assume that galaxies are not aligned with their neighbours or, equivalently, that $\langle\varepsilon\rangle$ is zero in the absence of lensing. In this way, any observed correlation between average galaxy orientations must be due to the effects of weak lensing. Unfortunately, theoretical predictions exist that galaxies may be significantly aligned with their neighbours over a distance of several Mpc (*e.g.* Crittenden *et al.* 2000; Catelan *et al.* 2000). Assuming that galaxy shapes are at least partly determined by the shape and angular momentum of their dark matter halos, this intrinsic alignment might arise during two stages in the evolution of the galaxy:

- The decoupling of the proto-galaxy from the Hubble flow. Tidal gravitational forces and torques from the surrounding LSS can stretch (ellipticals) or spin up (spirals) the dark matter halos. In this scenario, adjacent proto-galaxies are affected by the same LSS and align both with it and with each other.

- Later dynamical interactions of galaxies with their neighbours. This effect has nothing to do with the surrounding large scale density field, so the galaxy alignments, although themselves correlated, would not be correlated with LSS. This difference could, in theory, allow the two scenarios to be distinguished in real data.

Intrinsic galaxy alignments may indeed provide a useful probe of structure formation under gravitational collapse, and constrain models of galaxy evolution (Heavens *et al.* 2000; Croft & Metzler 2000; Heavens 2003). However, they contaminate weak lensing surveys, mimicking the coherent shear signal to produce a systematic bias.

Attempts to measure the level of the intrinsic alignments signal (Brown *et al.* 2000; Lee & Penn 2000; Heymans *et al.* 2003), or to calculate it analytically (Crittenden *et al.* 2000; Hui & Zhang 2002), or via numerical simulation (Heavens *et al.* 2000; Croft & Metzler 2000; Jing 2002) have produced a range of predictions varying by over an order of magnitude. Intrinsic alignments are a particular problem for shallow lensing surveys, in which the predominantly nearby galaxies are also close to each other in real space, or deep lensing surveys whose source galaxies are split into redshift slices. Redshift tomography can be used to trace the evolution of structure formation over time, but it again isolates galaxy pairs that are likely to be physically close.

At the most pessimistic end of the predictions (*e.g.* Jing 2002; Hui & Zhang 2002), if a galaxy's light is exactly aligned with its dark matter halo, intrinsic alignments might affect the 2D shear statistics in lensing surveys even as deep as ours. Fortuntately, numerical simulations of structure formation by van den Bosch *et al.* (2002) show that this is unlikely. They estimate a median (projected) misalignment angle of $\sim 30^\circ$ between a galaxy's light and its dark matter halo. Intrinsic alignments can therefore be ignored in our survey (*e.g.* Heymans *et al.* 2003). In chapter 6, we shall also assume that sufficiently accurate photometric redshifts will be available for galaxies in future 3D surveys to down-weight the contribution from close pairs. Such techniques (King & Schneider 2002; Heavens & Heymans 2002) can leave negligible contamination from intrinsic alignments.

3.3.7 Overlapping isophotes

One final problem for shear measurement that needs to be mentioned, but which is frequently overstated, concerns the overlapping isophotes of adjacent objects (van Waerbeke *et al.* 2000). Real data does not contain the isolated images that are required for the calculation of their shape moments (3.5). This calculation can be biased by a second galaxy lying along a line of sight closer than the projected size of the Mexican hat weight function – even if the two galaxies are far apart in redshift. The galaxies' shapes did not respond to shears or smears in the way that their combined, "peanut-shaped" isophotes would suggest. However, it is hoped that the orientations of such false pairs occur equally in all directions. So long as the two galaxies are not used as a pair in the calculation of shear correlation functions (and we shall ignore all galaxy pairs closer than $1'$ as suggested by the simulations of Bacon *et al.* (2001)), this effect therefore adds noise to a result but does not bias it.

3.4 Results

3.4.1 Correlation functions

Having compiled catalogues of shear estimators for many distant galaxies within our survey, we shall now measure the shear-shear correlation functions (2.81) and (2.82). All groups' constraints on cosmological parameters have currently been drawn from this two-point moment. Since the fields are widely separated, we shall not try to calculate the correlation function in the entire survey area. Our pencil-beam survey strategy instead has the advantage that we can measure the correlation function $C_i^f(\theta)$ on (relatively small) scales contained within many independent fields f. The limited number of galaxies in each field burdens individual measurements with shot noise; but they can be combined into *shear correlation function estimators*

$$C_i(\theta) \simeq \frac{1}{N_f} \sum_{f=1}^{N_f} C_i^f(\theta) \,, \tag{3.18}$$

by simply averaging over the total number of fields N_f in each survey. In practice, we exclude between eight and twelve fields from the average (for both Keck and WHT surveys), chosen at each θ-bin as 3σ outliers in $C_1^{\rm SG}$, $C_2^{\rm SG}$, or C_3. Most of these fields were excluded on all scales. However, this scheme did allow a few fields to be included at small θ but excluded at large θ (or vice versa), reflecting the scales on which their PSF was well-modelled and suitably corrected.

The pencil-beam survey strategy also allows us to calculate the uncertainty in $C_i(\theta)$, automatically including the contribution to errors from both statistical shot noise and cosmic variance variance. A measure of the entire error budget, apart from systematic contributions, is given on all scales by

$$\sigma^2[C_i(\theta)] \simeq \frac{1}{N_f^2} \sum_{f=1}^{N_f} \Big[C_i^f(\theta) - C_i(\theta) \Big]^2 \,. \tag{3.19}$$

The results are shown for the Keck survey in figure 3.8, and for the WHT survey in figure 3.9. In both cases, the measured values are consistent with the theoretical predictions shown as three solid lines (for C_1 and C_2) or zero (for C_3). The three lines demonstrate the level of uncertainty due to the imperfectly known source redshift distribution. From the bottom up, the lines correspond to a median source redshift of $z_s = \{0.8, 0.9, 1.0\}$, in a standard ΛCDM model ($\Omega_m = 0.3$, Ω_Λ=0.7, $\Gamma = 0.21$ and $\sigma_8 = 1.0$). These figures also include dotted lines showing the star-galaxy correlation functions (3.15). On these fields, PSF correction has apparently been performed sufficiently well to provide only a negligible contribution to observational systematics.

We have also estimated the statistical errors alone (*i.e.* neglecting cosmic variance). These are useful for comparison to older surveys that quoted only this value, and to

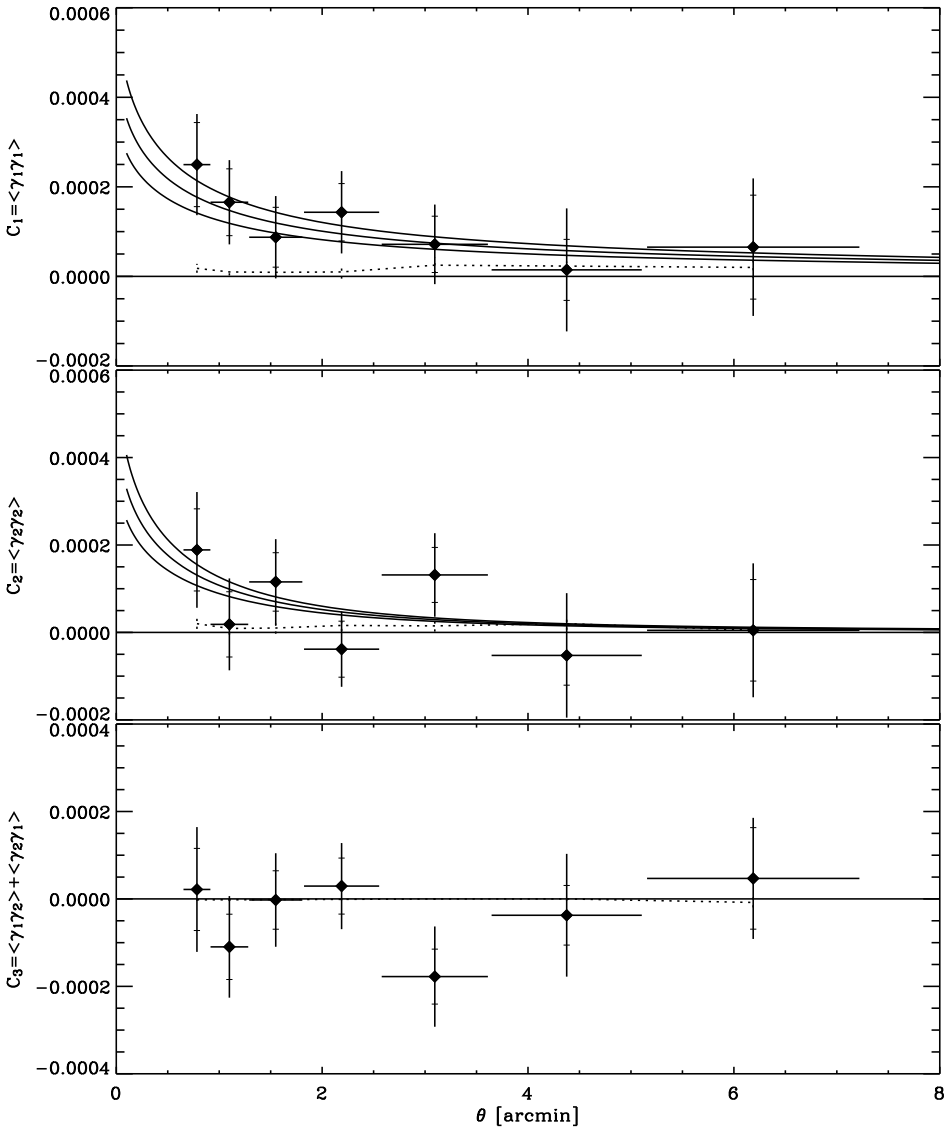

Figure 3.8: Observed shear-shear correlation functions from the Keck survey. The inner error bars correspond to statistical errors (shot noise) only. The outer error bars also include the contribution from cosmic variance. The results are compatible with the theoretical predictions, shown as solid lines. From the bottom up, these correspond to a median source redshift of $z_s = \{0.8, 0.9, 1.0\}$, in a fixed ΛCDM model with $\Omega_m = 0.3$, Ω_Λ=0.7, $\Gamma = 0.21$ and $\sigma_8 = 1.0$. The star-galaxy correlation functions, shown as dotted lines barely visible above the x-axes, demonstrate the success of the PSF correction for galaxy shapes, and the low level of systematic errors from this source.

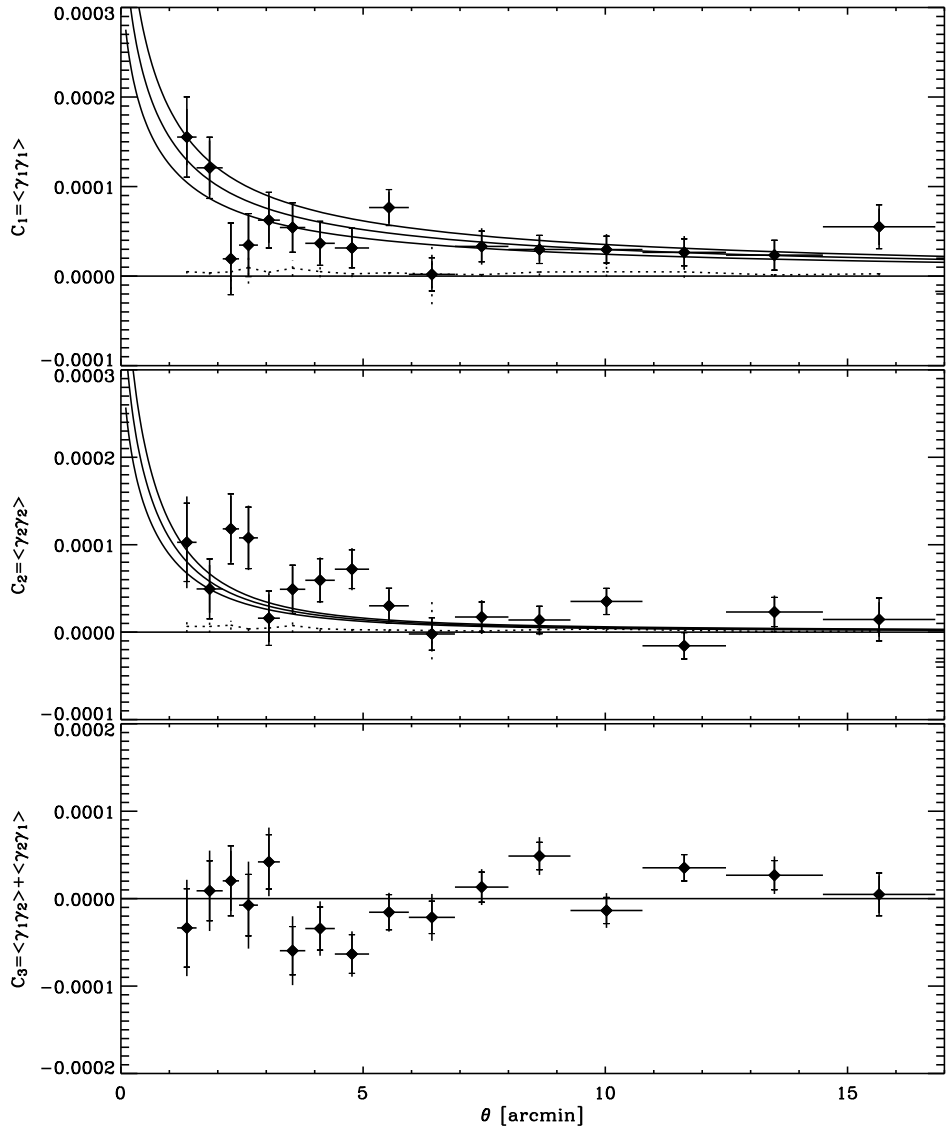

Figure 3.9: Observed shear-shear correlation functions from the WHT survey. Note the change of scale in the y-axis from figure 3.8.

provide an indication of the statistical significance of the detection of the cosmic shear signal.

$$\sigma^2_{\rm stat}[C_i(\theta)] \simeq \frac{\sigma^2_\epsilon}{\sqrt{N_{\rm pairs}(\theta)}} \tag{3.20}$$

where $\sigma^2_\epsilon \equiv \langle\gamma_1^2\rangle = \langle\gamma_2^2\rangle$ is the intrinsic ellipticity variance of individual galaxies, and $N_{\rm pairs}(\theta)$ is the number of galaxy pairs used in the angular bin centered on θ. The measured ellipticity dispersion is $\sigma_\epsilon = 0.31$ in Keck data and $\sigma_\epsilon = 0.30$ in WHT data. The excellent imaging performance and speed of the 10m Keck telescope. The fraction of the error on the Keck correlations functions due to statistical errors is smaller on all scales

than the fraction of the WHT errors.

The measurements of the correlation functions on different angular scales probe the same structures, and are generally not independent. Our pencil-beam survey strategy proves useful for a final time, because we can directly calculate the full *covariance matrices of the correlation functions*

$$\mathrm{cov}[C_i(\theta), C_j(\theta')] \simeq \frac{1}{N_f^2} \sum_{f=1}^{N_f} \left[C_i^f(\theta) - C_i(\theta) \right] \left[C_j^f(\theta') - C_j(\theta') \right] . \tag{3.21}$$

These again include the both shot noise and sample variance. The covariance between θ-bins will be required to properly fit cosmological parameters to our data.

The C_1 covariance matrices for the Keck and WHT data are shown in figure 3.10. Similar matrices are found for the covariance between different angular scale in C_2, and the cross-correlation between C_1 and C_2. The Keck data points have significant covariance on angular scales larger than $\sim 3'$, due to the elongated field geometry of the ESI camera. The WHT data points have significant covariance on all scales, because narrower bins were used. These are very useful to perform the numerical integrations required for the E-B decomposition and the calculation of shear variance in cells, but it curiously enlarges the error bars on cosmological parameters. Tighter constraints are obtained by doubling up the θ-bins in WHT data, calculating the correlation functions anew, and using only half as many data points to constrain parameters.

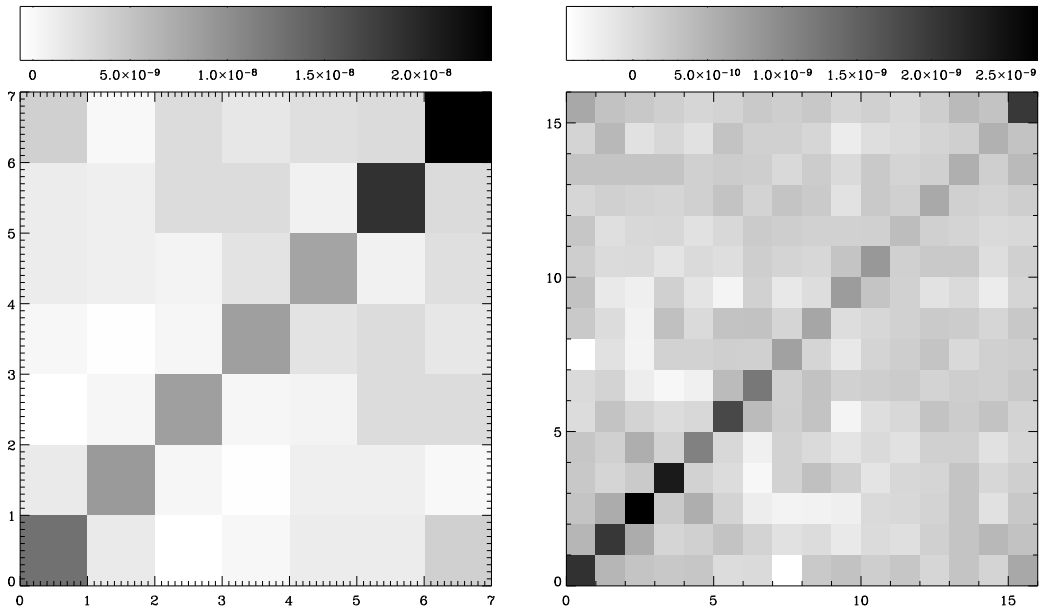

Figure 3.10: Covariance matrices, for Keck survey data (left) and WHT survey data (right), showing the correlation between different angular scales in the measured correlation function C_1 in figures 3.8 and 3.9. Similar matrices are found for the covariance between different angular scale in C_2, and the cross-correlation between C_1 and C_2.

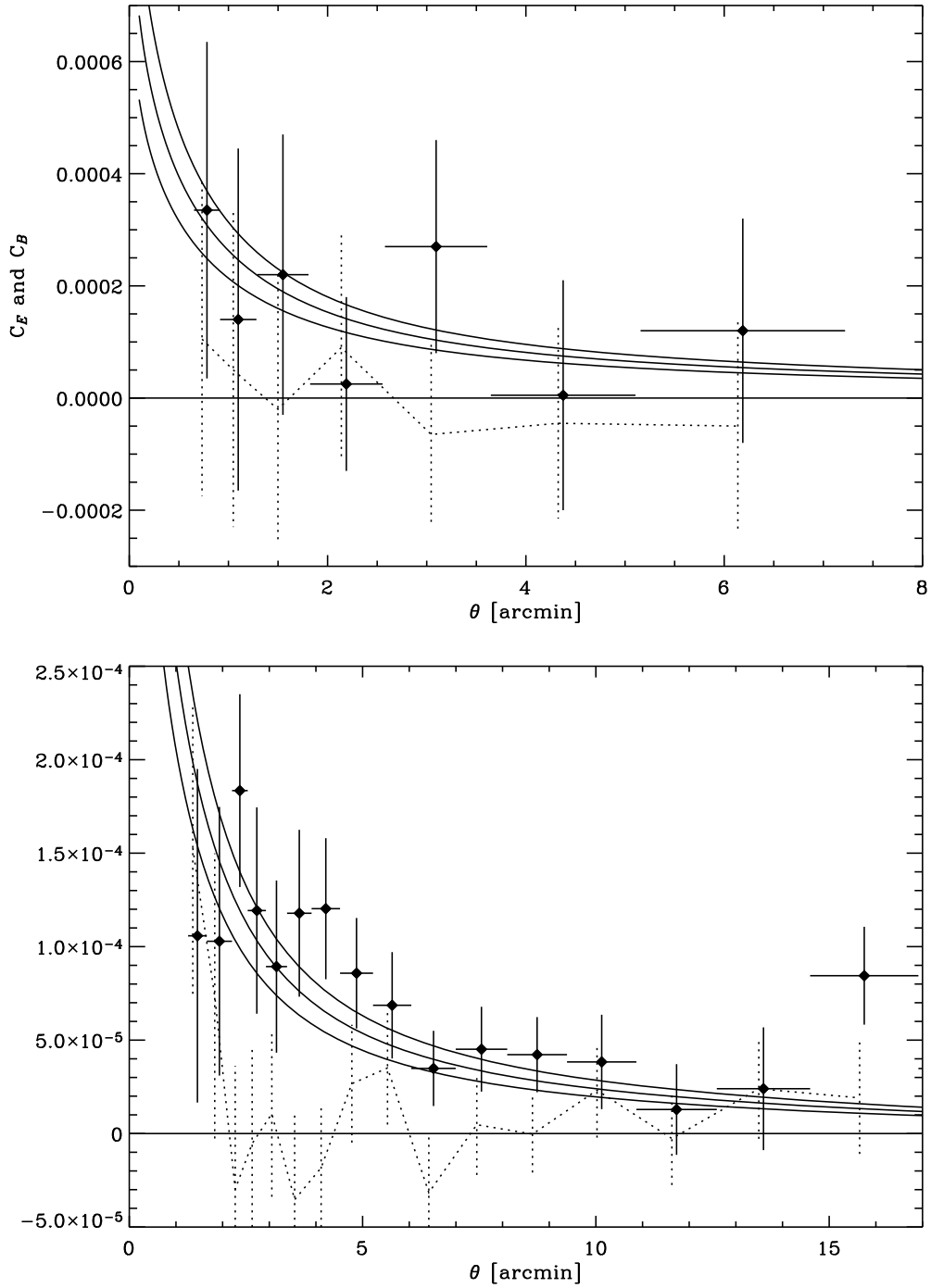

Figure 3.11: E-B decomposition of the Keck survey data (top) and WHT survey data (bottom). The solid lines show the E-modes; the dotted lines the B-modes. In both cases, the E-mode results are compatible with the theoretical curves. As before, these correspond to a median source redshift of $z_s = \{0.8, 0.9, 1.0\}$, in a fixed ΛCDM model with $\Omega_m = 0.3$, Ω_Λ=0.7, $\Gamma = 0.21$ and $\sigma_8 = 1.0$. The Keck data has B-modes consistent with zero on all scales, although the survey area is only barely sufficient to permit this decomposition. The WHT data has B-modes consistent with zero on all scales, bar the first two bins and the final bin. Since these appear to be contaminated with B-modes, they will be discarded for the calculation of cosmological parameter constraints.

3.4.2 E-B decomposition

A decomposition of the shear correlation functions into E-modes, which are produced by cosmic shear plus systematics, and B-modes, which include only systematics, is shown in figure 3.11. As described in section §2.2.7, the finite extent of the correlation functions to high angular scales means that $C_E(\theta)$ and $C_B(\theta)$ are determined only up to a constant of integration. This should be added to $C_E(\theta)$ and subtracted from $C_B(\theta)$. It has been determined for the Keck survey by best-fitting the B-mode data to zero, using the error bars to weight the contributions from the different bins. For the Keck data, we thus added 1.16×10^{-04} to the E-modes and subtracted the same value from the B-modes. Using the same process for the WHT data, the value was 2.68×10^{-05} (*c.f.* expected value of 2×10^{-05} for truncation at $16'$, with $z_s = 0.8$ in a ΛCDM cosmology).

After the subtraction of this constant, B-modes in the Keck data are consistent with zero B-modes on all scales. However, the Keck survey area is barely sufficient to permit this decomposition and the measurement of the E-modes is very noisy. The much larger WHT survey successfully divides the signal into E- and B-modes, with very encouraging results. There is slight contamination on small scales, and the final bin is noisy: so the bins at $\theta < 2$ and $\theta > 15$ will not be included in the calculation of cosmological parameter constraints. On all other scales, however, the B-modes are consistent with zero. This demonstrates that the data reduction was sufficiently well performed to avoid many of the problems commonly associated with the measurement of weak gravitational lensing (see §3.3).

3.4.3 Shear variance in cells

The variance of the shear in circular cells has often been used to express cosmic shear results in the past, and is useful for comparison between groups. We present our results in this form, along with those from similarly deep lensing surveys, in figure 3.12. These surveys use data from 8.5 sqaure degree VIRMOS-DESCART survey on the 3.6m *Canada-France-Hawaii Telescope* (CFHT) by van Waerbeke *et al.* (2001); the 1.25 square degree COMBO-17 survey on the 2.2m La Silla telescope by Brown *et al.* (2003); the 0.36 square degree Medium Deep Survey with the *Wide Field and Planetary Camera* on HST by Refregier *et al.* (2001); and 0.27 square degrees of random fields observed in the parallel-mode of the *Space Telescope Imaging Spectrograph* (STIS) on HST by Rhodes *et al.* (2003). All of these deep surveys appear to prefer a higher value of σ_8 around unity, in contradiction of recent measurements of x-ray selected cluster abundances that suggest $\sigma_8 \approx 0.75$ (Seljak 2001).

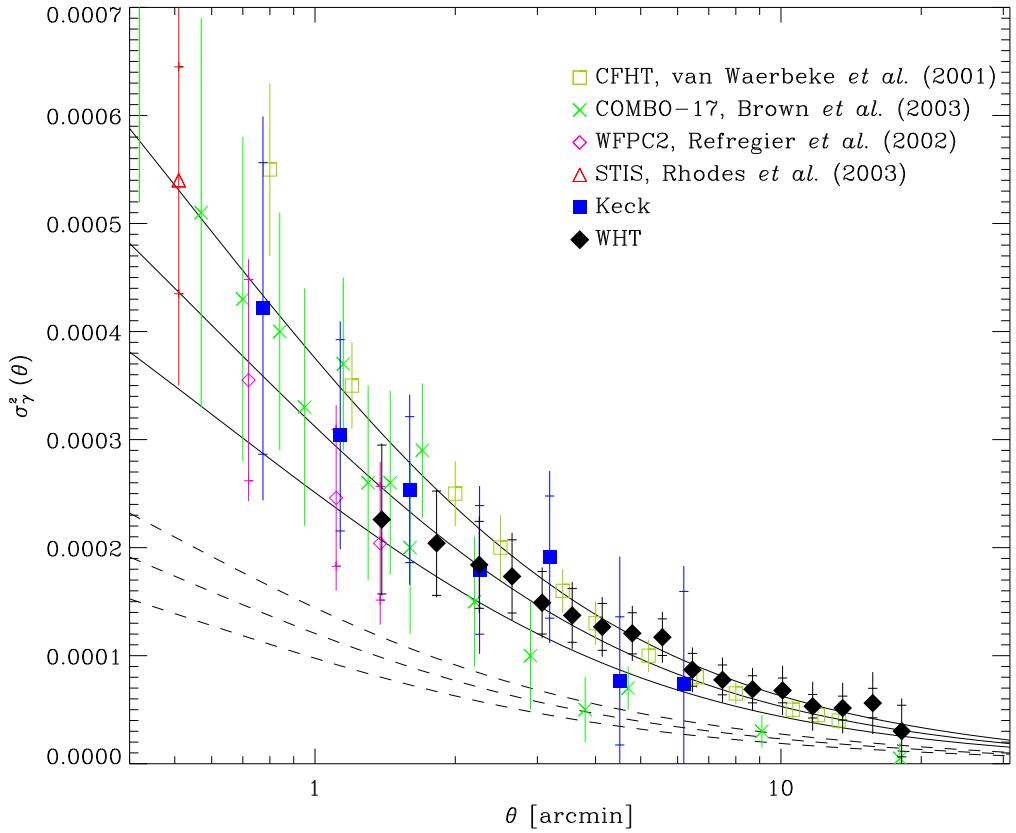

Figure 3.12: Shear variance in (circular, top-hat) cells, as a function of the radius of the cells. Our results are compared to those from similarly deep surveys by other groups (see text). The solid lines show the theoretical predictions, as before, for a fixed ΛCDM model with $\Omega_m = 0.3$, Ω_Λ=0.7, $\Gamma = 0.21$ and $\sigma_8 = 1.0$, assuming a median source redshift of $z_s = \{0.8, 0.9, 1.0\}$. The dashed lines show theoretical predictions for the same three median source redshifts, but in a universe with $\sigma_8 = 0.7$, compatible with recent measurements of x-ray selected cluster abundances.

3.4.4 Cosmological parameter fitting

We now use a Maximum Likelihood technique to determine the constraints set by our observations upon the cosmological parameters Ω_m, the total mass-density of the universe, and σ_8, the normalisation of the matter power spectrum at 8 Mpc. The analysis directly uses the observed correlation functions $C_1(\theta)$ and $C_2(\theta)$, proceeding as in Bacon *et al.* (2003), except that theoretical predictions are calculated with the fitting functions of Smith *et al.* (2003) rather than those by Peacock & Dodds (1996). This has the effect of lowering our final constraint on $\sigma_8\Omega_m^{0.5}$ by about 5%.

The theoretical correlation functions (2.79) were first calculated by Alexandre Refregier, at many points in a 2D grid across the Ω_m *vs* σ_8 plane. The median redshift for source galaxies was fixed to $z_s = 1.0$ for the Keck survey, and to $z_s = 0.8$ for the WHT survey, and the power spectrum shape parameter set to $\Gamma = \Omega_m h = 0.21$, as indicated by recent observations of clustering in galaxy redsift surveys (Percival *et al.* 2001; Szalay *et al.* 2003). Note that this constraint on Γ, which sets the position of the peak of the

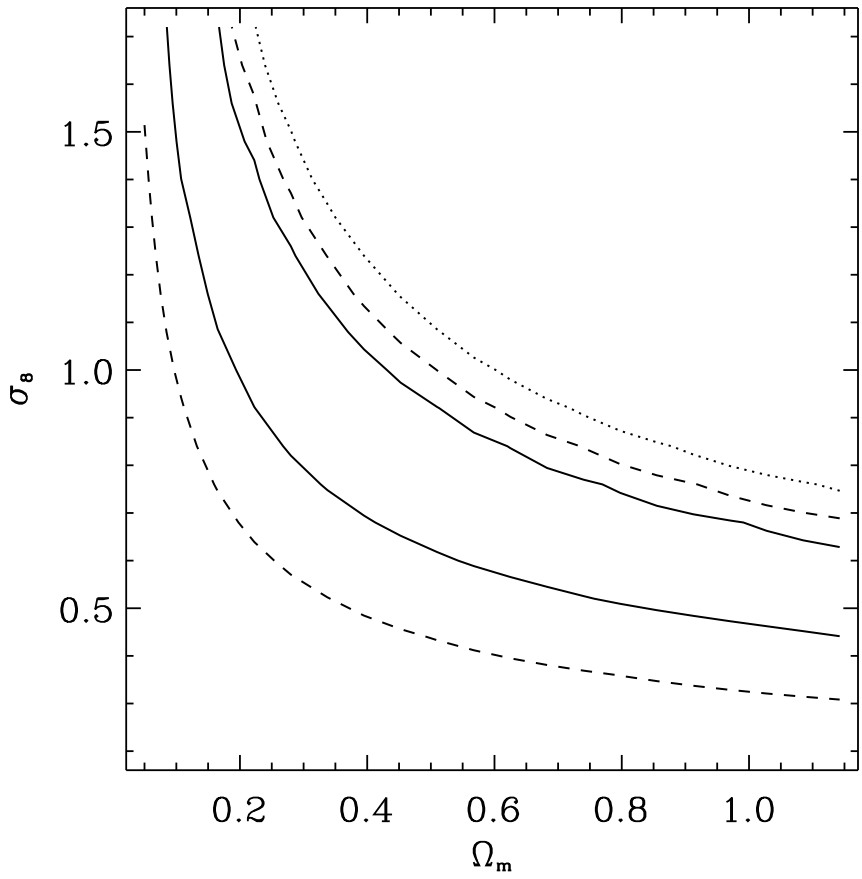

Figure 3.13: Constraints upon cosmological parameters Ω_m and σ_8, from a maximum-likelihood analysis of the Keck survey data. The 68% (solid), 95% (dashed) and 99% (dotted — only one side visible) confidence limits include statistical errors and non-Gaussian cosmic variance. However, they include neither the calibration of the shear measurement method, nor uncertainty in the source galaxy redshift distribution. These sources of error are considered seperately in the text.

linear power spectrum, is equivalent to a constraint on the Hubble parameter h. Errors on these parameters will be considered seperately. We then fitted the observed shear correlation functions $\vec{d}(\theta)$ to the theoretical predictions $\vec{t}(\theta)$, calculating the *log-likelihood function*

$$\chi^2 \equiv (\vec{d}(\theta) - \vec{t}(\theta, \Omega_m, \sigma_8))^T \, \mathrm{cov}[C_i(\theta), C_j(\theta')] \, (\vec{d}(\theta) - \vec{t}(\theta, \Omega_m, \sigma_8)) \tag{3.22}$$

throughout the grid. We thus explore parameter space in this plane, and minimise χ^2 to find the best-fit cosmological model. To compute confidence contours, we numerically integrate the *likelihood function*

$$L(\Omega_m, \sigma_8) \equiv e^{-\chi^2/2} \, . \tag{3.23}$$

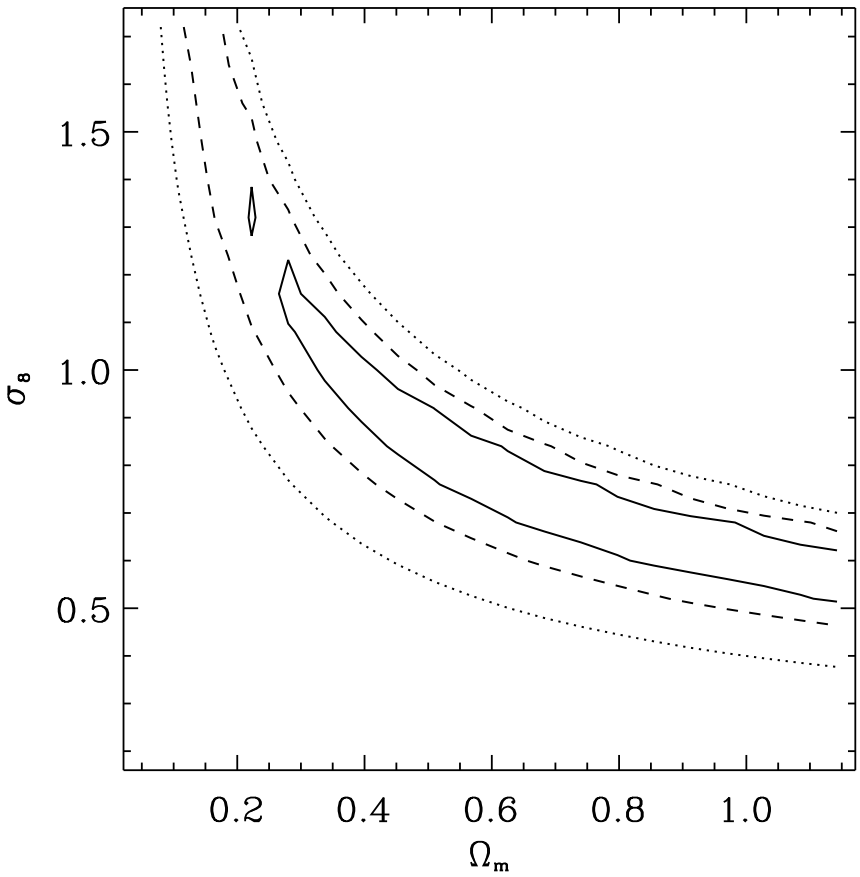

Figure 3.14: Constraints upon cosmological parameters from the WHT survey data, showing the 68%, 95% and 99% confidence limits, as in figure 3.13.

The constraints from Keck and WHT data are presented in figures 3.13 and 3.14. The contours show 68%, 95% and 99% confidence limits, including statistical error and non-Gaussian sample variance. They reveal the well-known degeneracy between Ω_m and σ_8 when using only two-point statistics, although the leverage created by the wide range of angular scales probed by the WHT survey is beginning to exclude small values of $\Omega_m < 0.25$. A similar result was observed by the large cosmic shear surveys of van Waerbeke *et al.* (2001) and Bacon *et al.* (2003), where data on many angular scales exluded large values of $\Omega_m > 0.6$.

A good fit to the 68% confidence level from our Keck data is given by

$$\sigma_8 \left(\frac{\Omega_m}{0.3} \right)^{0.52} = 1.01 \pm 0.19 \, , \tag{3.24}$$

while the WHT data is well-fit by

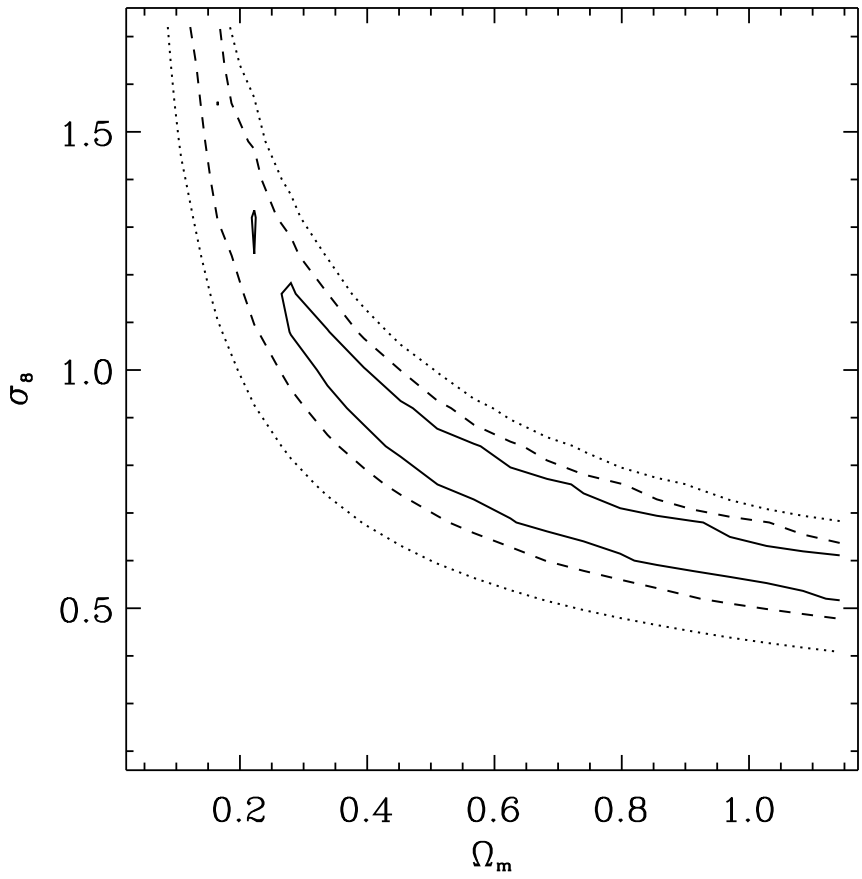

Figure 3.15: Constraints upon cosmological parameters after marginalisation over both surveys, showing the 68%, 95% and 99% confidence limits, as in figure 3.13.

$$\sigma_8 \left(\frac{\Omega_m}{0.3} \right)^{0.52} = 1.11 \pm 0.10 \,, \tag{3.25}$$

for $0.25 < \Omega_m < 0.8$. Marginalising over both results, by multiplying their two likelihood functions, gives a constraint from a combined survey. The confidence contours are shown in figure 3.15, and the 68% confidence level is well-fit by

$$\sigma_8 \left(\frac{\Omega_m}{0.3} \right)^{0.52} = 1.09 \pm 0.09 \,, \tag{3.26}$$

with $0.1 < \Omega_m < 0.8$.

Note that this includes only the statistical error and sample variance. We can propagate other sources of error by noting that

$$C_i(\theta) \propto \Omega_m^{1.46} \sigma_8^{2.45} z_s^{1.65} \Gamma^{-0.11} (P^\gamma)^{-2} \tag{3.27}$$

around $\theta = 5'$, in a fiducial ΛCDM cosmological model with $\Omega_m = 0.3$, Ω_Λ=0.7, $\Gamma = 0.21$ and $\sigma_8 = 1.0$. Adding to this (in turn) the 10% source redshift uncertainty, the 15% prior on Γ, and the 5% shear calibration uncertainty gives a final 68% CL constraint for the combined survey of

$$\sigma_8 \left(\frac{\Omega_m}{0.3}\right)^{0.52} = 1.09 \pm 0.090 \pm 0.073 \pm 0.007 \pm 0.044 \quad (3.28)$$

$$= 1.09 \pm 0.12 \,, \quad (3.29)$$

where the errors are combined in quadrature. This result therefore includes all contributions to the total error budget: statistical noise, sample variance, covariance between different angular scales, systematic measurement and detection biases, source redshift uncertainty, and marginalisation over priors on other parameters.

3.4.5 Discussion

Our measurement is relatively high, but still agrees at 1σ with other cosmic shear results from deep surveys by van Waerbeke *et al.* (2002), Refregier *et al.* (2002), and Rhodes *et al.* (2003). Our results are consistent within 1.5σ with WMAP CMB results (Spergel *et al.* 2003), and also agree with the old cluster abundance normalisation (Eke *et al.* 1998; Viana & Liddle 1999; Pierpaoli *et al.* 2001). However, our results disagree at the 3σ level with newer estimates of the cluster-abundance normalisation, derived using an observational rather than theoretical mass-temperature relation (Borgani *et al.* 2001; Seljak 2001; Rieprich & Böhringer 200; Viana *et al.* 2001). This discrepancy could arise from unknown systematics in either the cluster or cosmic shear methods. The two techniques probe similar scales, so Amara & Refregier (2003) concluded that higher order, non-Gaussianity of the mass distribution could not account for the different measurements. Further studies are needed for the cluster method, to understand the difference between the observed mass-temperature relation and that found in numerical simulations, and more reliable shear measurement methods are required for the cosmic shear method. It is important to understand the origin of the discrepancy between cosmic shear and cluster abundance results. If this is not explained by other arguments, it could point towards a failure of the standard ΛCDM paradigm, and therefore have important consequences for cosmology.

Our results are also incompatible at the $2 \rightarrow 3\sigma$ level with results from shallower cosmic shear surveys by Hoekstra *et al.* (2002) and Jarvis *et al.* (2002). This discrepancy could arise from the shape measurement methods: the object selection cuts are different, and neither of those methods have been calibrated upon simulated data (if the same calibration factor were incuded in those results, they would become similar to our own). An assortment of shape measurement methods are currently being tested and calibrated upon the same input images, using the image simulation method described in chap-

ter 5 (Bridle *et al.* in prep.). The discrepancy with shallow cosmic shear surveys could alternatively arise from uncertainty in the redshift distribution of background galaxies in the deep data. Especially after catalogue cuts in object size, it is difficult to determine the precise redshift distribution of the included background galaxies. As seen in equation (3.28), source redshift uncertainty is currently a major component of the total error budget. The cosmic shear analysis of the deep multicolour COMBO-17 survey (Brown *et al.* 2003) could indeed take advantage of photometric redshifts, and did then measure a comparatively low value for $\sigma_8(\Omega_m/0.3)^{0.49} = 0.72^{+0.08}_{-0.09}$. However, those results exhibit a peculiar angular dependence that is neither fully understood nor fully consistent with theoretical predictions (see figure 3.12). This discrepancy therefore remains unresolved. It could be more definitively explained by the incorporation of spectroscopically-confirmed DEEP2 galaxy redshifts (Davis *et al.* 2000) into future cosmic shear surveys (Miyazaki *et al.* in prep.) or by future wide-field imaging surveys in multiple optical and near infra-red colours from space. This issue will be further explored in chapter 6.

4 Shapelets

4.1 The shapelets formalism for image analysis

4.1.1 Motivation

As seen in chapter 3, the limiting factor for all current cosmic shear surveys is the control of systematics in image analysis and galaxy shape measurement. To accurately quantify and investigate these systematic effects, we now introduce the "shapelets" formalism. This was first introduced in Refregier (2003; hereafter Shapelets I), and in this thesis we shall particularly need to develop further techniques using "polar shapelets".

Shapelets provides an accurate way to model a (localised) object within an image array, capturing all of its structure and faithfully reproducing the morphology of any galaxy. The surface brightness of the image is expressed in shapelet space as a weighted sum of orthogonal basis functions, rather like Fourier or wavelet synthesis. The shapelet basis functions are perturbations around a Gaussian. These prove mathematically convenient for many tasks in image processing and manipulation commonly used in astronomy.

Refregier & Bacon (2003; hereafter Shapelets II) showed how shapelets could be used to form shear estimators for weak gravitational lensing. They extend the domain of weak lensing measurement beyond the quadrupole moments of galaxy shapes, to also include their higher order shape moments. Chang & Refregier (2002) used the elegant properties of shapelets under Fourier transform to reconstruct images, and to measure weak lensing, with interferometers. Kelly & McKay (2003) used shapelets to quantita-

tively classify galaxy morphologies in the Sloan Digital Sky survey. A related method has also been independently suggested by Bernstein & Jarvis (2002; hereafter BJ02).

In this chapter, we shall first develop the formalism of polar shapelets, and analytically derive some useful results. We shall then describe a new method to perform a shapelet decomposition, dealing with the typical problems in real, observational data: including pixellisation, noise and a point-spread function. We shall finally develop methods to optimise a shapelet decomposition, maximising the data compression ratio and the overall quality of image reconstruction. Where it is necessary to test our method upon realistic galaxy morphologies, we shall use objects in the Hubble Deep Fields (Williams *et al.* 1996, 1998; hereafter HDFs). These provide typical examples of the irregular galaxy shapes that should be found in deep, high-resolution cosmic shear surveys in the near future.

In chapter 5, we shall then use the shapelet parameterizations of HDF galaxies to simulate images from future cosmic shear surveys, containing morphologically accurate objects. Since the manufactured observations will have known input shapes, we shall be able to use them to test and calibrate shear measurement methods. In chapter 6, we shall use the image simulations to predict the precision of shear recovery from future surveys, under a variety of observing conditions, instrumental configurations and survey strategies.

4.1.2 Advantages of shapelets

Figure 4.1 demonstrates the superb quality of shapelet-based image reconstruction that is possible for all galaxy morphologies. The first column shows I_{F814W} band images of real HDF galaxies. The middle column shows a shapelet model of the galaxy, and the third column the residual, always consistent with noise. Particularly for this sort of irregular or spiral galaxies, the shapelet models are far superior to equivalent techniques using only traditional radial profiles. GALFIT (Peng *et al.* 2002), for example, is completely unable to deal with even spiral arms. The residuals shown in plots similar to figure 4.1 are much worse than those using shapelets.

There are also many practical and computational advantages of a shapelet decomposition. The basis functions were specifically chosen for their convenient mathematical properties. Objects in shapelet space can be enlarged, rotated or sheared by very simple operations. Various linear combinations of shapelet coefficients measure an object's size, flux, and other aspects of its morphology. One coefficient, for example, contains the object's Gaussian-weighted ellipticity that wold be used by KSB. The shapelet basis functions are also invariant under Fourier transform, up to a phase factor. This renders convolutions and deconvolutions (*e.g.* from a PSF) easy to perform analytically.

Data compression ratios as high as 50 are possible with a shapelet decomposition (Shapelets I), by keeping only those shapelet coefficients above a significance threshold,

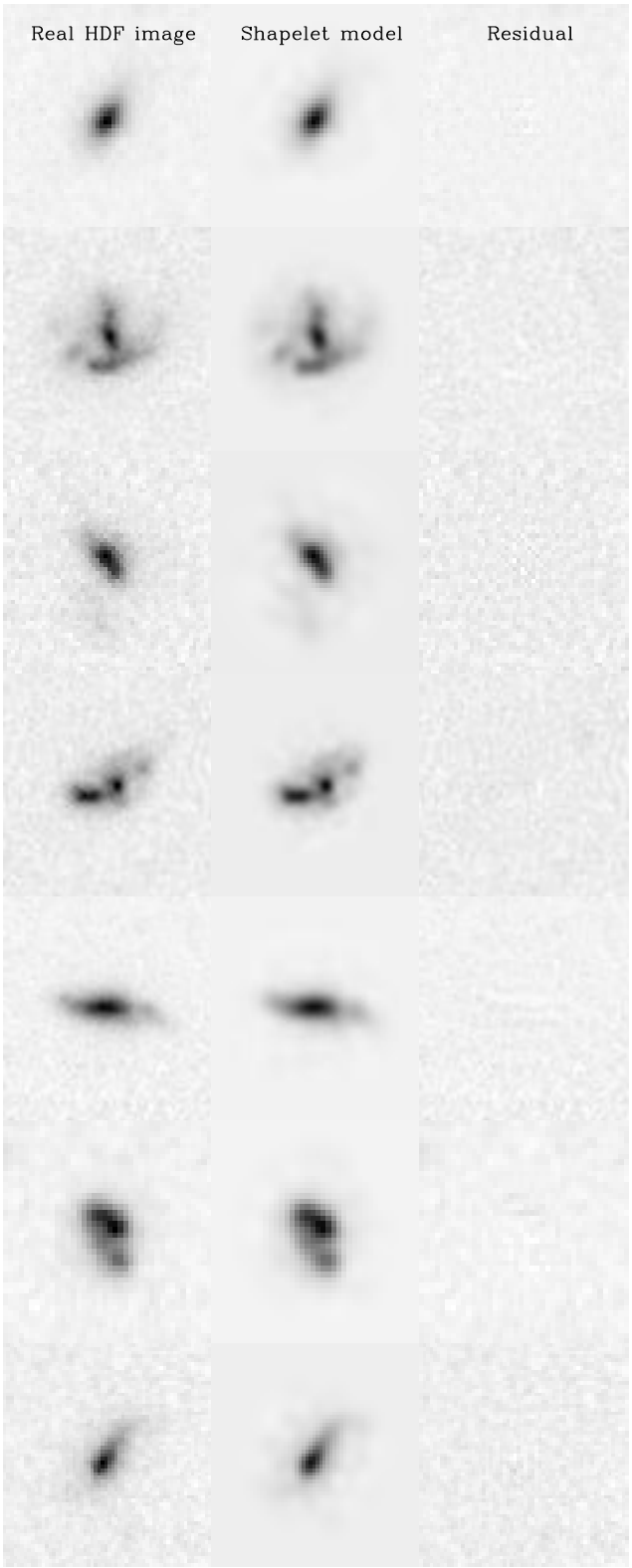

Figure 4.1: Shapelet decomposition of a selection of HDF I-band galaxies. Even irregular galaxy morphologies can be well-modelled with this technique. In all cases, the first column shows the original HDF image and the middle column shows the shapelet model with $n_{\max} = 14$. The third column shows the residuals. The image size and colour scale is different for each row.

or by truncating the expansion at high orders. Truncating the expansion sets a minimum and maximum physical scale of interest: conveniently for typical galaxy morphologies, the resolution of a shapelet model is also greatest near the centre. A small amount of information is then discarded at higher spatial frequencies. However, it is possible to ensure that this lost information is consistent with noise, by requiring the final reconstruction to have a reduced χ^2 less than unity. Furthermore, data compression with shapelets is achieved via the parameter-independent truncation of a series. Shapelet's complete basis set avoid the requirement in GALFIT (Peng *et al.* 2002) or GIM2D (Simard 1998) to specify in advance the number and type of profiles for each model. A Karhunen-Loéve decomposition would also require models to be specified in advance for both the image morphology and for the noise.

Finally, the orthonormality of the shapelet basis set guarantees a unique and linear one-to-one mapping from the image plane to the coefficients. This simplification, and many of shapelets' convenient mathematical properties are lost to methods, such as PIXON (Piña & Puetter 1993), that use an over-complete basis set.

4.1.3 Disadvantages of shapelets

There are two main criticisms often levelled at shapelets. The first is that it may not easily capture the extended wings of many galaxies. Practical computation requires a truncation of high-order shapelet coefficients. However, this leaves the shapelet basis set incomplete, and an expansion around a Gaussian is not ideally matched to typical exponential or de Vaucouleurs profiles. A demonstration that our algorithm does use sufficient numbers of coefficients is the remarkable match in the concentration index between shapelet models and real galaxies shown in §5.3. In fact, the ability of a shapelet decomposition to recognise correlations between adjacent pixels may even enable our model to extend further than SEXTRACTOR into the wings of a faint object on the threshold of detection, where the flux in individual pixels is lost beneath the level of background noise.

The second criticism is a potentially greater problem for our method. The truncation of a shapelet decomposition (or indeed any basis set that is complete, rather than over-complete) can produce artefacts in the image reconstruction. Spurious residuals emerge that resemble one basis function, due to the near-cancelling of large positive and negative coefficients in others. For shapelets, this is typically seen as ringing, and is particularly apparent around long and thin galaxies, which are less well-matched to the circular basis functions. Preserving the linearity of a shapelet decomposition also prevents the imposition of a positive-definite constraint. The spurious residuals can therefore appear either as extra positive flux or as negative holes. However, we note that this occurs widely in other methods; including wavelets, where it is only removed by a (non-linear) projection in wavelet space onto the sub-space of positive solutions.

While most artefacts are only at the level of even modest background noise, we turn around this disadvantage in §5.2.5. There we use the absence of any negative holes in a shapelet model or a simulated image as a first-order check that they are realistic.

4.2 Shapelet basis functions

4.2.1 Cartesian shapelets

Any smooth function, like the surface brightness $f(x, y)$ of a galaxy, can be expressed as

$$f(\vec{x}) = \sum_{n_1=0}^{\infty} \sum_{n_2=0}^{\infty} a_{n_1,n_2}\, \phi_{n_1,n_2}(\vec{x};\beta)\ , \tag{4.1}$$

where the *shapelet coefficients* a_{n_1,n_2} are weights to be determined, and the dimensionful *shapelet basis functions*

$$\phi_{n_1,n_2}(\vec{x};\beta) \equiv \frac{H_{n_1}\left(\frac{x}{\beta}\right)\, H_{n_2}\left(\frac{y}{\beta}\right)\, e^{-\frac{|\vec{x}|^2}{2\beta^2}}}{\beta\, 2^n \sqrt{\pi n_1! n_2!}} \tag{4.2}$$

are plotted in figure 4.2. $H_n(x)$ is a Hermite polynomial of order n, and β is a scale size. These Gauss-Hermite polynomials form a complete and orthonormal basis set. This ensures that the shapelet coefficients can be determined by simply evaluating the *overlap integral*

$$f_{n_1,n_2} = \int\int_{-\infty}^{\infty} f(\vec{x})\, \phi_{n_1,n_2}(\vec{x};\beta)\, \mathrm{d}^2x\ . \tag{4.3}$$

Like a Fourier or wavelet transform, a shapelet expansion (4.1) can be truncated in practice at some finite $n_{\max}$. The array of shapelet coefficients is typically sparse for most galaxy morphologies, which can therefore be accurately modelled using only a few numbers. As shown in Shapelets I, data compression ratios are frequently as high as 60:1.

However, our choice of Gauss-Hermite basis functions is governed not by the physics of galaxy morphology but by the mathematics of image manipulation. As we will see in §4.2.4, a shapelet parameterization is mathematically convenient for many tasks common in astronomy and other sciences. We find that the original Cartesian shapelets are most useful for initial decomposition, because they are separable in x and y, and they can be integrated within square pixels. The model can then be easily converted into polar shapelets, whose interpretation is more intuitive.

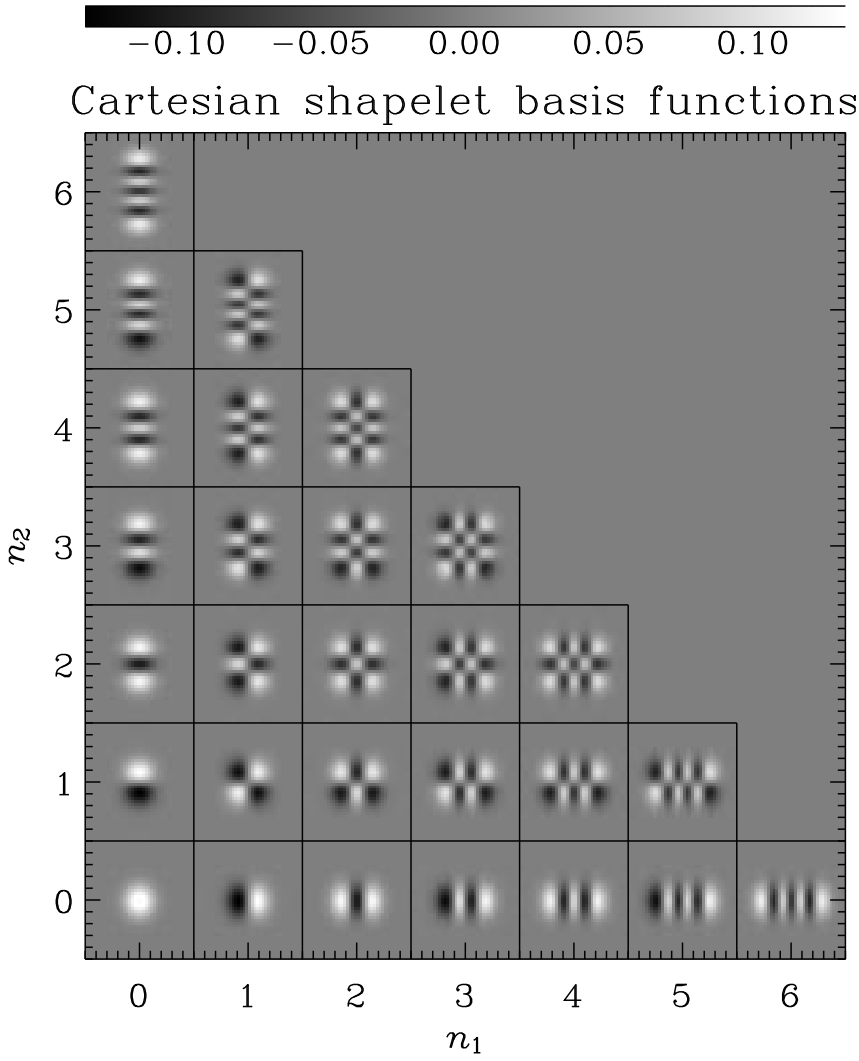

Figure 4.2: Cartesian shapelet basis functions. These are perturbations around a Gaussian and are parameterized by two integers, n_1 and n_2, which describe the number of oscillations in the x and y directions respectively. Shapelets are a complete basis set, which can be used to parameterize arbitrary galaxy morphologies.

4.2.2 Polar shapelets

Polar shapelets were suggested in Shapelets I as an orthogonal transformation of the Cartesian basis states. In this thesis, we shall develop the idea further. It will become apparent that polar shapelets have all the useful properties of Cartesian shapelets, including a Gaussian weight function that sets a scale size β, while being separable instead in r and θ. This renders many operations more intuitive, and polar shapelet coefficients are easily interpreted for common astronomical tasks as Gaussian-weighted quadrupole, octopole, *etc.* moments of the surface brightness.

The "polar Hermite polynomials" $H_{n_l,n_r}(x)$ described in Shapelets I are related to *associated Laguerre polynomials*

$$L_p^q(x) \equiv \frac{x^{-q}e^x}{p!}\,\frac{\mathrm{d}^p}{\mathrm{d}x^p}\left(x^{p+q}e^{-x}\right)\ , \tag{4.4}$$

for $n_l < n_r$ by

$$H_{n_l,n_r}(x) \equiv (-1)^{n_l}\ (n_l!)\ x^{n_r-n_l}L_{n_l}^{n_r-n_l}(x^2)\ . \tag{4.5}$$

Here n_l and n_r can be any non-negative integers. Wherever possible in this thesis, we shall rationalize to the simpler $\{n,\ m\}$ notation, where $n = n_r + n_l$ and $m = n_r - n_l$. Consequently, the only allowed states for polar shapelets are those for which n and m are both even, or n and m are both odd. Equivalently, n can be any non-negative integer, and m is any integer between $-n$ and n, in steps of two. This condition will not be written explicitly alongside every summation, for the sake of brevity; however it will be assumed throughout.

Note that different conventions have been used to define the Laguerre polynomials, particularly in mathematical work before the 1960s. The $p!$ term is omitted in many older textbooks, and caution must be used with the resulting relations. Several useful recursion relations can be derived to simplify the calculation of the polynomials (*e.g.* Boas 1983):

$$L_0^q(x) = 1 \tag{4.6}$$

$$L_1^q(x) = 1 - x + q \tag{4.7}$$

$$L_p^q(x) = \left(2 + \frac{q-1-x}{p}\right)L_{p-1}^q(x) - \left(1 + \frac{q-1}{p}\right)L_{p-2}^q(x) \tag{4.8}$$

$$\frac{\mathrm{d}L_p^q(x)}{\mathrm{d}x} = x^{-1}\left[pL_p^q(x) - (p+q)L_{p-1}^q(x)\right] \tag{4.9}$$

$$\frac{\mathrm{d}L_p^0(x)}{\mathrm{d}x} = \frac{\mathrm{d}L_{p-1}^0(x)}{\mathrm{d}x} - L_{p-1}^0(x)\ . \tag{4.10}$$

We can therefore construct the dimensionful *polar shapelet basis functions*

$$\chi_{n,m}(r,\theta;\beta) \equiv \frac{(-1)^{\frac{n-|m|}{2}}}{\beta^{|m|+1}}\left[\frac{\left(\frac{n-|m|}{2}\right)!}{\pi\left(\frac{n+|m|}{2}\right)!}\right]^{\frac{1}{2}} r^{|m|}L_{\frac{n-|m|}{2}}^{|m|}\left(\frac{r^2}{\beta^2}\right)e^{\frac{-r^2}{2\beta^2}}e^{im\theta}\ , \tag{4.11}$$

and these are plotted in figure 4.3. Note the slight difference in normalisation from BJ02 by a factor of β. This ensures that, as in the case of Cartesian shapelets, our polar shapelet basis functions are both *complete*:

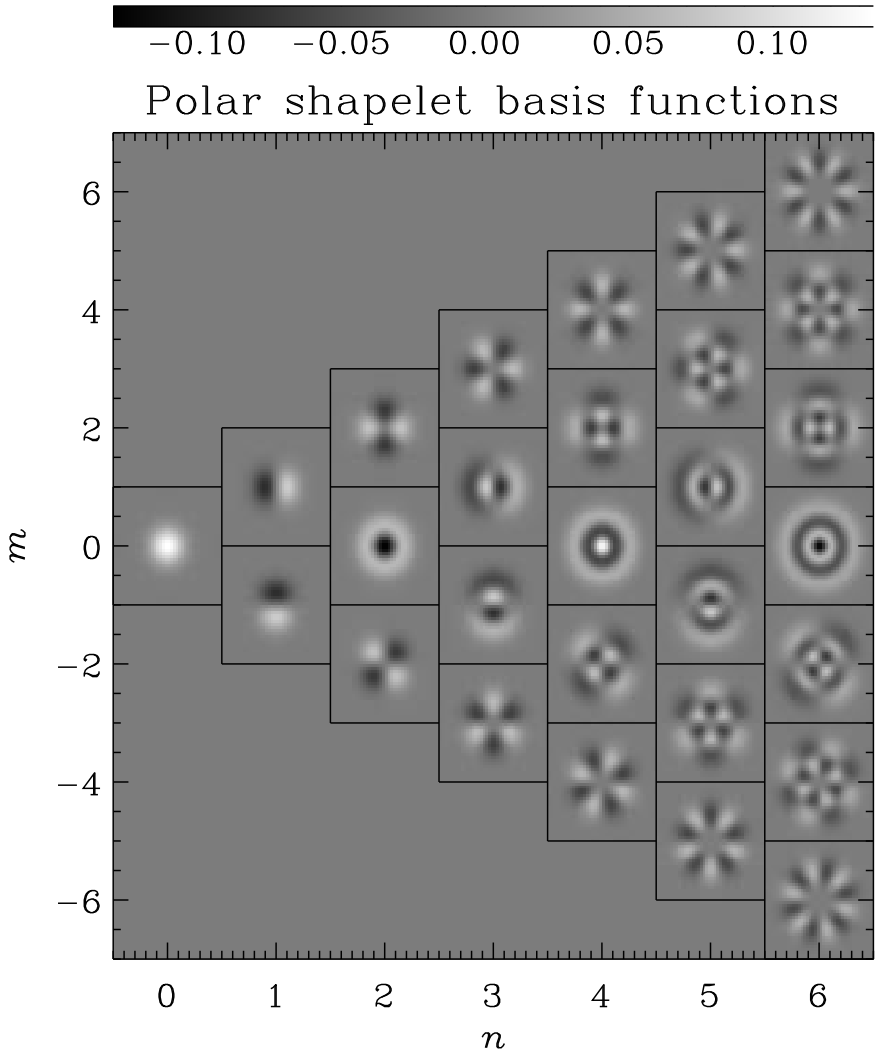

Figure 4.3: Polar shapelet basis functions. The real part of the complex functions are shown in the top half ($m \geq 0$) of the plot, and the imaginary part in the bottom half of the plot. The basis functions with $m = 0$ are wholly real. In a shapelet decomposition, an object is modelled by a sum of these basis functions, with each weighted by a complex coefficient whose magnitude determines the strength of the component, and whose phase sets its relative orientation.

$$\sum_{n=0}^{\infty} \sum_{m=-n}^{n} \chi_{n,m}(r,\theta;\beta)\chi_{n,m}(r',\theta';\beta) = \delta(r-r')\delta(\theta-\theta') \tag{4.12}$$

(Wünsche 1998) and *orthonormal*:

$$\int_0^{2\pi} \mathrm{d}\theta \int_0^{\infty} \chi^*_{n,m}(r,\theta;\beta)\ \chi_{n',m'}(r,\theta;\beta)\ r\ \mathrm{d}r = \delta_{n,n'}\delta_{m,m'}\ , \tag{4.13}$$

where δ is the Kronecker delta and the asterisk denotes complex conjugation. The surface brightness of a galaxy $f(r,\theta)$ in polar coordinates may therefore be decomposed into

$$f(r,\theta) = \sum_{n=0}^{\infty} \sum_{m=-n}^{n} f_{n,m} \chi_{n,m}(r,\theta;\beta) \ , \tag{4.14}$$

with the polar shapelet coefficients $f_{n,m}$ given by the *overlap integral*

$$f_{n,m} = \int_0^{2\pi} \mathrm{d}\theta \int_0^{\infty} f(r,\theta)\ \chi_{n,m}(r,\theta;\beta)\ r\ \mathrm{d}r \ . \tag{4.15}$$

Recall that n is any non-negative integer, although in practice the series may be truncated at $n \leq n_{\mathrm{max}}$, and m is any integer between n and $-n$, in steps of two.

4.2.3 Interpretation of complex variables

Both the polar shapelet basis functions $\chi_{n,m}$ and coefficients $f_{n,m}$ are generally complex variables. However, note that the basis functions obey the symmetries

$$\chi_{n,-m}(r,\theta;\beta) = \chi^*_{n,m}(r,\theta;\beta) = \chi_{n,m}(r,-\theta;\beta) \ , \tag{4.16}$$

where the asterisk denotes complex conjugation.

In practice, we are interested in real functions $f(\vec{x})$, such as the surface brightness of a galaxy. Equations (4.13) and (4.16) imply that $f(\vec{x})$ is real if and only if

$$f_{n,-m} = f^*_{n,m} \ . \tag{4.17}$$

For example, the $m = 0$ coefficients are wholly real numbers. All others are paired with their complex conjugate above and below the line $m = 0$. Thus, even though the coefficients $f_{n,m}$ are generally complex, the number of independent parameters for a real function is the same as in the case of Cartesian shapelets.

4.2.4 Relation to the Quantum Harmonic Oscillator

Gaussian-weighted Hermite or Laguerre polynomials also are well known as eigenfunctions of the 2D Quantum Harmonic Oscillator. This makes the convenient notation (and many results) of quantum mechanics instantly available to shapelets. In Shapelets I, it was found convenient to represent a Cartesian shapelet decomposition in bra-ket notation as $|n_1, n_2\rangle$. The Cartesian basis functions were raised or lowered into neighbouring states via *Cartesian shapelet ladder operators*,

$$\hat{a}_1^\dagger |n_1, n_2\rangle \equiv \sqrt{n_1 + 1}\ |n_1 + 1, n_2\rangle \tag{4.18}$$

$$\hat{a}_1 |n_1, n_2\rangle \equiv \sqrt{n_1}\ |n_1 - 1, n_2\rangle \ , \tag{4.19}$$

plus equivalent expressions for $\hat{a}_2^\dagger$ and $\hat{a}_2$.

There is no simple formulation for an equivalent $\hat{a}_n$ and $\hat{a}_m$ to act upon a polar shapelet decomposition $|n,m\rangle$. However, we can construct *polar shapelet ladder operators*

$$\hat{a}_r^\dagger = \frac{1}{\sqrt{2}}\left(\hat{a}_1^\dagger + i\hat{a}_2^\dagger\right) = \frac{1}{2}\left(x + iy - \frac{\partial}{\partial x} - i\frac{\partial}{\partial y}\right) \quad (4.20)$$

$$\hat{a}_l^\dagger = \frac{1}{\sqrt{2}}\left(\hat{a}_1^\dagger - i\hat{a}_2^\dagger\right) = \frac{1}{2}\left(x - iy - \frac{\partial}{\partial x} + i\frac{\partial}{\partial y}\right) \quad (4.21)$$

$$\hat{a}_l = \frac{1}{\sqrt{2}}\left(\hat{a}_1 + i\hat{a}_2\right) = \frac{1}{2}\left(x + iy + \frac{\partial}{\partial x} + i\frac{\partial}{\partial y}\right) \quad (4.22)$$

$$\hat{a}_r = \frac{1}{\sqrt{2}}\left(\hat{a}_1 - i\hat{a}_2\right) = \frac{1}{2}\left(x - iy + \frac{\partial}{\partial x} - i\frac{\partial}{\partial y}\right) , \quad (4.23)$$

so that

$$\hat{a}_r^\dagger|n,m\rangle = \sqrt{\tfrac{n+m+2}{2}}\,|n+1,m+1\rangle \quad (4.24)$$

$$\hat{a}_l^\dagger|n,m\rangle = \sqrt{\tfrac{n-m+2}{2}}\,|n+1,m-1\rangle \quad (4.25)$$

$$\hat{a}_l|n,m\rangle = \sqrt{\tfrac{n-m}{2}}\,|n-1,m+1\rangle \quad (4.26)$$

$$\hat{a}_r|n,m\rangle = \sqrt{\tfrac{n+m}{2}}\,|n-1,m-1\rangle . \quad (4.27)$$

The Hamiltonian and angular momentum operators in this basis are

$$\hat{H}|n,m\rangle = \left(\hat{a}_r^\dagger\hat{a}_r + \hat{a}_l^\dagger\hat{a}_l + 1\right)|n,m\rangle = (n+1)|n,m\rangle , \quad (4.28)$$

and

$$\hat{L}|n,m\rangle = \left(\hat{a}_r^\dagger\hat{a}_r - \hat{a}_l^\dagger\hat{a}_l\right)|n,m\rangle = m|n,m\rangle . \quad (4.29)$$

Consequently, n corresponds to the Quantum Mechanical energy level and m the angular momentum quantum number.

Polar shapelet coefficients are thus easily interpreted as Gaussian-weighted quadrupole, octopole, etc. moments of the surface brightness, where m is the number of tangential oscillations. A few applications of $\hat{a}$ and $\hat{a}^\dagger$ ladder operators also describe rotations, dilations and all other simple SO2 group transformations to first order in shapelet space. This particularly includes image shearing, such as that produced by weak gravitational lensing. We shall further discuss these operations in §4.3.

As a rseult of the uncertainty principle of Quantum Mechanics, which relates position and momentum, the polar shapelet basis set is invariant under Fourier transformation (up to a phase factor i^n and scale change $\beta \to \beta^{-1}$). This is most obvious for the ground $f_{0,0}(\vec{x})$ state, which is a plain Gaussian and therefore trivially invariant. As described for Cartesian shapelets in Shapelets II, this greatly simplifies the analytic convolution and deconvolution of objects from a PSF. Convolution becomes no more than a bra-ket matrix multiplication, and deconvolution just requires a matrix inversion.

4.2.5 Conversion between Cartesian and polar shapelets

It is useful to be able to switch between the two forms of shapelets, as each have uses in different situations. A set of Cartesian shapelet coefficients $|n_1, n_2\rangle$ can be transformed into polar shapelet representation using the *conversion matrix*

$$|n_l, n_r\rangle\langle n_1, n_2| = 2^{-\frac{n}{2}} i^m \left[\frac{n_1! n_2!}{n_r! n_l!}\right]^{\frac{1}{2}} \delta_{n_1+n_2, n_r+n_l} \sum_{n'_r=0}^{n_r} \sum_{n'_l=0}^{n_l} i^{-m'} \begin{pmatrix} n_r \\ n'_r \end{pmatrix} \begin{pmatrix} n_l \\ n'_l \end{pmatrix} \delta_{n', n_1} \ , \tag{4.30}$$

where the parentheses denote binomial coefficients. Note the correction of the bra-ket notation since equation (69) in Shapelets I.

This linear mapping is one-to-one and unique upon the lower-half arrays of (n_1, n_2) coefficients suggested by figure 4.2 (but not if a full square array is used). It merely rotates the shapelet coefficient axes in a Hilbert space, so no information is lost. Indeed, the axes happen to become closer to the optimal ones suggested by a Principal Component Analysis of real galaxy morphologies in the Hubble Deep Field. Discarding the lowest polar shapelet coefficients rather than Cartesian shapelet coefficients therefore results in even more efficient data compression.

4.3 Image manipulation and shape properties

4.3.1 Linear transformations

Linear transformations and image manipulation is simple in shapelet space. Let us consider a coordinate transformation $\vec{x} \to (1 + \Psi)\vec{x} + \vec{\epsilon}$, where $\vec{\epsilon} = (\epsilon_1, \epsilon_2)$ is a small displacement, in units of β, and Ψ is a 2×2 matrix parameterized as

$$\Psi = \begin{pmatrix} \kappa + \gamma_1 & \gamma_2 - \rho \\ \gamma_2 + \rho & \kappa - \gamma_1 \end{pmatrix} . \tag{4.31}$$

This is a generalization of the matrix $\mathcal{A}$ in equation (2.57), and now includes all SO2 group transformations. The parameters ρ, κ, ϵ and γ_i correspond to infinitesimal rotations, dilations, translations and shears.

For small transformation parameters, an image transforms as $f(\vec{x}) \to f'(\vec{x}) \simeq f(\vec{x} - \Psi\vec{x} - \vec{\epsilon})$, which can be written as

$$f' \simeq (1 + \rho\hat{R} + \kappa\hat{K} + \gamma_j\hat{S}_j + \epsilon_i\hat{T}_i)f \ , \tag{4.32}$$

where $\hat{R}$, $\hat{K}$, $\hat{S}_i$ and $\hat{T}_i$ are the operators generating rotation, convergence, shears and translations, respectively. Note that since the shapelet model of an object is smooth and analytic, these operators are exact and reversible.

4.3.2 Ladder operators

The operators were expressed in terms of Cartesian shapelet ladder operators in Shapelets I. Using equations (4.20) to (4.23), it is easy to write them in terms of the polar shapelet ladder operators as

$$\begin{aligned}
\hat{R} &= i\left(\hat{a}_r^\dagger \hat{a}_r - \hat{a}_l^\dagger \hat{a}_l\right) \;=\; i\hat{L} \\
\hat{K} &= 1 + \hat{a}_r^\dagger \hat{a}_l^\dagger - \hat{a}_r \hat{a}_l \\
\hat{S}_1 &= \frac{1}{2}\left(\hat{a}_r^{\dagger 2} - \hat{a}_r^2 + \hat{a}_l^{\dagger 2} - \hat{a}_l^2\right) \\
\hat{S}_2 &= \frac{i}{2}\left(\hat{a}_r^{\dagger 2} + \hat{a}_r^2 - \hat{a}_l^{\dagger 2} - \hat{a}_l^2\right) \\
\hat{T}_1 &= \frac{1}{2}\left(\hat{a}_r^\dagger + \hat{a}_l^\dagger - \hat{a}_l - \hat{a}_r\right) \\
\hat{T}_2 &= \frac{i}{2}\left(\hat{a}_r^\dagger - \hat{a}_l^\dagger - \hat{a}_l + \hat{a}_r\right) \,. \qquad (4.33)
\end{aligned}$$

This recovers the results of BJ02 §6.3.2, where a slightly different notation of $p = n_r$ and $q = n_l$ is used. They also exponentiate these operators and hence derive recursion relations for finite dilations, shears and translations in their appendix.

4.3.3 Coefficient mapping in shapelet space

Since the polar shapelet ladder operators have no simple forms for $\hat{a}_n$ and $\hat{a}_m$, it can be more convenient to consider the transformations as a mapping of $f_{n,m}$ coefficients. For example, a rotation is trivially

$$\hat{R} : f_{n,m} \to f_{n,m}\, e^{im\rho} \,. \qquad (4.34)$$

It will be useful later to note that a rotation through 180° can be written as

$$\hat{R}_{180^\circ} : f_{n,m} \to (-1)^m\, f_{n,m} \,. \qquad (4.35)$$

A dilation can likewise be performed in polar shapelet space simply by changing β. Alternatively, the scale size can be kept fixed by using the mapping

$$\begin{aligned}
\hat{K} : f_{n,m} \to (1+\kappa)\, f_{n,m} &+ \frac{\kappa}{2}\sqrt{(n-m)(n+m)}\, f_{n-2,m} \\
&- \frac{\kappa}{2}\sqrt{(n-m+2)(n+m+2)}\, f_{n+2,m} \qquad (4.36)
\end{aligned}$$

Note that this dilation operation conserves surface brightness while the area changes by a factor $(1+2\kappa)^{-1}$ (this is what happens in weak gravitational lensing). To perform an

enlargement which instead conserves total flux to first order, change the first $(1+\kappa)$ to $(1-\kappa)$.

$$\hat{K} : f_{n,m} \rightarrow (1-\kappa)\, f_{n,m} + \frac{\kappa}{2}\sqrt{(n-m)(n+m)}\, f_{n-2,m} \\ -\frac{\kappa}{2}\sqrt{(n-m+2)(n+m+2)}\, f_{n+2,m} \tag{4.37}$$

Rather than these first order approximations, dilations can also be performed easily to *general* order by making use of the $C_{\mathbf{n},m,l}$ convolution formalism in Shapelets I. Firstly, consider an image represented in shapelet space with scale size α. Clearly, this image will not be changed by convolution with a δ-function. The δ-function may be modelled as a $\chi_{0,0}$ state with very small β. However, in the $C_{\mathbf{n},m,l}$ convolution formalism of Shapelets I, the final image may be given an arbitrary new scale size γ. If γ is specifically chosen to differ from the initial scale size by $\gamma = (1+2\kappa)^{-1}\alpha$, the same object is modelled as before, but using a different shapelet scale size. Finally, multiply γ by $(1+2\kappa)$, to restore the scale size to its initial value; and the image shrinks or expands in the process.

Shears and translations can be performed using

$$\begin{aligned}\hat{S} &: f_{n,m} \rightarrow f_{n,m} \\ &+\frac{\gamma}{4}\left\{\sqrt{(n-m-2)(n-m)}\, f_{n-2,m+2} - \sqrt{(n+m+2)(n+m+4)}\, f_{n+2,m+2}\right\} \\ &+\frac{\gamma^*}{4}\left\{\sqrt{(n+m-2)(n-m)}\, f_{n-2,m-2} - \sqrt{(n-m+2)(n-m+4)}\, f_{n+2,m-2}\right\}\end{aligned} \tag{4.38}$$

and

$$\hat{T}_1 : f_{n,m} \rightarrow f_{n,m} + \frac{\epsilon_1}{2\sqrt{2}}\Big\{\sqrt{n+m}\, f_{n-1,m-1} + \sqrt{n-m}\, f_{n-1,m+1} \\ -\sqrt{n-m+2}\, f_{n+1,m-1} - \sqrt{n+m+2}\, f_{n+1,m+1}\Big\} \tag{4.39}$$

$$\hat{T}_2 : f_{n,m} \rightarrow f_{n,m} + \frac{i\epsilon_2}{2\sqrt{2}}\Big\{\sqrt{n+m}\, f_{n-1,m-1} - \sqrt{n-m}\, f_{n-1,m+1} \\ -\sqrt{n-m+2}\, f_{n+1,m-1} + \sqrt{n+m+2}\, f_{n+1,m+1}\Big\}\,. \tag{4.40}$$

Other image manipulations can also be represented as mappings of shapelet coefficients. Changes of flux by a factor B are trivially implemented by the mapping

$$\hat{B} : f_{n,m} \rightarrow B \times f_{n,m}\,. \tag{4.41}$$

It is also possible to circularize an object with the mapping

$$\hat{C} : f_{n,m} \rightarrow f'_{n,m} = \begin{cases} f_{n,m} & \text{if } m = 0 \\ 0 & \text{if } m \neq 0 \end{cases} \tag{4.42}$$

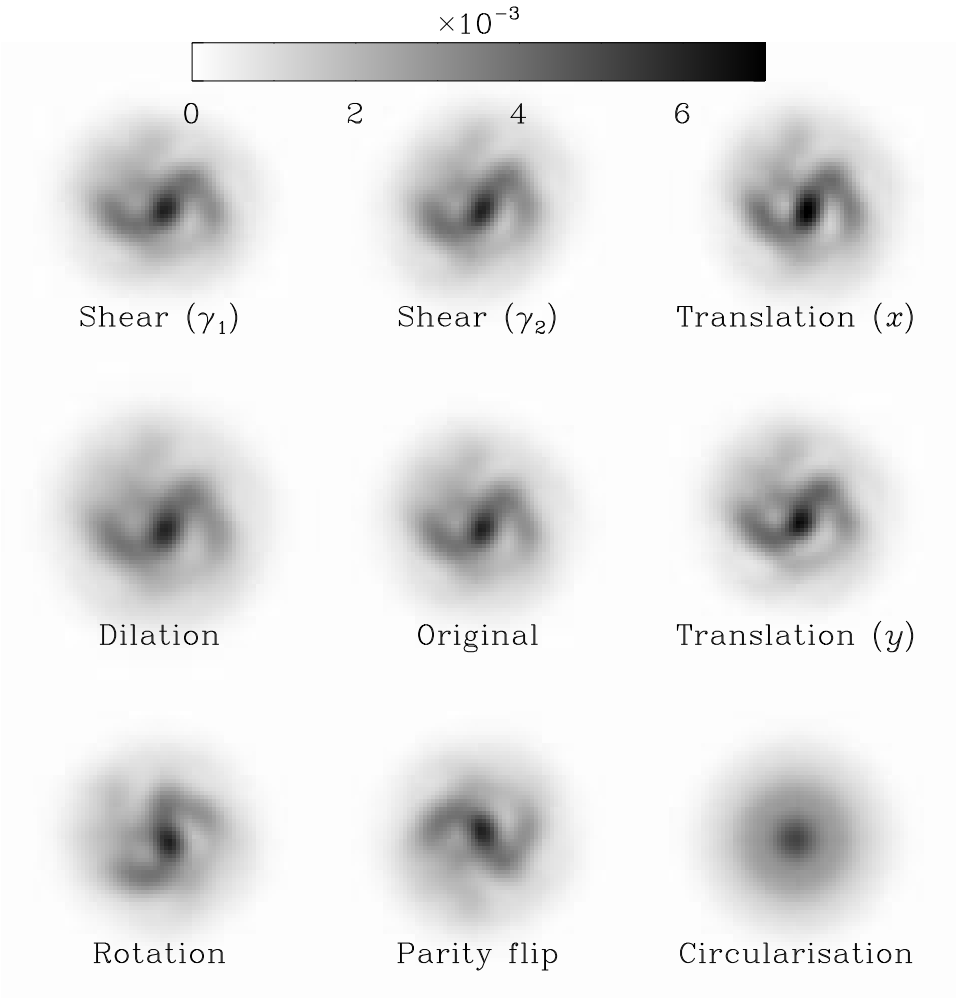

Figure 4.4: Some simple operations applied to a real galaxy image, by using the polar shapelet ladder operators or coefficient mappings as described in the text. The central image is the original galaxy. Starting at the bottom-left and proceeding clockwise, the other images show a rotation of $40°$, dilation of $\kappa = 1.3$, shears of $\gamma = 7\%$, translations of $2\frac{1}{2}$ pixels, circularisation and reflection in the x-axis.

or to flip an object's parity by reflection in the x-axis, using

$$\hat{P} : f'_{n,m} = f^*_{n,m} \, . \tag{4.43}$$

Combining this $\hat{P}$ with the rotation operator allows reflections to be performed in any axis. The action of these operators is demonstrated on a real galaxy image in figure 4.4. Note that it is ideal to increase $n_{\max}$ by adding extra coefficients (set to zero) when applying operators that map coefficients onto ones that had previously been truncated. Not much can be done about the coefficients with negative n that do not exist.

4.3.4 First-order statistics of galaxy shapes

Here we extend the work of Shapelets I using weighted combinations of shapelet coefficients to form estimators of galaxy shapes. We find the interpretation of polar shapelets more intuitive and the expressions below are usually more simple than their Cartesian equivalents. For example, the rotationally invariant part of an object is isolated into its $m = 0$ coefficients. The linear offset of an object from the origin is described by its $m = \pm 1$ coefficients and the ellipticity of an object by its $m = \pm 2$ coefficients. In these cases, the magnitude of the coefficients indicate an amount and the phases a direction.

Photometry

The most basic quantities to measure for an object $f(\mathbf{x})$ are its total flux (photometry), centroid position (astrometry) and size. Expressions for these, as weighted combinations of Cartesian shapelet coefficients, were given in equations (26) to (28) of Shapelets I. Either by performing the same integrals directly in polar coordinates,

$$\int_0^{2\pi} \int_0^{\infty} \chi_{n,m}(r,\theta;\beta)\; r \; \mathrm{d}r\mathrm{d}\theta = 2\sqrt{\pi}\beta \; \delta_{m0} \; , \tag{4.44}$$

or by transforming the Cartesian shapelet sums into polar shapelet space, it is easy to show that the total flux of an object F is

$$F \equiv \int f(\vec{x}) \; \mathrm{d}^2x \; = (4\pi)^{\frac{1}{2}}\beta \sum_n^{\text{even}} f_{n0} \; , \tag{4.45}$$

where the sum is over only even values of n, because odd values do not have an $m = 0$ coefficient. Notice that it is only these rotationally-invariant basis functions that contribute to the total flux. All other states have positive and negative regions which cancel out under integration around θ. A consequence of this is that it is easy to circularise an object by merely setting to zero all $m \neq 0$ coefficients.

Astrometry

It can similarly be shown that the centroid (x_c, y_c) is

$$x_c \equiv \frac{\int x f(\vec{x}) \; \mathrm{d}^2x}{\int f(\vec{x}) \; \mathrm{d}^2x} = \mathrm{Re}\left\{ \frac{(8\pi)^{\frac{1}{2}}\beta^2}{\mathrm{F}} \sum_{\mathrm{n}}^{\mathrm{odd}} (\mathrm{n}+1)^{\frac{1}{2}} \; \mathrm{f_{n1}} \right\} \tag{4.46}$$

and

$$y_c \equiv \frac{\int y f(\vec{x}) \; \mathrm{d}^2x}{\int f(\vec{x}) \; \mathrm{d}^2x} = \mathrm{Im}\left\{ \frac{(8\pi)^{\frac{1}{2}}\beta^2}{\mathrm{F}} \sum_{\mathrm{n}}^{\mathrm{odd}} (\mathrm{n}+1)^{\frac{1}{2}} \; \mathrm{f_{n1}} \right\} \tag{4.47}$$

Here the summation is over only odd values of n, because only these have the $m = \pm 1$ coefficients that behave in the desired manner under rotation.

Size and ellipticity

Measures for the size and ellipticity of an object can be derived from the unweighted quadrupole moments of the object, defined as

$$F_{ij} \equiv \int x_i x_j f(\mathbf{x}) d^2x \ . \tag{4.48}$$

Using the polar ladder operators from equations (4.20–4.23) to represent $x_i x_j$, one can show that the rms radius R of an object is given by

$$R^2 \equiv \frac{\int |\vec{x}|^2 f(\vec{x}) \ \mathrm{d}^2x}{\int f(\vec{x}) \ \mathrm{d}^2\vec{x}} \tag{4.49}$$

$$= \frac{F_{11} + F_{22}}{F} = \frac{(16\pi)^{\frac{1}{2}}\beta^3}{F} \sum_n^{\text{even}} (n+1) \ f_{n0} \ . \tag{4.50}$$

The unweighted complex ellipticity of the object is then given by

$$\varepsilon \equiv \frac{F_{11} - F_{22} + 2iF_{12}}{F_{11} + F_{22}} = \frac{(16\pi)^{\frac{1}{2}}\beta^3}{FR^2} \sum_n^{\text{even}} [n(n+2)]^{\frac{1}{2}} f_{n2} \tag{4.51}$$

Note that the complex shear notation of Blandford *et al.* (1991) arises here naturally.

All of these estimators correspond to unweighted quantities and converge for any galaxy with a shapelet spectrum steeper than n^{-2}. This includes both exponential and de Vaucouleurs profiles, as long as $n_{\max}$ is kept sufficiently low that surrounding noise is not being modelled by the high-n coefficients. It is therefore important to have a reasonable model of the noise per pixel. The error on series due to truncation at $n_{\max}$ can be calculated using any of a range of methods for Taylor series in *e.g.* Boas (1983).

It may even be the case that shapelets can be used to calculate these basic astronomical measures in a way that is more robust to noise than traditional techniques using isophotal cutoffs. The non-local shapelet fitting procedure recognises correlations between nearby pixel values, effectively summing their S/N, and can thus count object flux in extended wings that would be beneath the detection threshold in any individual pixel. Although the shapelet size measure R is an integrated rms size rather than a FWHM, a simple example of this is illustrated in figure 4.11. Shapelets give a larger estimate of size for many HDF galaxies than that expected from the equivalent SExTRACTOR detection. There are few estimates smaller than expected, suggesting that this really is measuring the extended wings. Shapelets could therefore be very useful for un-

ambiguous photometry and astrometry measurements in many branches of astronomy. One idea would be to find objects using wavelets, then decompose them and analyse them using shapelets.

4.3.5 Higher-order galaxy morphology diagnostics

Since the shapelet basis functions form a complete set, the shapelet decomposition of an object encodes all of the information available about its shape. It should therefore be possible to find other combinations of shapelet coefficients which distinguish between, and quantitatively classify, different galaxy morphologies. A galaxy's morphology is the result of its recent evolution; and two galaxies of a similar appearance are likely to be located in similar physical environments, or to have undergone similar merger and star formation events. Distinct galaxy populations can also be separated: perhaps into types which better trace the underlying mass distribution; perhaps into those which typically provide more reliable shear estimators. We shall also require such morphology diagnostics in chapter 5, to verify that our simulated images contain morphologically realistic objects.

The Hubble tuning-fork is the classic scheme for classifying galaxy morphologies (Hubble 1926, Sandage 1961, de Vaucouleurs 1959). Despite its wide acceptance, however, its morphology indices are unnaturally discrete, and they bear little resemblance to physical parameters in theoretical models of galaxy formation. Aside from the basic bulge/disc decomposition, the Hubble tuning fork fails to uniquely identify or distinguish between objects involved in very different modes of evolution. The number and pitch angle of spiral arms are now believed to be transient phenomena; the presence of a bar is of debatable significance; and many of the original diagnostics depend strongly upon seeing or distance to the source. Foremost, however, the Hubble sequence completely fails to classify 46% of objects beyond $z \simeq 0.6$, precisely the regime in which most weak lensing source galaxies are located. Rather than simply mimicking the Hubble tuning-fork, we shall therefore require a brand new classification scheme.

We begin with the premise that useful morphology estimators can be written linearly in shapelet space as

$$Q = \frac{\beta^s}{F} \sum_{n,m} w_{n,m} f_{n,m} \ , \tag{4.52}$$

where $w_{n,m}$ are arbitrary weights. We then restrict ourselves to using those combinations which are independent of the choice of β, to at least first order. This ensures that the iteration in §4.5.6 does not affect, to any great extent, the final result. Setting $\frac{\partial Q}{\partial \beta} = 0$ and using the right-hand side of equation (4.37) as $\frac{\partial f_{n,m}}{\partial \beta}$, it is easy to show that this implies

$$w_{n,m} = \frac{2s}{\sqrt{(n+m)(n-m)}}\, w_{n-2,m} + \sqrt{\frac{(n-m-2)(n+m-2)}{(n+m)(n-m)}}\, w_{n-4,m}\ , \tag{4.53}$$

where the second term should be ignored if it refers to non-existent states with negative n. The normalisation of $w_{0,0}$ is arbitrary, and can be set to ensure independence to changes of object flux. Notice that all quantities so formed mix coefficients with only one value of $|m|$. This value can be chosen to give Q the desired properties under rotation. Setting s =1, 2 or 3 in fact recovers precisely the flux, centroid or (un-normalised) quadrupole moments. This proves that these are the *only* β-invariant linear quantities with such dimensionality. Equations (4.45), (4.46), (4.47) and (4.50) are therefore not only independent of β to first order, which was all that was required in section §4.3.4, but in fact independent to all orders.

We can extend the above sequence by raising s further. Setting $s = 5$ and $m = 0$ gives the 2D unweighted kurtosis of the image, producing an estimate of the object's concentration. Unfortunately, setting s this high creates a series of shapelet coefficients that does not converge for realistic de Vaucouleurs or exponential galaxies.

Principal Component Analysis (PCA; *e.g.* Francis & Wills 1999) of a galaxy population can be used to find linear combinations of coefficients which do converge, and which most efficiently encode its shape information. This technique reduces the dimensionality of the parameter space needed to differentiate between galaxies, and hence determines their most statistically significant shape measures. For example, the first five principal components of the HDF galaxies in figure **??** can be combined to recover 90% of their shape information. However, as is always the case with this method, the interpretation of such results is problematic. Even the combinations of the first principal components are complicated, and an association between their shapes and the galaxy's physical properties or environment remains elusive. Kelly & McKay (2003) achieved more success with the same analysis upon galaxies in the Sloan Digital Sky Survey. Since all of the SDSS galaxies have known redshifts, it was possible in each case to set β to a constant *physical* scale of 2 kpc. This produced better-controlled shapelet decompositions, and galaxies of different Hubble types separated in shapelet space. However, no work has yet associated the principal components of a shapelet decomposition to tangible, physical properties.

An alternative approach is to copy other existing morphology estimators, which have already been developed and calibrated against such physical properties. Many attempts have been made to revise the Hubble sequence or to invent new classification schemes (*e.g.* Simard 1998; Bershady *et al.* 2000; Conselice *et al.* 2000; van den Bergh

2002; Conselice 2003). Indices of concentration, asymmetry and clumpiness have been shown to correlate respectively with evolutionary type, galaxy merger history and star formation rates. However, it is admitted that these parameters are currently calculated in a rather *ad hoc* manner. Fortunately, very similar quantities can be recreated from weighted combinations of shapelet coefficients, using the natural form and symmetries of the shapelet basis functions.

Concentration

Bershady *et al.* (2000) define a *concentration parameter*

$$C \equiv 5 \times \log\left(\frac{r_{80}}{r_{20}}\right) , \tag{4.54}$$

where r_{80} and r_{20} are the radii of circular apertures containing 80% and 20% of the object's total flux. This correlates well with a galaxy's Hubble type (Bershady *et al.* 2000) and also its mass (Conselice *et al.* 2002). To represent this quantity using shapelets, it will be necessary to integrate an object's flux out to a finite distance R. Evaluating the integral of all the basis functions in turn gives

$$\int_0^{2\pi}\int_0^R f(r)\; r\; \mathrm{d}r\mathrm{d}\theta = 4\sqrt{\pi}\beta \sum_n^{even} (-1)^{n/2}\; f_{n,0}\; I_n \; , \tag{4.55}$$

where

$$I_n = \frac{1}{2\beta^2}\int_0^R L_{\frac{n}{2}}\left(\frac{r^2}{\beta^2}\right) e^{\frac{-r^2}{2\beta^2}}\; r\; \mathrm{d}r \; . \tag{4.56}$$

A recursion relation for this integral may be found by integrating by parts once, then applying equation (4.8) n times:

$$I_n = 1 - L_n\left(\frac{R^2}{\beta^2}\right) e^{\frac{-R^2}{2\beta^2}} - I_{n-1} - I_{n-2} - \ldots - I_0 \; . \tag{4.57}$$

A less practical but closed form for I_n may be derived by repeatedly substituting equation (4.57) into itself, or by directly integrating equation (4.56) by parts n times,

$$I_n = 1 - L_n\left(\frac{R^2}{\beta^2}\right) e^{\frac{-R^2}{2\beta^2}} \; + \; 2\sum_{k=1}^{[n/2]} (-1)^k \left\{1 - L_{\frac{n-2k}{2}}\left(\frac{R^2}{\beta^2}\right) e^{\frac{-R^2}{2\beta^2}}\right\} \; . \tag{4.58}$$

This can finally be evaluated for various values of R, to find r_{80} and r_{20} as required.

Alternatively, we have noticed that a ratio of the two existing shapelet scale sizes, R^2 and β, is also rather effective (although this is obviously not independent of β). This makes for a somewhat simpler calculation and we propose this estimator instead. However, further work will need to be done to calibrate it to the physical properties of galaxies.

Asymmetry

Conselice *et al.* (2000) define an *asymmetry parameter*

$$A_{180} \equiv \frac{\sum_{\mathrm{p}ixels} |f(x,y) - f^{180^\circ}(x,y)|}{\sum_{\mathrm{p}ixels} f(x,y)} \,, \tag{4.59}$$

where the superscript denotes an image rotated through 180°. A term dealing with the background noise and sky level has been omitted here, these having been already dealt with during the shapelet fitting procedure. Asymmetry correlates with star formation rate (Conselice *et al.* 2000) and high asymmetry values often indicate recent galaxy interactions or mergers.

The sums over pixels can firstly be replaced with analytic integrals over the now-smooth shapelet models. Representing the models as a shapelet expansion and noting from equation (4.35) that a rotation through 180° merely changes the sign of all shapelet coefficients with odd m, it may be shown that

$$A = \frac{1}{F} \int_0^{2\pi} \int_0^{\infty} \left| \sum_{n,m} [1 - (-1)^m] \, f_{n,m} \, \chi_{n,m}(r,\theta) \right| \, r \, \mathrm{d}r \, \mathrm{d}\theta \tag{4.60}$$

$$= \frac{1}{F} \sum_{n,m} \Big(\, \langle n,m| \, (\hat{1} - \hat{R}_{180^\circ})^\dagger \, (\hat{1} - \hat{R}_{180^\circ}) \, |n,m\rangle \, \Big)^{1/2} \,. \tag{4.61}$$

Using the orthonormality condition (4.13), to take the integral inside the summation and evaluate it, we find

$$A = \frac{\sqrt{2}}{\pi F} \sum_{m,n}^{\mathrm{o}dd} |f_{n,m}| \,. \tag{4.62}$$

Estimators of asymmetry under rotations of 120° or 90° can be formed instead by summing only those shapelet coefficients with m not divisible by 3 or 4 respectively.

Clumpiness

A *clumpiness parameter* can also be quickly calculated in shapelet space, using the formula for convolution with a Gaussian given in Shapelets I.

$$S \equiv \frac{10}{F} \sum_{n,m} \Big(\, \langle n,m| \, (\hat{G}_\sigma - \hat{1})^\dagger \, (\hat{G}_\sigma - \hat{1}) \, |n,m\rangle \, \Big)^{1/2} , \tag{4.63}$$

where $\hat{G}_\sigma$ is the $G_{\mathbf{n},\mathbf{m}}$ operator for convolution with a Gaussian of width σ given in Shapelets I. This can be written in terms of polar shapelets, but is inelegant and provides less clarification that the notation in Shapelets I, so we omit it here.

Curvature

As noticed by Irwin & Shmakova (2003), the relative phases of the quadrupole and sextupole moments can be used as an indication of curvature. After ellipticity, the sextupole moments are the first additional terms induced in the shape of an object by second-order gravitational lensing. (Goldberg & Natarajan (2002) also advocate the use of octopole moments). If the sextupole moments are aligned in the correct way to the quadrupole ellipticity, shapelet models begin to form arclets, as are frequently seen near massive clusters. While the localised nature of shapelet basis functions means that they are not ideally suited to model highly extended *arcs*, they may be used in this way to identify *arclet* candidates. With the addition of this second-order technique, shapelets may also be more sensitive than quadrupole-only shear measurement methods in the slightly non-linear lensing regime around clusters, and to local gradients in their gravitational potential due to substructure.

We can combine either the Gaussian-weighted (a_{33}) or unweighted (set $m = 3$ and $s = 4$ in equation (4.52)) sextupole moment, S, with the corresponding quadrupole moment, Q, to form the *curvature estimator*

$$H = \frac{|Q|}{F^2}\left[\mathrm{Re}\{S'\} - \mathrm{Im}\{S'\}\right] \ , \tag{4.64}$$

where $S' = Se^{3i\Theta}$, a prior rotation by the angle $\Theta = [(-\theta_S - \frac{\pi}{2} + \frac{\theta_Q}{2})\mathrm{mod}\frac{\pi}{2}]$. This ensures that it is their relative phase, and that both the real and imaginary parts of S' are positive. (if they aren't, curvature should be pointing in the opposite direction anyway!) If H is positive, the object is curved and Θ is the direction towards the centre of curvature. If H is negative, the object is said to be "aligned".

Shear-invariant quantities

Only two different linear combinations of shapelet an object's shapelet coefficients are invariant under any shear:

$$\Gamma_1 \equiv (4\pi)^{\frac{1}{2}}\beta \sum (f_{0,0} + f_{4,0} + f_{8,0} + \dots) \tag{4.65}$$

$$\Gamma_2 \equiv (4\pi)^{\frac{1}{2}}\beta \sum (f_{2,0} + f_{6,0} + f_{10,0} + \dots)\,. \tag{4.66}$$

Their sum is of course the total flux F, which is also independent of the choice of scale size β.

Dividing Γ_i by F renormalises these quantities to be invariant under changes of flux. It would be useful if a shear estimator could be formed such that $P^\gamma = \Gamma_i/F$, in order to avoid the "Kaiser flow" of this quantity in the size vs magnitude plane (Kaiser 2000), due to the fact that only the post-shear P^γ can be measured from real data. Un-

fortunately, there is no linear combination of shapelet coefficients that is simultaneously independent of flux, β and the level of applied shear.

4.4 Shapelet decomposition of real data

4.4.1 Additional considerations needed for real data

In this section we shall describe an improved method for finding and decomposing objects in real data. The overlap integrals (4.3) and (4.15) are defined only for smooth functions, but real images are complicated by pixellisation, PSF convolution and observational noise. In order to overcome these problems, we shall adopt a somewhat different approach to the shapelet decomposition.

Our new method applies precisely the same PSF convolution and pixellisation to the basis functions as have acted upon photons *en route* to the telescope and detector. Having mimicked these processes, the altered basis functions are then fitted to the data using a least-squares method. This is an important advance, particularly for small galaxies or high-n coefficients that correspond to poorly-sampled basis functions with many oscillations per pixel. Least-squares fitting also enables us to simultaneously deconvolve the image from the telescope's PSF, and to deal linearly with numerical effects that introduce slight non-orthogonality into the shapelet basis functions.

4.4.2 Object detection

Objects are first detected in an image using SExtractor (Bertin & Arnouts 1996). Its friends-of-friends algorithm avoids the biases towards selecting objects with a particular size or orientation that particularly affect weak lensing analysis (see *e.g.* BJ02 §8). These biases are difficult to avoid with matched-filter detection methods like hfindpeaks (Kaiser, Squires & Broadhurst 1995). To detect objects in the Hubble Deep Field, we have adapted the SExtractor convolution mask and detection parameters from those used by Williams *et al.* (1996). In particular, we use a comparatively low S/N detection threshold, DETECT_THRESH, of 1.3. This affords recovery of faint galaxies and minimizes incompleteness, at the expense of many false-positive 'detections' of noise, which need to be flagged and filtered out later (see §4.5.6). Stars with CLASS_STAR $> 97\%$ are immediately discarded, as we wish to model only galaxies.

Small *postage stamp* regions are then extracted around each object. After experimenting on various data sets, we have found the SExtractor segmentation map highly sensitive to input settings and will use it only to identify background pixels rather than objects themselves. Our postage stamps are square, even when the object is highly elliptical, and $3 \times A + 5$ pixels on a side, where A is the SExtractor FWHM size parameter. This postage stamp is small enough to isolate most galaxies in typical data, but large enough to ensure that the shapelet basis functions are close to zero at its boundaries.

If these were not contained entirely within the postage stamp, the shapelet coefficients would become unconstrained during the fit, producing anomalous results.

For the Hubble Deep Field images, an inverse variance noise map is available that shows the noise in each pixel, as determined by the variation in observed flux between different exposures. If an inverse variance map is not available, our prescription to extract a postage stamp also leaves a small border of pixels around the edge of the image, which can be conveniently used to estimate the local background noise level. This level, multiplied by identity matrix, should then be used as the covariance matrix V in equation (4.75).

4.4.3 PSF deconvolution

Real data is inevitably seen after convolution with a telescope's Point Spread Function, due to atmospheric turbulence or 'seeing' (for ground-based observatories), aperture diffraction at the primary mirror, and imperfect tracking or optics optics within the camera. The combination of these effects can be measured from the non-pointlike size and shape of stars observed in an image. Shapelets I presented the matrix operation for convolving an image with a Gaussian PSF in shapelet space. Shapelets II extended this derivation to a general PSF and demonstrated PSF *de*convolution by matrix inversion. However, our new least-squares fitting method allows an elegant way to sidestep this potentially slow and numerically unstable method.

Our alternative approach is to convolve the basis functions with the PSF model in advance, and then to fit the new basis set to the data. The returned shapelet model is automatically deconvolved from the PSF. Fitting is important with this method, because the convolved basis functions are no longer necessarily orthogonal: amongst other things, overlap integrals may not therefore conserve the flux.

Figure 4.5 shows a 10×oversampled TINYTIM (Krist 1997) model of the WFPC2 PSF, with charge diffusion added. This diffraction-limited PSF is very peaky and has extended wings: it is not the type of function most compactly represented using shapelets. It is shown in the figure with logarithmic colour scales and as a shapelet decomposition up to $n_{\max}^{PSF} = 15$. This is sufficient to accurately capture the core and the first two diffraction rings (which are already more than two orders of magnitude below the maximum) but does not extend far into the low-level wings. In principle, this could be further extended at a cost to processor time by using more shapelet coefficients. However, there are limits upon the accuracy of TINYTIM (Krist 1995) model, and the four diffraction spikes from the secondary spider vary anyway as a function of CCD position.

4.4.4 Pixellisation

While the shapelet basis functions are smooth and continuous, typical astronomical data is discrete. To match the two, one must either smooth the data or pixellate the basis

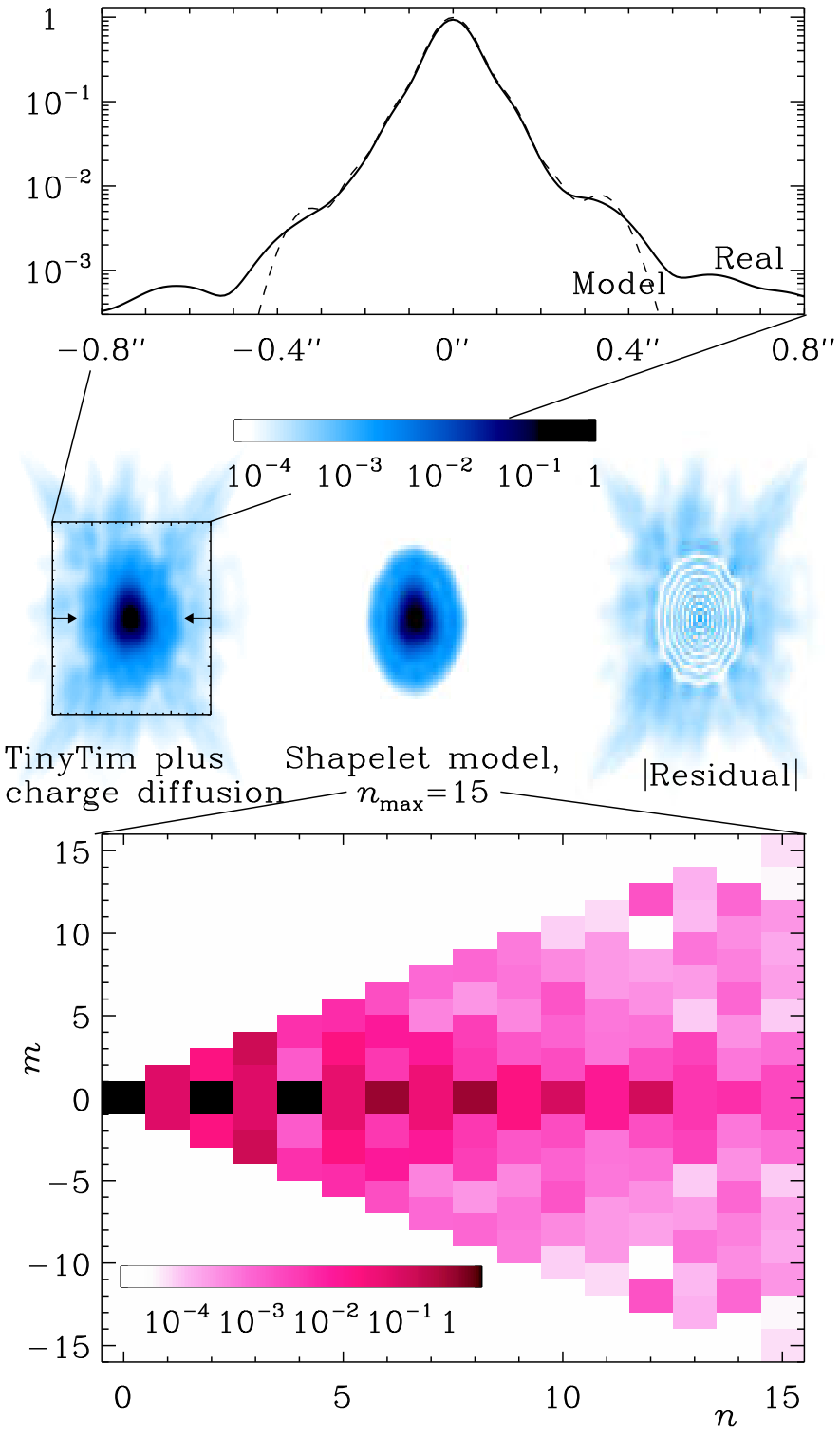

Figure 4.5: Shapelet model of the TINYTIM (Krist 1995) WFPC2 PSF plus charge diffusion. The top plot shows a horizontal slice through the centre of the PSF; the bottom shows the moduli of its polar shapelet coefficients to $n_{\max} = 15$. Note that the amplitude scales are logarithmic: the core is actually modelled very successfully out to the second diffraction ring, although for speed we do not capture the wings.

functions. One approach is to resample the data with a smaller pixel size, and smooth it by interpolating between the new pixels. However, this is very slow and requires an interpolation scheme to be defined. Rather than smooth the data, a different approach would be to discretise the smooth shapelet basis functions. This reduces the integrals in equations (4.3) and (4.15) to sums over pixel values, which are fast to compute but which are no longer analytically exact. One cannot simply use the central value of the basis function in each pixel, because this gives essentially random numbers for basis states whose oscillations are on the same scale as (or smaller than) the pixel size. In particular, the basis functions would no longer be guaranteed to remain orthonormal, placing a fundamental limit upon the accuracy of the model and quantities like its flux. We are not going to be able to avoid this entirely for real data, and least-squares fitting overcomes some concern, however it would be nice to minimise this effect as much as possible.

Fortunately, the Cartesian basis functions can be analytically integrated within rectangular pixels. We therefore work with these and only later convert the model to a polar shapelet representation, using equation (4.30). First consider the *one-dimensional Cartesian shapelet basis functions*

$$\phi_n(x) \equiv \left[2^n \pi^{\frac{1}{2}} n! \beta\right]^{-1} H_n\left(\frac{x}{\beta}\right)\, e^{-\frac{x^2}{2\beta^2}} \,. \tag{4.67}$$

from Shapelets I. The two-dimensional basis functions are simply the product $\phi_{n_1,n_2} \equiv \phi_{n_1}(x)\phi_{n_2}(y)$. Integrating by parts and using two well-known identities (see *e.g.* Boas 1983)

$$H_n(x) = 2xH_{n-1}(x) - 2(n-1)H_{n-2}(x) \tag{4.68}$$

and

$$\frac{\mathrm{d}H_{n-1}(x)}{\mathrm{d}x} = 2(n-1)H_{n-2}(x) \,, \tag{4.69}$$

one can obtain the recurrence relation

$$\begin{aligned} I_n &\equiv \int_a^b \phi_n(x)\,\mathrm{d}x & (4.70)\\ &= -\beta\sqrt{\frac{2}{n}}\left[\,\phi_{n-1}\,(x)\right]_a^b + \sqrt{\frac{n-1}{n}}\,I_{n-2} \,. & (4.71) \end{aligned}$$

Finally, note that

$$I_0 = \frac{\pi^{\frac{1}{4}}}{2}\left[\,erf(x)\right]_a^b \text{ and} \tag{4.72}$$

$$I_1 \;=\; -\sqrt{2}\Big[\,\phi_0\,(x)\Big]_a^b\,. \tag{4.73}$$

This supplies all the necessary integrals. Since the 2D Cartesian basis functions are separable in x and y, it is easy to extend this derivation to integrate within square CCD pixels:

$$I_{n_1,n_2} = \int_{a_1}^{b_1}\int_{a_2}^{b_2} \phi_{n_1}(x)\phi_{n_2}(y)\;\mathrm{d}x\;\mathrm{d}y = I_{n_1} \times I_{n_2} \tag{4.74}$$

where, if there is no "dead zone" around the edge of a pixel, $(b_i - a_i)$ is the angular size of a pixel. A pixel border that contains electronics and is therefore unresponsive to light can be included by altering the limits on the integral.

Note that even integration does not ensure exact orthogonality of the basis functions, because the fact that $\int \phi_{ij}\,\mathrm{d}^2x$ is calculated correctly does not imply that $\int \phi_{ij}\phi_{kl}\,\mathrm{d}^2x = 0$. Gram-Schmidt orthonormalisation could be performed on the discrete basis functions to find a linear combination of shapelet states that satisfy this condition. For our purposes, this slow operation is unnecessary because we then determine a galaxy's shapelet coefficients by fitting the functions to the data with a least-squares method. As long as the noise is unbiased, estimators like object flux will therefore be unbiased too.

4.4.5 Least-squares fitting

We have now convolved the shapelet basis functions with the telescope's Point Spread Function (PSF), and integrated them within pixels. This mimics the processes acting on photons *en route* to the CCD detector. We shall now fit shapelet coefficients to the data using a linear *least-squares method*

$$\mathbf{a} = (M^T V^{-1} M)^{-1} M^T V^{-1} \mathbf{f}\,, \tag{4.75}$$

where $\mathbf{a}$ is a vector of the derived shapelet coefficients, $\mathbf{f}$ the flux in each pixel arranged as a data vector, V the covariance matrix between pixel values and M is a matrix of each shapelet basis function evaluated in each pixel (see *e.g.* Lupton 1993). It is even possible to add a constant to the set of basis functions in order to fit (and thus remove) the background level; or a plane with variable slope in order to cope with either poor flat fielding or local background gradients. Although these extra basis functions is not strictly orthogonal, the technique works well in practice as long as there are sufficient pixels in the postage stamp that contain only background light.

If the noise per pixel is known, 1σ confidence limits can also be recovered on all of the assigned coefficients. If a complete pixel noise map is available (*e.g.* from multiple exposures stacked using DRIZZLE software (Fruchter & Hook 2002), this can be used to down-weight the contribution from noisy pixels where cosmic rays or hot/cold pixels were present in some of the exposures. As will be shown in §4.5, a fit achieving a reduced

χ^2 of unity has successfully modelled an object but smoothed over observational noise. Note that this method would be able to use the full covariance matrix between observed pixel values, although this information is generally not available. We are forced to ignore pixel-to-pixel correlations and use a diagonal matrix of pixel noise values for V. In real data, whether because of DRIZZLE or atmospheric seeing, the noise in adjacent pixels is indeed correlated. This simplification can therefore have a slight effect on statistics measured from very faint objects on the limits of detection (see chapter 5).

Using equation (4.30), we can finally convert the Cartesian shapelet model into polar shapelets for easier interpretation. For higher data compression ratios, shapelet coefficients with low absolute values, or low significance, can then be discarded as described in Shapelets I. If necessary, Principal Component Analysis of a population ensemble can improve the data compression still further. Our new technique works very well, producing successful PSF deconvolution and excellent image parameterization, as demonstrated in figure 4.1. It is an important advancement, particularly for small galaxies or high-n coefficients that correspond to oscillations within single pixels. Least-squares fitting enables us to simultaneously deconvolve the image from the telescope's PSF, take account of pixellisation and deal linearly with any slight non-orthogonality of shapelet basis functions.

4.5 Optimising the decomposition

4.5.1 The importance of a suitable choice for the shapelet scale size

Although the shapelet decomposition is linear in $f_{n,m}$, we need to specify in advance the centre of the basis functions $\vec{x}_0$ and their scale size β. Since we shall use the least-squares fitting method, we also need to determine in advance at what value of $n_{\max}$ to truncate the series. The number of statistically significant shapelet coefficients depends particularly upon the choice of β. For reasonable choices of the centre and scale size, the shape information of a galaxy is concentrated within only the first few coefficients, and a high image compression ratio is possible. However, if β is not well-matched to the image, or $\vec{x}_0$ is improperly centred, the series will require many more shapelet coefficients to capture similar shape information.

In this section, we shall first use some properties of polar shapelets to describe the effect that these choices have on the shapelet decomposition. We shall then demonstrate how $n_{\max}$, β and $\vec{x}_0$ may be chosen with a practical algorithm to optimise image reconstruction.

4.5.2 Radial profiles

Our discussion may be simplified by initially considering an object with concentric and circular isophotes. This can be parameterized purely by its radial profile and thus re-

$$
\begin{aligned}
\chi_{0,0}(r) &= \frac{1}{\beta\sqrt{\pi}}\, e^{\frac{-r^2}{2\beta^2}} \\
\chi_{2,0}(r) &= \frac{-1}{\beta\sqrt{\pi}} \left[1 - \frac{r^2}{\beta^2}\right] e^{\frac{-r^2}{2\beta^2}} \\
\chi_{4,0}(r) &= \frac{1}{\beta\sqrt{\pi}} \left[1 - 2\frac{r^2}{\beta^2} + \frac{1}{2}\left(\frac{r^2}{\beta^2}\right)^2\right] e^{-r^2/2\beta^2} \\
\chi_{6,0}(r) &= \frac{-1}{\beta\sqrt{\pi}} \left[1 - 3\frac{r^2}{\beta^2} + \frac{3}{2}\left(\frac{r^2}{\beta^2}\right)^2 - \frac{1}{6}\left(\frac{r^2}{\beta^2}\right)^3\right] e^{-r^2/2\beta^2} \\
\chi_{8,0}(r) &= \frac{1}{\beta\sqrt{\pi}} \left[1 - 4\frac{r^2}{\beta^2} + 3\left(\frac{r^2}{\beta^2}\right)^2 - \frac{2}{3}\left(\frac{r^2}{\beta^2}\right)^3 + \frac{1}{24}\left(\frac{r^2}{\beta^2}\right)^4\right] e^{-r^2/2\beta^2} \\
\chi_{10,0}(r) &= \frac{1}{\beta\sqrt{\pi}} \left[1 - 5\frac{r^2}{\beta^2} + 5\left(\frac{r^2}{\beta^2}\right)^2 - \frac{5}{3}\left(\frac{r^2}{\beta^2}\right)^3 + \frac{5}{24}\left(\frac{r^2}{\beta^2}\right)^4 + \frac{1}{120}\left(\frac{r^2}{\beta^2}\right)^5\right] e^{-r^2/2\beta^2}
\end{aligned}
$$

Table 4.1: The first few rotationally-invariant ($m = 0$) polar Shapelet basis functions.

duces the task to a one-dimensional problem. It also creates obvious symmetries which simplify the selection of β. Averaging an object's surface brightness $f(\vec{x})$ in concentric rings about its centre gives its *radial profile*

$$\overline{f}(r) = \frac{1}{2\pi} \int_0^{2\pi} f(r,\theta)\, \mathrm{d}\theta \,. \tag{4.76}$$

If the object has been decomposed into polar shapelets as in equation (4.15), it is easy to show that it can be written as

$$\overline{f}(r) = \sum_n^{\text{even}} f_{n0}\, \chi_{n0}(r) \,. \tag{4.77}$$

This simple expression results from the fact that only the $m = 0$ states are invariant under rotations. Computing the object profile in polar shapelet state is very simple as it amounts to summing over $m = 0$ states, which reduce to

$$\chi_{n0}(r) = \frac{(-1)^{n/2}}{\beta\sqrt{\pi}} L_{\frac{n}{2}}(r^2/\beta^2) e^{-r^2/2\beta^2} \,, \tag{4.78}$$

where n is even and $L_q(x) = L_q^0(x)$ is a Laguerre polynomial.

Real galaxies tend to have similar and well-defined radial profiles. A good fit for spiral galaxies is obtained with the exponential profile, $f(r) \propto e^{-r/r_0}$, where r_0 is a characteristic radius. The de Vaucouleurs profile $f(r) \propto e^{-(r/r_0)^{0.25}}$ provides a good fit to elliptical galaxies. Figure 4.6 shows the radial reconstruction of an exponential profile, by numerically calculating the integral in equation (4.15). The top panel shows the reconstruction for several values of the shapelet scale β, in units of r/r_0. In all cases, only states with $n \leq n_{\text{max}} = 20$ were used in the reconstruction.

As can be seen in figure 4.6, the quality of the reconstruction depends upon the choice of β. For small values ($\beta \lesssim 0.4 r_0$) the reconstruction is oscillatory and cuts off

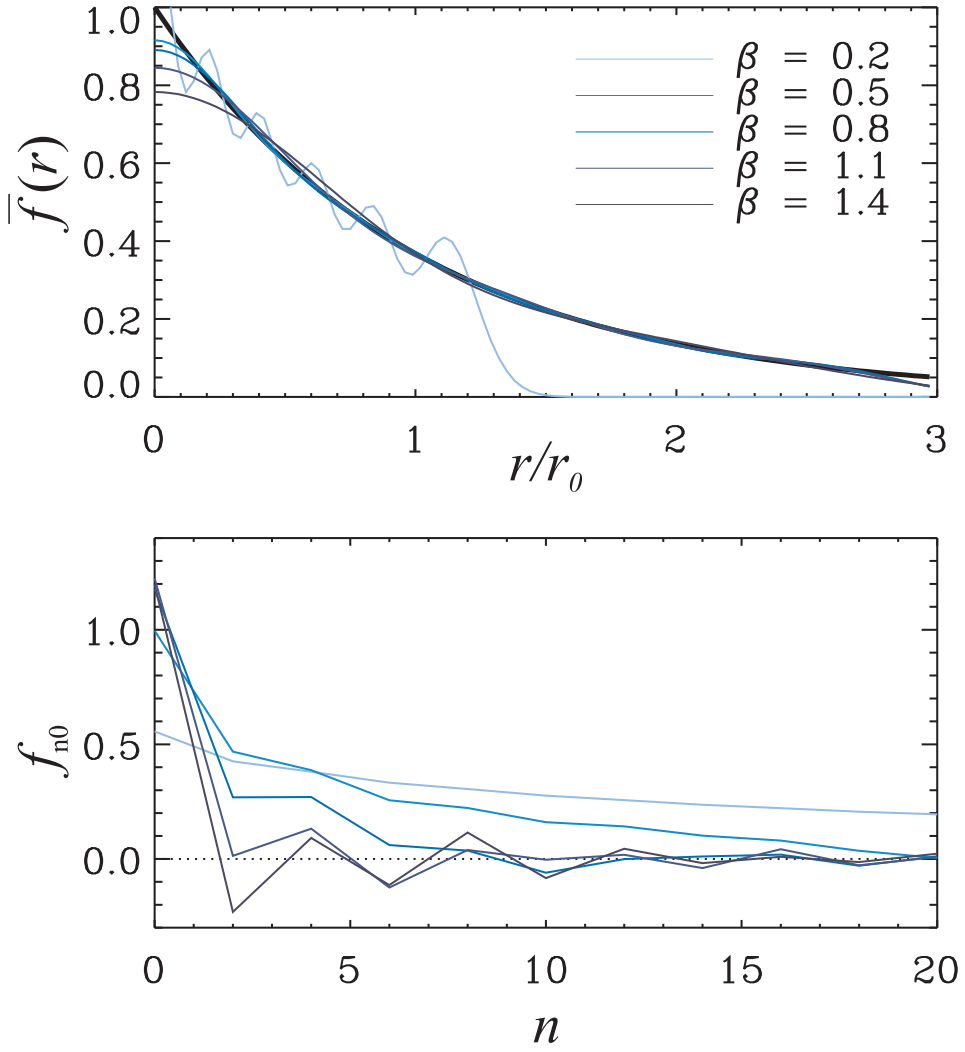

Figure 4.6: Decomposition of an exponential profile into radial polar shapelets. Top panel: The thick dark line shows the input exponential profile. The reconstructed profile is shown for different values of the shapelet scale β with $n_{\max} = 20$. Bottom: the corresponding shapelet coefficient profile f_{n0} vs shapelet order n.

the profile at large radii ($r \lesssim 1.5r_0$). For large values ($\beta \gtrsim 0.8r_0$), the reconstruction fails to reproduce the cusp at small radii ($r \lesssim 0.4r_0$) and exceeds the true profile at $r \simeq 0.6r_0$. This excess or truncation of the wings is due to an unfortunate mis-match in the profiles of typical galaxies and these useful basis functions. The ringing, particularly at low β, is an inevitable consequence of using a complete basis set rather than an over-complete one. In this regime, a shapelet decomposition of a spiral galaxy will involve the subtraction of one relatively large shapelet coefficient from another. However, for intermediate values ($0.5r_0 < \beta < 1.1r_0$), the reconstruction is good throughout the range $0.1r_0 \lesssim r \lesssim 2.8r_0$. This range can of course be expanded by including shapelets of higher orders. As $n_{\max} \to \infty$, the input model can be recovered with arbitrary precision.

We return to the case of real (non-concentric) galaxies in figure 4.7, which shows a

spiral galaxy from the HDF. Its spiral arms make fitting a de Vaucouleurs profile troublesome, but r_0 is approximately 12 pixels. The left-hand column shows the increasing complexity of a shapelet model with increasing $n_{\max}$. In this column, β is allowed to vary in order to minimise the least-squares difference between the model and the HDF image, shown at the bottom. Notice in particular the rotation in the object's core ellipticity, as more shapelet coefficients resolve the spiral arms ($2 \leq n_{\max} \leq 8$). KSB's ellipticity measurement would be equivalent to that from the decomposition with $n_{\max} = 2$, however this ellipticity is not well determined! The middle column shows shapelet decompositions with varying β, but fixed $n_{\max} = 20$. Their residuals are plotted in the right hand column. As in figure 4.6, we find that the best overall image reconstruction uses $0.5r_0 \lesssim \beta \lesssim 0.7r_0$. This is perhaps at the low end of the range suggested by figure 4.6 because of the extra high-frequency detail that needs to be modelled within the spiral arms.

4.5.3 Shapelet spectrum

The corresponding behaviour in shapelet space is apparent in the bottom panel of figure 4.6. The $f_{n,0}$ coefficients can be thought as the 'profile' of the galaxy in shapelet space or 'shapelet spectrum'. For low values of β the shapelet profile is very flat, showing that the power is distributed almost evenly throughout all orders. For $\beta = 0.5r_0$, the coefficients $a_{\mathrm{n,m}}$ are seen numerically to be $\propto (n+1)^{-2}$. This steepness is vital to ensure the convergence of the galaxy shape estimators formed from series of shapelet coefficients in §4.3.4. Convergence is optimum at $\beta \approx 0.8r_0$, with $a_{\mathrm{n,m}} \propto (n+1)^{-2.5}$. For higher values of β, the signs of $a_{\mathrm{n,m}}$ begin to alternate, and the convergence of the absolute values falls below $\propto (n+1)^{-2}$ once more at $\beta \approx 1.1r_0$.

Thus we have found a fairly wide range of β values that produce a good shapelet reconstruction, with information suitably concentrated for the series in §4.3.4 to converge, and an acceptable value of $n_{\max}$ for practical computation. Of course, the convergence of the shapelet series is poor with values of β outside this range, and impractically large values of $n_{\max}$ would be required for faithful image reconstruction. We shall now explore practical ways to find β values that lie within this range, and to hone our choice towards the optimum value.

4.5.4 Optimisation methods in the literature

There exist several distinct philosophies in the literature for the practical selection of $n_{\max}$ and β in related methods. They differ both in the goals set for for an ideal decomposition and the way to achieve it.

- Shapelets I suggested a geometrical argument using θ_{min}, $\theta_{\max}$: the minimum (PSF or pixel) and maximum (entire image) sizes on which information exists. This

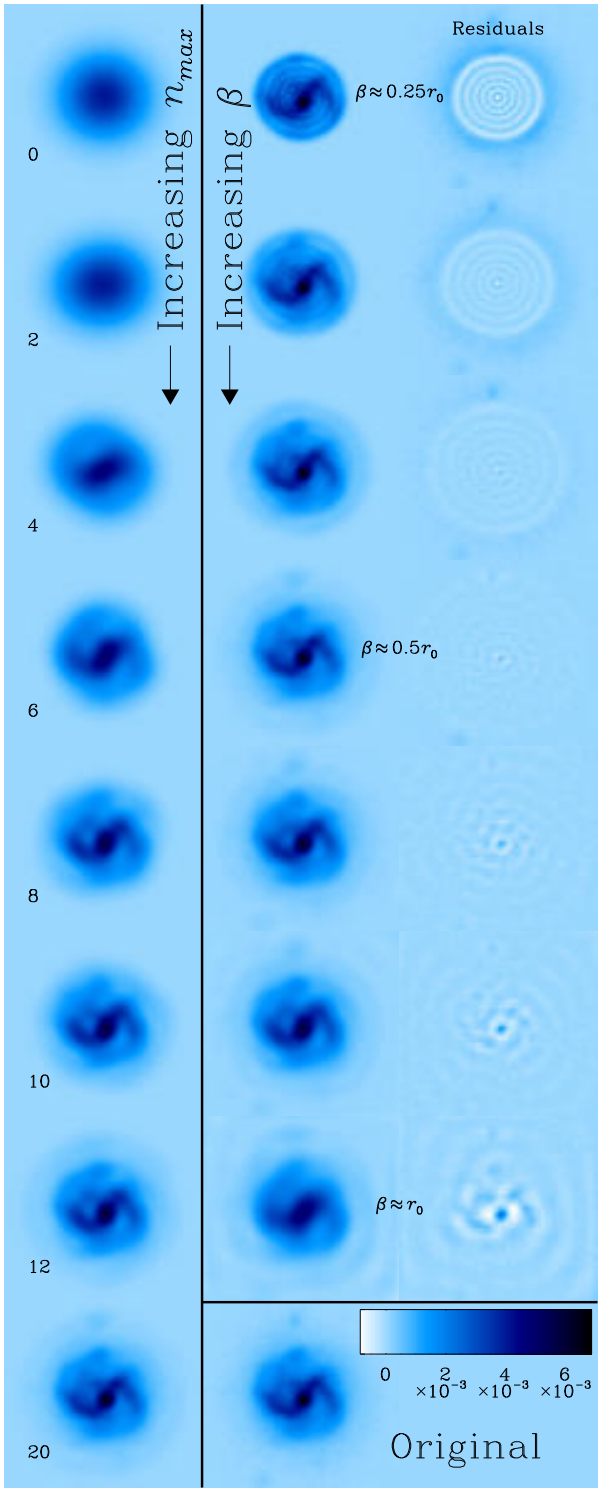

Figure 4.7: Shapelet decomposition of a real spiral galaxy in the HDF. The best-fit de Vaucouleurs profile has $r_0 \simeq 12$ pixels. The left hand column shows the shapelet model building up in complexity with increasing $n_{\max}$. For each of these, β is varied to minimise the least squares difference between the data and the model. The two right hand columns show the effect of varying β with fixed $n_{\max} = 20$. The residual between these models and the original, in the bottom-right, is smallest with $\beta \simeq 0.5 r_0$.

could be iterated using functional rules on $\vec{x}_0$ and r_f^2 as defined by shapelet coefficients. However, the coefficients change as a function of $n_{\max}$; nor is it clear what the rules should be.

- Van der Marel & Franx (1993) fit 1D Gauss-Hermite polynomials to spectral lines. They arbitrarily fix $n_{\max} = 6$, finding this sufficient probably because their spectra have relatively high S/N and the lines a nearly Gaussian profile. $\vec{x}_0$ and β are obtained from a best-fitting Gaussian. This also determines a_0 and in 1D is equivalent to constraining $a_1 = a_2 = 0$, *i.e.* the derivatives of the Gaussian with respect to $\vec{x}_0$ and β. The number of variables is reduced and the problem rendered tractable. Unfortunately, this does not help us in 2D because while both $a_{1\pm1}$ can be forced to zero by varying $\vec{x}_0$, no unique recipe can be found for setting the three $n = 2$ states using only one value β.

- Van der Marel et al. (1994a,b) relax the constraint on a_1. This is an improvement since a_1 is only the first term of an expression for the centroid, expanded using *all* odd a_n in equations (4.46) and (4.47). Without the higher order corrections, the true object centroid is moved slightly from the origin: amongst other things rendering rotations and shear operations more complicated. Instead, they set $\vec{x}_0$ from theoretical rest wavelength of a line. Unfortunately, astrometric calibration clearly cannot be done with such accuracy. Nor has the $n = 2$ problem been solved.

- Kaiser, Squires & Broadhurst (1995) combine fitting with a stand-alone object detection algorithm, HFINDPEAKS. Translated into shapelet language, their approach is roughly equivalent to placing $\vec{x}_0$ at data peaks then fitting a 2D Gaussian with width β such that S/N ν in a_{00} is maximised.

- Bernstein & Jarvis (2002) propose a similar approach. They prescribe β by requiring $a_{20} = 0$, while moving $\mathbf{x}_0$ to ensure $a_{1\pm1} = 0$. Higher coefficients are then determined afterwards by linear decomposition. To first order, the β constraint is equivalent that for HFINDPEAKS. This may indeed be the optimal decomposition for weak lensing as the shear signal in the quadrupole moments gets concentrated into just one number. a_{22} elegantly happens to be $\propto \gamma$, and automatically has maximum S/N for shear measurement after PSF deconvolution. However, a predisposition towards particular states for one purpose often leads to poor overall image reconstruction, so this is not necessarily ideal for all applications.

- Marshall (in prep.) describes a fully Bayesian approach to applying the shapelet transform in the context of image reconstruction. Here, $\vec{x}_0$, β and $n_{\max}$ are varied in order to maximise the evidence (the probability of observing the data, marginalised over all shapelet coefficients). At high S/N, this method gives a value of β which approaches the same as that from our χ^2 method below, but otherwise tends to

prefer a fractionally larger β, conservatively eliminating some 'noise' in favour of a smoother image reconstruction. However, this is computationally slow, a serious issue when analysing several thousand galaxies in a catalogue.

4.5.5 Minimising χ^2 of image reconstruction

Our solution to the problem of n_{max}, β selection is to optimise overall image reconstruction, as defined by reduced χ^2. This is ideal for many applications, including accurate PSF deconvolution. However, it unavoidably dilutes information content between more coefficients than the methods of KSB and BJ02. Fortunately, the power of shapelets is that these additional coefficients really do exist. As shown in Shapelets I §3.4, uncorrelated and unbiased pixel noise becomes white noise in shapelet space, evenly spread between the coefficients, so it is indeed feasible to try to extract signal from them all. For example, after combining information from higher-order coefficients, our approach can not give a worse shear measurement than KSB, although it can be better: particularly for higher S/N objects. Image reconstruction with our method is also demonstrably better than other techniques. Our least-squares fitting of shapelet basis functions is therefore more than a simple recovery of old ideas. Rather than maximising the density of information *ad hoc*, we instead seek to maximise the total *quantity* of information.

An example of χ^2 contours in the β *vs* $n_{\max}$ plane, is shown in figure 4.8. The horizontal trough is typical for all galaxies, although with varying levels of noise. There is an optimum β for image reconstruction, decreasing slightly as more coefficients are added, but roughly independent of $n_{\max}$. The reconstruction improves to arbitrary precision as $n_{\max} \to \infty$. However, not all of these coefficients are significant, and computation speed (as well as data compression) is increased dramatically with truncation in $n_{\max}$. A decomposition with $\chi^2_r = 1$ is sufficient to model the object while smoothing over and removing any observational noise. We therefore search $\{\mathbf{x}_0, \beta, n_{\max}\}$ space with goals of:

$$\frac{\mathrm{d}\chi^2}{\mathrm{d}\beta} = 0 \,, \tag{4.79}$$

$$\vec{x}_c = 0 \,, \tag{4.80}$$

and

$$\chi^2_r = 1 \text{ or flattens out } \frac{\mathrm{d}\chi^2_r}{\mathrm{d}n_{\max}} < \sigma\left(\chi^2_r\right) \simeq \sqrt{\frac{2}{n_{pixels}}} \tag{4.81}$$

These determine the centre and size of the basis functions which achieve a suitable image reconstruction using as few parameters as possible. The first constraint ensures that the scale β is well-matched to the image, and that $n_{\max}$ can be small. The second constraint gets the centre of the basis functions correctly on the centre of the image, where $\vec{x}_c$ is defined as a sum of shapelet coefficients in equations (4.46) and (4.47). The third constraint guarantees that sufficient coefficients are included, but not too many. Equa-

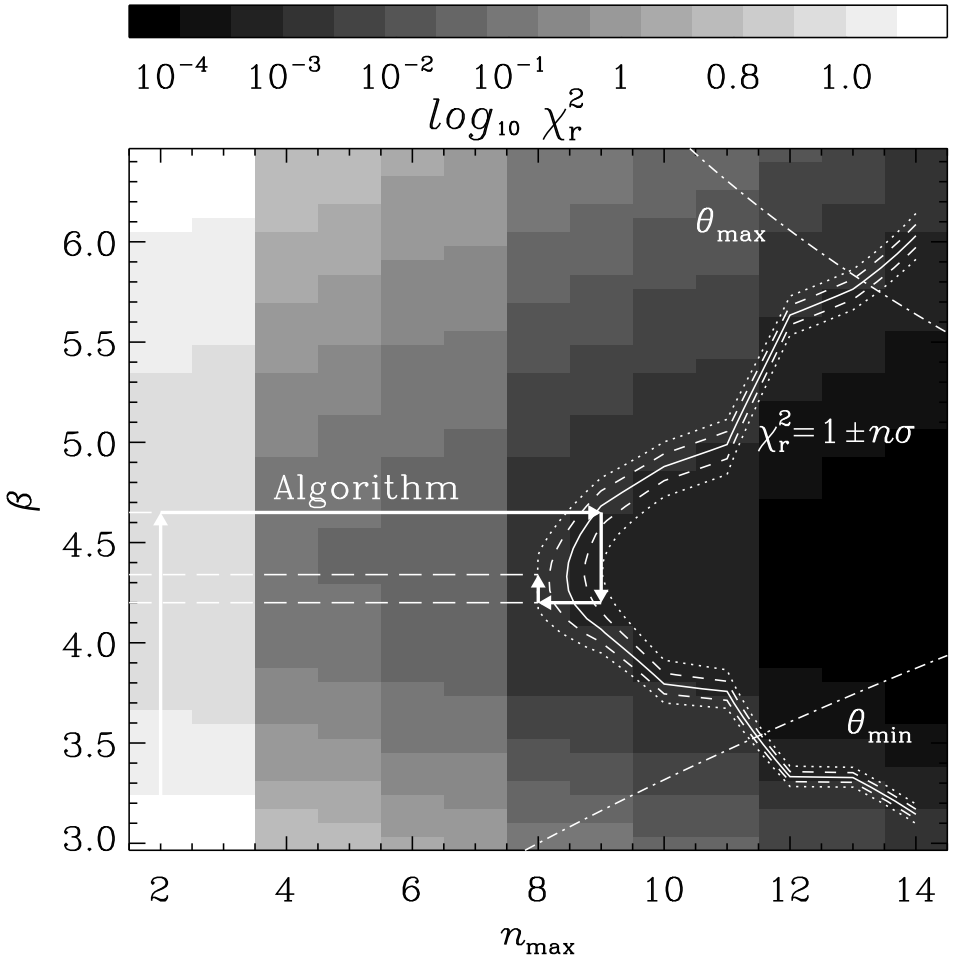

Figure 4.8: χ^2 contours on a β *vs* $n_{\max}$ plane for an elliptical galaxy in the HDF with medium S/N. The roughly horizontal trough is very typical. The arrows show individual steps (each containing several sub-steps) made by our optimization algorithm. Also shown are geometrical $\theta_{min}, \theta_{\max}$ constraints and the target $\chi^2_r = 1$ contour.

tion (4.81) also includes a flatness condition, which is particularly important for galaxies with a near neighbour or for some noisy objects. In these cases, adding extra shapelet coefficients may not significantly improve a fit; so the series is truncated early.

4.5.6 A practical implementation

The simultaneous implementation of these three constraints is numerically non-trivial because it requires both minimisation (in the β direction) and root finding (in the $n_{\max}$ direction), in a space with one axis inherently discrete. This section describes code that we have devised to do this. Its stepwise approach iterates towards the optimal solution, and is demostrated in figures 4.8 and 4.9.

SExtractor outputs (Bertin & Arnouts 1996) are used to make an initial guess at the centre $\vec{x}_0$ and size β to be used for the shapelet decomposition. The process is stable with respect to these choices, within reasonable limits. We initially set $n_{\max}$=2 to perform

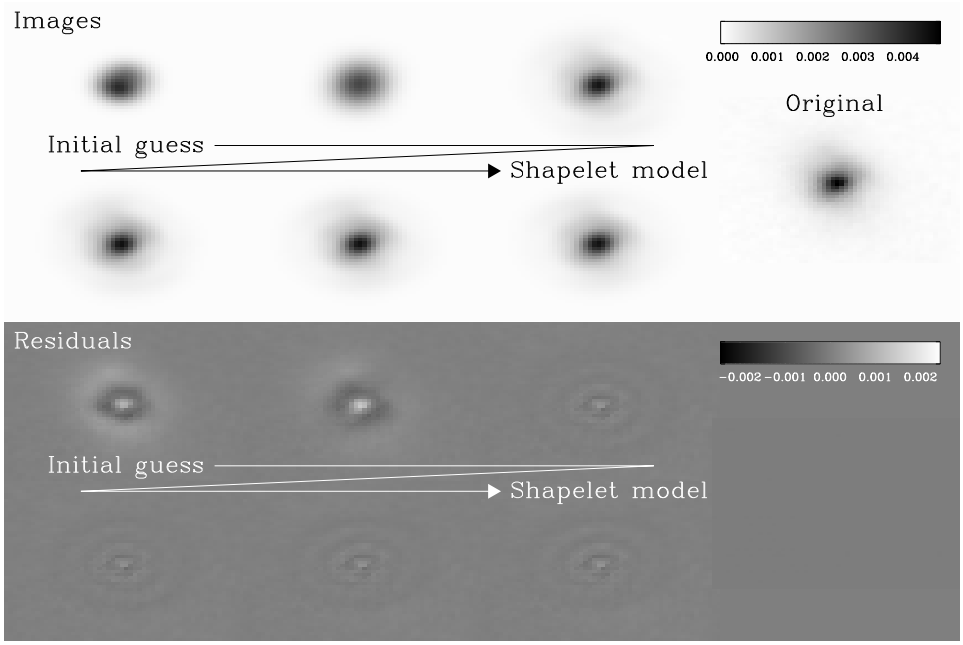

Figure 4.9: Shapelet decomposition of object in figure 4.8. Images are shown corresponding to the shapelet decomposition at all the vertices along the path taken by our algorithm.

a quick first iteration.

Firstly, β is quickly varied at $n_{\max} = 2$ to minimise χ^2 using a 1D version of the Numerical Recipes AMOEBA routine: vertically in figure 4.8. During each step of the iteration, the centroid is simultaneously shifted to re-zero series (4.46) and (4.47) in the shapelet coefficients. Since the calculation of the centroid is independent of β for isolated objects (see §4.3.5), this part of the interation is both very stable and very fast. Figure 4.8 also shows the additional geometrical constraints of $\theta_{min} > 0.2$ pixel and $\theta_{\max}$ not falling off the edge of the postage stamp. These act as hard boundaries to the region of parameter space which the iteration is allowed to explore.

Secondly, $n_{\max}$ is increased until criterion (4.81) is satisfied: horizontally in figure 4.8. This is done in steps of two and then fine-tuned at the end. Of course, if two values of $n_{\max}$ fall within the allowed limits, the lower value is taken. After this, if the object warranted more coefficients than the initial guess of $n_{\max} = 2$, β and $\vec{x}_0$ are again readjusted at the new $n_{\max}$. The process then repeats another $n_{\max}$ search, starting back at $n_{\max} = 2$ and increasing again in steps of two. The algorithm terminates when either of these processes return to the same value as they started, with all three criteria (4.79) to (4.81) being met. On trial data, the algorithm has a ∼86% convergence rate, with many of the remainder being either close galaxy pairs or false-positive SExtractor 'detections' of noisy garbage. These objects are flagged and excluded — with a selection function roughly independent of magnitude. Depending upon the complexity of the galaxy involved, our algorithm takes up to ∼ 1s on a 1Ghz PC.

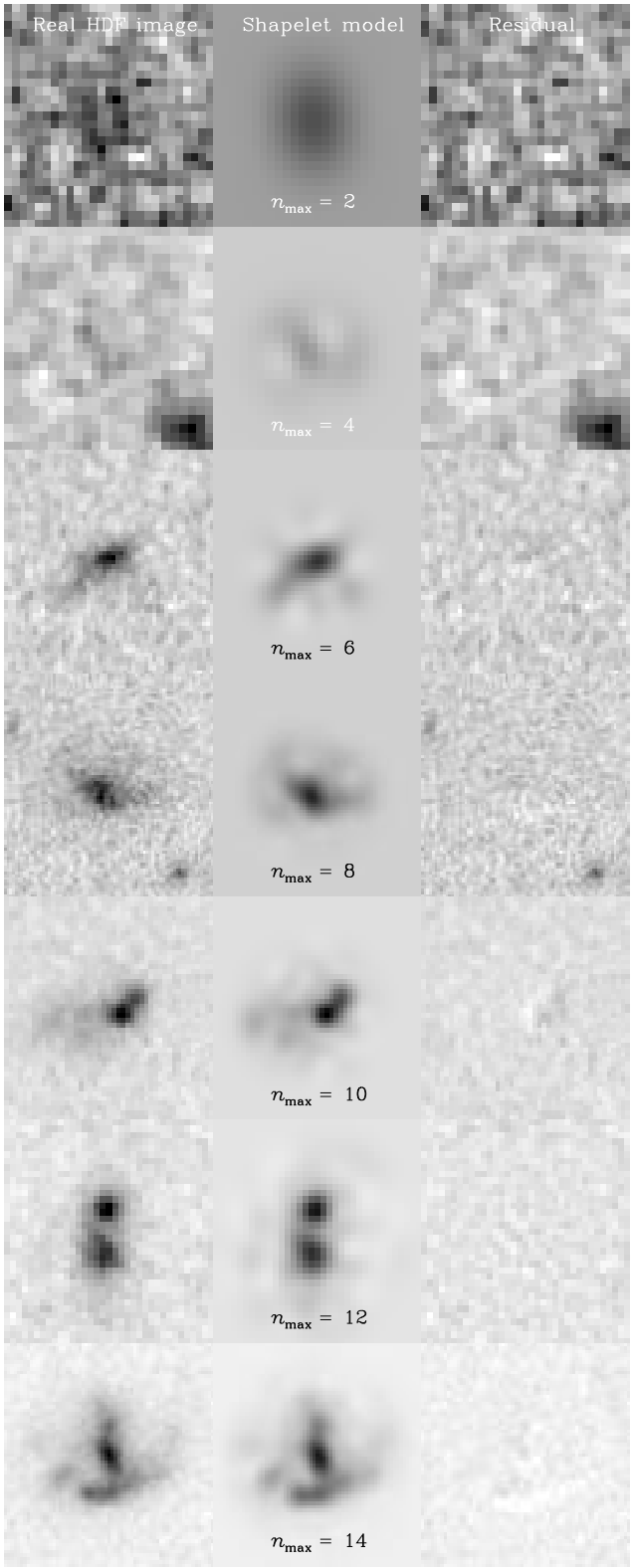

Figure 4.10: Shapelet modelling of a selection of HDF I-band galaxies. Higher S/N galaxies typically require more shapelet coefficients so we display a variety of source galaxies, noting the shapelet $n_{\max}$ required to reach a reconstruction with $\chi^2_r = 1$. In all cases, the first column shows the original HDF image; the middle column shows the shapelet model; the right column shows the residual. The image size and colour scale is different for each row.

4.5.7 Performance

We have described an algorithm to first detect objects within an image using SExtractor, then to optimise the shapelet parameters β, $n_{\max}$ and $\vec{x}_c$ for reconstructing each object. The algorithm produces a final catalogue of shapelet decompositions for ~ 500 objects per square arcminute in the HDFs. This is 81% of the 'objects' initially detected by SExtractor. The iteration fails to converge to $\chi^2_r \leq 1$ for 42 close galaxy pairs (identified from a segmentation map), 36 objects because of their proximity to bright stars or to the edge of the image, and 60 more objects across the HDFs. These are mainly false detections of noise due to the low initial S/N detection threshold set for SExtractor (see section §4.4.2). Note that the number of decompositions which fail as close galaxy pairs is roughly independent of magnitude. In fact, the slope of the number counts for galaxy pair members is within 1σ of that for all the galaxies in the HDF. This is important, in order to avoid problems in the next chapter.

Figure 4.1 displays a selection of bright HDF galaxies successfully modelled using shapelets, and figure 4.10 displays another selection at various levels of S/N. Achieving a faithful reconstruction of the images, allowing for the local background noise level, requires an $n_{\max}$ of only 2, 3 or 4 for faint galaxies. Brighter or larger objects, which contain more detail, require an increasing number of shapelet coefficients; although nothing more than $n_{\max} = 20$ is required for all HDF objects. The right-hand column of figure 4.10 shows the reconstruction residuals, which are consistent with noise even for irregular galaxy morphologies.

The smooth, analytic shapelet models can be easily transformed in shapelet space, to implement many common astronomical tasks. Rotations, enlargments and translations can all be performed with simple combinations of quantum mechanical $\hat{a}^\dagger$ and $\hat{a}$ ladder operators acting upon coefficient vectors $|n, m\rangle$. PSF convolution and deconvolution is also possible via an analytic bra-ket matrix multiplication.

Linear combinations of shapelet coefficients can be formed to describe the size, brightness and morphology indices of an object. The reliability of these shapelet-based estimators is shown by a comparison with the equivalent SExtractor measurements of HDF galaxies in figure 4.11. In performing the shapelet decomposition of all these HDF galaxies, we have incidentally created a complete morphological catalogue of galaxy shapes at this depth. This catalogue will be of great use in the next chapter.

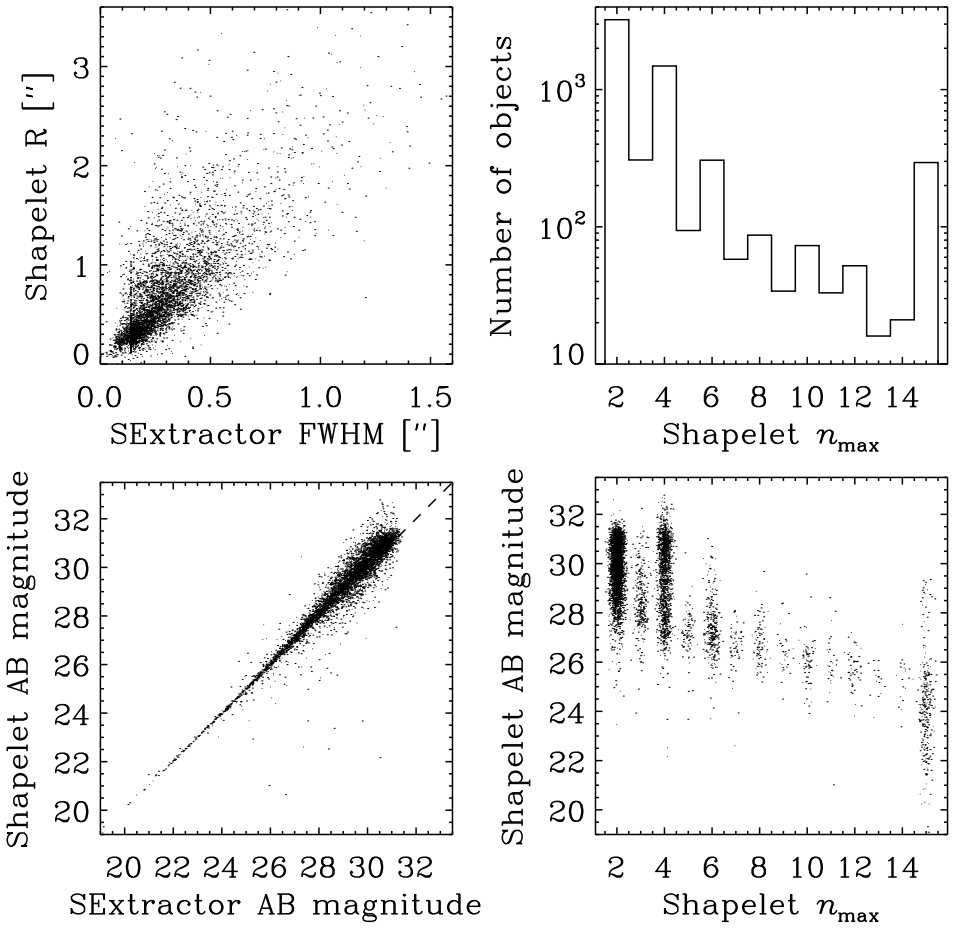

Figure 4.11: Recovery of objects from the HDF as shapelet parameters. Statistics are shown of the shapelet decomposition algorithm without PSF deconvolution, and various comparisons made with SExtractor measurements of the same objects. Points in the bottom-right plot have at random been slightly offset for clarity.

5

Simulations of astronomical images

5.1 The need for simulated observations

As astronomical surveys are growing in size and scope, so image analysis methods are increasing in complexity and accuracy. In order to calibrate these new methods, it is essential to have a large sample of images containing objects whose properties are somehow already known. Since all real data is subject to the uncertainties of observational noise, telescope aberration and seeing, several software packages have been developed to manufacture artificial images (*e.g.* SKYMAKER (see Erben *et al.* 2001) or ARTDATA in IRAF (Tody 1993)). The accuracy of image analysis methods can then be assessed by comparing their output to the known input image properties that were specified before the addition of such observational effects.

The image simulation packages currently available are particularly valuable for imitating deep ground-based data. However, they limit themselves to a representation of galaxies as parametric forms such as symmetric de Vaucouleurs or exponential profiles. Deep space-based images, on the other hand, contain many irregular or asymmetrical galaxies with complex resolved features such as spiral arms, mergers and dust lanes. One possibility for simulating space images, utilised by Bouwens, Broadhurst & Silk (1998), is to repeatedly reuse well-resolved galaxies from the Hubble Deep Fields (HDFs; Williams *et al.* 1996, 1998). However, this restricts us to morphology templates from a relatively bright and nearby sample. Fainter galaxies cannot be used because they have been significantly contaminated with background noise. Consequently, the morphological properties of the faint galaxy population are not fairly represented. This method also

faces the difficulty that the same real galaxies must be reused many times within one simulation. Although the HDFs are indeed very deep (I_{F814W}=27.60 at 10σ, Williams *et al.* 1996), they only cover a small area ($\sim$6 square arcminutes each) and contain a finite number of galaxies. Even if we were to source our real galaxies from larger surveys such as the Groth strip (Groth *et al.* 1994) or the Medium Deep Survey (Ratnatunga, Griffiths & Ostrander 1999), we would still face the difficulty of using particular real galaxies many times in a large simulation.

In this chapter, we present a method for simulating deep images that contain genuinely unique objects, yet replicate the morphological distribution of galaxies in the HDF at all depths. This method has the advantage of allowing us to simulate arbitrarily large, deep surveys with no repetition of galaxy shapes. It also allows us to know accurately the intrinsic properties of each galaxy, before adding telescope-specific noise properties, systematic effects and convolution with a Point-Spread Function (PSF).

Our method is to first decompose all objects in the HDFs into shapelet parameterizations. Using just a few coefficients, these can completely quantify the shape properties of all galaxies, including spiral arms, bars and arbitrary radial profiles. We then model their distribution of shapelet coefficients, and draw from this probability distribution new sets of shapelet coefficients, representing new galaxies. In particular, we take into account the covariance between shapelet coefficients so that, for example, shapes depend upon magnitude and size (*e.g.* faint galaxies appear more irregular than bright ones). In this method, we therefore do not input any model of physical morphology or evolution. Rather, we exclusively use the measured statistics of the shapelet coefficient distributions from a real galaxy sample, as a function of magnitude and size. The new galaxy images can then be analytically convolved with any PSF, pixellated, and given an appropriate amount of noise for any exposure time down to the depth of the HDF.

These simulations have several significant applications. We can use them to calibrate the effectiveness of image analysis and detection methods such as SExtractor (Bertin & Arnouts 1996), IMCAT (Kaiser, Squire & Broadhurst 1995), GIM2D (Simard 1998), GALFIT (Peng *et al.* 2002) and wavelet routines (*e.g.* Meyer 1993). By examining the errors on shape measurement at various signal-to-noise levels of galaxy detection, we can also predict the precision of future experiments requiring accurate shape measurement. In chapter 6, this technique will be applied to a proposed cosmic shear survey from space.

5.2 Image simulation with shapelets

5.2.1 Generation of a source catalogue and treatment of the PSF

The first step in our method is to detect and model HDF galaxies as shapelets, through the procedure described in chapter 4.

The algorithm creates a catalogue of optimised shapelet decompositions for ~ 500 objects per square arcminute in the HDFs. However, this represents only 81% of the 'objects' initially detected by SExtractor. Approximately two dozen of the brightest galaxies require a decomposition with $n_{\max} > 15$. To simplify later analysis, these are prematurely truncated at this point, with $\vec{x}_0$ and β chosen to give the best possible, if slightly imperfect, shapelet fit. The iteration also fails to converge to $\chi^2_r \leq 1$ for a further 42 close galaxy pairs (identified by the SExtractor segmentation map); 36 objects because of their proximity to bright stars or the edge of the image; and 60 more objects across the HDFs, which are mainly false detections of noise due to the low S/N detection threshold set for SExtractor (see section §4.4.2). Note that the number of decompositions which fail as close galaxy pairs is roughly independent of magnitude. Indeed, the slope of the number counts for galaxy pair members is within 1σ of that for all the galaxies in the HDF.

We shall later require a parametrized catalogue of real galaxy morphologies. During the modelling of the HDF galaxy shapes, we must in general account for the PSF of the WFPC2 camera which has smeared the images. Since our objective here is to simulate only HST images, we do not correct for the PSF. It is naturally contained within the shapelet models of the galaxy images and intentionally left unaltered. Our simulated images will end up being automatically smeared by the WFPC2 PSF, effectively circularised because of the random reorientation of new galaxies.

For other applications, including the simulations described in chapter 6, it may be desirable to simulate observations from other telescopes such as the JWST (`http://www.stsci.edu/ngst/`), SNAP (`http://snap.lbl.gov/`) or GAIA (`http://astro.esa.int/gaia/`). It would then be necessary to take account of their different instrumental properties. The ideal way to do this would be to deconvolve HDF galaxies from the WFPC2 PSF analytically in shapelet space (see Shapelets II §3), and then to reconvolve simulated galaxies with a new PSF at the end. Unfortunately, we have found this method difficult to implement in practice. The process of deconvolution naturally pushes information into high-n and m shapelet coefficients, as shown in Shapelets I figure 8. Although the ensuing galaxy reconstructions are still realistic, information about the overall galaxy morphology distribution is spread thinly over an increased number of coefficients. This distribution is no longer sufficiently well sampled by galaxies in the HDFs for the smoothing-and-resampling method presented in §5.2 to be effective.

An alternative solution exists to simulate images with a PSF of the same size or larger than that of HST. The WFPC2 PSF can be conveniently maintained throughout the simulations, and the images convolved again at the end with a second, 'difference' kernel. This kernel is intended to make up the difference between the original PSF of WFPC2 and that of the new instrument. It can be obtained by deconvolving the WFPC2 PSF from the new PSF, an operation performed easily in shapelet space (see Shapelets II §3). This is the technique that will be used in chapter 6.

5.2.2 A Tuning Fork in multi-dimensional shapelet space

A sample of galaxy morphologies can be thought of as a distribution of points in a multi-dimensional shape parameter space. This is illustrated by the cartoon in figure 5.1. The axes in this space might represent size, magnitude, position angle (P.A.) and so on. Each point corresponds to a particular galaxy with a specific morphology, and various correlations may emerge between variables. For example, the classic Hubble tuning-fork diagram (Hubble 1926, Sandage 1961, de Vaucouleurs 1959) relates the object ellipticity, the bulge/disc ratio, and the extent to which the spiral arms are unwound. GIM2D (Simard 1998) and GALFIT (Peng 2002) software use axes parametrized by the relative amounts of exponential or de Vaucouleurs/Sérsic functions (de Vaucouleurs 1959, Sérsic 1968) required to fit the galaxy's radial profile.

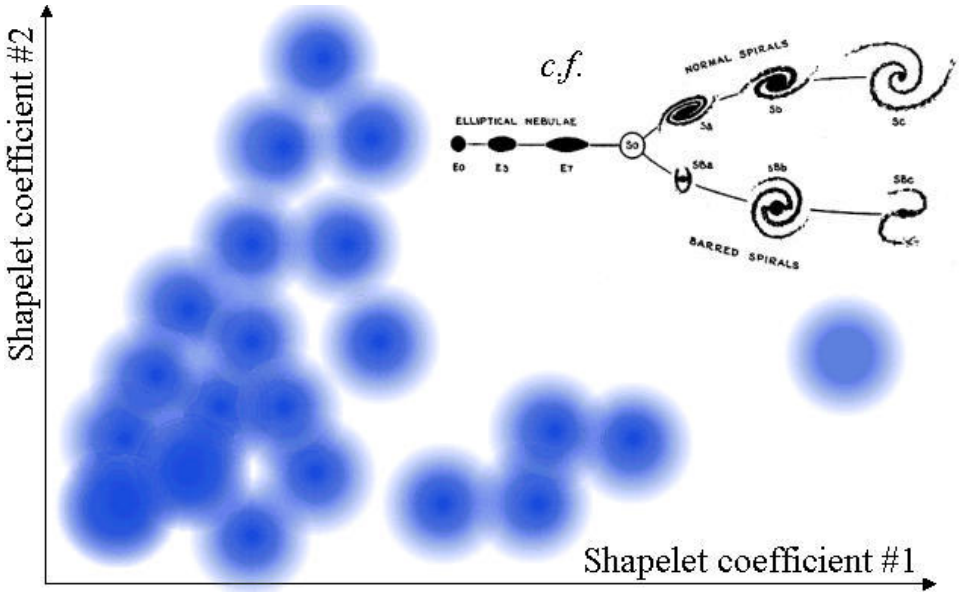

Figure 5.1: Idealised representation of a slice through shapelet morphology parameter space, where each dimension corresponds to a shapelet coefficient. The points represent the position of an observed HDF galaxy in shapelet space. Their distribution encode the underlying morphology distribution of real galaxies, like a multi-dimensional Hubble sequence. This morphology distribution can be smoothed and resampled to generate an unlimited number of unique, yet realistic galaxy shapes for the image simulations.

In this thesis, we shall instead choose the axes of our galaxy morphology distribution to be the magnitudes and phases of the (complex) polar shapelet coefficients. We shall first describe the properties of this "shapelet parameter space". In section §5.2.3, we shall then argue that the underlying Probability Density Function (PDF) of galaxy morphology is relatively simple in this parameter space, and may be recovered from a finite sample of galaxies like those in the HDFs.

Projections of the shapelet parameter space onto various coefficient axes are shown in figure 5.2. Each point in the top-left panel represents a data vector encoding the shape

information about one HDF galaxy. Collectively, they describe the overall morphology distribution of distant galaxies. This distribution is shown, smoothed, in the top-right panel; the remaining panels show other projections. Notice that there are correlations evident in the parameters, which correspond to the construction of the familiar shapes of galaxies. In the bottom-right plot, for example, deviations from the diagonal show twisting isophotes that can grow, with higher order basis functions, into spiral arms. It is also important to notice that some regions of parameter space are empty. A random set of shapelet coefficients will not produce a realistic galaxy shape: there is not even a positive definite constraint imposed upon an image in the shapelet formalism.

Galaxies are all pre-rotated so that their a_{22} coefficient is aligned with the horizontal. They are also flipped, if necessary, so that the sign of the a_{42} phase is positive. This ensures that the outer isophotes of all objects twist in the same, anti-clockwise sense. Correlations between other shapelet coefficients are maintained in order to preserve the morphology of the galaxy. This process considerably compresses parameter space, without loss of information. Any two well-sampled objects, which are identical apart from their orientation or handedness, will now decompose into identical shapelet coefficients. This increases the sampling density of parameter space, allowing it to be better populated wuth only a finite number of source galaxies. When new, simulated galaxies are created, they will be randomly rerotated and half of them will be flipped back.

Two other axes are required for our parameter space, since real galaxy morphologies clearly vary as a function of size and magnitude (see *e.g.* figure 5.5). Storing the shapelet scale factor β separately allows large HDF galaxies to occupy different regions of parameter space to small ones. Similarly, using magnitude as another parameter allows galaxies of different luminosities to have different types of shape. The middle-left plot of figure 5.2 demonstrates that fainter galaxies can be more irregular, with a higher ellipticity dispersion. Since shapelet coefficients (including a_{00}) scale as the flux, once we include magnitude as an independent parameter, we can divide all a_{nm} coefficients by a_{00}. This removes explicit magnitude dependence from these quantities and coincidentally ensures a convenient version of adaptive smoothing at a later stage (see §5.2.4). The degenerate parameter $a_{00} = 1$ is now removed, and size and magnitude are treated in the same way as any other axis of the parameter space from now on.

Note that any orthogonal transformation of the shapelet basis functions would maintain their useful properties of completeness, orthogonality and Fourier transform invariance. For instance, Cartesian shapelets could be used instead. However, these would not permit the convenient factoring out of the object's orientation and handedness. Using Principal Components Analysis (PCA), it is possible to determine the set of axes that most compactly describe our galaxy population. However, both elliptical and spiral galaxy shapes are already quite simple to manufacture with only a few polar shapelet coefficients; we therefore avoid the extra complication of PCA in this thesis.

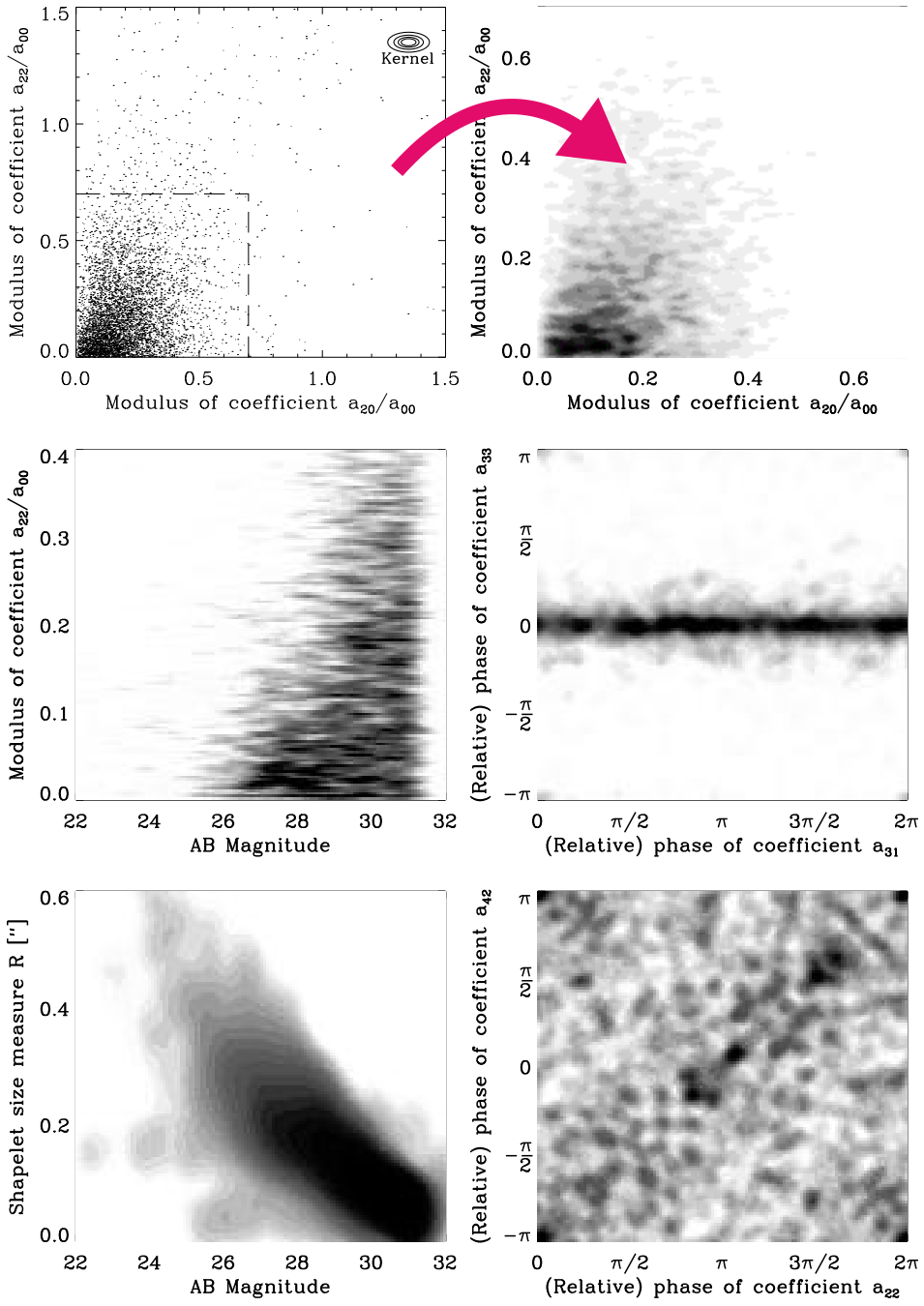

Figure 5.2: Phase space correlations and smoothing in the shapelet parameter space. The top left panel displays the position of measured HDF galaxies along two axes of shapelet space; the top right panel shows the probability distribution produced by smoothing this distribution. The other left panels display further projections of the PDF onto shapelet coefficient, size and magnitude axes, while the remaining right panels display phase correlations between shapelet coefficients. The colour scale is logarithmic in the bottom left panel.

5.2.3 Recovery of the smooth underlying PDF of galaxy morphologies

The top-left panel of figure 5.2 shows a slice through the parameter space of galaxy morphologies, populated by δ-functions representing real, observed shapes. Unlike a distribution parametrized simply by bulge/disc ratios and disc inclination angles, it is not obvious *a priori* that an underlying, smooth PDF should exist for galaxy morphologies in shapelet space. However, the compact shapelet representation of astronomical objects suggests that this ought to be the case, and we shall attempt to recover it by smoothing this parameter space.

Once the validity of the smoothed PDF has been established, it will be a simple matter to resample it and thus to synthesise a population of galaxies. Monte Carlo techniques can be used to generate unlimited numbers of realistic galaxies in this fashion, to fill any amount of sky area in a simulated imaging survey.

The remaining panels of figure 5.2 demonstrate that the parameter space is indeed smooth in those places where it is well sampled. We assume that some other regions are equally smooth, but poorly sampled because of the finite number of galaxies in the HDF. We note that voids are also expected in the parameter space, where the shapelet expansions do not correspond to realistic galaxy shapes. We shall therefore be careful not to smooth the PDF with large smoothing lengths which would significantly encroach upon these voids. However, limited perturbations around HDF galaxies may indeed recover realistic morphologies.

Without an explicitly physical model of galaxy morphology and evolution built in to shapelets, it is the final results that must provide the ultimate verification of our statistical method. In §5.2.4, we show that it is indeed possible to find a smoothing length for the PDF that recovers objects which appear to represent realistic shapes. In §5.3 we demonstrate quantitatively that their global properties are realistic, by comparing real and simulated populations of galaxies via morphology diagnostics commonly used on deep images.

5.2.4 Multivariate kernel smoothing method

Many practical approaches have been devised to smooth discrete samplings of a multivariate PDF. Our main constraint in selecting one of these methods is the very high dimensionality of our data set. The median $n_{\max}$ required for objects in the HDF is 4. However, even with the efficient data compression that shapelets can afford, models of the highest S/N galaxies use values for $n_{\max}$ as high as 15. Adding object size and magnitude, this corresponds to 137 total coefficients, and this is therefore the maximum number of dimensions required.

To smooth and resample this dataset, we have chosen the Kernel smoothing method which is eloquently reviewed by Silverman (1986). Kernel smoothing can be considered as an alternative to using histograms. It avoids the ambiguity of binning and instead

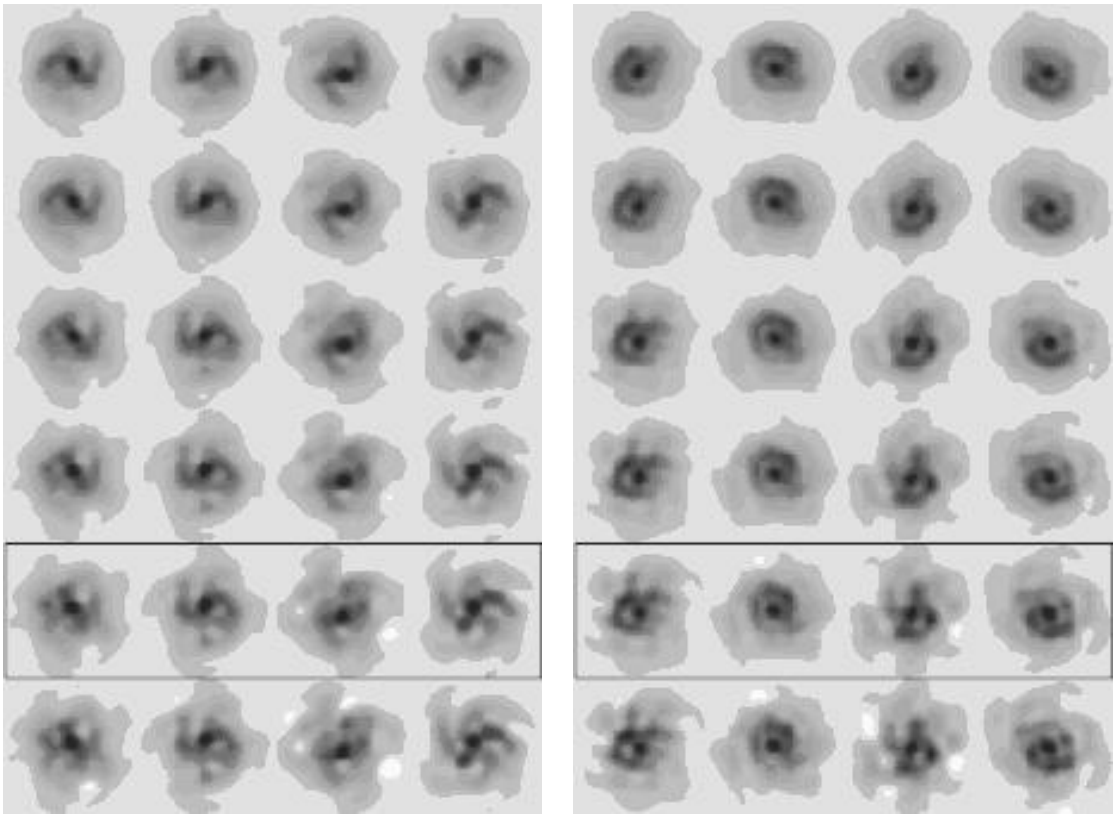

Figure 5.3: The effect of perturbing galaxy morphologies in shapelet space. Each image in the top row shows a real HDF galaxy, rotated by random angles. Its shapelet coefficients are incrementally perturbed in successive rows, although its overall flux is kept constant for the purpose of this plot. A degree of perturbation corresponding to our choice of the smoothing length λ_i is shown inside the box: these images represent typical simulated galaxies. Perturbations larger than λ_i produce objects which contain significantly negative pixel values. The left panel depicts a spiral galaxy; the right panel a more typical irregular form. The colour scale is logarithmic.

yields a smooth analytic curve. For one-dimensional data, each sample data point is replaced by a smooth Gaussian kernel. To create a PDF, all the kernels can be summed and then normalised to integrate to unity. The width of these smoothing Gaussians still remains to be decided, but methods exist for optimising this factor. Each kernel can even be given a different width, calculated as a function of a quick local density estimate, in order to produce adaptive smoothing.

In data with more than one dimension, each sample point is replaced by a multivariate kernel. To help overcome the difficulties associated with the leaking of probability density into the wings of many-dimensional kernels, we replace the Gaussian with a more compact *Epanechnikov* kernel (Epanechnikov 1969),

$$K(\delta x_i) = \begin{cases} \frac{3}{4\lambda_i}\left(1 - \left(\frac{\delta x_i}{\lambda_i}\right)^2\right) & \text{for } -\lambda_\mathrm{i} < \delta \mathrm{x_i} < \lambda_\mathrm{i} \\ 0 & \text{elsewhere ,} \end{cases} \tag{5.1}$$

where we have reformatted the shapelet coefficients of each HDF galaxy into a data vector x_i, and δx_i are deviations in shapelet space from these real data points. In each case, i is a coefficient index running from 1 to 137. λ_i are smoothing widths which will be determined for each direction of our PDF space in §5.2.5. Isodensity contours of this kernel are multivariate ellipses whose axes are aligned with those of the co-ordinate axes (see figure 5.2). In general, they could be allowed to point in any direction (Sain 1999), but we do not find this to be necessary.

We implement an adaptive smoothing of our PDF by reparametrizing a_{nm} as $\frac{a_{nm}}{a_{00}}$. Given a constant λ_i, this creates an effective smoothing kernel for each object of widths $\lambda_i' = a_{00}\lambda_i$. This functional form is useful because the brighter HDF objects are less frequent, and are therefore more isolated in probability space. Since a_{00} roughly correlates to total flux, we obtain a larger smoothing radius for brighter objects and better recover the underlying probability distribution. We shall prove that this recipe does produce realistic morphologies in §5.3.

5.2.5 Generation of a simulated galaxy catalogue

Having recovered a realistic and analytic PDF of galaxy morphologies, we now wish to resample this distribution to generate brand new galaxy populations. The main advantage of the kernel smoothing approach now becomes apparent. Without resorting to costly numerical integration, Silverman (1986) §6.4.1 presents a quick bootstrap method to generate a Monte-Carlo sample from a PDF constructed with δ-functions smoothed by kernels $K(\delta x)$. We take the following steps to simultaneously smooth and resample the parameter space of HDF galaxies

$$\left.\begin{array}{ll} \textit{Step } 1: & \text{R}\textit{andomly select one of the original HDF} \\ & \text{g}\textit{alaxies, uniformly and with replacement.} \\ \textit{Step } 2: & \text{G}\textit{enerate a small perturbation } \delta x_i \textit{ from} \\ & \text{t}\textit{he probability density function } K(\delta x_i). \\ \textit{Step } 3: & \text{A}\textit{dd } \delta x_i \textit{ to the shapelet coefficients } x_i \textit{ of} \\ & \text{t}\textit{he HDF galaxy. This simulates a new} \\ & \textit{galaxy, sampled from the overall PDF.} \end{array}\right\} \quad (5.2)$$

This approach is arrived at by simply regarding the PDF as a sum of small kernels rather than one overall function. Individually, these kernels are quick to compute; and the dimensionality of the PDF can even be lowered for faint objects that require fewer coefficients. The perturbations can be quickly sampled from an Epanechnikov kernel $K(\delta x)$ by generating three random numbers from a uniform probability distribution between $-\lambda_i$ and λ_i. If the first does not have the highest absolute value, take it and discard the rest; otherwise take the second. Iterating this procedure to generate sufficient objects for

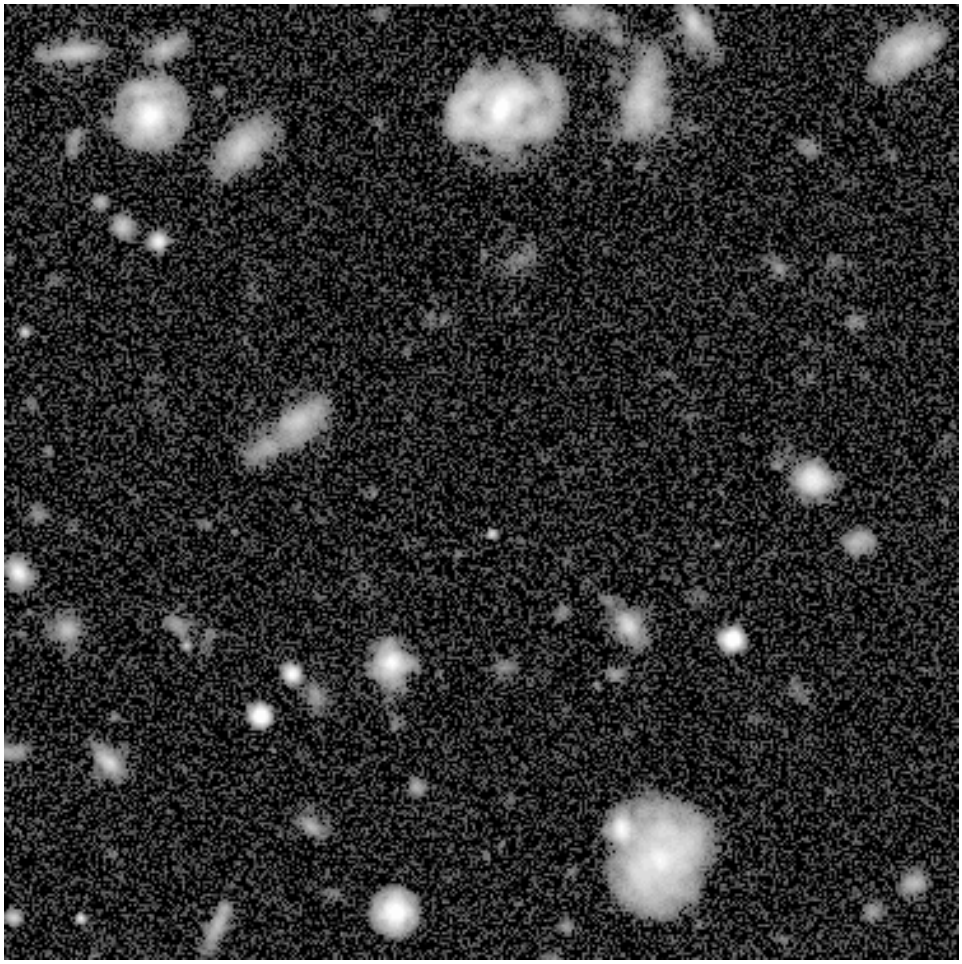

Figure 5.4: Sample HDF-depth simulated I-band image, $30'' \times 30''$.

a simulated Hubble Deep Field requires only a few minutes on a 1GHz PC.

We must now decide how to choose the overall smoothing length λ_i. If $\lambda_i \equiv 0$, the kernel is a δ-function and the original HDF objects are recovered exactly. This arrangement will create simulations of limited practical use, but in §5.3 they act as an intermediate test of the shapelet decomposition. As $\lambda_i \to \infty$, the coefficients for simulated galaxies become completely random and the objects become unrealistic. In this limit, since no positive-definite constraint is ever imposed in the shapelets formalism, we find that simulated objects exhibit undesirable holes of negative flux. Figure 5.3 shows realisations of how a typical galaxy from the HDF is altered by increasingly large perturbations to its shapelet coefficients, showing negative flux for large λ_i perturbations.

We therefore require a choice of λ_i which is sufficiently large to produce new galaxies, yet sufficiently small to maintain realistic morphological properties. By measuring the minimum pixel values of many different galaxy realisations, we find suitable results if $\lambda_{phase} \lesssim 15^\circ$ and $\lambda_{moduli} \lesssim 4\times$[mean separation between nearest neighbours in that dimension]; beyond these values, negative holes rapidly appear. For the purposes of this

paper, we therefore fix λ_i to these limiting values. This still represents relatively weak smoothing, but the variety and realism of generated morphologies is pleasantly surprising: polar shapelets are indeed sufficiently close to the Principal Components of galaxy morphology that small perturbations in shapelet space correspond to reasonable and realistic changes within galaxy types. A quantitative demonstration of these remarkable results is presented in §5.3.

5.2.6 Generation of images

A Monte Carlo population of genuinely new yet realistic objects has been extracted from the PDF of galaxy morphology. These galaxies are now allocated random orientations and locations on the sky, at a density of 700 per arcmin^2. This constant has been calibrated to recover the same total number counts, after the addition of noise, as are measured in the HDFs (see §5.3.1). No attempt is made here to correctly model the 2-point correlation function of galaxy positions, or to include galaxy mergers beyond those sufficiently advanced to appear as one object in the input SExtractor catalogue.

The correct slope in the size and magnitude distributions are automatically ensured over a wide range of validity, since size and magnitude are intrinsic variables of the PDF (see the bottom-left panel of figure 5.2). However, it is important to consider the question of completeness in our simulations for very faint galaxies. A discrepancy could arise through either non-detections of faint HDF galaxies by SExtractor or non-convergence of their shapelet decompositions. The first effect is minimised by our choice of SExtractor parameters (see §4.4.2) and the second is shown in §4.5.6 to be under control. However, the number counts of galaxies at the very faint end ($I \gtrsim 29$) are also highly sensitive to the the precise background noise properties (see §5.2.7). For this reason, we choose not to consider galaxies fainter than $I = 29$.

At the bright end, we also expect the simulations to be incomplete, since the HDFs were intentionally chosen by STScI as areas containing few large, bright galaxies. In the future, we shall extend our simulations in this respect by incorporating "Groth survey strip" (Groth *et al.* 1994) and ACS galaxies into the object source catalogue. One could also compensate for any known incompleteness by preferentially selecting for under-represented galaxy types in step 1 of procedure (5.2).

5.2.7 Modelling telescope and observational effects

The shapelet models of galaxy images are actually analytic functions. These can quickly be convolved with a PSF that has also been decomposed into shapelets, using the matrix operation in Shapelets II §3.1. Stars can also be included in an image, given a magnitude distribution, by repeatedly placing the shapelet model of the PSF in an image at the appropriate flux amplitude. All of these analytic objects are then integrated within square pixels of the same 0.0398″resolution as the DRIZZLEd Hubble Deep Field. Our images

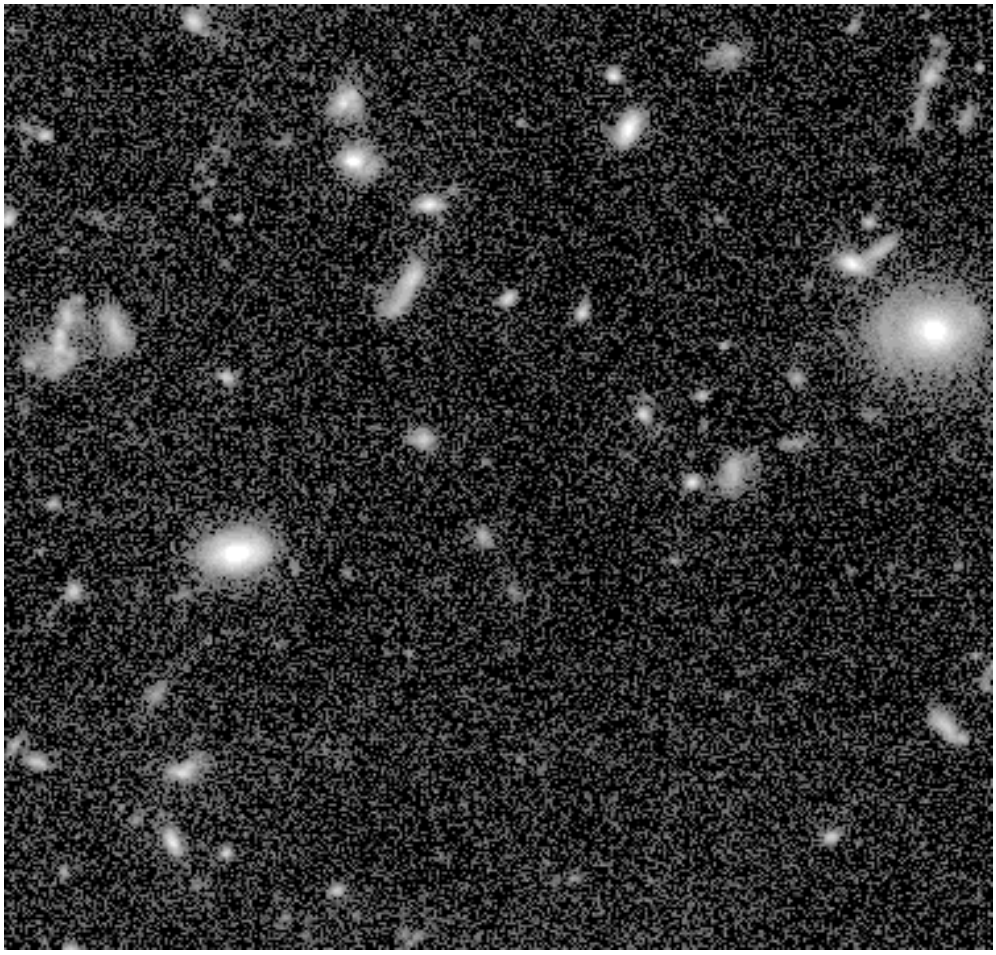

Figure 5.5: Section of the real HDF, with the same size and scale as figure 5.4.

have a somewhat larger solid angle than the HDFs because the missing quarter from the WFPC 'L' is restored.

Observational noise can now be added, at a level appropriate to the desired exposure time. We have simply added photon counting noise (proportional to the square root of the raw pixel values), and Gaussian background noise (with an amplitude determined from the HDF itself). However, it would be easy to add a background level, cosmic rays and even instrumental distortions: the shearing for which could be performed conveniently in shapelet space before pixellisation. A further effect, not included in our simple model, is noise that is correlated between adjacent pixels. Aliasing occurs as a side-effect of the DRIZZLE algorithm, which recovers image resolution by stacking several dithered exposures. This aliasing can make it possible to detect slightly fainter objects and also introduces some spurious objects at very low S/N. The steep slope of the real number counts beyond $I = 29$ exacerbates this problem, and we would not yet trust the noise model on our simulations for galaxies any fainter than this.

Final output is as a FITS image, a sample of which is displayed in figure 5.4. Larger

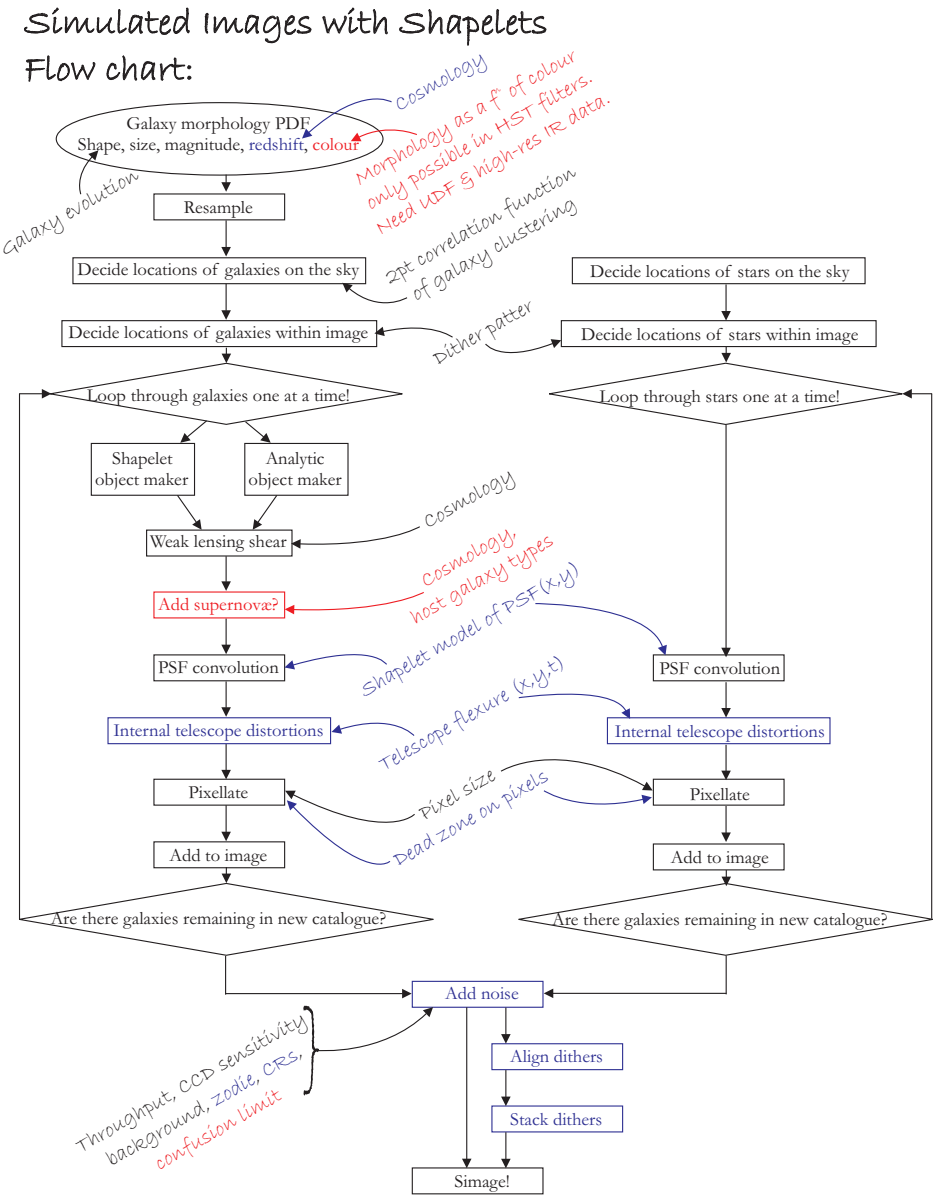

Figure 5.6: Flowchart showing the steps taken to produce a simulated image. These steps mimic the processes acting on photons en route from a distant galaxy to a telescope. The required inputs from cosmology, an engineering model of the telescope and a survey strategy are shown in a script font. Black ink shows steps that are already implemented. Blue ink shows steps that are not currently in use, but which could easily be added. Red ink shows steps that would be more difficult to include. For example, type Ia supernovæ could be superimposed upon the images, to simulate the second goal of the SNAP mission.

images may be downloaded via anonymous `ftp` from the shapelets web page at `http://www.ast.cam.ac.uk/$\sim$rjm/shapelets`. Notice the wide range of galaxy morphologies and behaviours present in figure 5.4. In particular, features resembling spiral arms, dust lanes and resolved knots of star formation are present, together with various radial profile shapes. By eye, the simulated galaxies look very similar to those in a similarly-scaled section of the HDF itself, reproduced in figure 5.5. An overview of our method is shown by the flowchart in figure 5.6. We shall quantitatively examine whether our simulation effectively mimics the morphology distribution of HDF galaxies in the following section.

5.3 Statistical tests of simulated images

We now demonstrate quantitatively that our simulated images are realistic, in the sense that commonly used morphology measures for our galaxies match the distributions of those for galaxies in the HDFs. First, we consider the number counts and size distributions, using photometry and size measures from SExtractor (Bertin & Arnouts 1996).These ought to be roughly consistent by construction, because they are closely related to two of the axes in our parameter space. Then we compare more detailed morphology measures, such as concentration (Bershady *et al.* 2000), asymmetry (Conselice *et al.* 2000a), clumpiness (Conselice *et al.* in preparation) and ellipticity. These are not automatically expected to match, because our shapelet-based PDF does not directly represent these quantities. Thus, a comparison between these properties for simulated and real data provides a rigorous and fair test of how realistic our simulations are.

5.3.1 Size and magnitude distributions

In order to carry out these tests, we first apply the SExtractor object-finding and shape measurement package on the version 2 reductions of the HDF-N and HDF-S (Williams *et al.* 1996, 1998), together with a 6 arcmin^2 simulated image of the same depth. As an intermediate test, we also analyse a simulated image containing shapelet reconstructions of galaxies drawn from a PDF left as δ-functions. These should be identical to the objects in the HDF and act as a test of the shapelets modelling procedure rather than the perturbations in shapelet space. In all four cases, approximately 320 galaxies brighter than $I \leq 29$ were detected per arcmin^2. For the galaxies only, we extracted observed magnitudes (MAG_BEST) and sizes (FWHM_IMAGE).

Figure 5.7 compares the size *vs* magnitude distributions of the simulated images with those of the two HDFs, excluding the stars. Figure 5.8 then shows the galaxy number counts for real and simulated cases in more detail. These match well over six or more orders of magnitude, whether the simulations used a δ-function PDF or the full version. Note, however, that the noise in the simulated images is not aliased in the same way

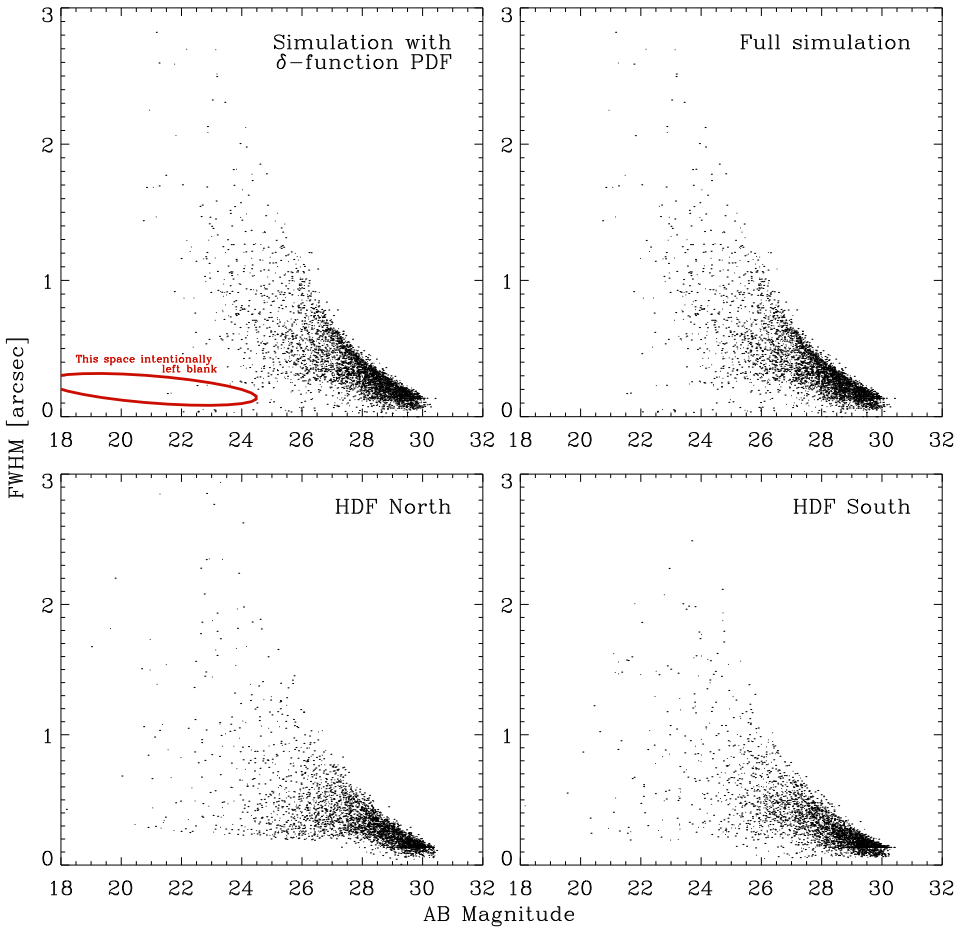

Figure 5.7: Size *vs* magnitude plane for 6 arcmin^2 I-band images to HDF depth, measured with SExtractor. Top-left panel: for a simulated image containing shapelet reconstructions of HDF galaxies (the PDF kept as δ-functions). Top-right panel: for a simulated image with galaxies perturbed in shapelet space. Bottom panels: for real galaxies in the Hubble Deep Fields North and South, calculated using the same SExtractor input parameters as reference. The stellar locus is omitted from all panels.

as the DRIZZLE algorithm has caused the real data to become (see §5.2.7). The number counts beyond $I \sim 29$ are highly sensitive to background noise properties, and are indeed increased in the simulated image if we artificially smooth the noise. Clearly DRIZZLE is something that needs further attention in a future implementation.

For the present purposes, we apply magnitude cuts and compare only the brighter objects, which are unaffected by such minor changes. These cuts are at levels determined by the stability of an individual diagnostic to noise. Figure 5.9 compares the size distribution of the simulated objects brighter than $I = 29$ with those of the HDF galaxies, as found by SExtractor. We find that there is excellent agreement in the shape of this distribution: the median and standard deviation FWHM for real galaxies in the HDFs are 0.30″and 0.24″. For simulated objects, these figures are 0.31″and 0.23″. This agree-

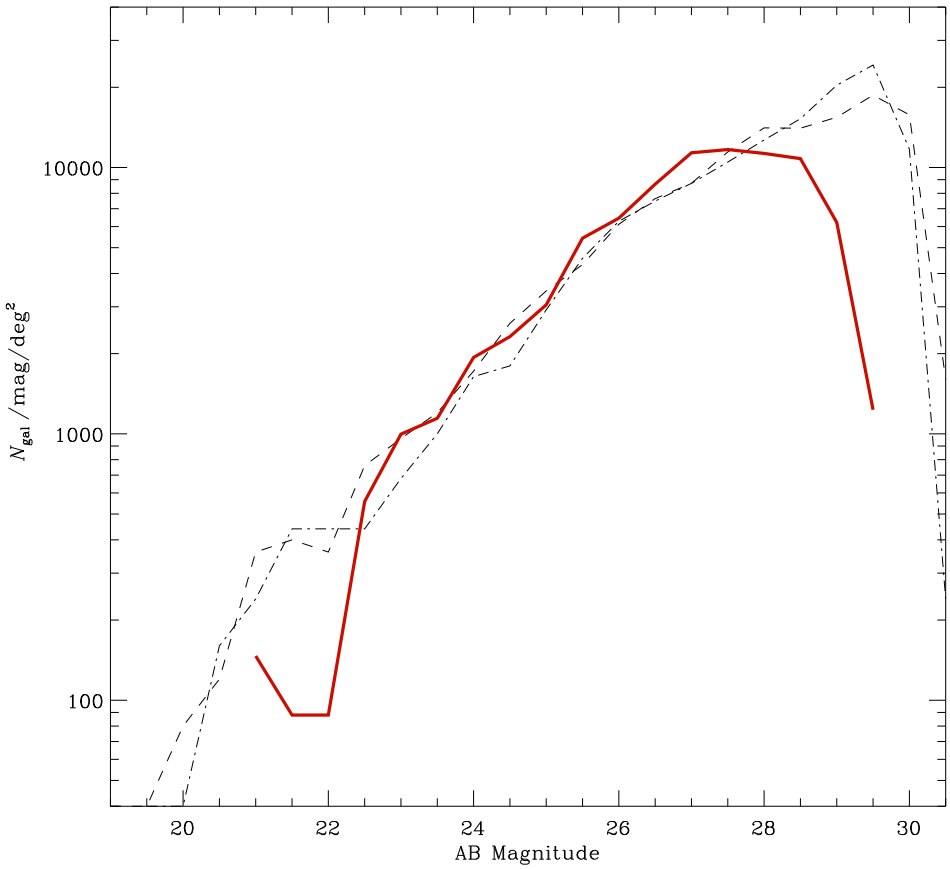

Figure 5.8: Number counts in simulated I-band images (solid red), normalised by area on the sky. Also shown are number counts for the Hubble Deep Field North (dot-dashed) and South (dashed).

ment comes about partly (but not entirely) by construction. It was somewhat expected that our simulated images will closely match real data in terms of their magnitude and size distributions, but the final high precision is encouraging.

5.3.2 Galaxy morphology diagnostics

We can more stringently test the reliability of our algorithm to reproduce properties of real galaxies by measuring morphological parameters which are entirely independent of shapelets. We apply a series of commonly used morphology diagnostics to two different realisations of the simulated images. A first version, containing unaltered shapelet models of HDF galaxies, tests the shapelet modelling process in isolation. A second simulated image, with galaxies drawn from the fully smoothed morphology PDF tests the fairness of these perturbations in shapelet space.

A first basic analysis is to determine the gross shape of galaxies, *i.e.* their ellipticities. The ellipticity of all the galaxies was obtained from SExtractor. Following a

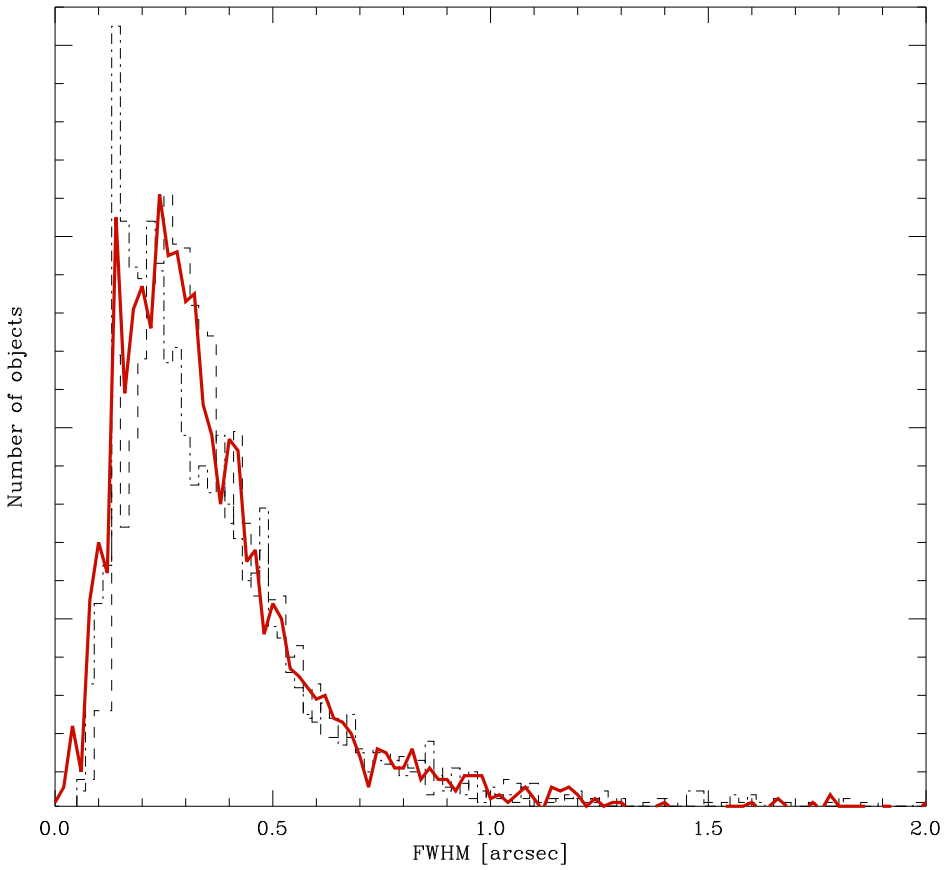

Figure 5.9: Size distribution of objects in a 6 arcmin^2 simulated image with limiting magnitude $I = 29$ (solid red). Also shown are size distributions for the Hubble Deep Field North (dot-dashed) and South (dashed).

convention in weak lensing literature, we here define two independent components of ellipticity as

$$e_1 \equiv \frac{\mathrm{A\_}IMAGE^2 - \mathrm{B\_}IMAGE^2}{\mathrm{A\_}IMAGE^2 + \mathrm{B\_}IMAGE^2} \cos(2 \times \mathrm{T}HETA\_IMAGE) \tag{5.3}$$

$$e_2 \equiv \frac{\mathrm{A\_}IMAGE^2 - \mathrm{B\_}IMAGE^2}{\mathrm{A\_}IMAGE^2 + \mathrm{B\_}IMAGE^2} \sin(2 \times \mathrm{T}HETA\_IMAGE) \tag{5.4}$$

where A_IMAGE and B_IMAGE are the lengths of the major and minor axes of the ellipse, and THETA_IMAGE is the angle between the major axis and the horizontal (all parameters supplied by SExtractor). Figure 5.10 compares this ellipticity distribution of the real and fully simulated objects brighter than $I = 29$. Again, these are in excellent agreement: with standard deviations in $e = \sqrt{e_1^2 + e_2^2}$ of 0.64 for real data, 0.62 for simulated data using a δ-function PDF and 0.62 for simulated data using the full PDF.

The four images have also been passed through the model-independent morphol-

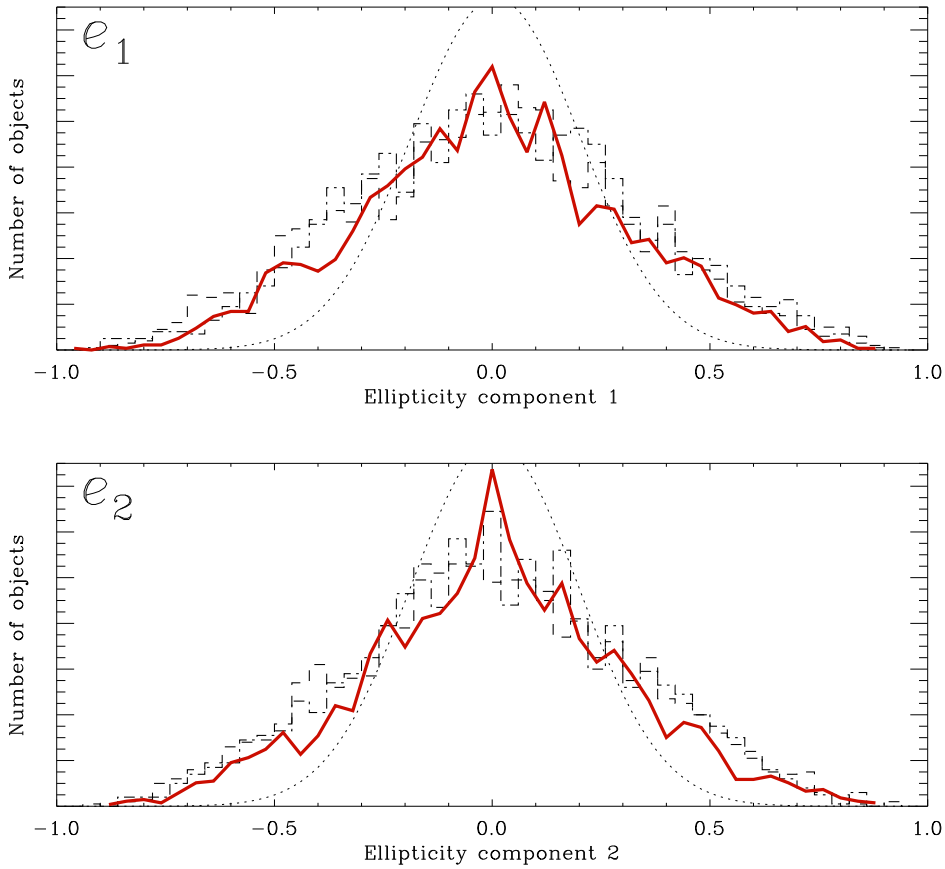

Figure 5.10: Ellipticity distribution, as defined in equations (5.3) and (5.4), of objects in 6 arcmin^2 simulated image with limiting magnitude $I = 29$ (solid line). Also shown is the ellipticity distribution for the Hubble Deep Fields North (dot-dashed) & South (dashed), and a Gaussian with the same mean and rms (dotted).

ogy software developed by Conselice *et al.* (2002a), Bershady *et al.* (2000) and Conselice (2003), in order to measure the concentrations (C), asymmetries (A) and clumpiness (S) values of the real and simulated galaxies. We first describe how these three quantities are calculated, and then compare the distributions obtained for these measures from real data and simulations. These 'CAS' parameters are very informative, as all nearby galaxy types (ellipticals, spirals, dwarfs, *etc.*) fall in distinct regions of CAS space (Conselice 2003). These parameters thus capture most of the variation in galaxy structures and have frequently been used for quantitative morphology classification.

The concentration index, C, is defined in terms of the ratio of the radii containing 80% (r_{80}) and 20% (r_{20}) of the object's total flux:

$$C \equiv 5 \times \log\left(\frac{r_{80}}{r_{20}}\right) . \tag{5.5}$$

For the total flux, we use the flux within an aperture 1.5 times the size of the Petrosian

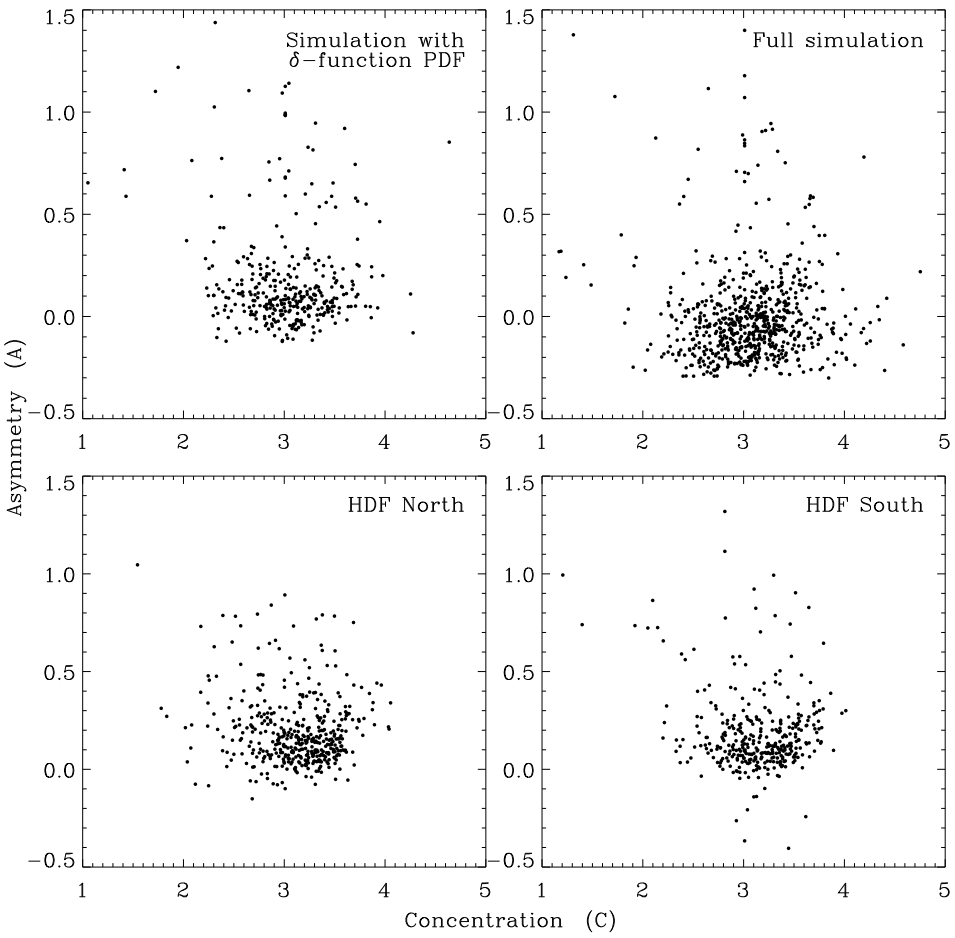

Figure 5.11: Concentration *vs* asymmetry, as defined in equations (5.5) and (5.6), for 6 arcmin^2 images with limiting magnitude $I = 26$. Top-left panel: for a simulated I-band image containing shapelet reconstructions of HDF galaxies (the PDF kept as δ-functions). Top-right panel: for a simulated image with galaxies perturbed in shapelet space. Bottom panels: for real galaxies in the Hubble Deep Fields North and South.

radius at $\eta = 0.2$ (Bershady *et al.* 2000). The η parameter is defined as the ratio of the surface brightness at a radius divided by the surface brightness integrated within the radius, such that at the centre of a galaxy, $\eta = 1$ and at the very edge of a galaxy (where its surface brightness is 0), $\eta = 0$.

Typical values of C for real galaxies range from approximately 2 to 6. Galaxies with $C > 4$ are usually ellipticals or spheroidal systems: a galaxy with an $r^{1/4}$ profile has $C = 5.2$. A purely exponential disc galaxy has $C = 2.7$ (Bershady *et al.* 2000). Objects with lower light concentrations are shown by Graham *et al.* (2001) to be systems with low central surface brightnesses and often low internal velocity dispersions. Low concentration values are also found for dwarf galaxies (*e.g.* Conselice *et al.* 2002). The concentration index thus correlates, within some scatter, with the total mass of a galaxy.

The asymmetry index used in this paper (called A_{180} in Conselice *et al.*2000a,b) is

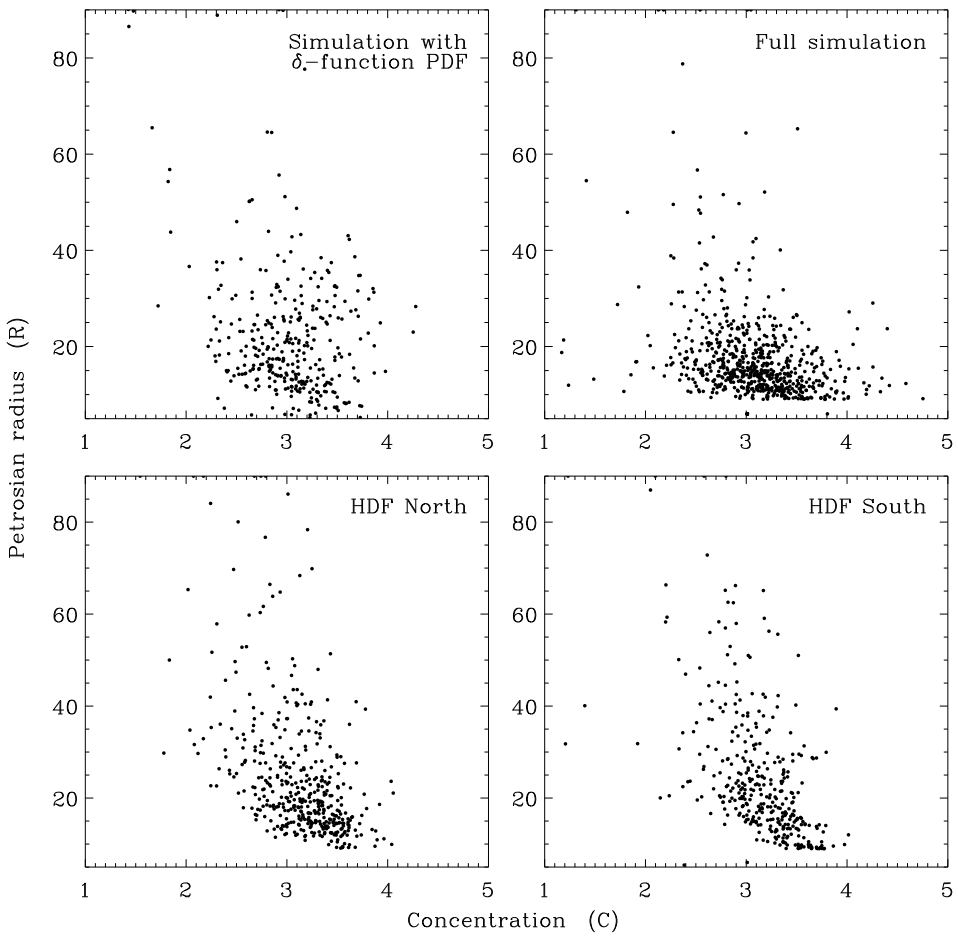

Figure 5.12: Concentration *vs* Petrosian radius, as defined in equation (5.5) and the text, for 6 arcmin^2 square images with limiting magnitude I = 26. Panels are ordered as in Figure 5.11.

calculated by rotating an image by 180° and subtracting the it from the original. Then we evaluate

$$A \equiv \min\left[\frac{\sum |I_{x,y} - I^{180}_{x,y}|}{\sum |I_{x,y}|}\right] - \min\left[\frac{\sum |B_{x,y} - B^{180}_{x,y}|}{\sum |I_{x,y}|}\right], \tag{5.6}$$

where $I_{x,y}$ is the galaxy surface brightness in the (x, y) pixel of the image, $B_{x,y}$ the sky background in the same pixel, and superscripts denote rotations. Sums are over all pixels within the same $\eta = 0.2$ Petrosian radius from which the total light measurement is made. Minimisation is then over different choices of the centre of rotation $\vec{x}_c$ (see Conselice *et al.* 2000a).

The asymmetry index is sensitive to any physical processes in a galaxy that produce asymmetries in light distributions, such as star-formation, galaxy interactions/mergers, and projection effects such as dust lanes. There is a general correlation between the asymmetry value and the $(B - V)$ colour (Conselice *et al.* 2000a). Since most galaxies

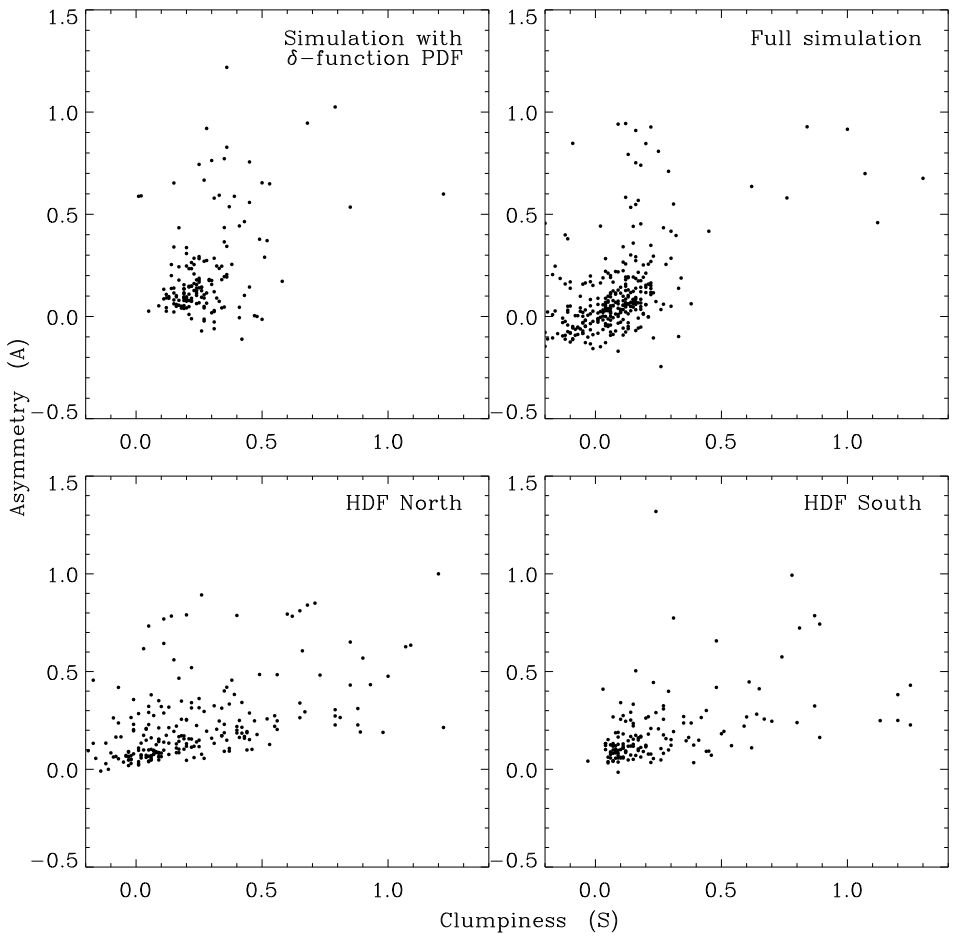

Figure 5.13: Asymmetry *vs* clumpiness, as defined in equations (5.6) and (5.7), for 6 arcmin^2 square images with limiting magnitude I = 25. Panels are ordered as in Figure 5.11.

are not edge-on systems, star formation and galaxy interactions/mergers are the dominant effects that produce asymmetries in real galaxies. These two effects can often be distinguished, however. Systems with asymmetries $A > 0.35$ are generally created by interactions or mergers (Conselice 2003, Conselice *et al.* 2003). However, other merger events can have more modest asymmetry values. From this and more detailed studies of the asymmetry index, it has been concluded that A is most sensitive to bulk structures in galaxies (Conselice 2003).

The clumpiness parameter, S, is a measure of the high-spatial frequency component of galaxies. It is calculated by smoothing a galaxy's image with a smoothing length σ, then subtracting this smoothed version $I^{\sigma}_{x,y}$ from the original image. This leaves a residual map containing only those features with a high-spatial frequency. Summation is again performed over pixels within the $\eta = 0.2$ Petrosian radius, although those from the central cusp are ignored. Also including a correction for the background $B_{x,y}$, the clumpiness is then defined as

	HDF-N	HDF-S	Simulation with δ-function PDF	Full simulation
$\langle C \rangle$	3.11	3.13	3.03	3.07
rms C	0.39	0.40	0.44	0.42
$\langle A \rangle$	0.18	0.17	0.19	0.07
rms A	0.20	0.22	0.27	0.25
$\langle S \rangle$	0.23	0.28	0.27	0.08
rms S	0.28	0.28	0.15	0.19
rms e	0.64	0.64	0.62	0.62

Table 5.1: Galaxy morphology statistics. The first two columns show results for real objects, taken from the Hubble Deep Fields. Compare this with objects in simulations created using a δ-function PDF or the full shapelet-morphing procedure.

$$S \equiv 10 \times \frac{\sum_{xy} |I_{x,y} - I^{\sigma}_{x,y}| - \sum_{xy} |B_{x,y} - B^{\sigma}_{x,y}|}{\sum_{xy} I_{x,y}} \,. \tag{5.7}$$

The clumpiness index is sensitive to the instantaneous rate of star formation, and correlates very well with Hα equivalent widths; it also correlates to a lesser degree with broad-band colors (Conselice 2003). Other details of its calculation and properties are discussed in detail in Conselice (2003).

We also use the Petrosian radius R (Petrosian 1976) to characterise the galaxies, defined as the position where $\eta = 0.2$. The Petrosian radius is found to be a better index than the SExtractor FWHM radius for determining morphological sizes, as SExtractor radii are based on isophotal thresholds which will represent different physical distances from the galactic centre depending on the distance to the galaxy. Because η is a ratio of surface brightnesses in a given galaxy, the run of η with r in a galaxy is immune to many such types of systematic effects (Sandage & Perlmutter 1990) and Petrosian radii are found to be a stable tool for deriving morphological parameters independent of distance (Bershady *et al.* 2000).

We are now in a position to compare the measurements for C, A, S and R for real and simulated images. Projections from this morphological parameter space for real and simulated data are displayed in figures 5.11–5.13, and relevant statistics are compiled in table 5.1.

As can be seen from the scatter in the plots, the agreement between simulations and real data is rather good: we are very pleased by the encouraging results. The matching distributions of the concentration parameter puts to rest one criticism frequently levelled at shapelets (see §4.1.3), that a truncated Gaussian-Laguerre expansion may not stretch far enough spatially to capture the extended wings of typical astronomical objects. Clearly our algorithm sets $n_{\max}$ high enough to avoid this problem while still modelling the HDF galaxies using only a few coefficients.

The final population of simulated galaxies does contain asymmetry values lower than those in the real data, although the distributions agree within 1σ. This slight discrepancy is neither due to deficiencies in the shapelet modelling procedure, nor to the increased clustering of galaxies at short separations in real data, because it is absent from the simulation created with a δ-function PDF. Decreased object asymmetry must therefore be a by-product of the PDF smoothing. There is no obvious *a priori* reason why this should happen. Even m states are symmetric and odd m states anti-symmetric, so if the absolute values of all coefficients are randomly changed by the same amount, the overall symmetry of the object should stay constant. However, our nearest-neighbour prescription from §5.2.5 results in an average smoothing length across typical even m states, and particularly the $m = 0$ states, of approximately twice that for odd m states. This may simply be because the first state is even, and the smoothing length tends to get shorter as n increases. A more sophisticated adaptive smoothing method might be found to prevent this effect, but we have not pursued that idea here. We note the asymmetry discrepancy, but note also that it is relatively small.

The behaviour of the clumpiness parameter is also reasonable. Truncation in shapelet modelling smooths galaxies slightly, and thus removes the tail of objects with very high S. Morphing in shapelet space apparently acts to then smooth some of the galaxies further. This is peculiar because, if anything, the galaxies in figure 5.3 appear by eye to become more clumpy as the smoothing length is increased. Overall, the agreement of the simulated distributions with real data is remarkably consistent with the field-to-field variation between the two HDFs. Indeed, clumpiness is a rather unstable statistic to measure. For example, even the slight rise in mean clumpiness for the δ-function simulation might be significant: especially since it is apparent despite the missing tail at high S. It is possible that the increase is caused by residual artefacts in the shapelet models, but more plausibly because the noise in our simulated images is not correlated between adjacent pixels. The HDFs themselves have been DRIZZLEd in order to achieve their high resolution, a process which also aliases the image. As a simple approximation to this effect, we have tried smoothing the noise slightly in our simulations, by a top hat kernel 3 pixels wide. This process does indeed remove the slight disparity observed in the simulated clumpiness distribution, but simultaneously creates many false detections of faint, circular objects from the noise at the magnitude limit around $I \geq 29$.

Therefore we conclude that our shapelet simulations obtain similar morphology distributions to those found in real data. This is most encouraging as these were not arranged by construction, and the level of realism seen here is a strong vindication of the shapelet modelling of galaxies. Perturbing shapelet parameters to create new galaxies can introduce a few minor deviations, but these are small compared to natural variation between objects, and are well understood and quantified. We can therefore use shapelets as a tool for investigating galaxy morphology and for creating realistic simulated images.

5.3.3 Comparison to other methods

There have been many packages in the literature which simulate astronomical observations, including SKYMAKER (see Erben *et al.* 2001) and ARTDATA in IRAF (Tody 1993). These typically parametrize galaxy shapes using simple physical models such as ellipses with de Vaucouleurs or exponential profiles. The smooth variation allowed for these parameters enables them to generate an unlimited number of unique simulated galaxies. These methods are particularly valuable for simulating images from ground-based telescopes. Unfortunately, deep images from HST contain galaxies with resolved features more complex than these analytical models, so such simulations are useful in only a limited regime.

This was realised by Bouwens, Broadhurst & Silk (1998), who designed simulations to investigate the evolution of galaxy morphology in the HDF. Indeed, their work succeeds in ruling out pure luminosity evolution of galaxies: which precisely demonstrates the need for deep image simulations to contain more irregular and asymmetric morphologies. Their method repeatedly places the few brightest HDF galaxies onto a simulated image, and is similar to that which ours would have been, had we left the PDF as an (unsmoothed) sum of δ-functions. Some physics can be added to rescale and redshift these few sources, but it remains a very small population from which to simulate a large imaging survey, and containing members drawn exclusively from the local universe. Creating realistic images was not the intention of Bouwens, Broadhurst & Silk (1998) and, for our objectives, their method would require the addition of more physics (*e.g.* galaxy evolution, star formation histories, redshift distributions, *etc.*).

Our technique attempts to capture the best aspects of both methods, by defining a smooth parameter space that can yield an unlimited number of unique galaxies, but also contains a rich diversity of their morphologies (potentially any morphology, in fact, since the set of shapelet basis functions is complete). Since the parameter space is populated via statistical rather than physical arguments, it is the many tests to which we have subjected our simulated images that demonstrate the validity of our method. We find a regime spanning six orders of magnitude in luminosity where our simulations are valid, and their statistical properties match those of real data. This ability to produce simulated images containing galaxies with realistic morphologies is a significant advance.

A useful extension to this work will be to include 'Groth survey strip' (Groth *et al.* 1994) galaxies and ACS data when constructing the morphology probability distribution. This will provide future simulations with a more extensive sample of large, bright galaxies, improving the fidelity of the simulations in this region of parameter space. A method is also in development to generate multi-colour simulated images using several HDF passbands and photometric redshifts.

6

Future cosmic shear surveys

6.1 The next generation of surveys

6.1.1 Future goals for weak lensing

The most important responsibility for any lensing survey is the control of observational systematics. Almost all of these effects act to increase the observed signal by mimicking (in some cases very realistically) the shear induced by gravitational lensing. Perhaps the most reassuring result from current cosmic shear surveys is therefore the broad agreement between measurements taken on different telescopes, and by different groups using different analysis methods. This agreement has demonstrated the success of gravitational lensing as a direct probe of the dark matter distribution with the control of its systematic effects at roughly the $\sim 10\%$ level. The next obvious steps are to tighten this control by using improved analysis techniques (perhaps shapelets), and to tighten the cosmological parameter constraints from two-point statistics by performing larger, dedicated lensing surveys. These should also be able to measure three-point statistics, which provide an independent constraint on Ω_m (Bernardeau, van Waerbecke & Mellier 1997).

Lensing surveys can also achieve more than simple cosmological parameter constraints. Techniques for weak shear measurement has now been successfully demonstrated to the wider astrophysical community, with the requests for further accounting for systematic effects provided via the E-B decomposition and other cross-checks. It has also become possible to locate halos in cosmic shear surveys, selected purely by their mass (*e.g.* Wittman *et al.* 2001; 2003). Mass reconstructions from weak lensing data

will also become increasingly useful (§6.4.2). Through shear inversion (Kaiser & Squires 1993) or aperture mass statistics (Schneider & Bartelmann 1997), lensing can be used to create *maps* of the dark matter distribution. These can be compared directly to the light distribtuion, to invesitagate bias as a function of scale.

Peaks in the mass maps can also be isolated, to form a mass-selected cluster catalogue (*e.g.* Weinberg & Kamionkowski 2002; Hoekstra 2002). This would be an invaluable input into classical tests of cosmology, including halo abundancy statistics. Quantitative study of high-sigma mass fluctuations is one of the most promising methods to break degeneracies in cosmological parameter estimation, particularly constraining $\Omega_{\rm m}$ (*e.g.* van Waerbeke & Mellier 1997; Cooray, Hu & Miralda-Escudé 2000; Munshi & Jain 2001; Schneider 2002). The next generation of lensing surveys should be able to measure higher-order statistics of the density distribution and thus investigate its non-Gaussianity. This might be brought about by non-Gaussian primordial seeds, topological defects, or the complicated process of non-linear structure formation. In the latter case, the evolution in skewness over time would provide a direct test of the gravitational instability paradigm for structure formation.

Furthermore, studying individual groups and clusters from high resolution mass maps, rather than treating mass fluctuations statistically, will lead to a better understanding of astrophysical phenomena like biasing or the mass-temperature relation (Weinberg *et al.* 2002; Huterer & White 2003; Smith *et al.* 2003). Large mass overdensities can already be found within our WHT survey (Massey *et al.* in preparation), and dark matter maps have been recovered from Subaru data (Miyazaki *et al.* 2002). However, the mass sensitivity and resolution of such maps is limited primarily by the number density of useable background sources. Even with a perfect shear measurement method, many source galaxy shapes need to be averaged in any one resolution element. This is most easily achieved by deeper imaging, and in better seeing. With more accurate photometry, it may also be possible to measure a simultaneous constraint from the magnification effect of weak lensing (Jain 2002).

Although gravitational lensing is achromatic and shape measurement may be performed in any colour, future surveys will benefit greatly from multi-colour data. Reliably ascertained photometric redshifts will reduce the current errors due to uncertainty in the source redshift distribution (and remove the need for the single source sheet approximation). They will also enable redshift tomography to trace the evolution of structure (Refregier *et al.* 2002); and even make possible an entirely 3D mass reconstruction, as demonstrated in Taylor (2003a), Hu & Keeton (2002), Bacon & Taylor (2002), Massey *et al.* (2003) and Jain & Taylor (2003). 3D dark matter mapping and mass-selected cluster catalogues will directly trace the evolution of structure. The knowledge of this evolution places a strong lever arm on constraints for the equation of state parameter w of Dark Energy, via its effect upon the cosmological growth rate of structures. Essential for this technique are well-resolved, multi-colour images of background galaxies out to large

distances.

Such dramatic improvements in both the quality and quantity of weak lensing data will leave future measurements limited by the precision of shape measurement algorithms. The Kaiser, Squires & Broadhurst (1995; KSB) method used in chapter 3 and throughout the literature is nevertheless decidedly out of date. Erben *et al.* (2001) found KSB able to recover shears between 1% and 3% with a precision of $10\% \rightarrow 15\%$. Bacon *et al.* (2001) found similar results, plus the necessity for an (unexplained) calibration factor. Modern shape measurement techniques are being developed, to incorporate higher order shape moments or Bayesian statistics. In order to make full use of future cosmic shear surveys, such methods will need a shear sensitivity of around 1%. Some of these methods will be discussed further in §6.3.3.

6.1.2 Cosmological models with Dark Energy

We consider a cosmological model with the same matter components as in chapter 2, plus an additional dark energy (or "quintessence") component with present density parameter Ω_Q. The equation of state of the dark energy is parametrized by $w = p_Q/\rho_Q$, which we assume to be constant, and which generalises the case for a cosmological constant, where it is equal to -1. The evolution of the expansion parameter a is given by the Hubble constant H through the *modified Friedmann equation*

$$\frac{\dot{a}^2}{a^2} = H_0^2 \left(\Omega_m a^{-3} + \Omega_Q a^{-3(1+w)} + \Omega_\kappa a^{-2} \right) , \tag{6.1}$$

where the total and curvature density parameters are Ω and $\Omega_\kappa = 1 - \Omega$, respectively.

Dark energy has several effects on weak lensing statistics (Ma *et al.* 1998). First, it modifies the expansion history of the universe $a(t)$. As a result, both the angular-diameter distance and the growth rate of structures are modified. The latter effect is amplified by the non-linear evolution of structures. In some quintessence models, dark energy also modifies the linear power spectrum on large scales. We will ignore that effect since these scales are not easily probed by weak lensing surveys.

6.1.3 Ground-based lensing surveys

Several new instruments have been built with weak lensing in mind and installed on telescopes where a large survey can be carried out. MEGACAM (Boulade *et al.* 2000) has been installed on the 3.6m *Canada-France-Hawaii Telescope* (CFHT) on Mauna Kea. It has a 1 square degree field of view, with $0.19''$ pixels, and, importantly has a large fraction of telecscope time dedicated to a survey mode. The CFHT *Legacy Survey* began in mid-2003 and, over the following 5 years, will image 208 square degrees in u, g', r', i' and z' bands, down to $r' = 25.7$. The r'-band observations are scheduled as overrides during good weather to permit accurate shape measurement. If problems with camera optics

can be solved, this survey should produce image quality similar to our WHT observations but over a huge area to drive down noise and tighten constraints on cosmological parameters.

Suprime-cam (Miyazaki *et al.* 2002b) has been installed on the 8.2m *Subaru* telescope on Mauna Kea. It has a 0.25 square degree field of view, and a pixel scale of $0.20''$. The camera was specifically designed for weak lensing measurements, and has excellent image quality with median seeing of $0.61''$. An ongoing survey of ~ 40 square degrees using this large telescope combines the high image quality and data acquisition rate of Keck with the large field of view of WHT. Measurements of the shear correlation function on many scales should determine $\sigma_8\Omega_m^{0.6}$ to within 3%, and a measurement of the skewness of the convergence field should break this degeneracy, providing an independent constraint upon Ω_m within 8% (Miyazaki 2003, personal communucation).

Other telescopes, whose entire design is being optimised for weak lensing, are also under construction. The 4m *Visible and Infrared Survey Telescope for Astronomy* (VISTA) is being built at Cerro Paranal in Chile (`http://www.vista.ac.uk`), with first light is expected in early 2006. VISTA will then spend $\sim 75\%$ of its time dedicated to long-term surveys, including a cosmic shear survey. Its wide-field cameras include a 1 square degree near-IR camera with $0.34''$ pixels, plus (possibly) a 2.25 square degree optical camera with $0.25''$ pixels. The image quality should be ideal for weak lensing, given the specialised options that were considered during its design, including the simultaneous use of two guide stars to improve tracking and reduce field rotation during exposures.

The *Large-aperture Synoptic Survey Telescope* (LSST) is a proposed 8.4m telescope, with a three mirror design that creates an effective 6.9m primary mirror (`http://www.lsst.org`). At the time of writing, LSST has not yet secured funding, but it holds great promising for future weak lensing measurements and time-domain studies. LSST's 7 square degree field of view will enable it to survey all of the sky (about 14,000 square degrees) visible from the telescope site to $R = 24$ in five nights. This process will be continually repeated, and the stacked images should be excellent for weak lensing analysis. The three-mirror design reduces astrometric distortions across the wide field, and the 2 Gigapixel CCD produces a pixel scale of $0.2''$.

6.1.4 Space-based lensing surveys

Although dedicated ground-based surveys can image large areas relatively quickly, the figure of merit for a lensing survey needs to include more than the oft-quoted *étendue*, a product of the survey area and the flux gathering power of a telescope (Tyson *et al.* 2002; Kaiser *et al.* 2002). An ideal weak lensing survey must also boast a control over observational systematics, minimise image degradation due to the PSF, and account for the size-magnitude distribution of its resolved background galaxies

Observing from space is the ideal way to increase the sensitivity, depth and resolu-

tion of weak lensing surveys, while simultaneously reducing the systematics that hinder shape measurement. The higher number density of useable source galaxies improves the sampling of the shear field, and more information can be extracted from each highly-resolved object. This qualitatively improves the performance of a survey for weak lensing, and opens up new opportunities to which surveys can advance. Shear sensitivity is raised for a spacecraft over a ground-based telescope for the additional reasons listed below.

- **More objects have measurable shapes**

  Although not as much sky area could be surveyed as from the ground, the spatial density of resolved objects is an order of magnitude (compare figure 6.7 with those in chapter 3). This more densely samples the cosmic shear field, allowing the study of individual mass structures in their own right, as well as the statistical ensemble.

- **The shape of individual galaxies are more precisely measured**

  Not only is the image resolution higher from a diffraction-limited PSF in space, but many other observational hindrances are removed. Tracking errors, telescope flexure and variable focus misalignment are all negligible in a long orbit. Correction for PSF and instrumental distortions is much easier above the atmosphere, and calibration can be performed upon a set of many images rather than from the limited information available in each one alone. Shape measurement becomes more accurate for each galaxy sampling the cosmic shear field; and more reliable, or possible at all, for small, distant galaxies.

- **Galaxy redshifts are known accurately and to a greater depth**

  Stable photometry and the ease of observing in the infra-red without atmospheric absorption lines permots the calculation of photometric redshifts with the best possible accuracy. This improves estimates of the redshift distribution of source galaxies, uncertainty in which is a major contribution to the error budget in current lensing surveys. Projected 2D power spectra and maps can be drawn in several redshift slices, using redshift tomography. More ambitiously, cluster catalogs and dark matter maps can be constructed directly in 3D (Bacon & Taylor 2002; Massey *et al.* 2003), enabling the 3D correlation of mass and light and the tracing of the growth of mass structures.

- **Galaxies are farther away**

  The higher resolution and especially the much deeper magnitude limits possible from space means that the source population is both more distant and spread over a wider range of redshifts. The emergence and growth of structures can therefore be traced from earlier epochs, giving a better handle on cosmological parameters (see paper III). Furthermore, recent numerical simulations (Jing 2002; Hui & Zhang 2002) suggest that intrinsic galaxy alignments impact lensing surveys to a greater depth in redshift than previously assumed. If this is confirmed, intrinsic alignments will mimic and bias cosmic shear signal in all but the deepest surveys, where the galaxies are farther apart in real space. Using 3D positions of galaxies from SNAP photo-zs, it will be possible to isolate close galaxy pairs and to measure their alignments, or to optimally down-weight close pairs thus reducing their impact (King & Schneider 2002; Heavens & Heymans 2002).

Weak lensing observations are thus ideally suited to a wide-field space-based imager. Relatively small-scale observations have already been successful using HST (Refregier *et al.* 2002; Rhodes *et al.* 2001; Casertano, Ratnatunga & Griffiths 2003). These particularly improve the measurement of shear correlations in galaxy pairs at close angular separations. However, the limited field of view avaiable from HST makes larger surveys prohibitively time-consuming. As a concrete example of the dedicated surveys that will become available around the end of this decade, we shall consider the planned *Supernova/Acceleration Probe* (SNAP) mission. Engineering models for SNAP are sufficiently well developed for us to perform detailed and quantitative simulations of its performance in order to predict its sensitivity to weak gravitational lensing. Most of SNAP's engineering limitations and design trade-offs will indeed be borne by any similar wide-field imager in space. SNAP can therefore be considered a quantitative baseline for any generic space mission in the near future.

6.2 Supernova/Acceleration Probe (SNAP) satellite

6.2.1 Mission overview

The *Supernova/Acceleration Probe* (SNAP) satellite is a wide-field 2m space telescope, funded jointly by the United States' Department of Energy and NASA, and planned for launch in 2010. The acronym may seem portentous, but apparently the word "snap" is not a synonym for "break suddenly" in American English. The latest design from the Lawrence Berkeley Laboratories is shown in figure 6.1. SNAP's primary objective is to detect type Ia supernovæ at high redshift. After various calibration factors derived from their light curves and spectra, these can be used as standard candles to extend Hubble's law to greater distances. Observing several thousand supernovæ out to $z \sim 1/7$ will

measure the deceleration parameter q and the Dark Energy equation of state parameter w with a precision of about 10%. SNAP will also be used for a weak lensing survey that will provide complementary constraints on cosmological parameters and address some of the issues in the previous section.

SNAP will be placed in a long three-day orbit, spending little time in the shadow of the Earth and with a constant orientation to the sun (Rhodes *et al.* 2003). This steady thermal environment will create a more stable PSF, improving deconvolution and more accurate correction for the distortion of objects' shapes. After its initial cool-down and calibration period, SNAP will begin approximately 40 months' of observation in a twin survey strategy that is discussed in sections §6.2.3 and §6.2.4. Extra time spent observing calibration frames, transmitting data to Earth or passing through radiation zones on the orbit give the telescope a predicted observing efficiency of 85% during the primary missions. After their completion, SNAP is likely to be operated as a guest observer observatory on a competitive basis. For further details of the SNAP mission see Aldering, *et al.* (2002), Kim, *et al.* (2002;2003), Lampton *et al.* (2002a; 2002b), Massey *et al.* (2003a; 2003b), Refregier *et al.* (2003), Rhodes *et al.* (2003) Tarle *et al.* (2002) and Perlmutter *et al.* (2002).

6.2.2 Instrumental characteristics

Many of the stringent optical requirements for following the light curves of faint supernovæ are compatible with the desired instrumental properties for measurements of weak lensing. Indeed, most of SNAP's limitations and trade-offs will be born by any similar wide-field imager from space. The detailed engineering models which are available for SNAP therefore act as a useful baseline for a generic space mission which will inevitably face similar engineering difficulties and reach similar solutions.

SNAP will have a 0.7 square degree field of view, wider than that of HST and with $\sim 5\times$higher instrument throughput, enabling it to efficiently survey the large area needed to constrain cosmological parameters. The focal plane will be covered by a mosaic of six optical and three near infra-red fixed filters spanning 350nm–1.7μm (Perlmutter *et al.* 2003). These will be permanently attached to the detectors and unmovable once the spacecraft is deployed but arranged in a pattern that allows a contiguous survey region to be imaged in all nine bands by scanning the telescope in steps across the sky. The NIR detectors are twice as big as the optical CCDs, conveniently doubling the exposure times in NIR bands compared to those in the optical, and enabling excellent photometric redshifts. The NIR colours are essential for this purpose, as we shall see in section §6.3.6.

The FWHM of the PSF will be approximately 0.13″at 800nm, where galaxy shapes are likely to be measured. The high and thermally stable orbit will keep the PSF (and any internal optical distortions that could otherwise mimic cosmic shear) even more constant than that of HST (which "breathes" as it enters and exits a huge temperature

Figure 6.1: Cutaway view of the proposed SNAP satellite design, reproduced courtesy of the SNAP collaboration. This view shows the internal light baffles, the 2m primary mirror and the three sturdy support struts of the secondary mirror. The solar panels are fixed to the outside of one side of the craft, with a radiator in the opposite direction. Their orientation with respect to the sun is permanently maintained in order to minimise thermal expansions and contractions that would otherwise induce optical distortions, mimicking the shear produced by gravitational lensing.

differential inside the shadow of the Earth). SNAP's PSF will be constantly monitored via the examination of non-saturated stars that happen to fall within the survey and occasional observations of globular or open star clusters. These will be required at least at the beginning and end of the survey, and each time there is a focus change in the telescope. The main contributions to the PSF are diffraction from the aperture and the three secondary support struts; geometric abberations along the optical path; and charge diffusion within the CCDs. These effects were modelled by Rhodes *et al.* (2003), using ray tracing through the latest engineering models of the telescope design. Their simulation of the baseline or time-averaged SNAP PSF is shown in figure 6.2, along with a shapelet decomposition. Note, for example, the excess power in the $m = \pm 6, \pm 12$ modes due to diffraction from the three secondary support struts. We shall not consider here the small variation of the PSF over time or across the focal plane. We assume that these effects can be modelled accurately and accounted for during the data reduction.

The stable photometry from the three-day orbit may even permit the use of weak lensing magnification as well as shear information (see *e.g.* Jain 2002; 2003). Whether directly measured or inferred from the shear field, this in turn is useful to correct for the effect of lensing on the distance moduli to the SNAP supernovæ (Dalal *et al.* 2003; Perlmutter *et al.* 2002).

6.2.3 Wide survey strategy

The SNAP survey strategy is divided into two primary missions. A wide survey will cover 300 square degrees in all nine bands. Four dithered 500s exposures will be taken at each pointing to reach a stacked depth of AB 27.7 in R (for a point source at 5σ). The wide survey will take five months to complete.

The wide survey has been designed primarily for weak lensing and the sacrifice of depth for width will put the tightest possible constraints on cosmological parameters. The large observed area reduces the need for a scattered-field, pencil-beam survey approach like that used with WHT and Keck to reduce the impact of cosmic variance. Therefore, the survey will be contained within one or two contiguous areas, in order to improve the sensitivity to various other science investigations, and also to consider more goals for the weak lensing survey. For example, the stable optics will allow shear correlation functions to be measured between galaxies on different exposures, and therefore at pair separations that can extend into the linear regime of the power spectrum.

6.2.4 Deep survey strategy

The SNAP mission will also include a deep survey, covering 15 square degrees in all nine bands, to a much fainter magnitude limit. Four 300s observations will be taken, once every four days, over a period of 32 months. The differences between successive images will be searched for type Ia supernovæ and to measure their light curves. Stacking all

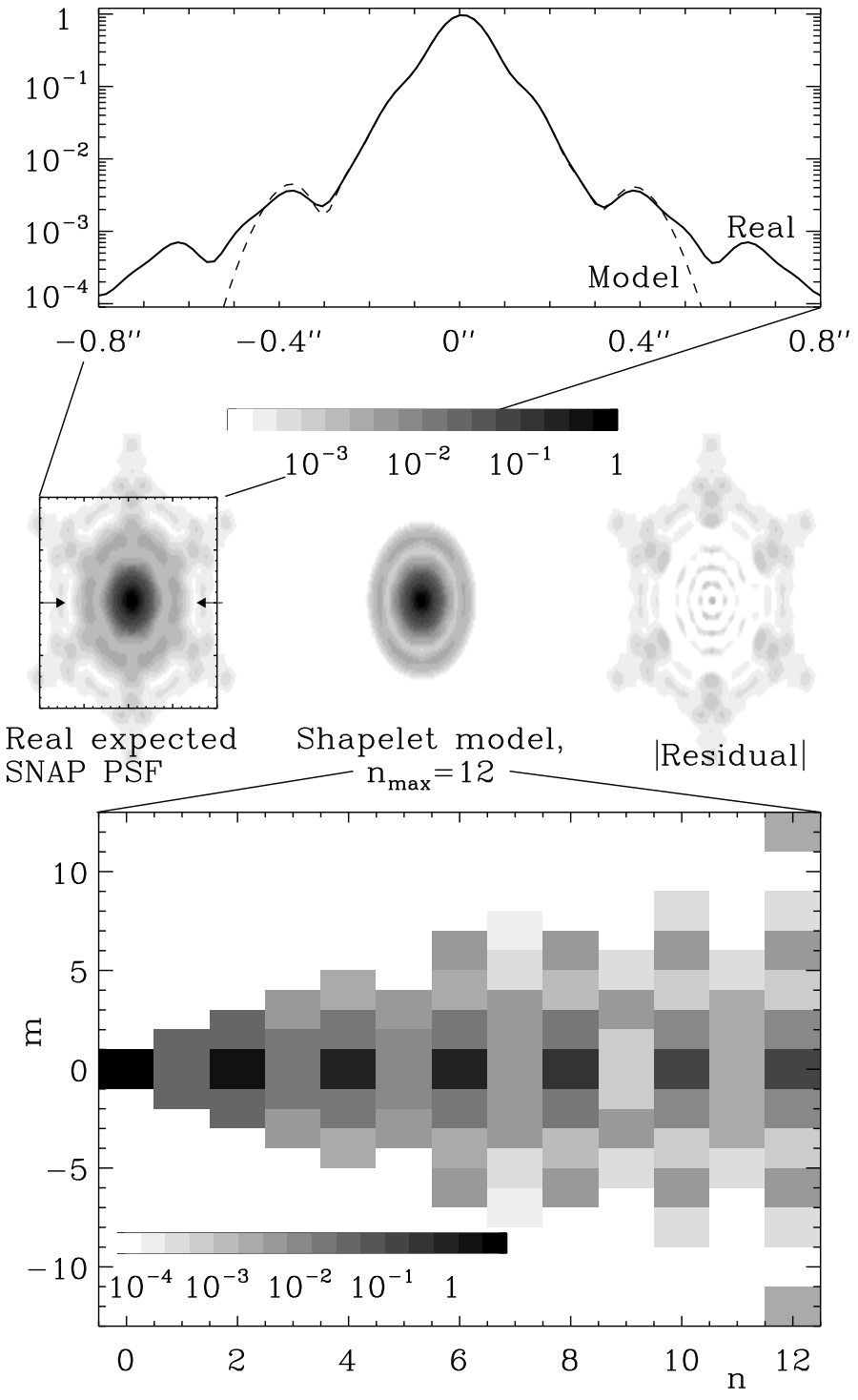

Figure 6.2: Shapelet decomposition of the proposed SNAP PSF. *Top panel*: a horizontal slice through the center of the real (solid line) and shapelet-reconstructed (dashed line) PSF. The middle panels shows, in 2-dimensions, the real PSF, its recovery using shapelets and the residual difference between the two, from left to right respectively. *Bottom panel*: the moduli of the corresponding polar shapelet coefficients with order up to $n_{max} = 12$. Note that all intensity scales are logarithmic. The circular ($m = 0$) core is modelled to an accuracy of about 10^{-3} and the beginnings of six-fold symmetric structure is seen as power in the $m = \pm 6$ and $m = \pm 12$ shapelet coefficients.

the many exposures will also create a very deep image with a total integration time of 144,000s in each optical filter and twice that in each infrared filter. This will reach an AB magnitude of 30.2 in R (for a point source at 5σ).

Approximately 60% of the observing time will be spent on imaging. The remaining 40% of the time will be spent obtaining spectra of supernovæ. During spectroscopy, the imagers will be left switched on and any coincidental further integration within the survey region will be in addition to these numbers.

The deep survey will be useful for several weak lensing studies. The extremely high number density of resolved background galaxies can produce a detailed two-dimensional (projected) map of the mass distribution which shows clusters, filaments, and structure down to the scale of galaxy groups. The nine filters will provide photometric redshifts for almost all these galaxies, accurate to $\Delta z \approx 0.04$. This will allow the division of the detected galaxies into redshift bins in order to trace the evolution of the mass power spectrum. Furthermore, recent theoretical developments make possible a direct inversion of the shear distribution, simultaneously taking into account all the redshift information (Taylor 2001; Hu & Keeton 2002; Bacon and Taylor 2002; paper II). Using this technique, mass maps can also be created directly in three dimensions. A mass-selected cluster catalogue can then be extracted from these.

6.3 Simulated SNAP observations

6.3.1 Shapelet-based image simulations

The shapelet-based image simulation method described in chapter 5 was developed precisely to mimic deep, high resolution space-based data. It is therefore ideal to simulate the performance of SNAP, and has been tuned to the instrument and mission specifications outlined in section §6.2. We shall attempt to measure the shear field in simulated data at a variety of noise levels and after convolution with the SNAP PSF. Since all of the galaxies possess a well-known size, magnitude and input shear, the comparison of input shear to output shear will allow us to determine the recovery accuracy and the precision possible from this mission.

The presence of realistic and irregular galaxy morphologies in the simulation is vital for this procedure, because an object's response to shear is a function of its overall shape. Earlier work (Bacon *et al.* 2001; Erben *et al.* 2001) used only azimuthally symmetric simulated galaxies: oversimplifying the task. Figures 6.3 and 6.4 show $30' \times 30'$ sections of shapelet-based image simulations of the SNAP wide survey and to the depth of the HDF. The SNAP deep fields will be about 2 magnitudes deeper than the HDF. However, deeper surveys with the ACS on board HST are awaited to accurately model the galaxy number counts and morphology distribution at this depth. They can be compared to a simulated HST image in figure 5.4, or a section of the real HDF in figure 5.5.

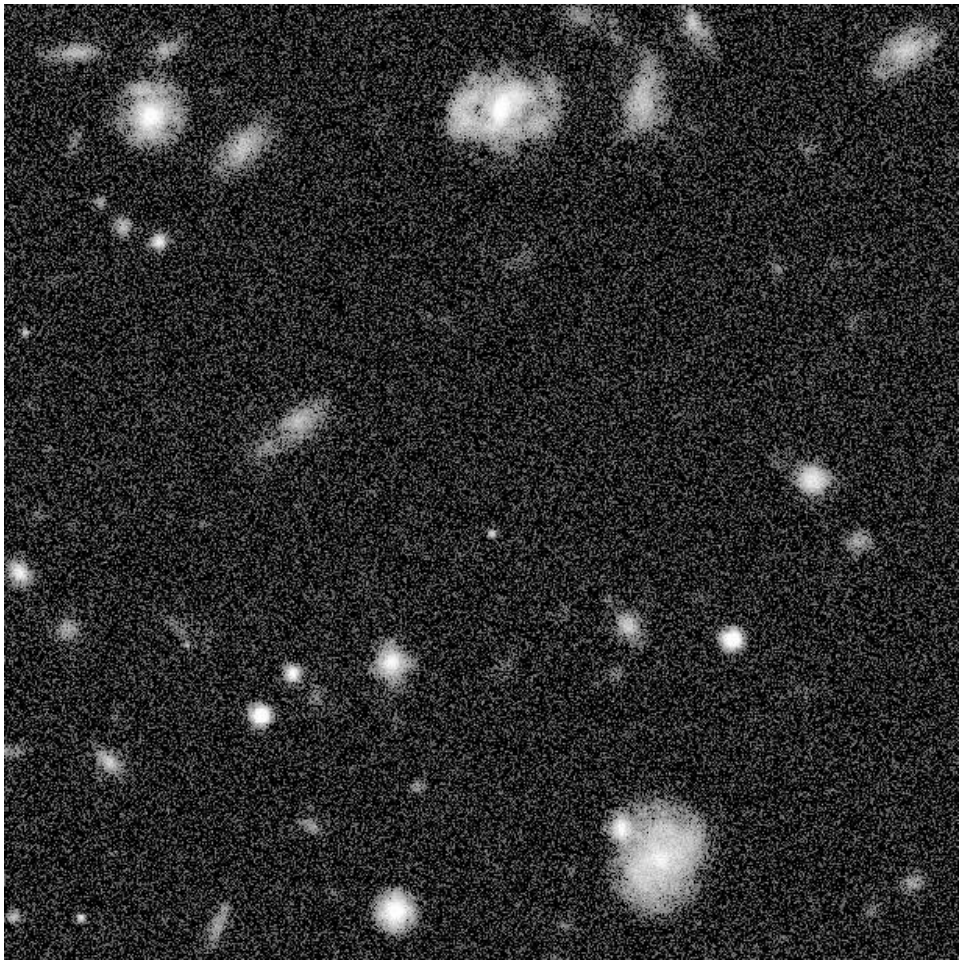

Figure 6.3: $30'' \times 30''$ portion of a simulated SNAP I-band image to the depth of the proposed SNAP wide survey.

Figure 6.5 shows the size-magnitude distribution of the simulated images to both depths (top panels). Once again, the simulations reproduce the statistics of the real HDFs (bottom panels).

The predicted SNAP PSF at the middle of the illuminated region of the focal plane was obtained for the current satellite design using raytracing, aperture diffraction and CCD diffusion by Rhodes *et al.* (2003). The PSF and its decomposition into shapelets are illustrated in figure 6.2. As shown on the top panel of figure 6.2, our model includes the second diffraction ring and is accurate to nearly one part in 10^3. It does not include much of the extended low-level diffraction spikes, which we ignore. Convolution with this residual PSF pattern adds less than 0.7% to the ellipticity of any exponential disc galaxy that passes the size cut into the lensing catalogue (see §6.3.3). Given the further factor of G^{-1} in equation (6.5), to convert ellipticity into shear, this residual thus has a negligible impact upon shear measurement within the accuracy of the current methods.

Simulated images used to calibrate the shear measurement method (see §6.3.3) are

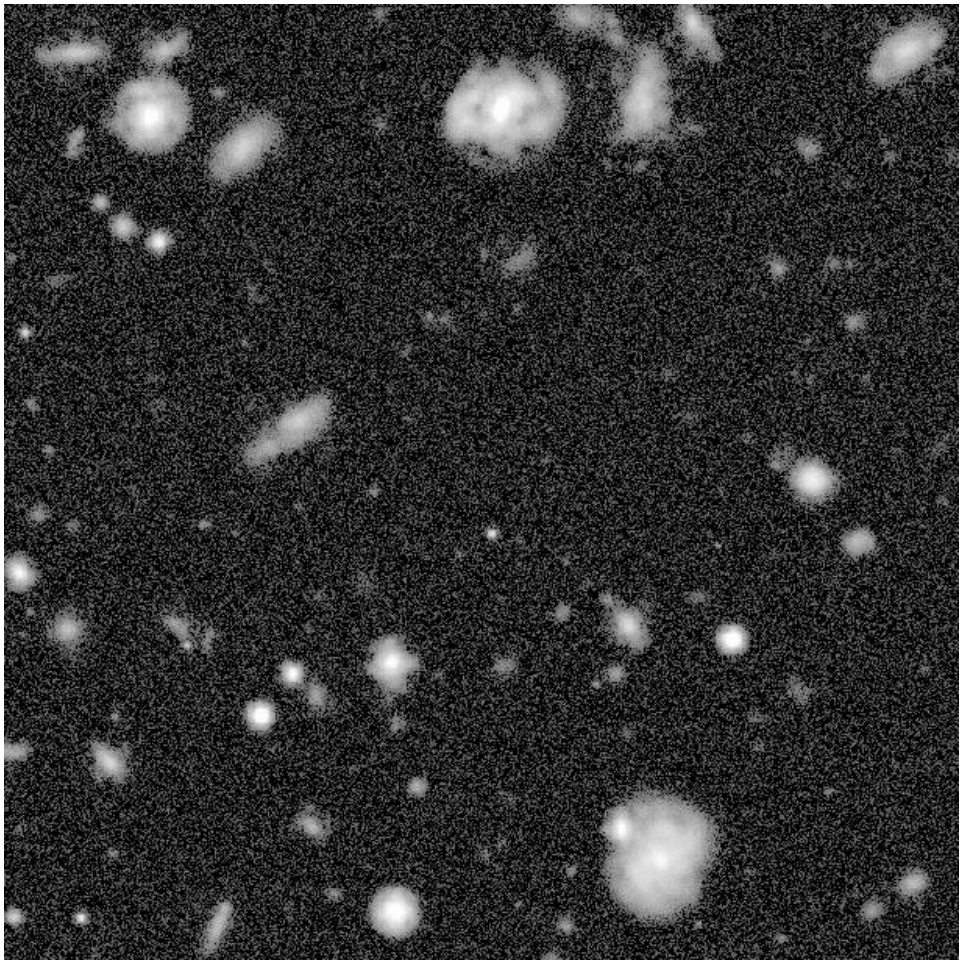

Figure 6.4: $30'' \times 30''$ portion of a simulated SNAP I-band image to the depth of the Hubble Deep Fields. The SNAP deep survey will be deeper than this, but further real data from the ACS on HST are awaited to accurately simulate the galaxy number counts and morphology distribution at these depths.

first sheared and then convolved with the full SNAP PSF shown in figure 6.2. For this application, it is essential that the shearing is applied before the smearing. Shear measurement methods have been designed to correct for precisely this sequence of events, which occurs in the real universe. However, our simulated galaxies were modelled on real HDF objects which had already been naturally convolved with the WFPC2 PSF when the HDF images were taken. Consequently, our simulations exhibit smoothing from both a circularised WFPC2 PSF, (plus shearing), plus a SNAP PSF. This double PSF artificially reduces the rms ellipticity of galaxies by approximately $\sim$2% and increases the size of a point source by 22%. One should note that the first PSF convolution occurs, and the galaxy orientations are randomized, all before shearing. This effect therefore corresponds to a small alteration in the intrinsic shape distribution of galaxies but does not bias the shear measurement.

Simulated images used to predict the lensing efficiency as a function of exposure time

(see §6.3.4) are produced differently. It is essential to ensure realistic size distributions and galaxy number counts in these simulations. However, they do not need to have an artificial shear added. The randomised orientations of simulated galaxies ensures that the mean shear is zero, with merely a scatter of object ellipticities due to their intrinsic shapes. The objects are then convolved by the PSF difference between the HST and SNAP. This is obtained by deconvolving the WFPC2 PSF from the SNAP PSF model, in shapelet space. Smoothing galaxies with this smaller kernel is enough to convert an observation with HST to one with SNAP, ensuring a correct distribution of galaxy sizes and rms ellipticity, although with zero mean shear.

6.3.2 Limitations of the simulations

Although every effort has been taken to ensure the realism of the image simulations, they are not completely perfect. We shall need to bear in mind the following limitations:

- **No instrumental distortions or cosmic rays**

  The SNAP wide survey strategy includes four dithered exposures at each pointing. This will enable the removal of cosmic rays and, if necessary, the simultaneous measurement of instrumental distortions. Because of the high orbit and slow thermal cycle, instrument flexure and the PSF are expected to be very stable (see Rhodes *et al.* 2003). It should therefore be possible to map internal distortions and compensate for them even on small scales, using periodic observations of stellar fields. Consequently, neither cosmic rays nor astrometric distortions are added to the simulations.

- **Single exposures**

  The SNAP CCD pixels are $0.1''$ in size and thus under-sample the PSF. To compensate for this, several dithered exposures will be stacked, as usual for HST images, using the DRIZZLE algorithm (Fruchter & Hook 2002). (Alternatively, galaxy shapes may be fitted simultaneously from all of the exposures.) DRIZZLE recovers some resolution, and will be particularly effective for the multiply-imaged SNAP deep survey, but has the side-effect of aliasing the image and correlating the noise in adjacent pixels. We have not yet included this entire pipeline in the simulations, but merely implemented a smaller pixel scale and model background noise that is higher in each pixel (although uncorrelated). Following the example of the Hubble Deep Field final data reduction, we choose $0.04''$ pixels. Unfortunately, the detection and shape measurement of very faint galaxies is sensitive to the precise noise properties of an image. Because of these instabilities, our simulated images are

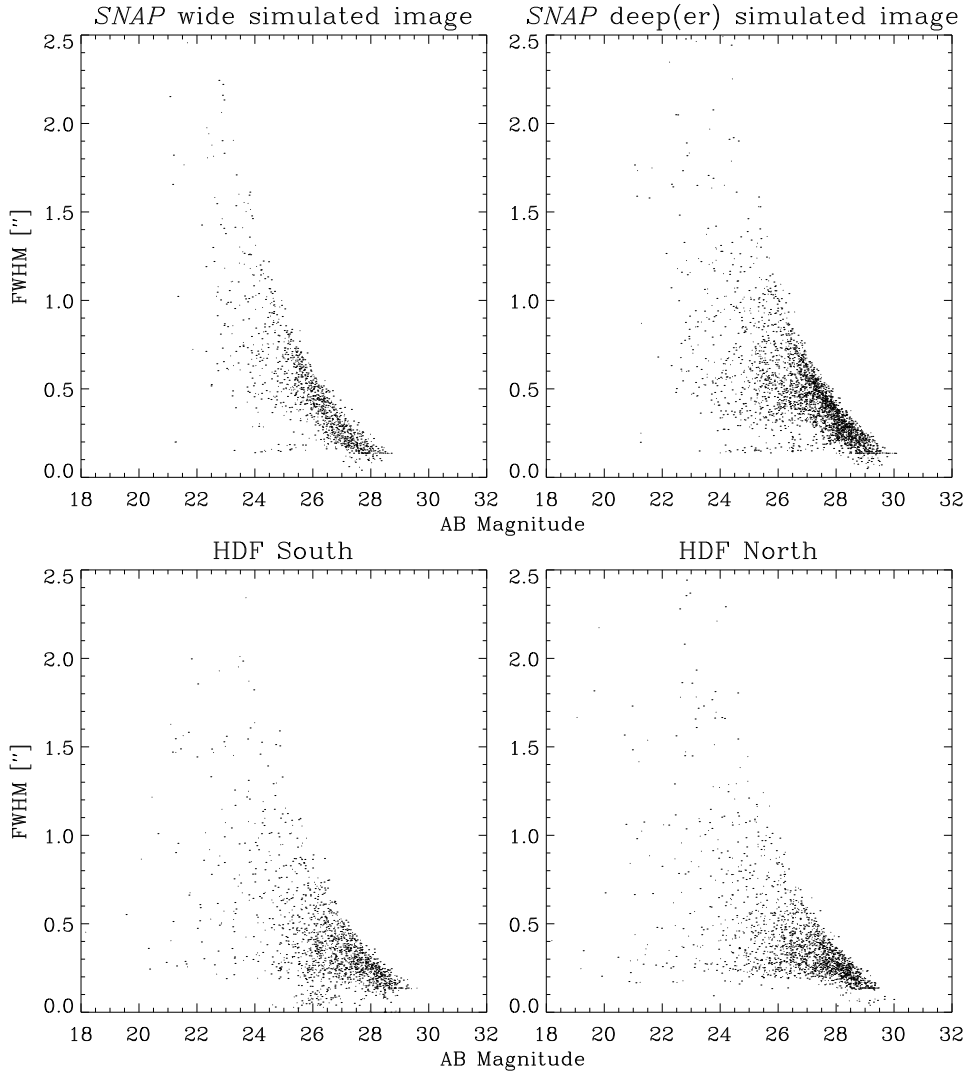

Figure 6.5: Size vs magnitude as determined by SExtractor with a S/N cutoff at $\nu = 1.5$. Top panels are for simulated SNAP I band images of the same size as the Hubble Deep Field. For reference, the bottom panels are of the HDFs themselves using the same SExtractor parameters.

only reliable down to approximately $I \simeq 29.5$ (see Massey *et al.* 2003). This is just below the magnitude cut applied by our shear measurement method at $I = 29.1$. A further investigation will include full use of DRIZZLE and more detailed noise models. We will also address the issue of pointing accuracy, and consider the consequences of 'dead zones' around the edges of the pixels which house the CCD electronics and are therefore unresponsive to light.

- **Based upon the HDF**

The image simulations are based upon the galaxies in the HDF, which is itself a special region of space selected to contain no large or bright objects. As a result,

our simulations do not yet include these either. The source catalogue is being expanded as GOODS ACS data becomes publicly available.

- **Monochromatic**

  The image simulations are currently monochromatic, in the HST $F814W$ (hereafter I) filter. Since gravitational lensing is achromatic, shear measurement can be performed in any band: indeed, all tested shear measurement methods so far use only one colour at a time. I or R bands are typically chosen for shear measurement because of the increased galaxy number density, advanced detector technology, and small PSF at these wavelengths. Surveys like COMBO17 (Brown *et al.* 2003), and VIRMOS/Descartes (van Waerbeke *et al.* 2002) are leading a trend to use additional multicolour photometry to provide photometric redshifts of the source galaxy population. The SNAP surveys will be simultaneously observed in 9 bands. We have not simulated this multicolour data, but it will inevitably raise the S/N of shear estimation for every source galaxy. At a minimum, image coaddition or simultaneous fits to shapes in several colours will increase the effective exposure time. Something more ambitious, like shifting to the rest-frame R or the rotating disc dis-alignment suggested by Blain (2002), might even reduce systematic measurement biases. Further work is needed in cosmic shear methodology to investigate the optimal use of multicolour data. However, it can already be said that our current monochromatic approach will yield a conservative estimate of the lensing sensitivity expected from future analyses.

6.3.3 Shear measurement method

We shall now attempt to recover the known input properties of our simulated images, by measuring galaxy shapes in the noisy data. The accuracy and calibration of shear measurement methods will determine the precision with which it will be possible to measure shear from any observations with a given level of noise. A selection of modern shear measurement methods are currently in development, which will be as sensitive or more sensitive than KSB. These methods include shapelets (Refregier & Bacon 2003; Refregier, Massey & Bacon in preparation) and others that incorporate higher-order or differently-normalised shape moments, Bayesian statistics, or other ideas (*e.g.* Bernstein & Jarvis 2002; Bridle *et al.* 2003; Kaiser 2000).

Of these, the most developed method is the shapelets-based shear measurement method described in Refregier & Bacon (2003). However, since the images themselves were created using shapelets, we shall not use the shapelets. We shall therefore conservatively restrict our investigation to using a variant of the KSB method developed by Rhodes, Refregier & Groth (2000; hereafter RRG). This method is optimised for space-

based observations, and has already been used extensively on HST images (Rhodes *et al.* 2001; Refregier *et al.* 2002). It is therefore ideal for our purposes. RRG differs from KSB by using unnormalised ellipticities during PSF correction, and assuming that the isotropic part of the PSF is Gaussian. This results in much simpler forms for P^{sh} and P^{sm}; and keeping the method linear for longer helps to make it more stable (*c.f.* Kaiser 2000). However, it is only possible to use unnormalised ellipticities because if number counts of objects is fairly stable between fields; and the extra condition on the PSF is really only justifiable for diffraction-limited observations from space.

Similarly to KSB, RRG forms a measure a galaxy's two-component ellipticity ϵ_i from the Gaussian weighted quadrupole moments of its surface brightness $I(\theta)$,

$$\epsilon_i \equiv \frac{\{J_{11} - J_{22},\ 2J_{12}\}}{J_{11} + J_{22}} \tag{6.2}$$

where

$$J_{ij} \equiv \frac{\int d^2\theta\ \theta_i\ \theta_j\ w(\theta)\ I(\theta)}{\int d^2\theta\ w(\theta)\ I(\theta)}\ , \tag{6.3}$$

and $w(\theta)$ is a Gaussian of width adjusted to match the galaxy size. The unweighted PSF moments are measured from a (simulated) starfield and RRG corrects the galaxy ellipticities to first order for PSF smearing. Occasional unphysical ellipticities, $|\epsilon| > 2$, are excluded, along with galaxies fainter than AB 26.5 (for the wide SNAP survey) or AB 29.1 (for the deep SNAP survey), or galaxies smaller than

$$R \equiv \sqrt{\frac{1}{2}\left(J_{11} + J_{22}\right)} \leq 1.7\text{pixels}. \tag{6.4}$$

These values have been chosen to yield reasonably stable results. RRG finally provides the shear susceptibility conversion factor, G, to generate unbiased shear estimators $\hat{\gamma}_i$ for an ensemble of objects, given by

$$\hat{\gamma}_i = \frac{\langle \epsilon_i \rangle}{G}\ , \tag{6.5}$$

where G depends upon the fourth order moments J_{ijkl} of a galaxy population, defined similarly to equation (6.3), and is equivalent to the P^{γ} factor in the KSB method. In our simulated SNAP images, G is of order 1.6.

An artificial shear has been applied uniformly upon all of the objects in a simulated 7.5 arcmin^2 deep SNAP survey image, in the $\gamma_2 = 0$ and $\gamma_1 = 0$ directions, before the addition of noise, and convolution with the SNAP PSF. Figure 6.6 demostrates the recovery using the RRG method to measure galaxy shapes and correct for the PSF smearing. The recovery is reassuringly linear, although the measured slope (dotted line) is underestimated compared to the expected response (dashed line). This inconsistency is probably due to instabilities in the KSB-family of shear measurement methods, and may disap-

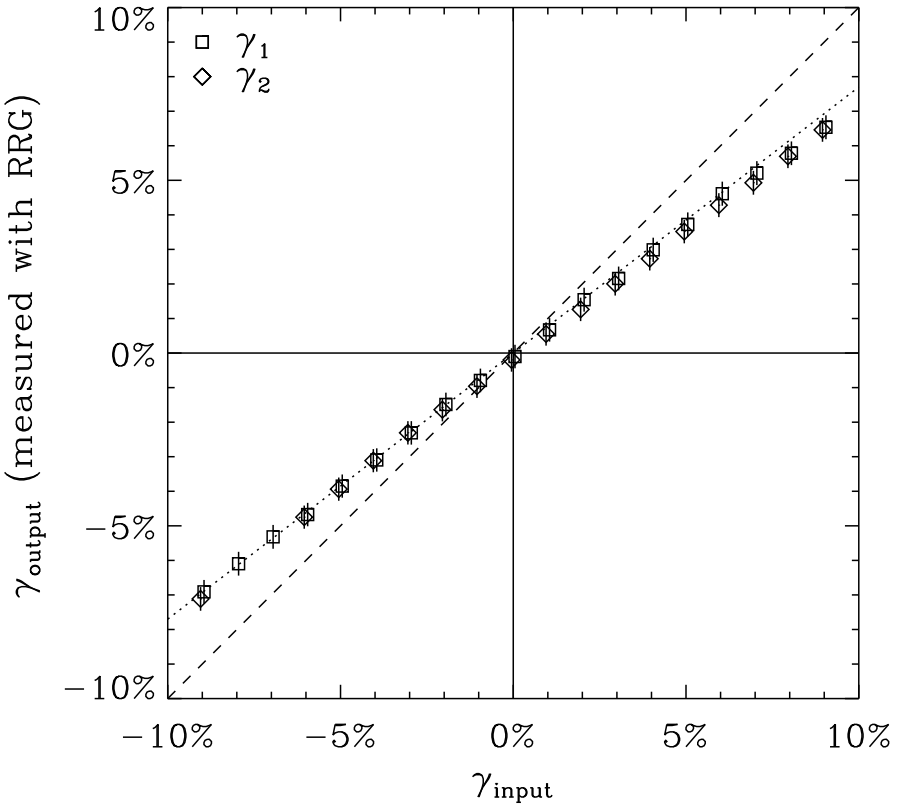

Figure 6.6: The applied shear γ_{in} in the shapelet simulated images vs its recovery γ_{out} using an independent measurement method (Rhodes, Refregier & Groth 2000). The image used is one 7.5 arcmin^2 realization of the SNAP deep survey shown in figure 6.4. The recovery is linear, but the slope of the fitted line (dotted) is flatter than that expected (dashed line).

pear with better techniques.

For the purposes of our current work, we see this calibration factor as vindication of the procedure adopted in chapter 3, where an almost identical bias of $(0.85 \pm 0.04)^{-1}$ was observed when the KSB method was applied to simulated WHT data by Bacon *et al.* (2001). We shall therefore apply this linear correction factor to the shears and their errors measured from WHT data in chapter 3. For the higher-resolution SNAP data, and at the depth of the SNAP wide survey, this factor is $(0.87 \pm 0.04)^{-1}$. At the depth of the HDF, the calibration factor is $(0.79 \pm 0.03)^{-1}$.

6.3.4 Shear sensitivity of SNAP

We shall now determine the accuracy with which it is possible to recover the input shear from the noisy data, under a variety of observing conditions. Trade-off studies are under way for several alternative telescope designs, including the level of CCD charge diffusion, the pixel size, the effect of DRIZZLEing, and the coefficient of thermal expansion

in the secondary struts, which may be the main cause of temporal variation in the PSF (see Rhodes *et al.* 2003). Here we present the results of a study which uses the baseline design specifications and time-averaged PSF of the SNAP satellite. In this section, the PSF used is the residual between the HST and SNAP PSFs (see §6.3.1), in order to keep the size distribution of galaxies realistic for SNAP images.

The top panel of figure 6.7 shows the surface number density n_g of galaxies in a survey of a given exposure time $t_{\rm exp}$ on SNAP. The exposure times reflect a $\sim 5\times$ overall improvement in instrument throughput and detector efficiency over WFPC2 on HST (Lampton *et al.* 2002). The dashed line shows the number density $n_{g,\rm tot}$ of all the galaxies detected by SExtractor, after a S/N cut which is equivalent to $I < 29.1$ at the depth of the HDF. As discussed in §6.3.3, galaxies which are too faint, too small, or too elliptical are excluded from weak shear catalogs. The solid line shows the number density n_g of galaxies which are useable for weak lensing following the magnitude, size and ellipticity cuts. The error bars reflect the uncertainty in measuring number counts at low S/N and an estimated sample variance between the HDF-N and HDF-S.

An important cut in the weak lensing analysis is the size cut, which reduces the detected galaxy sample by about 30% at the depth of the HDF. This fraction is a strong function of PSF size, and is thus much larger for ground based imaging. As can be inferred from the top panel of figure 6.7, the SNAP wide survey ($n_g \simeq 100$ galaxies arcmin^{-2}) will thus provide a dramatic improvement over current ground-based surveys ($n_g \sim 25$ galaxies arcmin^{-2} are used by most groups; see *e.g.* Bacon *et al.* 2002).

The second panel of figure 6.7 shows the median magnitude, $I_{\rm m}$, of the galaxy catalogue before and after cuts in size and ellipticity by the weak lensing analysis software. This has been converted to a median redshift, $z_{\rm m}$, using equation (6.9). For the purposes of this plot, we assume that this relationship is still valid even after the size cut.

The third panel of figure 6.7 shows the rms error $\sigma_\gamma = \langle|\gamma|^2\rangle^{1/2}$ per galaxy for measuring the shear, after the PSF correction and shear calibration. The slightly increasing error at longer $t_{\rm exp}$ reflects the decreasing size of fainter galaxies, and correspondingly less resolved information content available about their shapes. Note that even after applying the calibration factor of $(0.79 \pm 0.03)^{-1}$ determined in section §6.3.3, there remains a small but significant difference between the rms scatter of galaxy ellipticities in the simulations and in real Groth strip data (Rhodes, Refregier & Groth 2001). The standard shape measures of SExtractor used in section §5.3 were not sufficiently sensitive to detect this small discrepancy, but clearly RRG is more exacting. RRG measures σ_e to be lower in the simulated images by another factor of ~ 0.8: perhaps because of the precise properties of the simulated background noise, or perhaps because the wings of simulated objects are truncated beyond the SExtractor isophotal cutoffs. Work is in progress to establish the precise origin of this effect. For the purposes of this thesis, we simply increase the error bars by this amount.

To map the shear, the noise can be reduced by binning the galaxies into cells. The

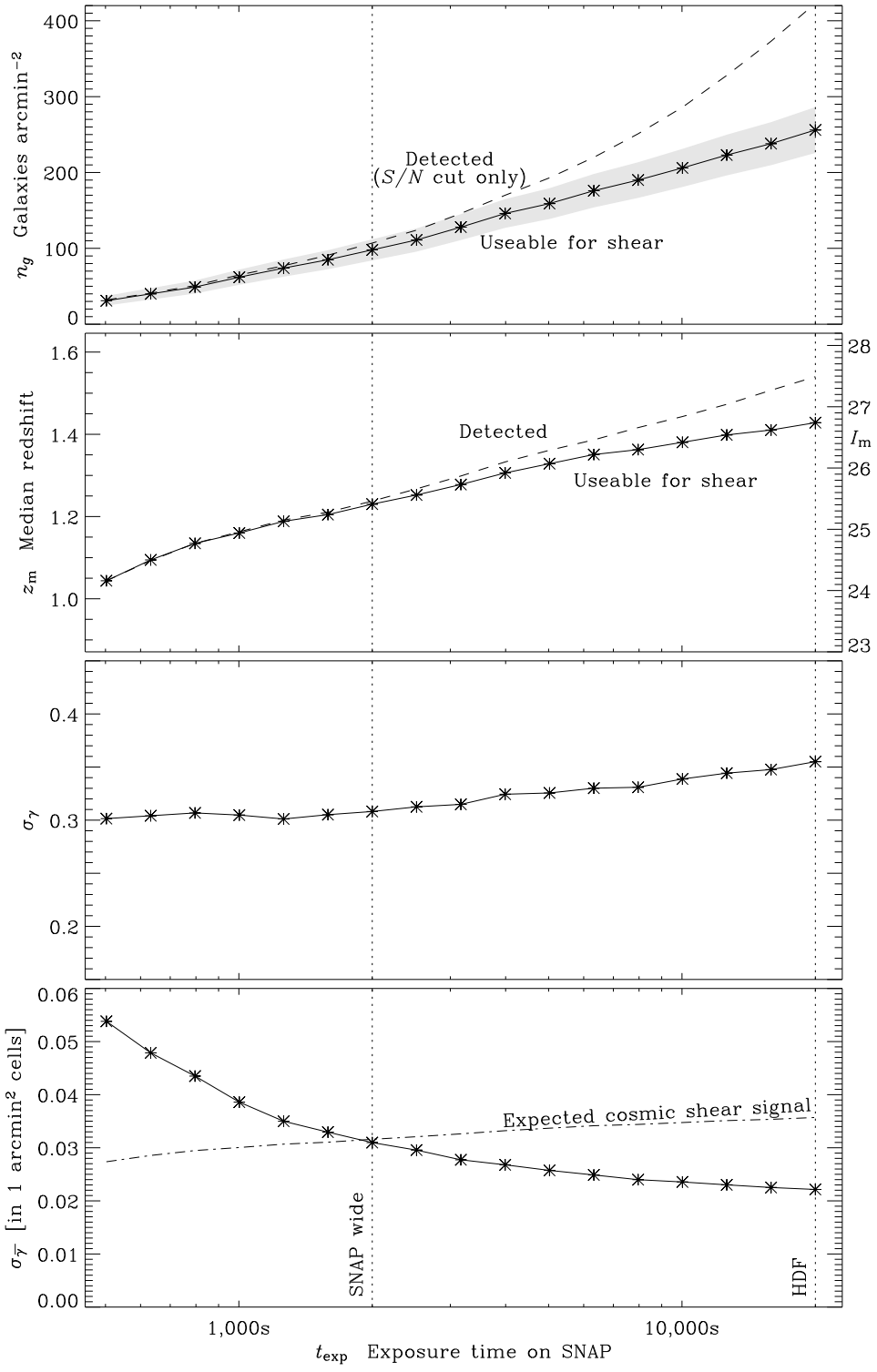

Figure 6.7: Shear sensitivity as a function of SNAP exposure time $t_{\rm exp}$. *Top panel*: the surface number density of all galaxies ($n_{g,\rm tot}$) detected by SExtractor and of the subset (n_g) of these useable for weak lensing, *i.e.* having survived further cuts in size and ellipticity by RRG (see text). *Second panel*: the median I band magnitude, $I_{\rm m}$, in the two subsets of the galaxy catalog, which has been interpreted as median redshift, $z_{\rm m}$, using equation (6.9). *Third panel*: the rms error $\sigma_\gamma = \langle|\gamma|^2\rangle^{1/2}$ per galaxy for measuring the shear γ, after PSF correction and shear calibration. *Bottom panel*: the rms error $\sigma_{\overline{\gamma}}$ for measuring the mean shear $\overline{\gamma}$ in 1 arcmin^2 bins. The dot-dashed line shows an estimate of the expected rms shear in a ΛCDM universe.

rms noise of the shear $\overline{\gamma}$ averaged in a cell of solid angle $A = 1$ arcmin^2 is given by

$$\sigma_{\overline{\gamma}} \simeq \frac{\sigma_\gamma}{\sqrt{n_g A}}, \tag{6.6}$$

and is plotted in the bottom panel of figure 6.7. The wide and deep SNAP surveys will thus afford a 1σ sensitivity for the shear of $\simeq 3.0\%$ and better than 2.2% on this scale, respectively. As a comparison, the rms shear expected from lensing on this scale in a ΛCDM model is approximately 3% (assuming $\Omega_{\rm m}$=0.3, Ω_Λ=0.7, σ_8=0.9, Γ=0.21). This signal increases with survey depth because the total lensing along a line of sight is cumulative. The wide SNAP survey will thus be ideal to map the mass fluctuations on scales of 1 arcmin^2, with an average S/N of unity in each cell. The recovery of simulated mass maps will be discussed in §6.4.2.

Note that the shear sensitivities presented here are conservative estimates, particularly for the deep SNAP survey. The image simulations extend so far only to the depth of the HDF. Future shear measurement methodology will also be more accurate and stable on any individual, resolved galaxy than the RRG method used in this paper. Higher order shape statistics (*e.g.* shapelets) will be used, as will simultaneous measurements in multiple colours and pre-selection of early-type galaxy morphologies.

6.3.5 Effect of size cut and pixel scale

Small, faint and highly elliptical objects are excluded from the final galaxy catalog in the RRG shear measurement method. Of all these cuts, it is the size cut that excludes the most objects. In an image at the depth of the HDF, about 30% of detected galaxies are smaller than our adopted size cut at $R = 1.7$ pixels. The exact position of this cut has been determined empirically to produce stable results, from experience with both HST data and our simulated images. The quantitative effects of moving the size cut are demonstrated in figure 6.8.

If the cut is moved to a larger size, fewer objects are allowed into the final galaxy catalog, and the shear field is sampled in fewer locations. Consequently, both dark matter maps and cosmic shear statistics become more noisy. If smaller galaxies are included in the catalog, the shear field is indeed better sampled, but the shape measurement error is worse on these galaxies. The bottom panel of figure 6.8 shows that moving the size cut to smaller objects has no net change in the precision of shear recovery: adding noisy shear estimators to the catalog neither improves nor worsens the measurement. A size cut at $R = 1.7$ pixels is optimal at the depth of the HDF and in the observing conditions modelled by our image simulations. To simplify comparisons of galaxy number density, the same cut has been applied to data at the depth of the SNAP wide survey. A different cut could have been adopted, producing fewer galaxies but each with more accurate shear estimators: the crucial figure $\sigma_{\overline{\gamma}}$ would not change. (This is especially true in the

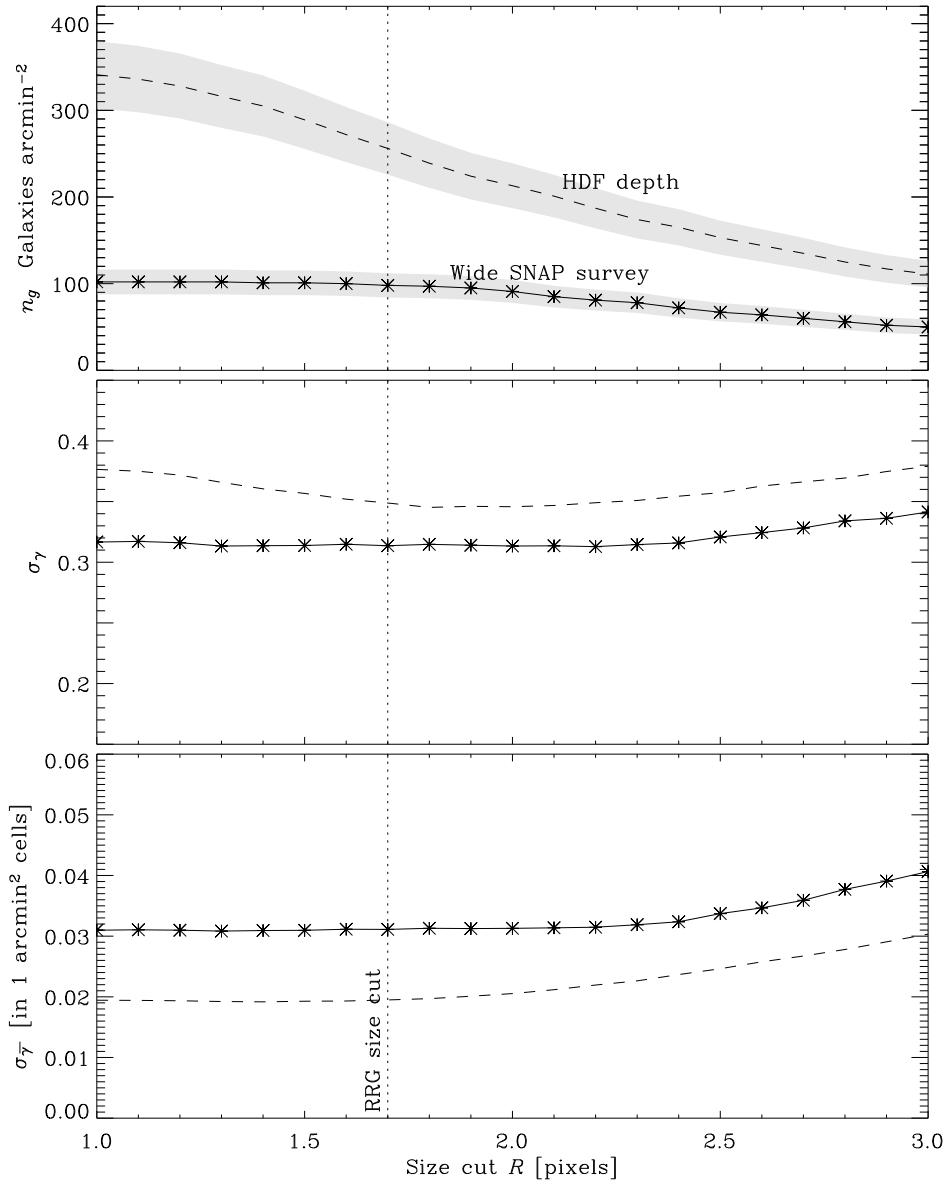

Figure 6.8: Shear sensitivity as a function of size cut R in the RRG shape measurement method for the wide SNAP survey (solid line) and at the depth of the HDF (dashed line). The vertical dotted line shows the fiducial value adopted elsewhere in our analysis. *Top panel*: the surface number density of galaxies useable for weak lensing. *Middle panel*: the rms error $\sigma_\gamma = \langle|\gamma|^2\rangle^{1/2}$ per galaxy for measuring the shear γ, after PSF correction and shear calibration. *Bottom panel*: the rms error $\sigma_{\overline{\gamma}}$ for measuring the mean shear $\overline{\gamma}$ in 1 arcmin^2 bins.

SNAP wide survey because of the relative dearth of small galaxies).

As described in section 6.3.2, we have assumed that an effective image resolution of 0.04″ can be recovered for SNAP data by taking multiple, dithered exposures, and either stacking them with the DRIZZLE algorithm or by fitting each galaxy's shape simultaneously in them all. The increase in image resolution from these techniques is vital for cosmic shear measurements. The number density of useable galaxies increases dramatically, and the measurement of their shapes is improved. Were it not possible to apply DRIZZLE or to recover this resolution, the large pixel scale currently proposed for SNAP would seriously impair shear measurement. A size cut at $R = 0.12''$ ($= 3$ pixels in figure 6.8) would roughly halve the number density of useable sources and correspondingly reduce the sensitivity to gravitational lensing.

6.3.6 Photometric redshift accuracy

Calculating the geometry of a gravitational lens system requires knowledge of the distance to the source galaxies. Although their shapes can be measured in any colour (usually R or I is most convenient), future lensing surveys will be greatly improved by multicolour observations for reliable photometric redshift (photo-z) estimation. This will reduce the current errors due to uncertainty in the redshift distribution of background sources, error from the single source sheet approximation; allow redshift tomography (Refregier et al. 2002); and even make possible an entirely 3D mass reconstruction, as demonstrated in Taylor (2003a), Hu & Keeton (2002), Bacon & Taylor (2002), Massey *et al.* (2003) and Jain & Taylor (2003). 3D cluster catalogues/dark matter mapping to literally trace the evolution of structure during cosmologically interesting epochs.

SNAP's thermally stable, 3-day long orbit is specifically designed for excellent photometry on supernovæ. Combining all 9 broad-band filters (6 optical, 3 NIR) will also provide an unprecedented level of photo-z accuracy, for all morphological types of galaxies over a large range of redshifts. In this section, we simulate SNAP photometric data in order to determine this precision.

The HYPERZ code (Bolzonella, Miralles & Pelló 2000) was used by Justin Albert to generate the observed magnitudes of a realistic catalog of galaxies following Lilly *et al.* (1995),

$$\frac{\mathrm{d}N}{\mathrm{d}I}(I) \simeq 10^{0.35\times I} \,, \tag{6.7}$$

where I is the I-band magnitude. The galaxies were assigned a distribution of Spectral Energy Distribution (SED) types similar to that in real data and containing ellipticals, spirals and starburst galaxies. Redshifts were assigned at random, and independently of spectral type, according to Koo *et al.* (1996) as verified by the DEEP collaboration (1999),

$$\frac{\mathrm{d}N}{\mathrm{d}z}(z) \simeq z^2 e^{-(z/z_m)^2} \,, \tag{6.8}$$

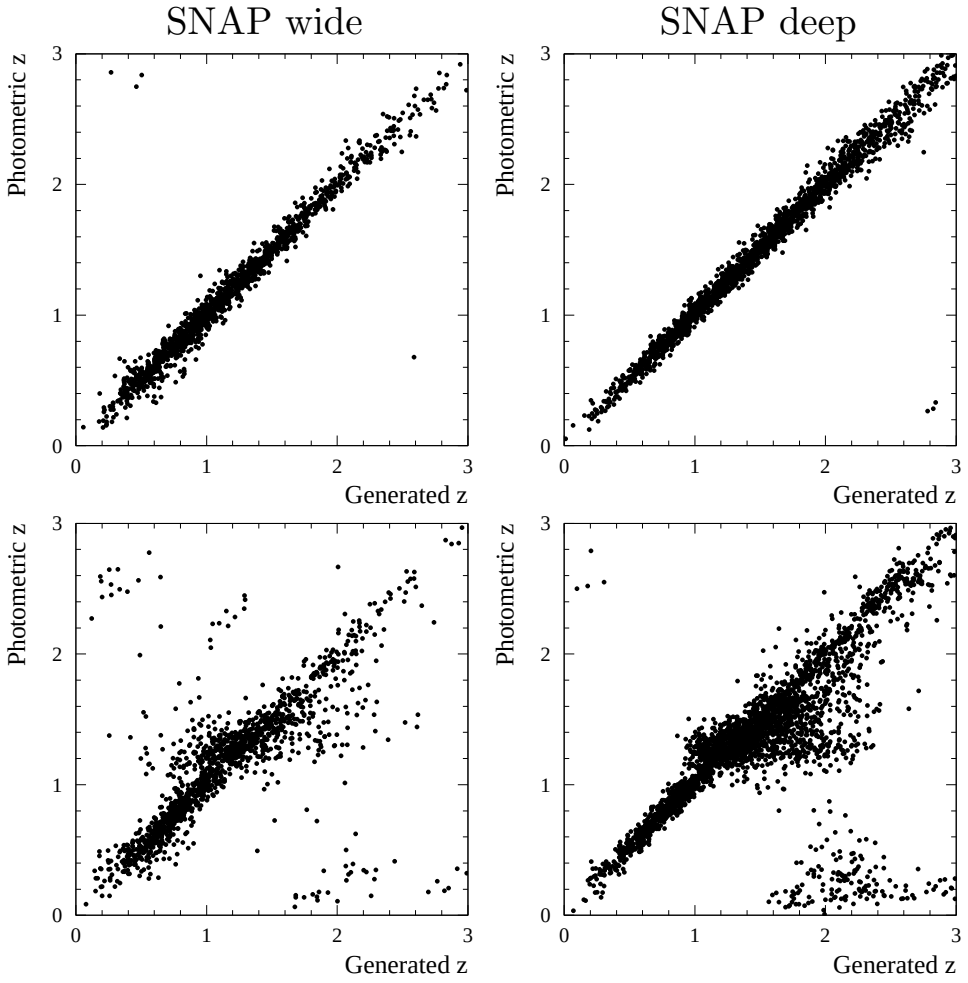

Figure 6.9: Recovery of redshifts of a realistic population of galaxies using HYPERZ with the SNAP filter set. *Top-left panel*: the wide survey, using all 9 colours. *Top-right panel*: the deep survey using all 9 colours. *Bottom row*: the same, but with only the 6 optical colours, as if the near IR HgCdTe data were not available.

where

$$z_m = 0.722 + 0.149(I - 22.0) \tag{6.9}$$

(Lanzetta, Yahil & Fernandez-Soto 1996). SNAP colours were then inferred by integrating the SED across filter profiles, adding an amount of noise corresponding to the exposure time and instrument throughput.

HYPERZ was then used again, to estimate redshifts for the simulated catalogue as if it were real data. Unlike the image simulations, the redshift catalogues can already be taken to the depth of both the wide and the deep SNAP surveys by extrapolating functional forms for the luminosity and redshift distributions in equations (6.7) and (6.8). Magnitude cuts were applied at AB 26.5 (wide) or AB 29.1 (deep) in R. Similar magnitude cuts were made in each filter, chosen at the 10σ detection level of an exponential disc galaxy with FWHM=0.12″ (Kim *et al.* 2002). Past experience with lensing data

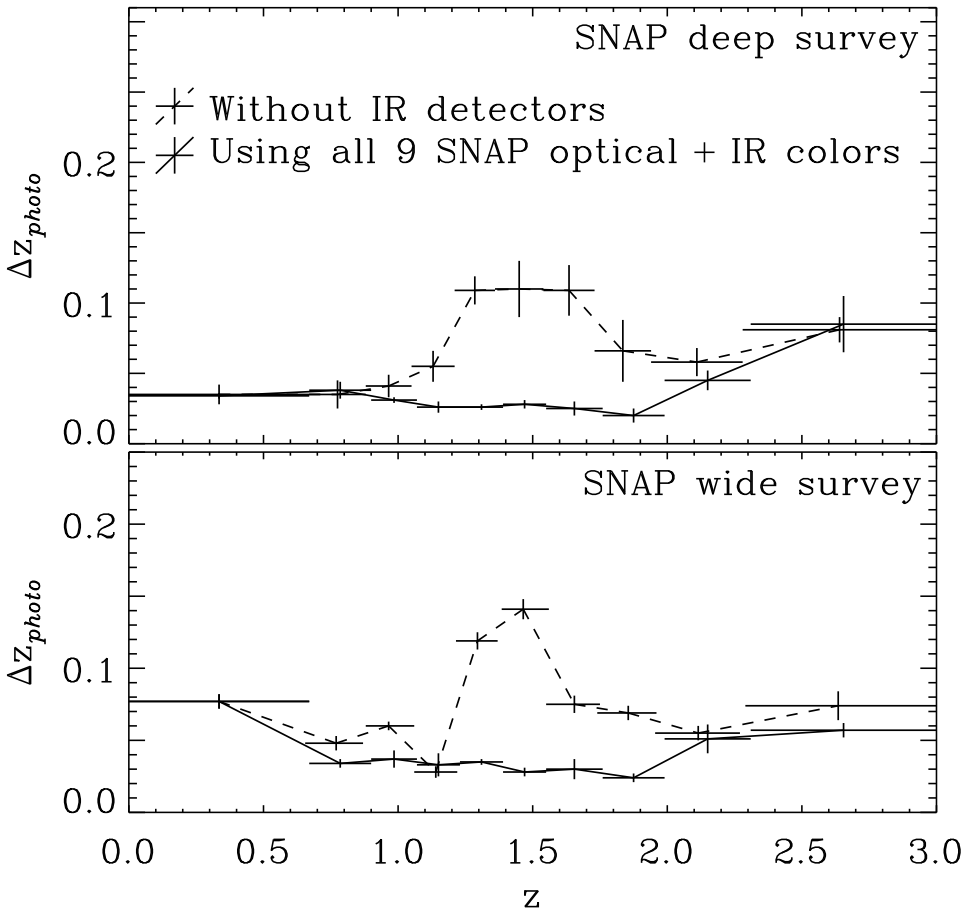

Figure 6.10: $\Delta z_{\rm photo}$, the rms scatter on photometric error estimation, as a function of increasing source redshift, z. Top panel: results for the SNAP deep survey. Bottom panel: results for the SNAP wide survey. In both cases, the solid line shows photometric redshift errors using observations in all 9 SNAP optical and near IR colours. The dashed lines show errors if the near IR HgCdTe data were unavailable.

(chapter 3 and Bacon *et al.* 2000) confirms that this is reasonable S/N limit. Note however that the size and ellipticity cuts implemented for the simulated images in §6.3.3 are not included in this procedure.

SNAP's stable 9-band optical and NIR imaging is ideal to produce exquisite photometric redshifts for almost all galaxies at $z \lesssim 3$ detected at 5σ in the I-band (see §6.3.6). This should be compared to the ∼38% completeness of photo-zs possible from the ground in the COMBO-17 data with a similar cut and a median redshift of $R \simeq 24$ (Brown *et al.* 2002). Figure 6.9 shows the precision of photometric redshifts in both the wide and deep SNAP surveys. All galaxy morphological types are included in this analysis. Clearly demonstrated is the need for the near IR HgCdTe detectors, a component of the satellite where a spacecraft has a clear advantage over the ground. Figure 6.10 shows the accuracy of the photo-zs as a function of source (photometric) redshift. Here,

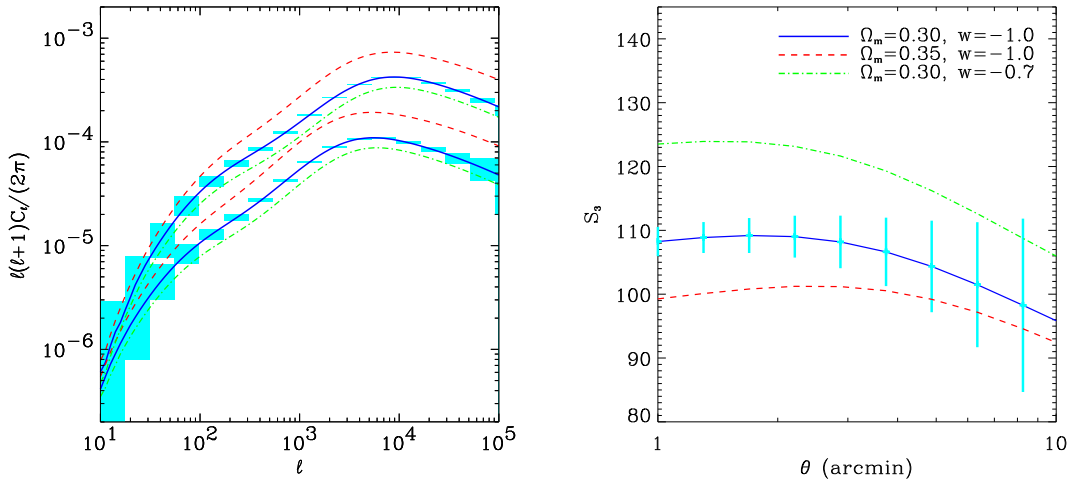

Figure 6.11: Weak lensing statistics for different cosmological models, adapted from Refregier *et al.* (2003b). Variations of 17% in Ω_m and of 30% in w about the fiducial ΛCDM model are displayed. Left: the weak lensing power spectrum C_l for two galaxy samples with median redshifts of 0.96 and 1.73. Right: skewness S_3 of the convergence κ as a function of scale θ. In each case, the expected band-averaged 1σ error bars for the SNAP weak lensing surveys are shown as blocks.

$\Delta z_{\rm photo}(z)$ is the rms of the core Gaussian in a double-Gaussian fit to horizontal slices through the distributions in figure 6.9.

6.4 Predicted performance of SNAP

6.4.1 Cosmological parameter constraints

Two- and three-point statistics of the cosmic shear field in the wide SNAP survey will be used to constrain cosmological parameters. Figure 6.11 shows the effect of varying Ω_m and w on the weak lensing power spectrum and skewness. The lensing power spectrum is shown for 2 bins of galaxy redshifts which can be derived from photometric redshifts. The error bars expected for the SNAP wide survey (using $A = 200$ deg^2, $\sigma_\gamma = 0.31$ and $n_g = 100$ deg^{-2}) are displayed. The excellent precision afforded by SNAP will easily distinguish the models shown, and thus detect small changes in the properties of dark energy (Refregier *et al.* 2003b).

The properties of the cosmic shear field can be quantified by several statistics. As before, we shall first use the basic weak lensing power spectrum (2.80). Considerable uncertainties remain for the non-linear power spectrum $P(k, z)$ in quintessence models (see discussion in Huterer 2001). Here, we shall use the prescription of Peacock & Dodds (1996) to evaluate it from the linear power spectrum. The growth factor and COBE normalization for arbitrary values of w can be computed using the fitting formulæ from Ma *et al.* (1999).

Non-linear gravitational instability is known to produce non-Gaussian features in the cosmic shear field. The power spectrum therefore does not contain all the information available from weak lensing. The most common measure of non-Gaussianity is the *skewness*

$$S_3(\theta) \equiv \frac{\langle \kappa^3 \rangle}{\langle \kappa^2 \rangle^2} \,, \tag{6.10}$$

where κ is the convergence which can be derived from the shear field γ_i and the angular brackets denote averages over circular top-hat cells of radius θ (Bernardeau *et al.* 1997). The denominator is the square of the convergence variance which is given by

$$\langle \kappa^2 \rangle = \langle \gamma^2 \rangle \simeq \frac{1}{2\pi} \int d\ell \; \ell C_\ell |W_\ell|^2 \,, \tag{6.11}$$

where $W_\ell \equiv 2\mathrm{J}_1(\ell\theta)/(\ell\theta)$ is the window function for such cells and C_ℓ is the lensing power spectrum given by equation (5). To evaluate the numerator $\langle \kappa^3 \rangle$ of equation (6), we use the approximation of Hui (1999) who used the Hyperextended perturbation theory of Scoccimarro & Frieman (1999). While more accurate approximations for third order statistics now exist (see van Waerbeke *et al.* 2001 and references therein), the present one suffices for our present purpose. The right-hand panel of figure 6.11 shows the skewness as a function of scale for the same cosmological models considered in the left-hand panel. The skewness is only weakly dependent on the angular scale θ, but depends more strongly on Ω_m and w.

We can compute the constraints which can be set on cosmological parameters using the *Fischer matrix*

$$F_{ij} = -\left\langle \frac{\partial \ln \mathcal{L}}{\partial p_i \partial p_j} \right\rangle \,, \tag{6.12}$$

where $\mathcal{L}$ is the Likelihood function, and p_i is a set of model parameters (*e.g.* Hu & Tegmark 1999). The inverse $\mathbf{F}^{-1}$ provides a lower limit for the covariance matrix of the parameters.

As a reference model, we consider a fiducial ΛCDM cosmology with parameters $\Omega_m = 0.30$, $\Omega_b = 0.047$, $n = 1$, $h = 0.7$, $w = -1$, consistent with the recent CMB measurements from the WMAP experiment (Spergel *et al.* 2003). In agreement with this experiment, we assume that the universe is flat, *i.e.* that $\Omega = \Omega_m + \Omega_Q = 1$. Note that the error ellipses vary in both size and orientation if a different fiducial cosmological model is used.

Figure 6.12 shows the constraints on the Ω_m–w plane that will be possible from a weak lensing analysis of the SNAP wide survey. The measurement of the weak lensing power spectrum at two different redshifts (or "redshift tomography") provides an important lever arm upon the growth of structure and the evolution of the power spectrum, improving the constraints significantly. Adding extra redshift bins has very little effect,

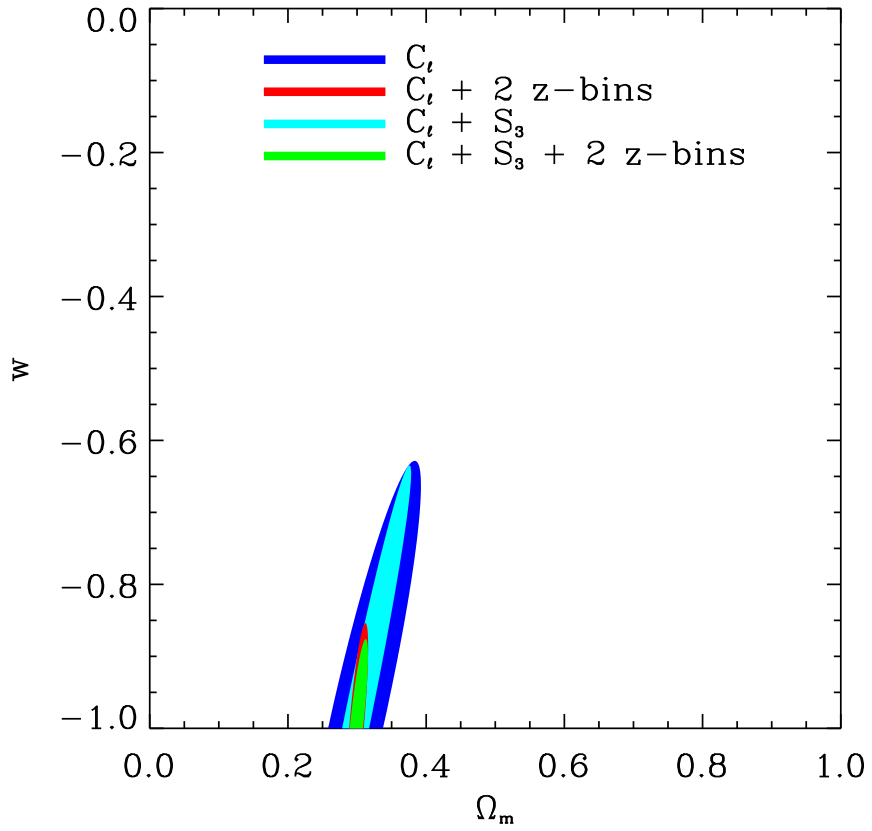

Figure 6.12: Predicted cosmological parameter constraints from SNAP weak lensing, reproduced from Refregier *et al.* (2003b). Contours show 68% CL limits constraints derived from the power spectrum C_l using the SNAP wide survey ($A = 300$ deg^2, $\sigma_\gamma = 0.31$ and $n_g = 100$ deg^{-2}). From top to bottom, the different colours show constraints with and without photometric redshifts, with the skewness S_3 and with all of them combined. A COBE normalisation prior was used.

because of the breadth of the lensing potential and the large overlap between foreground structures by each bin (making the bins narrower could also enhance the unwanted signal from intrinsic alignments). The addition of the skewness (at a single angular scale) does not improve the constraints much either. Figure 6.13 compares the constraints from weak lensing (using the power spectrum in two redshift bins and the skewness) to those which have been derived from a current supernova survey(Perlmutter *et al.* 1999) and a prediction for the SNAP supernova survey (Perlmutter *et al.* 2003; Kim *et al.* 2003; this includes systematic errors and a marginalisation over w', the time derivative of w). The SNAP weak lensing survey will therefore provide constraints on the nature of dark energy which are comparable with and complementary to those from the SNAP supernova survey.

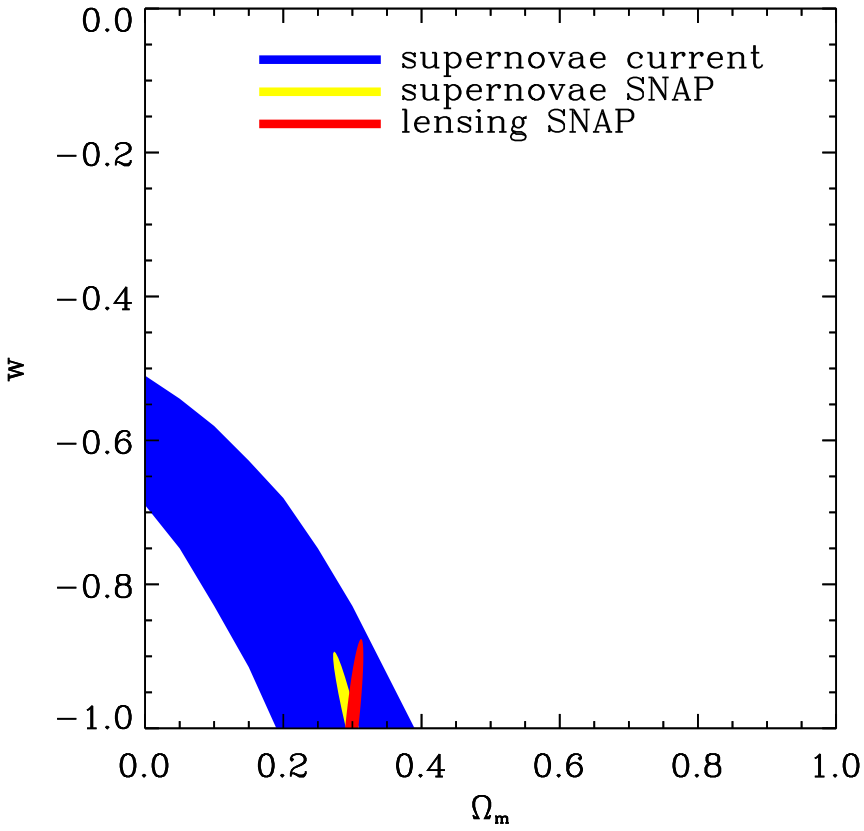

Figure 6.13: A comparison of the constraints derived from weak lensing with SNAP, reproduced from Refregier *et al.* (2003b). These constraints use the combined skewness and tomography statistics as before, but without the COBE prior. They are compared to constraints from current and future SNAP supernova surveys (Perlmutter *et al.* 1999; 2003).

6.4.2 Dark matter maps

We can also quantitatively predict the noise level present in the dark matter maps that could be produced from a space-based weak lensing survey. Because of the high number density of background galaxies resolved from space, this is one application where a mission like SNAP will fare particularly better than surveys from the ground.

To simulate observational data, we begin with shear maps created by raytracing through N-body simulations from Jain, Seljak & White (2000). We then add noise to these idealized data, corresponding to the predicted levels for SNAP or observing conditions at the currently most successful ground-based facilities. In each case, we then attempt to recover the input projected mass distribution by inverting the map of the shear into a map of the convergence κ. Convergence is proportional to the projected mass along the line of sight, by a factor depending on the geometrical distances between the observer, source and lensed galaxies (see *e.g.* Bartelmann & Schneider, 2001).

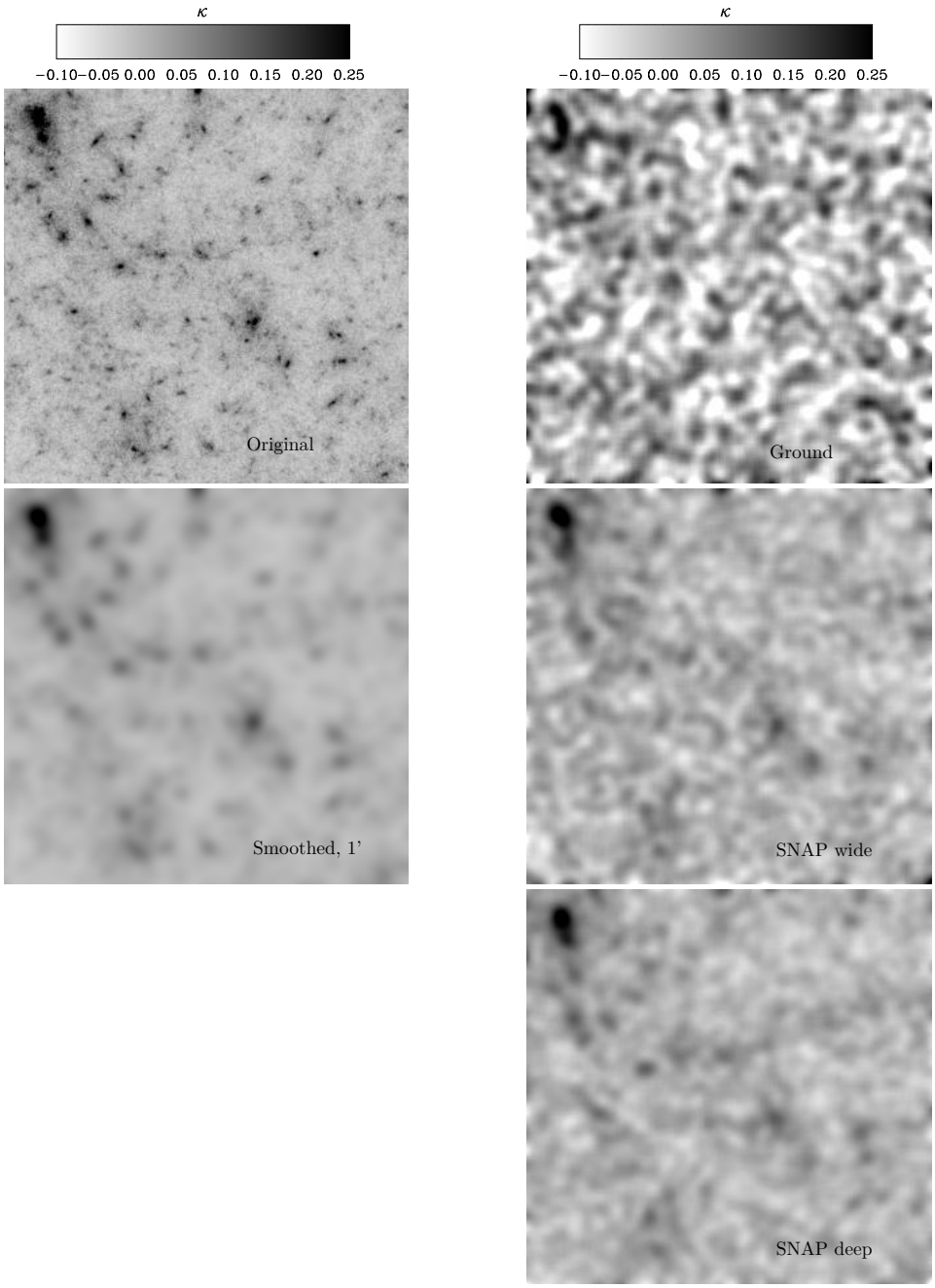

Figure 6.14: Reconstructed 2-dimensional maps of convergence κ, each $30' \times 30'$. Convergence is proportional to the total matter density along the line of sight, and can be deduced from the observed shear field. *Top-left panel*: simulated (noise-free) convergence map derived by raytracing through an SCDM N-body simulations of large-scale structure from Jain, Seljak & White (2000), in which the sources are assumed to lie at $z = 1$. *Bottom-left panel*: same map but smoothed with a Gaussian kernel with a FWHM of 1 arcmin. *Top-right panel*: Reconstruction of the convergence map with a noise realization corresponding to ground-based observations. Statistics are taken from a WHT survey by Bacon *et al.* 2002 ($n_g = 25$ arcmin^{-2} and $\sigma_\gamma = 0.39$). *Middle-right panel*: convergence map with much-improved recovery from the expected noise properties of the SNAP wide survey (*i.e.* $n_g = 105$ arcmin^{-2} and $\sigma_\gamma = 0.31$). *Bottom-right panel*: with accuracy expacted from the SNAP deep survey ($n_g = 259$ arcmin^{-2} and $\sigma_\gamma = 0.36$).

Figure 6.14 shows how the projected mass can be mapped from space and from the ground. The colour scale shows the convergence κ. The top panel of figure 6.14 shows a (noise-free) simulated convergence map from the ray tracing simulations of Jain, Seljak & White (2000) for an SCDM model. Underneath it is a version smoothed by a Gaussian kernel with an rms of $1'$ for comparison to the simulated recovery from observational data in the right-hand column. The right-hand column shows similarly smoothed mass maps that would be possible using (from top to bottom) a ground-based survey, the SNAP wide survey and the SNAP deep survey. These were produced by adding to κ, before smoothing, Gaussian random noise to each 1 arcmin^2 cell with an rms of $\sigma_{\overline{\gamma}}$ given by equation (6.6). For ground based observations, we set $\sigma_\gamma = 0.39$, and used $n_g = 25$ arcmin^{-2}, as is available for ground-based surveys (*e.g.* Bacon *et al.* 2002). For the SNAP wide and deep survey, the surface density of useable galaxies was taken to be $n_g = 105$ arcmin^{-2} and 259 arcmin^{-2}, and the rms shear noise per galaxy was taken to be σ_γ =0.31 and 0.36, respectively, as derived from figure 6.7. The galaxies are assumed to all have a redshift of z=1, which is a good approximation as long as the median redshift is approximately that value. As noted above, the surface density and median redshift will actually be higher for the SNAP deep survey, because only exposure times corresponding to that of the HDF were simulated.

From the ground, only the strongest features are resolved (*i.e.* massive clusters). From space, the very high density of resolved background galaxies allows the recovery of uniquely detailed maps, including some of the filamentary structure and individual mass overdensities down to the scale of galaxy groups and clusters. Thus, SNAP offers the potential of mapping dark matter over very large fields of view, with a precision well beyond that achievable with ground-based facilities.

The masses and locations of individual clusters can be extracted from such maps using, for example, the $M_{\rm ap}$ statistic (Schneider 1996; 2002), which has been applied successfully to find mass peaks in several surveys (*e.g.* Hoekstra *et al.* 2002a; Erben *et al.* 2000) andour own work; or the inversion method of Kaiser & Squires (1993; KS) which was used by Miyazaki *et al.* (2002). Marshall, Hobson & Slosar (2003) demonstrate the effectiveness of maximum entropy techniques to identify structures in KS lensing maps, using criteria set by Bayesian evidence. White *et al.* 2002 argue that using any detection method, a complete mass-selected cluster catalogue from 2D lensing data would require a high rate of false-positive detections, since the prior probability is for them to be *anywhere* throughout a given survey. This has been avoided in practice by secondary cross-checks of the lensing data with spectroscopy, deep x-ray temperature or SZ observations. Indeed, two previously unknown clusters have already been found in weak lensing maps and spectroscopically confirmed by Wittman *et al.* (2001; 2003). However, this does make it harder to resolve the debate on the possible existence of baryon-poor "dark clusters" (*e.g.* Dahle *et al.* 2003). These are a speculative population of clusters which would be physically different to and absent from the catalogues of optically or

x-ray selected clusters. Remaining dark-lens candidates (Erben *et al.* 2000; Umetsu & Futamase 2000; Miralles *et al.* 2002) have currently been eliminated as chance alignments of background galaxies (or possibly associations with nearby ordinary clusters Gray *et al.* 2001; Erben *et al.* 2003). If others could be found in high S/N weak lensing maps, they would present a challenge to current models of structure formation, and need to be accounted for in estimates of $\Omega_{\rm m}$; but they would be unique laboratories in which to decipher the nature of dark matter.

6.4.3 Outlook

A wide field, space-based imager would be ideally suited to observe weak gravitational lensing. We have used the relevant aspects of the baseline design for SNAP (Rhodes *et al.* 2003), and the shapelet-based image simulation method (chapter 5) to predict SNAP's sensitivity to shear, taking explicitly into account its instrumental throughput, limitations and sensitivity. This design is almost optimal because many requirements to find supernovæ are the same as those to measure weak lensing (stable imaging, small PSF, and excellent multicolour photometry).

The increased image resolution available from space makes possible the construction of high resolution projected dark matter maps with an rms shear sensitivity of $\sim$2.5% in every 1′ cell for the 300 square degrees wide SNAP survey and better than 1.8% for the SNAP deep survey (*c.f.* the expected mean signal in a ΛCDM universe is approximately 3%). Since gravitational lensing is sensitive to mass regardless of its nature or state, these maps will be unique tools for both astrophysics and cosmological parameter estimation. Statistical properties of the dark matter distribution will be precisely measured at several cosmological epochs and constraints made on $\Omega_{\rm m}$, σ_8 and w_q.

SNAP's simultaneous 9-band observations also open up new opportunities for 3-dimensional mapping via photometric redshift estimation (Taylor 2003a; Hu & Keeton 2002; Bacon & Taylor 2002). SNAP's photometry allows an excellent resolution of $\Delta z = 0.034$ in redshift. Massey *et al.* (2003) show that SNAP will measure mass concentrations in full 3D with a 1σ sensitivity of approximately $1 \times 10^{13} M_\odot$ at $z \simeq 0.25$ and $\simeq 5 \times 10^{13} M_\odot$ at $z \simeq 0.5$. In this fashion it will be possible to directly trace the non-linear growth of mass structures, and test the gravitational instability theory with high precision.

Space-based wide field imaging can be combined with weak shear measurements to produce 2D and 3D mass-selected cluster catalogues down to the scale of galaxy groups. Mass and light in the local universe can be mapped out with exquisite precision, thus offering exciting prospects for both astrophysics and cosmology.

7

Conclusions

We have measured the weak gravitational lensing "cosmic shear" signal, using independent surveys on two telescopes. This technique is sensitive to all mass, regardless of its nature and state, and our measurement does not rely upon the calibration of unknown physical processes like the x-ray mass-temperature relation. Cosmic shear is therefore an invaluable probe of the distribution of dark matter in the universe, and a direct measure of the amplitude of mass fluctuations. These are more easily predicted by theory than the indirect and complicated distribution of light. However, the most important challenges facing all measurements of weak gravitational lensing concern the control of systematic error. Imperfect telescope tracking, engineering faults within the telescope or optical misalignment within the camera, even at a level that is acceptable for most purposes, can artificially distort images and coherently elongating the shapes of adjacent galaxies in a way that mimics cosmic shear. Almost all such effects can therefore falsely increase the observed signal. They have been controlled in our surveys by careful data reduction, and data analysis techniques that have been calibrated upon simulated images with a known amount of shear. The agreement between our two independent surveys, along with statistical cross-checks that include an E-B decomposition of the observed shear fields, confirm that systematic contaminations are at a negligible level in our results.

By combining the surveys, we have measured the amplitude of the matter power spectrum $\sigma_8 \left(\frac{\Omega_m}{0.3}\right)^{0.52} = 1.09 \pm 0.12$, with $0.25 < \Omega_m < 0.8$, including all contributions to the 68% CL uncertainty: statistical noise, sample variance, covariance between angular bins, systematic effects, redshift uncertainty, and marginalisation over priors on other

parameters. This normalisation parameter is quite poorly constrained by other cosmological tests, which still disagree at the 3σ level, and which exhibit strong degeneracies with other parameters. Our measurement is relatively high, and one must remain aware that any unnoticed and uncorrected systematics would tend to lead to an overestimation of σ_8. However, our measurement does agree within 1σ with other cosmic shear results from deep surveys (van Waerbeke *et al.* 2002; Refregier *et al.* 2002; Rhodes *et al.* 2003). Our results are also consistent within 1.5σ with WMAP CMB results (Spergel *et al.* 2003), and agree with the old cluster abundance normalisation (Eke *et al.* 1998; Viana & Liddle 1999; Pierpaoli *et al.* 2001). Our results disagree at the 3σ level with newer estimates of the cluster-abundance normalisation, derived using an observational rather than a theoretical mass-temperature relation (Borgani *et al.* 2001; Seljak 2001; Rieprich & Böhringer 200; Viana *et al.* 2001). This discrepancy could arise from unknown systematics in either the cluster abundance or cosmic shear methods. Further studies are particularly needed to understand the difference between the observed mass-temperature relation and that determined from numerical simulations.

Our results are also incompatible at the 2–3σ level with results from shallower cosmic shear surveys by Hoekstra *et al.* (2002) and Jarvis *et al.* (2002). This discrepancy could be caused by either the different shape measurement methods used in these surveys (the object selection cuts vary, and neither of those methods have been calibrated upon simulated images). The discrepancy could alternatively arise from uncertainty in the redshift distribution of the background, source galaxies in deep data. This uncertainty should be definitively resolved by the incorporation of DEEP2 galaxy redshifts into future cosmic shear surveys, or by future wide-field imaging surveys in multiple colours from space.

We have extended the formalism of the "polar shapelets" technique for image analysis. Shapelets hold promise as a useful method both for shear measurement (Bacon & Refregier 2003; Massey, Refregier & Bacon in prep.), and for the quantitative classificaation of galaxy morphologies (*e.g.* Kelly & McKay 2003). We can now take observational effects into account, including noise, pixellisation and PSF convolution, during the decomposition of galaxy images from real data. We have developed techniques to improve the overall image reconstruction by finding the scale length β and number of modes $n_{\max}$ that produce the best shapelet coefficient fit; and we have written a practical, iterative algorithm to optimise the decomposition of objects in arbitrary images. The main component of this procedure is a careful choice of the scale size of the shapelet basis functions. We have also derived many useful new results in the formalism of polar shapelets, including expressions for galaxy photometry, astrometry and size parameters as linear combinations of shapelet coefficients, as well as higher-order quantitative galaxy morphology diagnostics.

We have applied shapelets in this thesis to simulate deep sky images of an arbitrarily large survey area, as might be observed from extended observations with the Hubble Space Telescope. The simulated images are populated with all morphological types of

galaxies, based upon those in the Hubble Deep Fields. In order to generate the morphology distribution, we decompose all HDF galaxies into shapelet components. These form a cloud of points in shapelet space, which we smooth to recover the underlying probability distribution of real galaxy morphologies. The smoothed distribution is then resampled, using an unbiased Monte-Carlo technique, to obtain new galaxies.

We place these simulated galaxies onto HDF-sized images, simultaneously including effects such as PSF, pixellisation, photon shot noise and Gaussian background noise. The level of detail in the resulting simulated galaxies includes features such as realistic radial profiles, spiral arms, dust lanes and resolved knots of star formation. We have noted that the global morphological properties of the simulated galaxy population must match those of real galaxies if our simulations are to be useful. We have demonstrated that this is the case by comparing various morphology diagnostics in simulated and real galaxies, including number counts as a function of magnitude, the size distribution, ellipticity distribution, and concentration, asymmetry and clumpiness indices. A test involving purely the shapelet decomposition and reproduction of the HDF galaxies preserves all of these statistics with high precision, and we conclude that a shapelet decomposition can successfully capture the morphological properties of all galaxy types. A few slight discrepancies are introduced to the statistics by perturbing their shapelet coefficients (or smoothing the morphology distribution) to manufacture genuinely new galaxy shapes. However, these differences are small compared to the natural variations between objects. Several minor effects have been well quantified by our various tests, and their causes understood for correction in future implementations.

The image simulations are in no way specific to gravitational lensing, and may be used for testing image analysis in various branches of astronomy. However, an important application has been to predict the sensitivity to weak gravitational lensing of future weak lensing surveys, using the proposed Supernova/Acceleration Probe (SNAP) satellite as a concrete example. The baseline specifications from engineering models of SNAP were used to tune the simulations to produce images from a wide-field space-based mission. Any such mission will face similar engineering constraints and science requirements for imaging quality, PSF stability, and multicolour photometry.

We have studied the accuracy with which weak lensing measurements could be made from a variety of survey strategies with SNAP, predicting the subsequent precisions of parameter constraints and mass reconstructions. We incorporate a realistic redshift distribution of source galaxies, and calculate the average precision of photometric redshift recovery using the SNAP filter set to be $\Delta z = 0.034$. By combining the power spectrum measured in several redshift bins and the skewness of the convergence field, we find that the SNAP wide survey will provide a measure w and Ω_m with a 68%CL uncertainty of approximately 12% and 1.5% respectively. These errors include marginalization over other cosmological parameters.

The high density of background galaxies resolved from space allows projected dark

matter maps with a rms sensitivity of 3% shear (and therefore S/N≈ 1) in 1 arcmin^2 cells. This will be further improved by the SNAP deep survey, which will be able to detect isolated clusters using a 3D lensing inversion techniques with a 1σ mass sensitivity of approximately $10^{13} M_{\odot}$ at $z = 0.25$ (Massey *et al.* 2003). Weak lensing measurements from space will thus be able to capture non-Gaussian features arising from gravitational instability and map out dark matter in the universe with unprecedented resolution. Since lensing is also sensitive to all mass, regardless of its nature and state, these maps will be unique tools for both astrophysics and cosmological parameter estimation in the near future.

References

Abazajian K. & Dodelson S. 2003, Phys. Rev. Lett. 91, 041301

Abraham R. *et al.* 1996, ApJS 107, 1

Aldering G. *et al.* 2002, Proc. SPIE 4835, 21

Amara A. & Refregier A. 2003, MNRAS submitted [astro-ph/0310345]

Bacon D., Massey R., Refregier A. & Ellis R. 2000, MNRAS 318, 625

Bacon D., Refregier A., Clowe D. & Ellis R. 2001, MNRAS 325, 1065

Bacon D., Refregier A., Ellis R. 2000, MNRAS 318, 625

Bacon D. & Taylor A. 2003, MNRAS 344, 1307

Bartelmann M., King J. & Schneider P. 2001, A&A 378, 361

Bartelmann M. & Schneider P. 2001, Physics Reports 340, 291

Baugh C., Cole S., Frenk C., Lacey C. 1998, ApJ 498, 504

Bernardeau F. 1999. *Proc. Cargese Summer Sch.*, Cargese, France, ed. M. Lachieze-Rey [astro-ph/9901117]

Bernardeau F., van Waerbecke L. & Mellier Y. 1997, A&A 322, 1

Bernardeau F., van Waerbecke L. & Mellier Y. 2002, A&A 389, 28

Bernstein G. & Jarvis M. 2002, AJ 123, 583 (BJ02)

Bershady M., Jangren A. & Conselice C. 2000, AJ 119, 2645

Bertin E. & Arnouts S. 1996, A&AS 117, 393

Blain A. 2002, ApJ 570, L51

Blandford R., Saust A., Brainerd T., Villumsen J. 1991, MNRAS 251, 600

Blinnikov S. & Moessner R. 1998, A&AS 130, 193

Boas M. 1983, "Mathematical Methods in the Physical Sciences" (London: Wiley)

Bolzonella M., Miralles J.-M. & Pelló R. 2000, A&A 363, 476

Borgani S., Rosati P., Tozzi P., Stanford S., Eisenhardt P., Lidman C., Holden B., Della Ceca R., Norman C., Squires G. 2001, ApJ 561, 13.

Boulade O. *et al.* 2000, Proc. SPIE "Astronomical Telescopes and Instrumentation 2000"

Bouwens R., Broadhurst T. & Silk J. 1998a, ApJ 506, 557

Bouwens R., Broadhurst T. & Silk J. 1998b, ApJ 506, 579

Brown M., Taylor A., Bacon D., Gray M., Dye S., Meisenheimer K. & Wolf C. MNRAS 341, 100

Brown *et al.* 2002, MNRAS submitted [astro-ph/0210213]

Carter D., Bridges T. 1995, *WHT Prime Focus and Auxiliary Port Imaging Manual* available at `http://lpss1.ing.iac.es/manuals/html_manuals/wht_instr/pfip`

Casertano S., Ratnatunga K. & Griffiths R. 2003, ApJ 598, L71

Catelan P., Kamionkowski M. & Blandford R. 2001, MNRAS 320, L7

Chang T. & Refregier A. 2002, ApJ 570, 447

Clowe D., Trentham N. & Tonry J. 2001, A&A 369, 16

Colless M. 1999, Phil.Trans.Roy.Soc.Lond. 357, 105

Cohen J., Hogg D., Blandford R., Cowie L., Hu E., Songaila A., Shopbell P. & Richberg K. 2000, ApJ 538, 29

Conselice C., Bershady M., Dickinson M. & Papovich C. 2003, AJ 126, 1183

Conselice C., Bershady M. & Gallagher J. 2000b, A&A 354, L21

Conselice C., Bershady M. & Jangren A. 2000a, ApJ 529, 886

Conselice C., Gallagher J. & Wyse R. 2002, AJ 123, 2246

Conselice C. 2003, ApJS 147, 1

Cooray A., Hu W. & Miralda-Escudé J. 2000, ApJ 535, L9

Copi C., Schramm D. & Turner 1995, Science 267, 192

Crittenden R., Natarajan P., Pen U.-L. & Theuns T. 2000, ApJ 559, 552

Croft R. & Metzler C. 2000, ApJ 545, 561

Dahle H., Pedersen K., Lilje P., Maddox S. & Kaiser N. 2003, ApJ 591, 662

Dahle H., *et al.* 2002, ApJ 139, 313

Dalal N., Holz D., Chen X. & Frieman J. 2003, ApJ 585, L11

Davis M., Newman J., Faber S. & Phillips A. 2000, Proc. of the ESO/ECF/STSCI workshop on Deep Fields

de Vaucouleurs G. 1959, Hand. Physik 53, 275

Dekel A. & Lahav O. 1999, ApJ 520, 24

Driver S. 1999 in "Looking Deep in the Southern Sky", eds F. Morganti and W. Couch. (Berlin: Springer-Verlag)

Einstein A. 1917, Sitzungsberichte der Königlich Preussischen Akademie der Wissenschaften 1, 142

Eke V., Cole S., Frenk C., Henry H. 1998, MNRAS 298, 1145

Epanechnikov V. 1969, Theory of Probability and Its Applications, 14, 153

Erben T., van Waerbeke L., Bertin E., Mellier Y. & Schneider P. 2001, A&A 366, 717

Erben T., van Waerbeke L., Mellier Y., Schneider P., Cuillandre J.-C., Castander J. & Dantel-Fort M. 2000, A&A 355, 23

Francis P. & Wills B. 1999, in "Quasars and Cosmology", A.S.P. conference series, eds. G. Ferland, J. Baldwin

Frenk C., White S. & Davis M. 1983, ApJ 271, 417

Fruchter A. & Hook R. 2002, PASP 114, 144

Gerhard O. 1993, MNRAS 265, 213

Goldberg D. & Natarajan P. 2002, ApJ 564, 65

Gray M., Ellis R., Lewis J., McMahon R. & Firth A. 2001, MNRAS 333, 544

Gray M., Taylor A., Meisenheimer K., Dye S., Wolf C. & Thommes E. 2002, ApJ 568, 141

Groth E. *et al.* 1994, BAAS, 185, 5309

Hämmerle *et al.* 2002, A&A 385, 743

Hamana T. *et al.* 2003, ApJ 597, 98

Heavens A., Refregier A. & Heymans C. 2000, MNRAS 319, 649

Heymans C. & Heavens A. 2003, MNRAS 339, 711

Heymans C., Brown M., Heavens A., Meisenheimer K., Taylor A. & Wolf C. 2003, MNRAS in press [astro-ph/0310174]]

Hoekstra H., Franx M., Kuijken K., Squires G. 1998, ApJ 504, 636

Hoekstra H., Yee H., Gladders M., Felipe Barrientos L., Hall P. & Infante L. 2002a, ApJ 572, 55

Hoekstra H., Yee H. & Gladders M. 2002b, ApJ 577, 595

Hoekstra H., van Waerbeke L., Gladders M., Mellier Y. & Yee H. 2002b, ApJ 577, 604

Hu W. & Keeton C. 2002, Phys. Rev. D 66, 3506

Hu W. & Tegmark M. 1999, ApJ 514, L65

Hubble E. 1926, ApJ 64, 321

Hui L. & Zhang J. 2003, ApJ submitted [astro-ph/0205512]

Huterer D. & White M. 2002, 578, L95

Jain B., Seljak U. & White S. 2000, ApJ 530, 547

Jain B. 2002, ApJ 580, L3

Jain B. & Seljak U. 1997, ApJ 484, 560

Jain B. & Taylor A. 2003, Phys. Rev. Lett. 91, 1302

Jarvis M. *et al.* 2003, AJ 125, 1014

Jing Y. 2002, MNRAS 335, L89

Joffre M. *et al.* 2000, ApJ 534, L131

Kaiser N., Squires G. & Broadhurst T. 1995, ApJ 449, 460 (KSB)

Kaiser N., Wilson G. & Luppino G. 2000, ApJ submitted [astro-ph/0003338]

Kaiser N. 1992, ApJ 388, 272

Kaiser N. 1998, ApJ 498, 26

Kaiser N. 2000, ApJ 537, 555

Kaiser N. & Squires 1993, ApJ 404, 441

Kaiser *et al.* 2002, http://poi.ifa.hawaii.edu/poi/documents/poi_book.pdf

Kamionkowski M., Babul A., Cress C. & Refregier A. 1998, MNRAS 301, 1064

Kauffmann G., Guiderdoni B. & White S. 1994, MNRAS 267, 981

Kim A. *et al.* 2002, Proc. SPIE 4836, 10

King L. *et al.* 2002, A&A 385, L5

King L. & Schneider P. 2003a, A&A 396, 411

King L. & Schneider P. 2003b, A&A 398, 23

Koo D. *et al.* 1996, ApJ 469, 535

Krist J. 1995, in "ADASS IV", A.S.P. conference series 349

Krist J. & Hook R. 1997, "The Tiny Tim User's Guide" (Baltimore: STScI)

Lahav O. *et al.* 2001, MNRAS 333, L961

Lampton M. *et al.* 2002a, Proc. SPIE 4849, 29

Lampton M. *et al.* 2002b, Proc. SPIE 4854, 80

Lanzetta K., Yahil A. & Fernandez-Soto A. 1996, Nature 381, 759

Lilly S. *et al.* 1995, ApJ 455, 108

Luppino G. & Kaiser N. 1997 , ApJ 475, 20

Lupton R. 1993, "Statistics in Theory and Practice" (Princeton: Princeton University Press)

Maoli R., van Waebeke L., Mellier Y., Schneider P., Jain B., Bernardeau F., Erben T., Fort B. 2001, A&A 368, 766

Marleau F. & Simard L. 1998, ApJ 507, 585

Marshall P., Hobson M. & Slosar A., MNRAS submitted [astro-ph/0307098]

Massey R., Bacon D., Refregier A. & Ellis R. 2001, A.S.P. conference series 283, 193, eds. T. Shanks & N. Metcalfe.

Massey R., Refregier A., Conselice C. & Bacon D. 2003, MNRAS in press [astro-ph/0301449]

Massey R., Refregier A., Rhodes J. *et al.* 2003, AJ submitted [astro-ph/0304418]

Mellier Y. 1999, ARA&A 37, 127

Meyer Y. 1993, "Wavelets: Algorithms and Applications", (Philadelphia: Society for Industrial and Applied Mathematics)

Miralles J.-M., Erben T., Haemmerle H., Schneider P., Fosbury R., Freudling W., Pirzkal N., Jain B. & White S. 2002, A&A submitted [astro-ph/0202122]

Miyazaki S. *et al.* 2002a, ApJ 580, L97

Miyazaki S. *et al.* 2002b, PASJ 54, 833

Mould J., Blandford R., Villumsen J., Brainerd T., Smail I., Small T., Kells W. 1994, MNRAS 271, 31

Munshi D. & Jain B. 2001 MNRAS 322 107

Myller-Lebedeff W. 1908, Mathematische Annalen, 64, 388

Odewahn S., Windhorst R., Driver S. & Keel W. 1996, ApJ 472, L13

Pen U., van Waerbeke L. & Mellier Y. 2002, ApJ 567, 31

Peng C., Ho L., Impey C., Chris D. & Rix H.-W. 2002, AJ 124, 226

Percival W. *et al.* 2001, MNRAS 327, 1297

Perlmutter S. *et al.* 1999, ApJ 517, 565

Perlmutter S. *et al.* 2003 `http://snap.lbl.gov`

Petrosian V. 1976, ApJ 209, L1

Piña R. & Puetter R. 1993, P.A.S.P., 105, 630

Pierpaoli E., Scott D. & White M. 2001, MNRAS 325, 77

Ratnatunga K., Griffiths R. & Ostrander E. 1999, AJ 118, 86

Refregier A., Rhodes J. & Groth E. 2002, ApJ 572, L131

Refregier A. 2003, MNRAS 338, 35 (Shapelets I)

Refregier A. & Bacon D. 2003, MNRAS 338, 48 (Shapelets II)

Refregier A. 2003, ARA&A 41, 645

Refregier A., Massey R., Rhodes J. *et al.* 2003, AJ submitted [`astro-ph/0304419`]

Reiprich T. & Böhringer H. 2002, ApJ 567, 716

Rhodes J., Refregier A., Groth E. 2000, ApJ 536, 79

Rhodes J., Refregier A. & Groth E. 2001, ApJ 552, L85

Rhodes J., Refregier A., Massey R. *et al.* 2003, AJ submitted [`astro-ph/0304417`]

Sérsic J. 1968, "Atlas de Galaxias Australes" (Cordoba: Obs. Astronomico)

Sain S. 1999, "Multivariate Locally Adaptive Density Estimation", Technical Report, Department of Statistical Science, Southern Methodist University

Sandage A. 1961, "The Hubble Atlas of Galaxies" (Washington: Carnegie Institute)

Schneider P., Ehlers J. & Falco E. 1992, "Gravitational Lenses", (Heidelberg: Springer Verlag)

Schneider P., van Waerbeke L. & Mellier Y. 2002, A&A 389, 729

Schneider P. 1996, MNRAS 283, 837

Schneider P. & Lombardi M. 2003, A&A 397, 809

Seljak U. 2001, MNRAS 337, 769

Silverman B. 1986, "Density Estimation for Statistics and Data Analysis" (London: Chapman and Hall)

Simard L. 1998, in "ADASS VII", A.S.P. conference series 145, 108

Smith G., Edge A., Eke V., Nichol R., Smail I. & Kneib J.-P. 2003, AJ 590, L79

Smith R., Peacock J., Jenkins A., White S., Frenk C., Pearce F., Thomas P., Efstathiou G. & Couchmann H. 2003, MNRAS 341, 1311

Stark J.-L., Pantin E. & Murtagh F. 2002, PASP 114, 1051

Szalay A. *et al.* 2003, ApJ 591, 1

Taylor, A. 2003a, Phys. Rev. Lett. submitted [`astro-ph/0111605`]

Taylor, A. 2003b, Davis Inflation Meeting [`astro-ph/0306239`]

Tody D. 1993, in "ADASS II", A.S.P. conference series 52, eds. R. Hanisch, R. Brissenden & J. Barnes, 173

Tyson A. *et al.* 2002, `http://www7.nationalacademies.org/bpa/1LSST.pdf`

Tytler D., Fan X. & Burles S. 1996, Nature 381, 207

Tytler D., O'Meara J., Suzuki N. & Lubin D. 2000, Physica Scripta 85, 12

Umetsu K. & Futamase T. 2000, ApJ 539, L5

van den Bosch F., Abel T., Croft R., Hernquist L. & White S. 2002, ApJ 576, 21

van der Marel R. & Franx M. 1993, ApJ 407, 525

van der Marel R. *et al.* 1994, MNRAS 268, 521

van Waerbeke L., Bernardeau F., Mellier Y. 1999, A&A 342, 15

van Waerbeke L. *et al.* 2000, A&A 358, 30

van Waerbeke L. *et al.* 2001, A&A 374, 757

van Waerbeke L., Mellier Y., Pelló R., Pen U.-L., McCracken H. & Jain B. 2002, A&A 393, 369

van Waerbeke L. *et al.* 2002, A&A 393, 369

van Waerbeke L. *et al.* 2002, proc. XVIII IAP Coll. [astro-ph/0212150]

Viana P., Liddle, A. 1996, MNRAS 281, 323

Viana P., Nichol R. & Liddle A. 2002, ApJ 569,75

Weinberg D., Davé R., Katz N. & Hernquist L. 2003, ApJ submitted [astro-ph/0212356]

Weinberg N. & Kamionkowski M. 2002 MNRAS 337 1269

White M., van Waerbeke L. & Mackey J. 2002, ApJ 575, 640

White S., Frenk C. & Davis M. 1983, ApJ 274, L1

White S., Davis M. & Frenk C. 1984, MNRAS 209, 27

Williams R. *et al.* 1996, AJ 112, 1335

Williams R. *et al.* 1998, A&AS 193, 7501

Wittman D., Tyson T., Kirkman D., Dell'Antonio I. & Bernstein G. 2000, Nature 405, 143

Wittman D., Tyson T., Margoniner V., Cohen J. & Dell'Antonio I. 2001, ApJ 557, L89

Wittman D. 2002. Lect. Notes Phys. 608, 55

Wittman D., Margoniner V., Tyson T., Cohen J. & Dell'Antonio I. 2003, ApJ 597, 218

York D. 2000, AJ 120, 1579

Errata